# Evaluation of the effect of diagenetic cements on element/Ca ratios in aragonitic Early Miocene (~16 Ma) Caribbean corals: Implications for 'deep-time' palaeo-environmental reconstructions

Naomi Barbara Griffiths

A thesis submitted in fulfilment of the requirements for the degree of Master of Philosophy at the University of London

Department of Earth Sciences
Royal Holloway College
University of London

January 2015

## Declaration:

I declare that the work presented in this thesis submitted to Royal Holloway University of London in fulfilment of the requirements for the degree of Master of Philosophy is all my own and where the work of others has been included their contribution has been acknowledged and fully referenced.

Naomi Griffiths

8th FEBRUARY 2015

# Abstract

The skeletons of scleractinian corals incorporate elemental and isotopic signatures that reflect ambient seawater conditions during the time of coral growth and thus represent important geochemical archives for palaeo-environmental reconstruction.

Most previous studies have focussed on Holocene and Late Pleistocene corals however attention has recently turned towards probing pre-Pleistocene records. This thesis examines for the first time the skeletal preservation and geochemistry of ~16 Ma old corals from the southern Caribbean.

Early Miocene corals from the Paraguaná Peninsula, northern Venezuela and modern specimens from Florida and Bermuda were investigated. X-ray diffraction analyses showed 1-2% calcite contamination in the fossil specimens. Light and electron microscopy revealed regions of excellent preservation juxtaposed with zones in-filled by several generations of aragonite and calcite cements in both fossil and modern corals. Brucite cements were confined to the modern coral specimens while pyrite, dolomite and hydrocarbon residues were noted in the fossil samples. Endolithic macro- and micro-boring activity was evident in both modern and fossil coral samples. Targeted laser ablation depth profile analyses showed increased Sr/Ca and decreased Mg/Ca ratios in aragonite cements compared to the values recorded in primary skeletal aragonite. For calcite cements these trends were reversed. B/Ca ratios were lower in both aragonite and calcite cements compared to primary aragonite. Estimates of the effect of 1% contamination by aragonite cements on Sr/Ca, Mg/Ca, B/Ca and U/Ca -based temperature reconstructions for the fossil corals produced anomalies of -1.2$^{o}$C, -0.2$^{o}$C, +0.3$^{o}$C and -0.1$^{o}$C respectively. Similar percentage calcite cement contamination produced temperature anomalies of +1.7$^{o}$C, +2.7$^{o}$C, +0.3$^{o}$C and -0.1$^{o}$C. Highly elevated and depleted Ba/Ca signatures were found in aragonite and calcite cements respectively, therefore care has to be exercised when reconstructing past flood or upwelling events from fossil corals. Targeted spatially-resolved analysis of well-preserved Early Miocene corals may yield reliable ‘deep-time’ palaeo-proxy information.

# Table of Contents

**Title Page** 1

**Declaration** 2

**Abstract** 3

**Table of Contents** 4

**List of Figures** 10

**List of Tables** 12

**Acknowledgements** 13

**Chapter 1: Introduction** 14

**1.1** General introduction 15

**1.1.1** Coral reef environments and distribution 15

**1.1.2** The Caribbean and northern South America in the Early Miocene 16

**1.1.3** Coral geochemical archives, proxies and diagenesis 17

**1.2** Aims and objectives of the thesis 18

**1.3** Chapter summaries 19

**Chapter 2: Fieldwork and physiography of the Paraguaná Peninsula, Bermuda and the Florida Keys** 23

**2.1** General introduction 24

**2.1.1** Early Miocene coral reef assemblages 24

**2.1.2** Rarity of well-preserved aragonitic fossil corals 25

**2.1.3** Hypotheses to be tested 27

**2.2** Fieldwork 27

**2.2.1** Field work methods and collection of sample materials 27

**2.2.2** Field locations (Cantaure Formation), Paraguaná Peninsula 29

**2.3** Physiography and climatic setting of the Paraguaná 33

**2.3.1** Cantaure Formation 35

**2.3.2** Lithology 35

**2.3.3** Fossil assemblages and environment of deposition 36

**2.4** Physiography and climatic setting of Bermuda 37

**2.5** Physiography and climatic setting of the Florida Keys 39

**Chapter 3: Materials and methods** **41**
**3.1** General introduction **42**
**3.2** Corals **42**
**3.2.1** Modern corals **42**
**3.2.1.1** *Siderastera siderea* (Ellis and Sollander, 1786) **43**
**3.2.1.2** *Siderastrea radians* (Pallas, 1766) **46**
**3.2.2** Miocene corals **48**
**3.2.2.1** *Siderastrea conferta* (Duncan, 1863) **48**
**3.2.2.2** *Montastraea limbata* (Duncan, 1863) **51**
**3.2.2.3** *Porites* (Link, 1807) **54**
**3.3** Laboratory methods **57**
**3.4** Imaging and X-ray diffraction **58**
**3.4.1** Digital imaging **58**
**3.4.1.1** Preparation of coral heads for imaging **58**
**3.4.1.2** Digital photography **58**
**3.4.2** Micro-computerised tomography (micro-CT) **59**
**3.4.2.1** Preparation of coral samples for micro-CT **59**
**3.4.2.2** Micro-CT imaging **60**
**3.4.3** Light microscopy **62**
**3.4.3.1** Thin section preparation **62**
**3.4.3.2** Light microscope imaging **62**
**3.4.4** Scanning electron microscopy (SEM) **62**
**3.4.4.1** Scanning electron microscope imaging **62**
**3.4.5** X-radiography **63**
**3.4.5.1** X-radiographic imaging **63**
**3.4.6** X-ray diffraction analysis (XRD) **63**
**3.4.6.1** Sample preparation for XRD **64**
**3.4.6.2** XRD analysis **65**
**3.5** Geochemical analysis **65**
**3.5.1** Measurement of element/Ca ratios by laser ablation inductively-coupled plasma mass spectrometry (LA-ICPMS) **65**
**3.5.1.1** Sample preparation for LA-ICPMS **66**
**3.4.1.2** Laser ablation inductively-coupled mass spectrometry **66**

**3.5.2** Laser ablation depth profile analysis **67**
**3.5.3** Measurement of the depth of material removed per laser pulse **68**
**3.5.4** $^{87}Sr/^{86}Sr$ isotope analysis **69**
**3.5.4.1** Sample preparation for $^{87}Sr/^{86}Sr$ isotope analysis **70**
**3.5.4.2** Strontium separation chromatography **71**
**3.5.4.3** **‘**Cathodeon’ bead preparation **71**
**3.5.4.4** Preparation and cleaning of the sample-holder and turret assembly **72**
**3.5.4.5** Isotopic analysis **72**
**3.5.4.6** Sr isotope data handling and correction **72**
**3.5.4.7** Determination of fossil coral age using strontium isotope stratigraphy **73**

**Chapter 4: Imaging and assessment of coral preservation** **74**
**4.1** General introduction **75**
**4.2** Description of the corals in hand specimen **77**
**4.2.1** Modern coral samples in hand specimen **77**
**4.2.2** Miocene coral samples in hand specimen **79**
**4.2.2.1** Surface weathering and staining **79**
**4.2.2.2** Hydrocarbon charging **80**
**4.2.2.3** Endolithic macroboring **80**
**4.2.2.4** Distribution of diagenetic alteration and hydrocarbon charging **80**
**4.3** Light microscopy **87**
**4.3.1** Observations on petrographic thin sections **87**
**4.3.1.1** Secondary aragonite cements **88**
**4.3.1.2** Calcite cements **89**
**4.3.1.3** Calcite neomorphism **90**
**4.3.1.4** Hydrocarbons **91**
**4.3.1.5** Cement and hydrocarbon distribution **91**
**4.3.1.6** Detrital grains **91**
**4.3.2** Binocular microscopy **91**
**4.4** Scanning electron microscopy **102**
**4.4.1** Modern corals **102**

**4.4.1.1** Secondary aragonite cements **102**
**4.4.1.2** High-magnesium calcite cements **104**
**4.4.1.3** Brucite cement **104**
**4.4.1.4** Bioerosion **105**
**4.4.2** Fossil corals **115**
**4.4.2.1** Secondary aragonite cements **115**
**4.4.2.2** Calcite cements **116**
**4.4.2.3** Iron sulphides **116**
**4.4.2.4** Dolomite **117**
**4.4.2.5** Brucite **117**
**4.4.2.6** Hydrocarbons **117**
**4.4.2.7** Bio-erosion and micro-boring **118**
**4.4.2.8** Dissolution **118**
**4.5** X-radiography **128**
**4.6** X-ray diffraction analysis **131**
**4.7** Assessment of preservation of primary aragonite in modern and fossil coral specimens **133**
**4.8** Conclusions **137**

**Chapter 5: The effect of cements on element/Ca ratios in fossil corals: Implications for palaeo-SST reconstructions** **138**
**5.1** General introduction **139**
**5.2** Geochemical composition of primary coral aragonite and cements **140**
**5.3** Sr/Ca **140**
**5.3.1** Sr/Ca ratios in skeletal aragonite and diagenetic cements **146**
**5.3.1** Diagenetic cements and estimated Sr/Ca temperature anomalies **147**
**5.4** Mg/Ca **148**
**5.4.1** Mg/Ca ratios in skeletal aragonite and diagenetic cements **148**
**5.4.2** Diagenetic cements and estimated Mg/Ca temperature anomalies **149**
**5.5** Ba/Ca **150**
**5.5.1** Ba/Ca ratios in skeletal aragonite and diagenetic cements **151**
**5.6** B/Ca **152**

**5.6.1** B/Ca ratios in skeletal aragonite and diagenetic cements **153**
**5.6.2** Diagenetic cements and estimated B/Ca temperature anomalies **154**
**5.7** U/Ca **154**
**5.7.1** U/Ca ratios in skeletal aragonite and diagenetic cements **155**
**5.7.2** Diagenetic cements and estimated U/Ca temperature anomalies **155**
**5.8** Conclusions **156**

**Chapter 6: The age of the Cantaure Formation** **158**
**6.1** General introduction **159**
**6.2** Coral age estimation **160**

**Chapter 7: Summary and Conclusions** **163**
**7.1** Summary **164**
**7.1.1** Assessment of skeletal preservation and diagenetic alteration **164**
**7.1.1.1** Observations on preservation and diagenesis **165**
**7.1.1.2** Modern coral diagenesis **165**
**7.1.1.3** Fossil coral diagenesis **167**
**7.1.2** Geochemical composition of primary coral aragonite and secondary cements **170**
**7.1.2.1** Sr/Ca **170**
**7.1.2.2** Mg/Ca **171**
**7.1.2.3** B/Ca **172**
**7.1.2.4** Ba/Ca **173**
**7.1.2.5** U/Ca **174**
**7.2** Conclusions **175**

**References** **177**
**Appendix 1** Otolith-based fish species from the Cantaure Formation, Falcón State, Venezuela. **199**
**Appendix 2** Mineral Powder Diffraction File Databook. Sets 1- 42. 1993. International Centre for Diffraction Data, Pennsylvania, USA. Conversion chart of 2θ to angstroms (D-spacing) for Cu *K-α* radiation compiled **202**

by M.J. Smith, University of Durham, UK.

**Appendix 3** Digital images showing LA-ICPMS targeted regions and tables showing element/Ca ratios and calculated temperature anomalies. **204**

**Appendix 4** Publications. **210**

# List of Figures

**Chapter 2:**


| | | |
|---|---|---|
| 2.1 | Satellite image showing Cantaure Fm collection sites | **29** |
| 2.2 | Collection locality photographs | **31** |
| 2.3 | Cantaure Fm macrofossil photographs | **32** |
| 2.4 | Sketch map of the Paraguaná Peninsula and the Cantaure Fm | **34** |
| 2.5 | Sketch map of Bermuda and the North Atlantic | **37** |
| 2.6 | Sketch map of north east Bermuda and Whalebone Bay | **38** |
| 2.7 | Sketch map of the Florida Keys | **39** |


**Chapter 3:**


| | | |
|---|---|---|
| 3.1 | Schematic diagram illustrating *S. siderea* septal plan | **44** |
| 3.2 | Schematic diagram illustrating *S. radians* septal plan | **46** |
| 3.3 | Schematic diagram illustrating *S. conferta* septal plan | **49** |
| 3.4 | Schematic diagram illustrating *M. limbata* septal plan | **52** |
| 3.5 | Schematic diagram illustrating *Porites* generic septal plan | **55** |
| 3.6 | Schematic cross-section showing micro-CT scanning set-up | **60** |


**Chapter 4:**


| | | |
|---|---|---|
| 4.1 | Modern coral samples hand specimen photographs | **78** |
| 4.2 | *S. conferta* hand specimen photographs | **81** |
| 4.3 | *S. conferta* hand specimen photographs | **82** |
| 4.4 | *S. conferta* corallite photographs | **83** |
| 4.5 | *M. limbata* hand specimen photographs | **84** |
| 4.6 | *M. limbata* hand specimen photographs | **85** |
| 4.7 | *Porites* sp hand specimen photographs | **86** |
| 4.8 | *S. conferta* petrographic thin section photographs | **93** |
| 4.9 | *S. conferta* diagenetic cement thin section photographs | **94** |
| 4.10 | *S. conferta* diagenetic cement thin section photographs | **95** |
| 4.11 | *M. limbata* petrographic thin section photographs | **96** |
| 4.12 | *M. limbata* diagenetic cement thin section photographs | **97** |
| 4.13 | *M. limbata* diagenetic cement thin section photographs | **98** |

| | | |
|---|---|---|
| 4.14 | *Porites* sp petrographic thin section photographs | **100** |
| 4.15 | Diagenetic cement binocular microscope photographs | **101** |
| 4.16 | *S. radians* scanning electron microscope (SEM) images | **107** |
| 4.17 | High magnesium calcite cement SEM images | **109** |
| 4.18 | Brucite and bioerosion SEM images | **110** |
| 4.19 | *S. siderea* skeletal structure and cement SEM images | **112** |
| 4.20 | Sponge galleries and aragonite cement SEM images | **114** |
| 4.21 | *S. conferta* skeletal structure and cement SEM images | **119** |
| 4.22 | *M. limbata* skeletal structure and cement SEM images | **121** |
| 4.23 | Hydrocarbon and diagenetic cement SEM images | **123** |
| 4.24 | *M. limbata* diagenetic layered cement SEM images | **125** |
| 4.25 | *Porites* skeletal structure and cement SEM images | **126** |
| 4.26 | *Porites* skeletal dissolution and alteration SEM images | **127** |
| 4.27 | X-radiographs of coral specimen skeletal structure | **129** |
| 4.28 | Fossil coral specimen XRD data plots | **131** |
| 4.29 | Petrographic thin section photographs and SEM images showing well-preserved primary skeletal aragonite | **135** |

**Chapter 5:**

| | | |
|---|---|---|
| 5.1 | Estimated proxy temperature anomalies | **145** |
| 5.2 | Skeletal aragonite and diagenetic cement Sr/Ca ratios | **145** |
| 5.3 | Skeletal aragonite and diagenetic cement Mg/Ca ratios | **148** |
| 5.4 | Skeletal aragonite and diagenetic cement Ba/Ca ratios | **151** |
| 5.5 | Skeletal aragonite and diagenetic cement B/Ca ratios | **152** |
| 5.6 | Skeletal aragonite and diagenetic cement U/Ca ratios | **154** |

**Chapter 6:**

| | | |
|---|---|---|
| 6.1 | Burdigalian chronostratigraphy and biostratigraphy | **159** |
| 6.2 | Estimated age of fossil coral samples determined from strontium isotope ratios | **161** |

# List of Tables

**Chapter 3:**


| | | |
|---|---|---|
| 3.1 | Modern siderastreid coral specimens | **42** |
| 3.2 | *Siderastrea siderea* key diagnostic characters | **45** |
| 3.3 | *Siderastrea radians* key diagnostic characters | **47** |
| 3.4 | Fossil coral specimens from Venezuela | **48** |
| 3.5 | *Siderastrea conferta* key diagnostic characters | **50** |
| 3.6 | *Montastraea limbata* key diagnostic characters | **53** |
| 3.7 | *Porites* key diagnostic characters | **56** |
| 3.8 | Coral samples selected for micro-CT scanning | **59** |
| 3.9 | Coral samples selected for XRD analysis | **64** |
| 3.10 | Coral samples selected for element/Ca geochemical analysis | **66** |
| 3.11 | Coral samples selected for $^{87}Sr/^{86}Sr$ isotope analysis | **71** |


**Chapter 5:**


| | | |
|---|---|---|
| 5.1 | Composition of skeletal aragonite and diagenetic cements in modern and Miocene corals determined by LA-ICPMS | **142** |
| 5.2 | Temperature anomaly estimates with 1% cement contamination | **144** |


**Chapter 6:**


| | | |
|---|---|---|
| 6.1 | $^{87}Sr/^{86}Sr$ isotope data and coral age estimation | **160** |

# Acknowledgements

I owe a huge debt of gratitude to my supervisors Dr Wolfgang Müller and Dr Ken Johnson for all their guidance, support and help during the years that I have spent researching this piece of work. I also gratefully acknowledge the wise advice and encouragement that I have received from my advisor Prof Margaret Collinson. I owe you all a very large round of drinks.

A very big 'thank-you' to Dr Alex Ball and Dr Lauren Howard at the NHM EMMA Department for all the training and advice regarding electron microscopy. Many hours of fun were spent peering at coral specimens in the SEM and I miss my days spent down there. A big 'thank-you' must also be extended to Neil Holloway at RHUL for making beautiful thin sections of my coral samples for me to analyse and image.

I would not have got to this stage without the support offered by my fellow students. Trips to the Hub for coffee and cake would not have been any fun without all the usual suspects trooping along to keep me company.

Finally I must also thank my long-suffering husband who has supported me in so many ways during the years I have spent studying.

# CHAPTER 1

INTRODUCTION

## 1.1 GENERAL INTRODUCTION

### 1.1.1 Coral reef environments and distribution

Coral reefs form one of the most diverse and important ecosystems on Earth, covering an estimated 2.84 million square kilometres of the world's tropical and subtropical oceans (Spalding et al., 2001). The reef-corals that build these large carbonate structures are highly sensitive to environmental conditions and their distribution is largely controlled by physical and chemical parameters such as sea-surface temperature, salinity, aragonite saturation state, illumination and sediment/nutrient load (Kleypas et al., 1999; Spalding et al., 2001). In modern oceans, optimum conditions for reef-coral growth occur in stable, oligotrophic environments supersaturated with aragonite and characterised by temperatures of 25 - 29$^{o}$ C and salinities of 33 - 36 ‰ (Spalding et al., 2001; Kleypas et al., 1999). Maps of reef-coral distribution show they are confined to tropical latitudes in a belt that extends from around 30$^{o}$ S to 30$^{o}$ N and are excluded from regions influenced by cold, nutrient-rich upwelling currents (e.g. eastern boundary currents and seasonal monsoonal upwellings) and the fresh-water plumes of sediment-laden rivers such as the Amazon and Orinoco (Spalding et al., 2001).

Around 7% of the world's coral reefs covering an estimated 20 thousand square kilometres are found in the Caribbean, located primarily around the Caribbean Islands and the Central American coast (Spalding et al., 2001). Today, declining water quality due to changes in land use, tourism and population growth pose an increasing threat to the long-term health and viability of the reefs (Spalding et al., 2001; Hughes et al., 2003) and this has led to an 80% reduction in hard coral cover on reefs across the Caribbean over the past three decades (Gardner et al., 2003). However, ecological changes induced by a decline in water quality are not confined to the modern world as the rock record testifies (Hallock and Schlager, 1986). In the Caribbean, coral reef ecosystems underwent a major environmental and ecological transition at the Oligocene/Miocene boundary that resulted in the removal or geographical restriction of nearly 50% of reef-coral genera and a prolonged hiatus in reef-building (Edinger and Risk, 1994). Prior to the transition, late Oligocene

Caribbean coral reefs were characterised by a diverse, cosmopolitan Tethyan biota and extensive carbonate reef production (Budd, 2000). However by the early Miocene, the region was populated by a much more endemic biota characteristic of the modern western Atlantic with species of *Montastraea* and *Porites* dominating small patch reefs (Budd, 2000). Large-scale carbonate reef-building did not fully recover until after a further reorganisation event at the Pliocene/Pleistocene boundary (Johnson et al., 2008).

### 1.1.2 The Caribbean and northern South America in the Early Miocene

The Early Miocene was a time of considerable global and environmental change. The climate was cooling due to a sharp decline in atmospheric $pCO_2$ (Pagani et al., 2005b) and the Oligocene/Miocene (O/M) boundary was marked by a rare congruence of low seasonality Milankovitch orbital cycles (low orbital eccentricity and an extended period of low amplitude variability in obliquity) that favoured the growth of ice sheets in Antarctica resulting in the transient southern hemisphere Mi-1 glaciation (Zachos et al., 2001). Following the O/M boundary event atmospheric $pCO_2$ levels began to rise, reaching a peak of around 400 ppm by volume at 22 Ma, before declining again to values of ~270 ppm by volume by the end of the Early Miocene (Pagani et al., 2005b).

Global ocean circulation was undergoing profound change due to the establishment of the Antarctic Circumpolar Current and the closure of the Tethys Seaway. Analyses of fully-coupled climate models investigating the effect on ocean circulation caused by the opening of the Drake Passage and establishment of the Antarctic Circumpolar Current and the closing of the Tethys Seaway have shown a reversal of volume transport between the Atlantic and the Pacific. Strengthened easterly currents permitted cooler, less saline water sourced from upwelling regions in the Pacific to enter the Caribbean through the Panama Seaway (Von der Heydt and Dijkstra, 2005). It has been suggested that these conditions led to increased nutrient availability and a regional decline in water quality in the southern Caribbean that had a profound impact on coral communities and survivorship during the Early Miocene (Von der Heydt and Dijkstra, 2005; Edinger and Risk, 1994; Edinger and Risk, 1995). Coral taxa able to withstand a combination of both low temperature and high

turbidity were found to have higher survivorship than corals tolerant of turbidity alone (Edinger and Risk, 1995).

Uplift and mountain-building were also altering the palaeo-geography and hydrography of northern South America and Amazonia during the Early Miocene. The Eastern Cordillera and Mérida Andes were undergoing a period of uplift and exhumation (Parra et al., 2005; Pindell et al., 1998) while complex regional tectonic changes and climatic shifts were transforming the extensive, northward-draining sub-Andean River System into the proto-Pebas wetland (Hoorn et al., 2010) with postulated marine connections to the southern Caribbean via the Llanos-Maracaibo and Llanos-East Venezuela Basins (Hovikoski et al., 2010). A large body of sedimentary and palaeontological evidence exists to support the idea of fluvial input from western Amazonia draining northwards and collected by a palaeo-Orinoco River (Díaz de Gamero, 1996; Hoorn, 1993; Hoorn, 1994).

Corals provide a rich archive of palaeoenvironmental information because they incorporate a broad array of geochemical tracers within their skeletons; are widely distributed throughout the tropics and can be accurately dated. Fossil corals collected from Cantaure Formation on the Paragauná Peninsula, northern Venezuela therefore offer potentially suitable subjects for geochemical analysis in order to elucidate the palaeo-environmental conditions in the southern Caribbean during the Early Miocene and discriminate between oceanic and fluvial causes for the decline in water quality during that time.

### 1.1.3 Coral geochemical archives, proxies and diagenesis

The aragonite skeletons of scleractinian corals incorporate element and isotope proxies that reflect the environmental conditions of the ambient seawater in which they grow and therefore represent important geochemical archives for the reconstruction of palaeo-climates and environments. Sr/Ca, Mg/Ca, B/Ca and U/Ca ratios and $\delta^{18}O$ have been utilized as proxies for sea surface temperature (SST) (e.g. Corrège, 2006; Swart et al., 2002; Sinclair et al., 1998). Ba/Ca ratios have been used to examine soil erosion, flood events and upwelling (Fleitmann et al., 2007; McCulloch et al., 2003; Montaggioni et al., 2006), while manganese and rare earth element (REE) concentrations have

been proposed as proxies for biological activity in coastal marine environments (Wyndham et al., 2004).

However, the aragonite in coral skeletons is metastable and susceptible to diagenetic alteration. Primary coral aragonite may be affected by a range of diagenetic processes such as dissolution, cementation, neomorphism, dolomitisation, compaction, bioerosion and microbial micritisation (Tucker and Wright, 1990; Flügel, 2004). Although skeletal diagenesis and alteration fabrics have been studied for over thirty years (e.g. James, 1974; McGregor and Abram, 2008; Nothdurft and Webb, 2009), it is only over the past two decades that researchers have turned their attention to examining the effects of diagenesis on geochemical proxies used for palaeo-climate reconstructions (e.g. Müller et al., 2001; Lazar et al., 2004; Allison et al., 2007; Hathorne et al., 2011). It is clear from these studies that diagenetic alteration can be a source of significant error in palaeo-SST reconstructions. For example, Hendy et al. (2007) reported cool temperature anomalies in modern *Porites* affected by skeletal dissolution and secondary aragonite cementation. Calcite cements have even more dramatic effects on palaeo-SST reconstructions producing significant warm temperature anomalies (Allison et al., 2007).

## 1.2 AIMS AND OBJECTIVES OF THE THESIS

The focus of this research is to examine a suite of fossil corals collected from the Cantaure Formation on the Paraguaná Peninsula, northern Venezuela in order to assess their skeletal preservation and potential for geochemical anlaysis and palaeo-environmental reconstruction.

This aims and objectives of this study are as follows:-

1. To document and compare skeletal preservation and diagenetic alteration in a suite of fossil corals collected from the Cantaure Formation, northern Venezuela with two modern fossil coral samples from Bermuda and the Florida Keys. Observations of skeletal preservation commence with the visual assessment of the coral samples

in hand specimen in order to document gross morphological features, weathering surfaces, bio-erosion and alteration. Assessment of coral preservation then proceeds with binocular and transmitted light microscopy of prepared coral blocks and petrological thin sections which permits the assessment of cement distribution, crystal morphology and sequence of diagenetic cement deposition before finally concluding with a detailed examination of the coral blocks in the scanning electron microscope in order to evaluate changes in skeletal micro-architecture due to bio-erosion and dissolution processes and to document cement crystal morphology.

2. To measure important proxy element/Ca ratios (Sr/Ca; Mg/Ca; Ba/Ca; B/Ca and U/Ca) in primary skeletal aragonite in modern and fossil corals and compare them with those measured in aragonite and calcite cements using depth-profile LA-ICPMS analyses. The results are then used to quantify the effects of diagenetic cements in the fossil specimens on element/Ca proxies used extensively in palaeo-temperature reconstructions.

3. To estimate the age of the fossil corals using $^{87}Sr/^{86}Sr$ isotope stratigraphy in order to confirm the published Early Miocene (Burdigalian) bio-stratigraphic age assigned to the Cantaure Formation.

## 1.3 CHAPTER SUMMARIES

### Chapter 1

Chapter 1 briefly describes modern topical reef coral distribution and the environments and conditions under which they flourish before narrowing the focus down to Caribbean corals and introducing the biotic turnover in reef corals that occurred at the Oligocene/Miocene boundary (the Oligocene-Miocene Transition) and the possible oceanic and tectonic causes for a decline in water quality in the Caribbean during the Early Miocene. The chapter then goes on to

outline the use of geochemical proxies incorporated within the aragonite skeletons of Scleractinian corals for palaeo-environmental reconstructions and the problems associated with interpretation of results in the presence of diagenetic cements. The chapter concludes with a description of the aims and objectives of the work.

**Chapter 2**

Chapter 2 is divided into three sections. The first section gives a brief overview of Early Miocene Caribbean coral assemblages and an explanation of why it is so rare to find unaltered aragonitic fossil corals. This section is illustrated by a list of published research documenting geochemical studies based on well-preserved pre-Quaternary corals. A list of the hypotheses to be test is also given at the end of this section.

The second section describes the field work methodology and sample sites. The physiography and climatic setting of the Paraguaná Peninsula is outlined followed by descriptions of the lithology, fossil assemblages and inferred environment of deposition published in the literature.

A synthesis of published work describing the physiography and climatic setting of Bermuda and the Florida Keys is outlined in the third section to provide information on the environmental settings from which the modern corals examined in this thesis were collected.

**Chapter 3**

Chapter 3 is divided into two main parts. The first part gives detailed species descriptions of the modern coral specimens (*Siderastera siderea; Siderastrea radians*) and the fossil coral specimens (*Siderastrea conferta; Montastraea limbata; Porites* sp) compiled from the literature and illustrated with species character diagrams.

The second part is divided into two subsections. The first subsection covers imaging and X-ray diffraction; the second subsection covers element geochemistry and isotope analysis.

The first subsection provides detailed descriptions of the methods used to assess coral skeletal preservation including light (binocular and transmission)

and variable pressure scanning electron microscopy. The use of Micro-CT is outlined for the determination of the most suitable planes for coral sectioning. X-ray diffraction analysis allows comparisons to be made with visual data and this method and its associated problems are detailed in the final part of this subsection.

The second subsection describes the depth profile laser ablation inductively-coupled mass spectrometry (LA-ICP-MS) methodologies used to obtain element/Ca ratios from coral primary skeletal aragonite and calcite and aragonite cements and the importance of this method for palaeontological studies is discussed. Variable pressure scanning electron microscopy and MeX software analysis were used to estimate the amount of material used per laser pulse and this method is also described here. The final part of this section provides a detailed description of the methods used to obtain age estimates based on $^{87}Sr/^{86}Sr$ isotope stratigraphy including sample selection and preparation, analysis and data handling.

**Chapter 4**

Chapter 4 presents visual evidence documenting skeletal preservation and diagenetic alteration in the modern and fossil coral specimens obtained by photographic imaging, light and electron microscopy and X-radiography. These data are compared with X-ray diffraction analyses in order to show the importance of microscopy in screening for the presence of secondary aragonite cement.

Detailed descriptions of the distribution and morphology of aragonite, calcite and brucite cements identified in the modern coral samples are presented and the importance of the role of endobiotic organisms in the erosion of skeletal material and the deposition of diagenetic cements is discussed.

The complex diagenetic history of the fossil corals is illustrated by the range of cements, their sequence of deposition and the presence of hydrocarbon charging. Observations on the distribution and morphology of aragonite, calcite, pyrite and dolomite cements and hydrocarbon deposits are presented and the importance of meteoric vadose and phreatic diagenetic environments on the deposition of calcite cements is discussed.

A comparison of the microanatomy and features of well-preserved primary skeletal aragonite in both modern and fossil corals is presented.

**Chapter 5**

Chapter 5 presents the results of high-spatial resolution depth-profile LA-ICPMS analyses of Sr/Ca, Mg/Ca, Ba/Ca, B/Ca and U/Ca in pristine skeletal aragonite, aragonite and calcite cements and hydrocarbon crusts in fossil *S. conferta* and *M. limbata* and compares the results with those for pristine skeletal aragonite in a sample of the modern coral *S. radians*. The behaviour and chemistry of the proxy elements are discussed and estimates of the effect of 1% cement contamination on palaeo- sea-surface temperature reconstructions based on Sr/Ca, Mg/Ca, Ba/Ca, B/Ca and U/Ca proxies are presented and compared with the published literature.

**Chapter 6**

Chapter 6 presents for the first time the results of age estimations for the Cantaure Formation based on $^{87}Sr/^{86}Sr$ isotope stratigraphy. An estimated age of ~16 Ma is given by $^{87}Sr/^{86}Sr$ isotope analysis of primary skeletal aragonite confirming the Early Miocene (Burdigalian) age assigned to the Cantaure Formation based on published biostratigraphic studies. A brief summary is given explaining why isotope stratigraphy is suitable for dating coral material of this age and a short literature review is included to show the new data are unique.

**Chapter 7**

Chapter 7 reviews the aims and objectives of the thesis and a summary of the observations made on the appearance and micro-architecture of primary skeletal aragonite and diagenetic cements in modern and fossil corals are presented. The geochemical proxy data and the impact of including 1% cement contamination in palaeo-temperature reconstructions are outlined. The chapter is completed with a summary of the conclusions drawn from the work presented in this thesis.

# CHAPTER 2

## FIELDWORK AND PHYSIOGRAPHY OF THE PARAGUANÁ PENINSULA, BERMUDA AND THE FLORIDA KEYS

# Chapter 2: Fieldwork and physiography of the Paraguana Peninsula, Bermuda and the Florida Keys

## 2.1 GENERAL INTRODUCTION

This chapter is divided into three sections. The first section provides a brief overview of research exploring the Oligocene-Miocene transition and Early Miocene Caribbean coral reef assemblages and an examination of the literature illustrating the rarity of fossil corals that preserve their original aragonitic skeletons. A list of hypotheses to be tested is also provided. The second section describes the methods used to collect and describe the fossil material and the field localities on the Paraguaná Peninsula. The third section describes the physiography of the Paraguaná Peninsula, Bermuda and the Florida Keys

### 2.1.1 Early Miocene Caribbean coral reef assemblages

The Oligocene/Miocene boundary was a period of profound biotic change in the Caribbean. Prior to the Oligocene-Miocene Transition, Oligocene Caribbean coral reefs were characterised by a diverse, cosmopolitan Tethyan biota which included globally extinct taxa such as *Astrocoenia* and *Antiguastrea* and regionally extinct genera such as *Favites* and *Diploastrea* (Budd, 2000). Large reef build-ups were common leading to the production of extensive carbonate formations such as the Lares and Juan Diaz Formations of Puerto Rico (Frost et al., 1983) and the Antigua Formation of Antigua (Weiss, 1994). However by the Early Miocene, Caribbean coral assemblages had undergone a profound reorganisation and the region was populated by a much more endemic biota with modern western Atlantic species such as *Montastraea* and *Porites* dominating the reef communities (Budd, 2000). Miocene reef-building was much less extensive with coral communities confined to small patch and fringing reefs in environments dominated by siliciclastic input such as the Tamana Formation of Trinidad (Johnson, 2001) and the La Boca and Valiente Formations of Panama (Coates et al., 2003; Johnson and Kirby, 2006).

### 2.1.2 Rarity of well-preserved aragonitic fossil corals

The polyps of scleractinian corals produce taxonomically distinct aragonite skeletons by a complex biomineralisation process that involves both organic and mineral components (Stolarski, 2003; Cuif and Dauphin, 2005; Tambutté et al., 2011). However, primary skeletal aragonite is metastable and rapidly transforms to calcite in most diagenetic environments (Dullo, 1984) resulting in loss of the original geochemical signatures and replacement of skeletal aragonite by diagenetic $CaCO_3$ bearing altered geochemical signatures (Tudhope et al., 2001; McGregor and Gagan, 2003). Primary coral aragonite may also be affected by dissolution, cementation, dolomitisation, compaction, bioerosion and microbial micritisation (Tucker and Wright, 1990; Flügel, 2004) which also have a significant effect on geochemical proxies.

Very little research has been published based on the geochemistry of deep-time fossil corals due to the difficulty of finding pristine, unaltered specimens. However notable studies that document pre-Quaternary aragonitic corals that have preserved their original geochemical signatures include the following:-

1. Roulier, L.M., Quinn, T.M. 1995. Seasonal- to decadal-scale climatic variability in southwest Florida during the middle Pliocene: Inferences from a coralline stable isotope record. Paleoceanography, 10, 429-443.
   Coral species = *Solenastrea bournoni*
   Age = 3.0 ± 0.5 Ma
   Stable isotope ($\delta^{18}O$; $\delta^{13}C$) study
   Location = Florida, U.S.A.

2. Denniston, R.F., Asmeron, Y., Polyak, V.Y., McNeill, D.F., Klaus, J.S., Cole, P., Budd, A.F. 2008. Caribbean chronostratigraphy refined with U-Pb dating of a Miocene coral. Geology, 36, 151-154
   Coral species = *Goniopora hilli*
   Age = 5.5 ± 0.15 Ma
   Dating study using the $^{238}U/^{206}Pb$-$^{207}Pb/^{206}Pb$ system
   Location = Cibao Valley, Dominican Republic

3. Mertz-Kraus, R., Brachert, T.C., Reuter, M. 2008. *Tarbellastraea* (Scleractinia): A new stable isotope archive for Late Miocene paleoenvironments in the Mediterranean. Palaeogeography, Palaeoclimatology, Palaeoecology, 257, 294-307.
   Coral species = *Porites* and *Tarbellastrea*
   Age = 7 Ma and 9 Ma
   Stable isotope ($\delta^{18}O$; $\delta^{13}C$) study
   Location = Crete, Greece

4. Brachert, T.C., Reuter, M., Felis, T., Kroeger, K.F., Lohmann, G., Micheels, A., Fassoulas, C. 2006. Porites corals from Crete (Greece) open a window into Late Miocene (10 Ma) seasonal and interannual climate variability. Earth and Planetary Science Letters, 245, 81-94.
   Coral species = *Porites*
   Age = 10 Ma
   Stable isotope ($\delta^{18}O$; $\delta^{13}C$) study
   Location = Crete, Greece

5. Ivany, L.C., Peters, S.C., Wilkinson, B.H., Lohmann, K.C., Reimer, B.A. 2004. Composition of the early Oligocene ocean from coral stable isotope and elemental chemistry. Geobiology, 2, 97-106.
   Coral species = *Archohelia vicksburgensis*
   Age = ~30 Ma
   Stable isotope ($\delta^{18}O$; $\delta^{13}C$) and element/Ca (Sr/Ca; Mg/Ca) study
   Location = Vicksburg, Mississippi, U.S.A.

Remarkably, aragonitic fossil corals from the Mesozoic are not unknown. Stolarski (2003) included three aragonitic coral specimens from Triassic localities renowned for their exceptional preservation in his study on coral microstructure and biomineralisation processes. These remarkable specimens include an unidentified conophylliid from the Middle Carnian San Cassiano Beds, Alpe di Specie in the Dolomites; *Pachysolenia cylindrica* (Cuif, 1975), a

pachythecaliinan from the Lower Norian, Alakir Çay, Turkey; and *Stylophyllum paradoxum* (Frech, 1890), a stylophyllinan from the Rhaetian of Fischerwiese, Northern Calcareous Alps, Austria.

### 2.1.3 Hypotheses to be tested

This work undertakes to test the following hypotheses:-

1. Do fossil corals from the Early Miocene Venezuelan Cantaure Formation preserve the micro-architecture and geochemical signatures of primary skeletal aragonite

2. What effect does the inclusion of 1% aragonite and calcite cements have on palaeo-environmental (Sr/Ca, Mg/Ca, Ba/Ca, B/Ca and U/Ca) proxies recovered from the Early Miocene fossil corals

3. Does the fossil coral strontium isotope age agree with the published Burdigalian biostratigraphic age assigned to the Cantaure Formation

## 2.2 FIELD WORK

Field work was undertaken on a short trip to Falcón State, north-western Venezuela in February 2009. The field trip comprised two main activities; field and laboratory work. Two days were spent in the field on the Paraguaná Peninsula examining the Cantaure Formation and collecting fossil scleractinian corals and teleost utricular and saccular otoliths (fish ear stones). Following the field work, a further five days were spent picking and identifying the fossil fish otoliths in a laboratory at the Universidad Nacional Experimental Francisco de Miranda (UNEFM) in Coro.

### 2.2.1 Field work methods and collection of sample materials

Notes were recorded in a field note book and images with an appropriate scale were acquired for each locality using a Canon EOS 350D 8 megapixel

camera fitted with a Canon 35 – 70 mm digital lens and built-in automatic flash unit (Canon Inc, Tokyo, Japan). GPS readings of latitude and longitude were recorded for each of the localities in the field note book. Photographs of the fossil scleractinian corals were taken *in-situ* with a scale bar before carefully removing the fossils from the sediment and placing in labelled cotton sample bags. Otoliths weathered out of the sediments and lying on the surface (surface samples) were collected and placed in labelled cotton sample bags prior to identification. Bulk sediment samples weighing approximately 1 kg were dug up with a trowel after removing ~ 10 cm of the weathered surface sediment and placed in labelled cotton sample bags in order to collect otoliths not subjected to surface weathering and erosion. The bulk sediment samples were processed by wet sieving through meshes of 8mm, 2mm and 150 μm. The residual material was air dried and stored in labelled, self-sealing polythene bags prior to picking and identification at the Universidad Nacional Experimental Francisco de Miranda in Coro. Otoliths were picked at 10x magnification under a stereomicroscope and identified to species level where possible from the taxonomic descriptions and images in Nolf and Aguilera (1998), Aguilera and Rodrigues de Aguilera (2003) and Aguilera and Rodrigues de Aguilera (2004). Coral identifications were made by K.G. Johnson at the Natural History Museum (NHM) in London. A full list of coral and otolith taxa is given in Appendix 1.

### 2.2.2 Field locations (Cantaure Formation), Paraguaná Peninsula

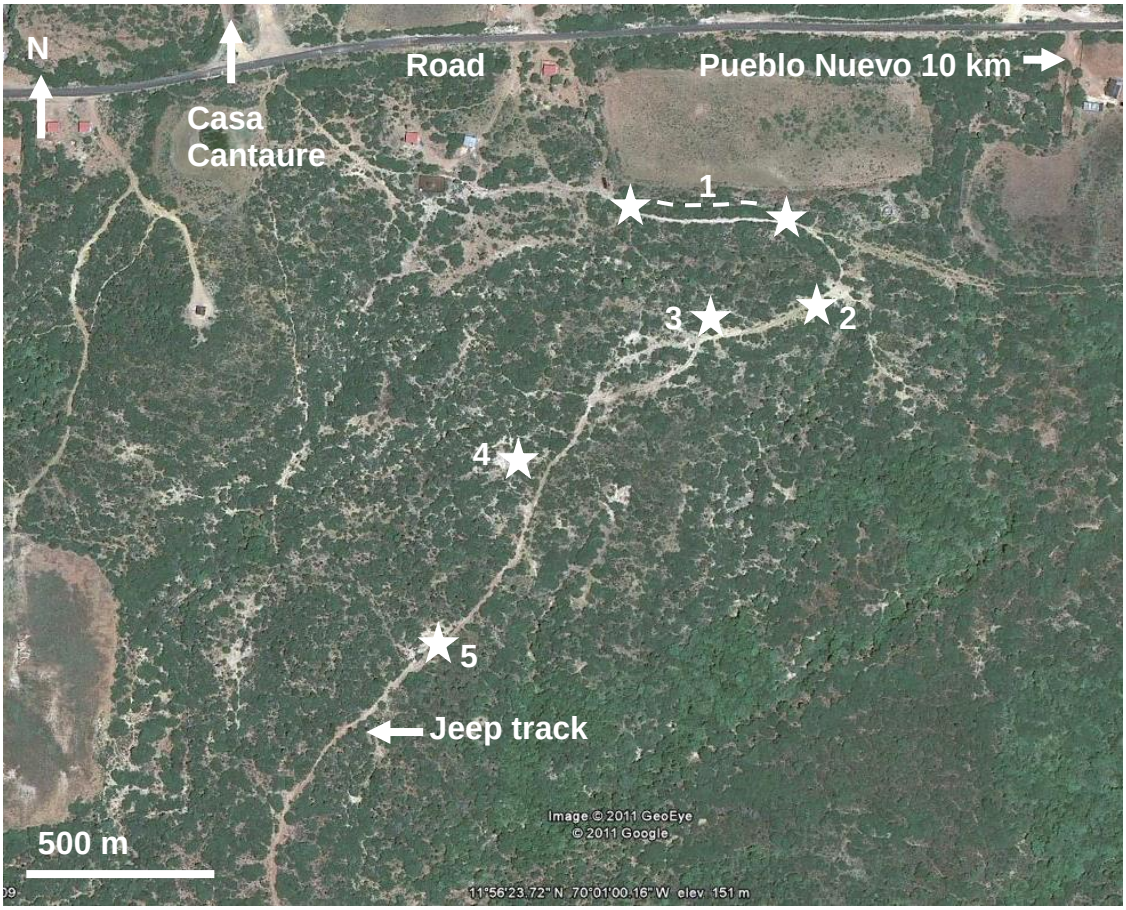


**Figure 2.1** Satellite image showing the location of the collection sites south of Casa Cantaure on the Paraguaná Peninsula, Venezuela (Google Earth 2011). The collection sites are located on a xerophytic scrub and cactus-covered, gently sloping hillside reached via a rough track that leaves the road south of Casa Cantaure, approximately 10 km west of Pueblo Nuevo (Figure 2.1).

**Locality 1:**

$11^{o}$ 56.503' N, $70^{o}$ 01.006' W to $11^{o}$ 56.503' N, $70^{o}$ 00.928' W.

Brown marls containing abundant fossil material (e.g., mollusc shells and shell fragments, otoliths, sharks teeth and fragments of crustacean carapaces). Bulk sediment and surface samples collected.

**Locality 2:**

11° 56.463' N, 70° 00.926' W.

Brown, gypsiferous marls containing relatively few fossils, mainly otoliths. Surface samples collected.

**Locality 3:**

11° 56.459' N, 70° 00.962' W.

Brown, gypsiferous marls containing abundant fossil material including mollusc shells and fragments, otoliths and a small fragment of the azooanthallate coral *Dendrophyllia* sp (Scleractinia). Bulk sediment and surface samples collected.

**Locality 4:**

11° 56.390' N, 70° 01.055' W.

Fine grained, brown, silty sands, containing abundant fossil material including a diverse molluscan fauna and numerous otoliths. Bulk sediment and surface samples collected.

**Locality 5:**

11° 56.304' N, 70° 01.079' W.

Brown marls containing isolated, fragmented, fist-sized heads of the zooanthellate corals *Montastrea* sp and *Solenastea* sp (Fig. 2.3) and mollusc shells and shell debris. Two coral heads were collected.

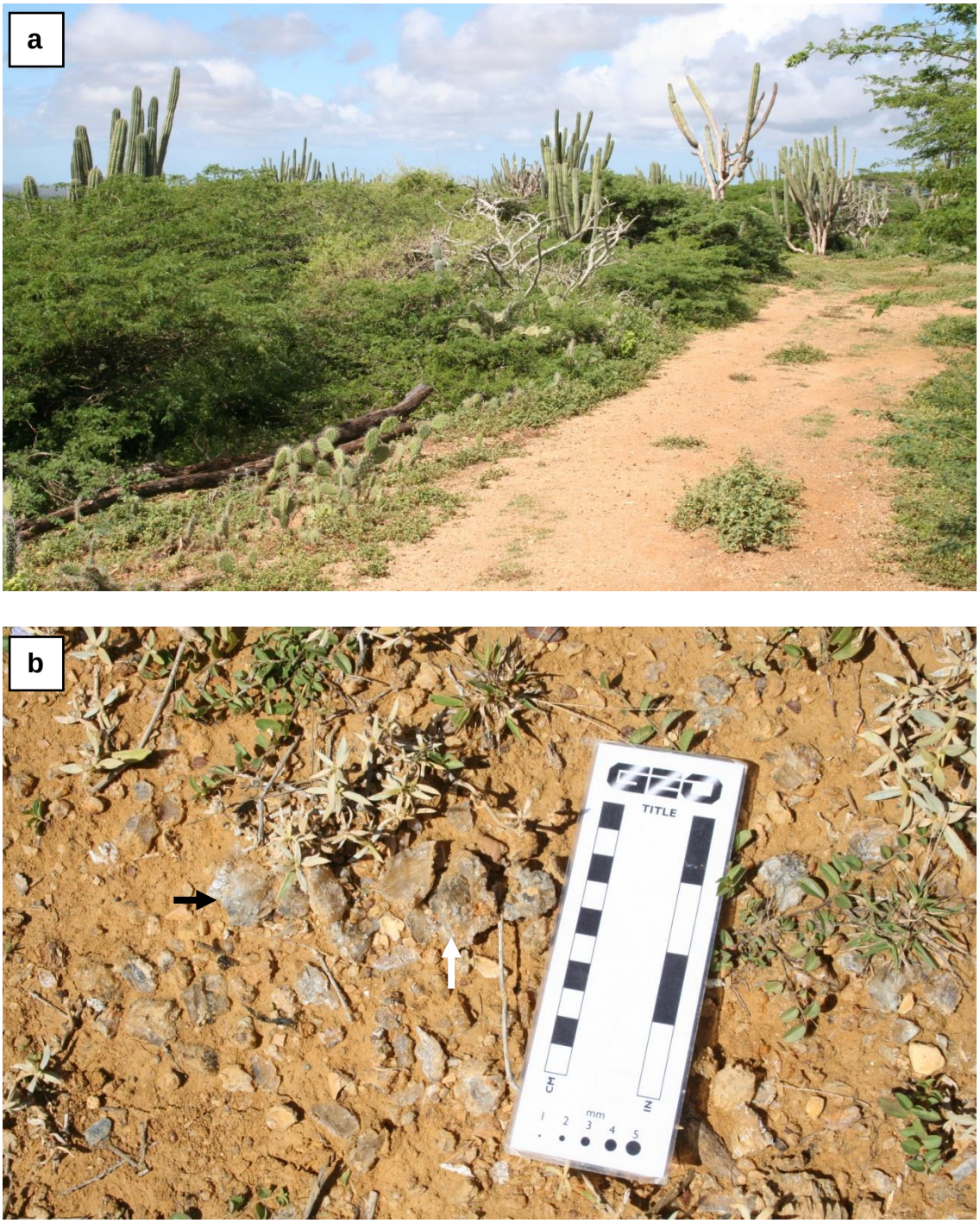


**Figure 2.2** Photographs showing the collection sites and Cantaure Formation sediments. **a** Jeep track flanked by xerophytic scrub and cactus at Locality 1. **b** Gypsum crystals (arrow) are present on the surface of the clayey sediments at Locality 2.

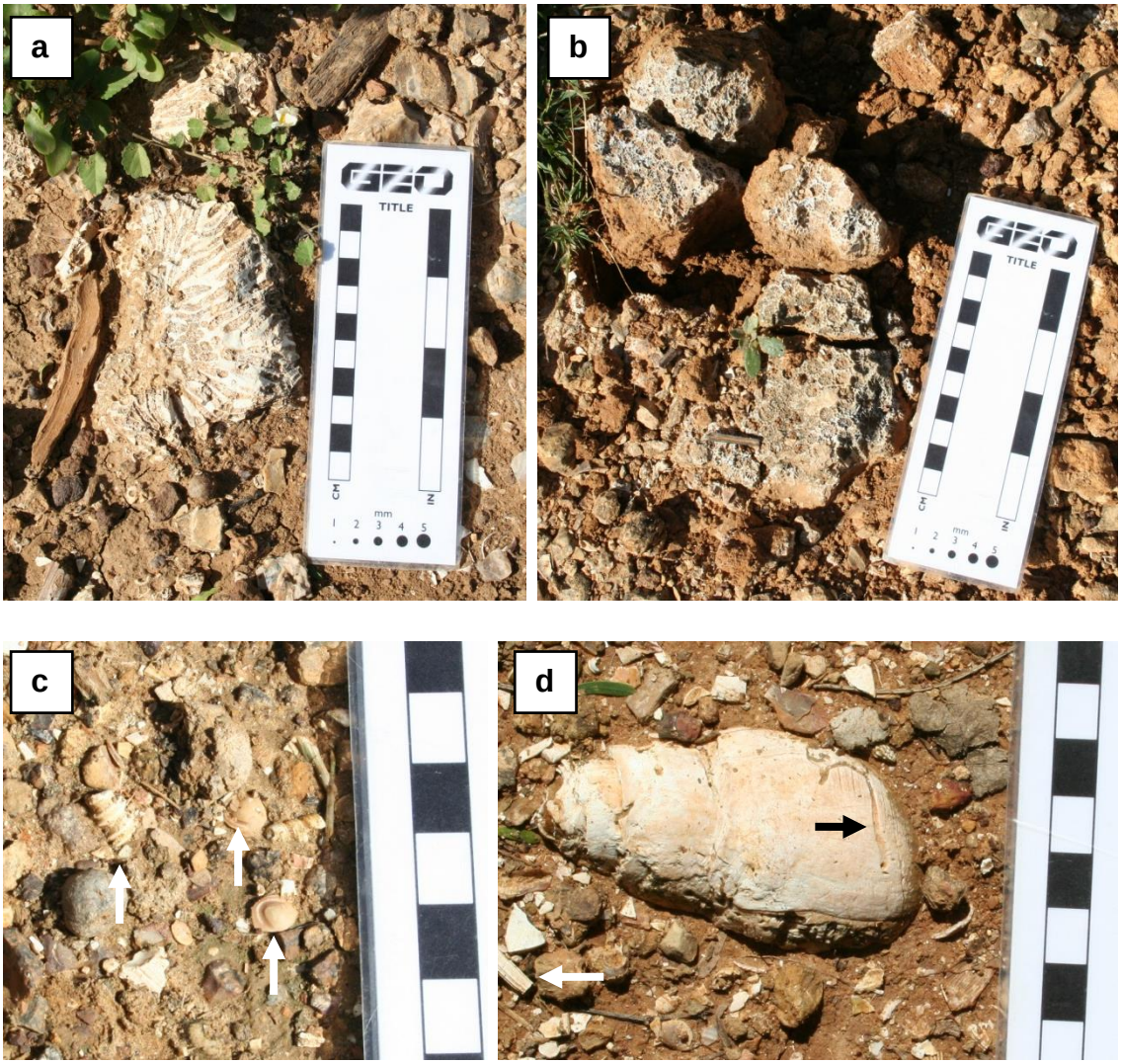


**Figure 2.3** Photographs showing examples of the fossil material found in the Cantaure Formation. **a** *Solenastrea* sp (Scleractinia) collected at Locality 5. **b** *Montastraea* sp (Scleractinia) collected at Locality 5. **c** Sciaenid otoliths and a fragment of *Turritella* (Gastropoda) at Locality 1. **d** Large unidentified gastropod mollusc shell partially buried in sediment and etched by a macro-boring organism (black arrow) with a fragment of the scaphopod mollusc *Dentalium* lying close by (white arrow) at Locality 1.

## 2.3 PHYSIOGRPAHY AND CLIMATIC SETTING OF THE PARAGUANÁ PENINSULA

The Paraguaná Peninsula is situated on the northern coast of Venezuela between 11°27' and 12°12' N and 69°35' and 70°12' W in Estado Falcón approximately 300 km northwest of Caracas (Figure 2.4a). The Paraguaná projects northwards out into the Caribbean and is bounded to the west by the Golfo de Venezuela and to the north and east by the Caribbean Sea. To the south, it is separated from the mainland by the shallow, sediment-laden Golfete de Coro (Miloslavich et al., 2003). The Paraguaná covers an area of approximately 3300 $km^2$ and is connected to the mainland by a narrow aeolian dune system and causeway forming the 27 km long Istmo de los Médanos (Figure 2.4b). The topography of the Paraguaná is generally rather subdued with flat coastal regions giving way to low hills in the interior and the prominent ridge of Cerro Santa Ana (830 m) (Alarcón, 2001). The Paraguaná and adjacent coastal regions are influenced by the northeast trade winds and the position of the inter-tropical convergence zone (ITCZ) and characterised by a tropical arid climate with low precipitation and high evaporation rates (Miloslavich et al., 2003). Present-day rainfall patterns are very variable (mean annual rainfall ~500 mm) with the highest precipitation usually occurring in the months of October to December (Edwards and Diaz, 2006). Daily air temperatures vary little throughout the year, ranging from 27°C to 30°C (U.S. National Climatic Data Centre, http://ww.ncdc.noaa.gov/oa/ncdc.html). However sea-surface temperatures show much greater seasonal variation, ranging from 21°C to 28°C (AquaMODIS SST, http://oceancolor.gsfc.nasa.gov/cgi/13) and are heavily influenced by the presence of seasonal cold upwelling fronts located off the coast at Punto Fijo and Cabo San Román (Miloslavich et al, 2003).

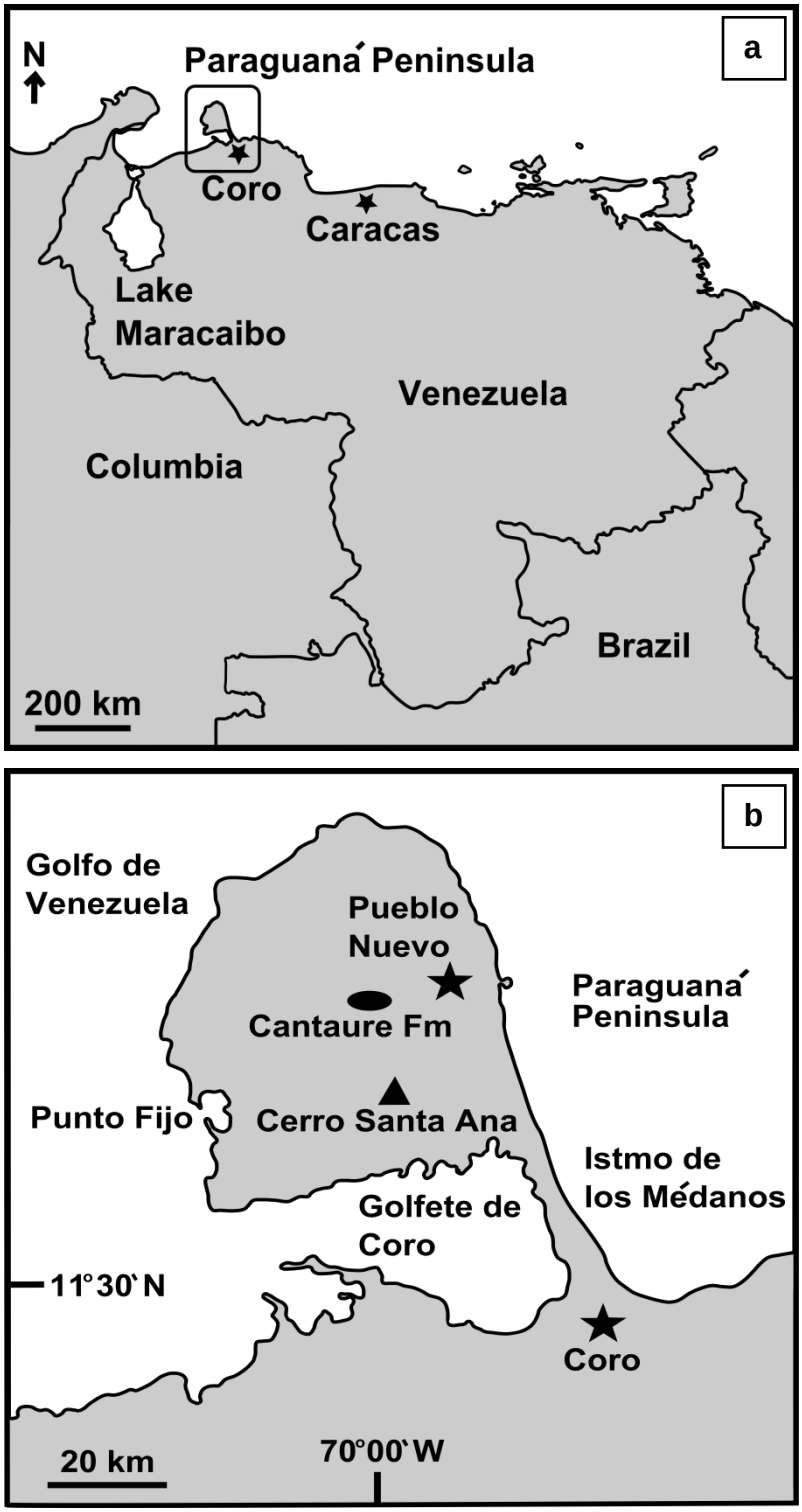


**Figure 2.4** Sketch maps showing the location of the Paraguaná Peninsula and the Cantaure Formation. **a** The Paraguaná Peninsula projects into the Caribbean from the northern coast of Venezuela. **b** The geographically restricted Cantaure Formation lies in the centre of the Paraguaná Peninsula.

### 2.3.1 Cantaure Formation

Outcrop of the Cantaure Formation is limited to the geographically restricted type locality described by Hunter and Bartok (1974) close to Casa Cantaure, approximately 10km west of Pueblo Nuevo on the Paraguaná Peninsula, Falcón State, Venezuela. The first lithological description of the Cantaure Formation was published by Jung (1965) based on an unpublished internal report produced for the Creole Petroleum Corporation in 1956. Confusion among mollusc workers regarding the exact location, stratigraphy and age of the type section resulted in different interpretations of the locality being published with descriptions of the diverse mollusc assemblages they collected (Hunter and Bartok, 1974). In 1974, Hunter and Bartok undertook a complete re-description of the type section in order to clarify the stratigraphy, age and correlations of the Cantaure Formation and this description was incorporated in the 3$^{rd}$ edition of the Stratigraphic Lexicon of Venezuela compiled in 1997 (Lorente, 1997).

### 2.3.2 Lithology

The base of the Cantaure Formation unconformably overlies the Paraguaná Granites and the metamorphic rocks of the Pueblo Nuevo Formation (Rey, 1996). Above the contact, the ~ 75 m thick Cantaure Formation commences with a shell breccia composed primarily of fragmented plates of *Balanus* sp (barnacles) with granite blocks of various sizes incorporated into it from the underlying basement. Silty marls intercalated with sandy horizons overlie the basal breccia, forming the lower part of the Formation exposed between Quebrada Barbasco and Casa Cantaure. Within this part of the section lies a distinctive horizon composed of unconsolidated shell beds comprising a diverse molluscan fauna (Hunter and Bartok, 1974). The upper part of the Cantaure Formation commences above the mollusc horizon and comprises marls alternating with thin algal limestones and occasional mollusc shell beds containing species common to the lower horizon. One kilometre west of Casa Cantaure, the algal limestones are replaced by marls and a shell bed composed primarily of the large oyster *Ostrea aff. aguaclarensis paraguanensis.* The top

of the Cantaure Formation is composed of marls and terminates in a limestone, the base of which forms the upper boundary of the Formation (Hunter and Bartok, 1974). The nature of the upper contact between the Cantaure Formation and the overlying limestones has been the subject of much debate. Jung (1965) considered the contact to be concordant. However, Hunter and Bartok (1974) considered the capping limestone to be post-Cantaure and pre-Pliocene in age. The latest interpretation by Rey (1996) suggests an unconformable contact between the Cantaure Formation and limestones of the Paraguaná Formation.

### 2.3.3 Fossil assemblages and environment of deposition

The Cantaure Formation contains a very diverse faunal assemblage particularly rich in mollusc and fish remains. Jung (1965) identified 146 species of mollusc of which 24 were new species. Subsequent work by Thomas and MacDonald (1970) and Esteves and Padrón (1996) have added a further 33 species. In addition, Nolf and Aguilera (1998) described a rich marine ichthyofauna (61 teleostean taxa) from otoliths with the Sciaenidae (drums and croakers) particularly well represented. A diverse assemblage of microfossils has also been described from the Cantaure Formation including planktonic and benthic foraminiferal fauna (Díaz de Gamero, 1974; Rey, 1996). Key planktonic foraminiferal species include the zonal markers *Globigerinatella insueta* and *Praeorbulina glomerosa*. Rey (1996) also reported the presence of ostracods, bryozoans (encrusting and bifoliated), micro-molluscs and pteropods belonging to the genus *Vaginella*.

The faunal associations found in the Cantaure Formation are indicative of a clear, tropical-marine, shallow-water (<50 m depth) coastal environment of normal salinity with occasional freshwater input (Nolf and Aguilera, 1998). This interpretation is in agreement with those of Jung (1965) and Díaz de Gamero (1974).

## 2.4 PHYSIOGRAPHY AND CLIMATIC SETTING OF BERMUDA

Bermuda is situated on a volcanic pedestal in the North Atlantic (32$^{o}$ 22.421 N, 64$^{o}$ 45.153' W) approximately 1000 km east-southeast of Cape Hatteras (Figure 2.5) and consists of an elongate cluster of five main islands and approximately 140 smaller limestone islets and cays forming a landmass of ~50 km$^2$ lying on the southern edge of the 650 km$^2$ Bermuda Platform (Garrett et al., 1971). The islands lie in mid-latitudes and experience an oceanic climate with weather patterns influenced by the position of the Arctic air mass and the Bermuda-Azores High, the Gulf Stream and strong westerly winds (Vacher and Rowe, 2004). The ocean surrounding Bermuda is influenced by meanders and eddies in the Gulf Stream resulting in higher temperatures than would be expected for the latitude. Ocean sea surface temperatures vary from 19$^{o}$ C in February/March to 27$^{o}$ C in August/September (Schroeder and Stommel, 1969) while sea surface temperatures in the shallow North Lagoon overlying the Bermuda Platform range from 16$^{o}$ C to 29$^{o}$ C (Beers and Herman, 1969). Oceanic and lagoonal salinities however, show very little variation, remaining close to a mean of 36.5 ‰ (Schroeder and Stommel, 1969; Beers and Herman, 1969). Clastic sediment input from the land is very low because the porous limestone islands do not carry any rivers or streams and the soils are only thinly developed (Beers and Herman, 1969).

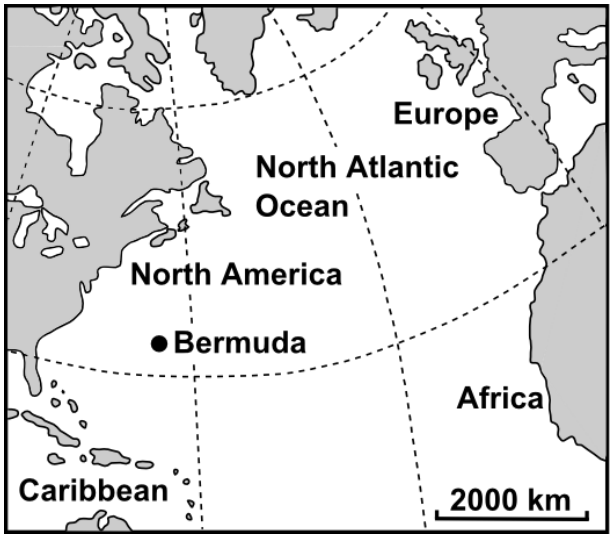


**Figure 2.5** Sketch map showing the location of Bermuda in the North Atlantic

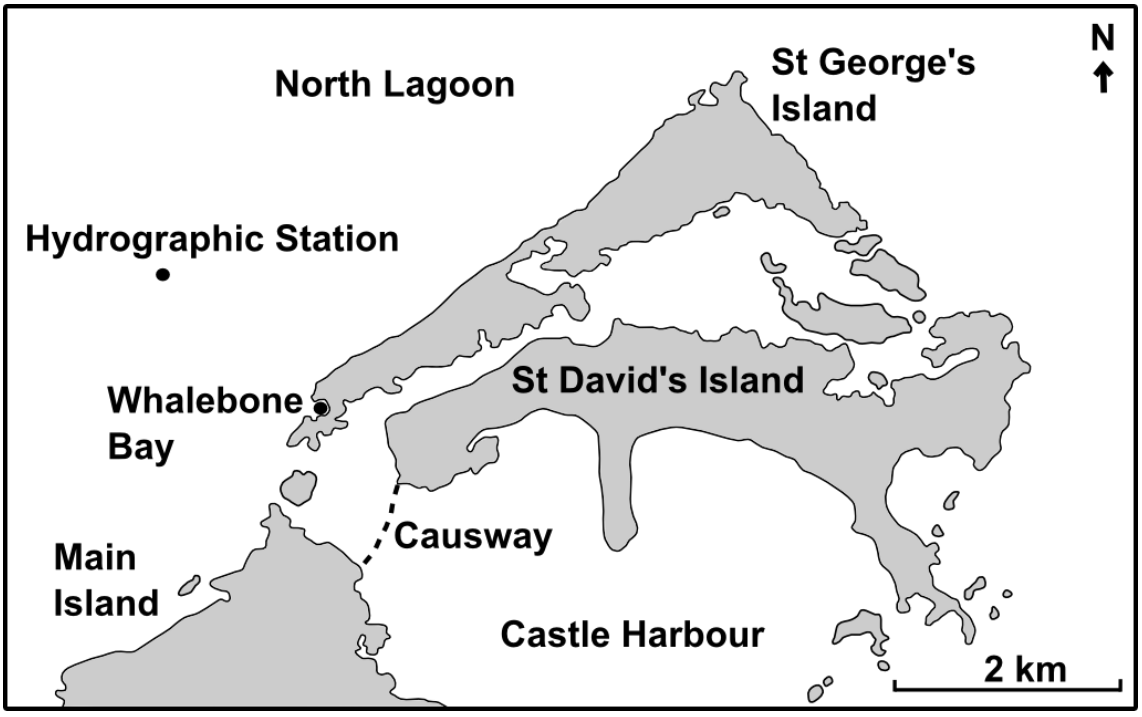


**Figure 2.6** Sketch map showing the location of Whalebone Bay on St George's Island, Bermuda

Rainfall is fairly constant throughout the year ranging from 10-12 cm month$^{-1}$ between December and July and 13-17 cm month$^{-1}$ between August and November. The higher rainfall during the summer months is due to the passage of thunderstorms and hurricanes, the slightly lower winter rainfall is associated with the passage of weather fronts (Vacher and Rowe, 2004).

Whalebone Bay is located at 32$^{o}$ 21' 52" N and 64$^{o}$ 42' 50" W on St George's Island. The westward facing bay is small (27,700 m$^{2}$) and nearly circular in outline with a narrow 75 m wide opening connecting it with the North Lagoon (Figure 2.6). The bay is shallow reaching a maximum depth of 5.5 m at the entrance and the hydrology is dominated by semi-diurnal slightly asymmetrical tides (Welsh et al., 1979). No surface streams drain into the bay due to the porous nature of the limestone island therefore nutrient cycling is based on the stranding, dessication and leaching of organic detritus washed up on the beach (Welsh et al., 1979).

## 2.5 PHYSIOGRAPHY AND CLIMATIC SETTING OF THE FLORIDA KEYS

The Florida Keys form an arcuate chain of low limestone islands and cays situated on the continental shelf just off the coast of the tip of the Florida Peninsula (Figure 2.7). The Keys extend from Soldier Key in the north (25° 35' N and 80° 09' W) down to Key West in the southwest (24° 32'N and 81° 48' W) and are divided into the Upper and Lower Keys. The Upper Keys extend north from Bahia Honda to Soldier Key while the Lower Keys extend south from Big Pine Key to Key West (Halley et al., 2004). The Florida Keys are separated by from the parallel carbonate ridges and patches of the outer Florida Reefs by a shallow, elongate basin called Hawk Channel. The channel is approximately 10 km wide and it extends 230 km from Fowey Rocks off Key Biscayne to Sand Key off Key West. Water depths in the centre of the channel range from 7 – 8 m in the north and progressively deepen further south ranging from 12 – 15 m (http://www.aoml.noaa.gov/flbay/pitts.html).

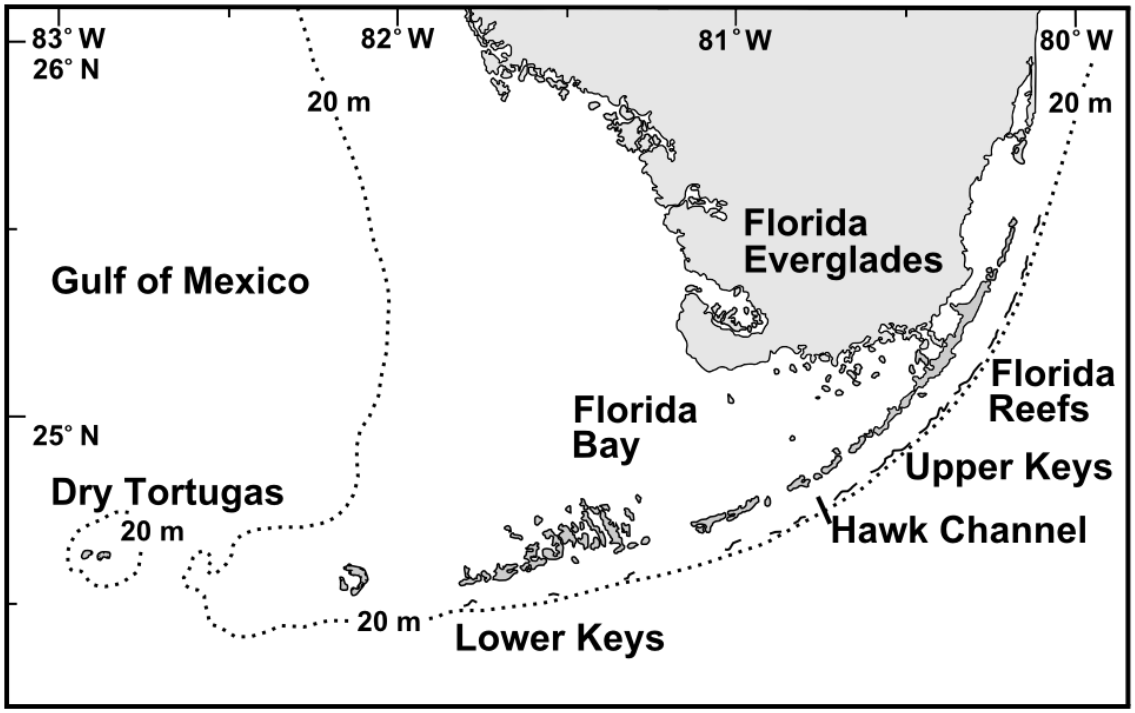


**Figure 2.7** Sketch map showing the location of the Florida Keys and the Florida Reefs

The Florida Keys are recognised as ecologically important and environmentally sensitive and are therefore protected by a patchwork of national wildlife refuges, parks and marine sanctuaries. The largest of these protected areas is the Florida Keys National Marine Sanctuary encompassing the islands and cays south of Broad Channel (http://floridakeys.noaa.gov/fknms_map/sanctuaryzoneboundaries.pdf).

The climate of the Florida Keys is subtropical with seasonal daytime temperatures ranging from 21$^{o}$ C in the winter (January) up to 28$^{o}$ C in the summer (July). Average annual rainfall is highly seasonal with two thirds of the precipitation occurring between the months of May and October when regular thunderstorms break over the Keys. The northern Keys experience higher rainfall (~140 cm yr$^{-1}$) compared to the drier southern Keys (~100 cm yr$^{-1}$) due to the existence of a pronounced rainfall gradient (Halley et al., 2004).

Ocean circulation on the Atlantic side of the Florida Keys is dominated by the Florida Current. The Florida Current originates at the point where the Loop Current is reflected round the Dry Tortugas and enters the Straits of Florida from the Gulf of Mexico. North of Cape Hatteras the Florida Current is deflected into the North Atlantic and becomes the Gulf Stream (Gyory et al., http://oceancurrents.rsmas.miami.edu/atlantic/loop-current.html; Gyory et al., http://oceancurrents.rsmas.miami.edu/atlantic/florida.html). Average sea surface temperatures range from 21$^{o}$ C in the winter up to 28$^{o}$ C in the summer (Halley et al., 2004).

# CHAPTER 3

MATERIALS AND METHODS

## 3.1 GENERAL INTRODUCTION

Chapter 3 introduces the materials and the methods used in this thesis to document skeletal preservation, determine element/Ca ratios and estimate the age of the fossil material.

The materials section is divided into two subsections covering modern and fossils corals. The basic skeletal architecture of each of the studied specimens is described in order to facilitate the interpretation and discussion of the geochemical data in later chapters. The laboratory methods section is divided into two subsections. Imaging and X-ray diffraction methodologies are covered in the first subsection while element geochemistry and isotope analysis are covered in the second subsection. All laboratory work is my own unless otherwise stated. Some of the methodologies described in this chapter are presented in Griffiths et al. (2013).

## 3.2 CORALS

### 3.2.1 Modern corals

Single specimens of live-collected *Siderastrea radians* (Pallas, 1766) and *Siderastrea siderea* (Ellis and Solander, 1786) from the North Atlantic (Table 3.1) were obtained in order to compare the preservation and geochemistry of Miocene *Siderastrea conferta* (Duncan, 1863) with modern siderastreid coral samples.

| Coral | Specimen No | Year | Location | Sample size (cm) |
|---|---|---|---|---|
| *S. siderea* | SID-D-1-I | 1994 | Florida | 5.8 x 3.9 x 0.5 |
| *S. radians* | NHMUK AZ 4879 | 1976 | Bermuda | 10.0 x 9.0 x 5.0 |

**Table 3.1** Modern siderastreid coral specimens.

The genus *Siderastrea* typically forms massive, rounded or platy colonies characterised by cerioid growth (corallites directly juxtaposed) and extramural budding (new corallites develop outside the wall of the parent corallite).
Corallite diameters vary, ranging from 3 – 8 mm depending on the species. The walls of the corallites are well-defined and linked by numerous synapticulae arranged in 2 – 5 synapticular rings. The septae are dentate and arranged in three or more septal cycles with septal numbers ranging from 30 – >60 per corallite. The columella varies in width and typically consists of numerous papillose trabeculae (NMITA, 2011; Vaughan, 1919; Foster, 1980a; Beck and Budd, 2008).

Species within the genus are differentiated using diagnostic characters such as the number of septa and the distance between the septal teeth, the corallite diameter and the structure of the wall and columella (Vaughan, 1919).

Five extant species are recognised worldwide, three of which occur in the Caribbean: *S. siderea*, *S. radians*, and *S. stellata* (Veron, 2000a). Four fossil species have been documented from Neogene sites across the Caribbean; *S. conferta*, (Duncan, 1863) *S. mendenhalli*, *S. silecensis*, and *S. pliocenica* (NMITA, 2011).

#### *3.2.1.1 Siderastrea siderea* (Ellis and Solander, 1786)

A slice of *Siderastera siderea* was acquired from Dr Jim Klaus, Department of Geological Sciences, the University of Miami, U.S.A. by Kenneth Johnson (NHM). The coral slice (Sid-D-1-l) was prepared from a live-collected colony harvested at a depth of ~15 m from Molasses Reef, Florida Keys, U.S.A. (25$^{o}$ 00.579’ N, 080$^{o}$ 22.471’ W) by Peter Swart, Rosenstiel School of Marine and Atmospheric Science (RSMAS), University of Miami, U.S.A. in April 1994. *Siderastrea siderea* is a slow-growing (5 – 8 mm yr$^{-1}$), long-lived (<100 yrs) species that typically forms encrusting or massive colonies over a metre in diameter (Veron, 2000a). *S. siderea* is a remarkably tough species, able to withstand poor water quality (high sedimentation and pollution) and adverse temperatures and salinities (Acevedo et al., 1989; Guzmán et al., 1994; Muthiga and Szmant, 1987; Guzmán and Tudhope, 1998).

The basic corallite plan for the species is shown in Figure 3.1. The morphological features of *S. siderea* are listed in Table 3.2.

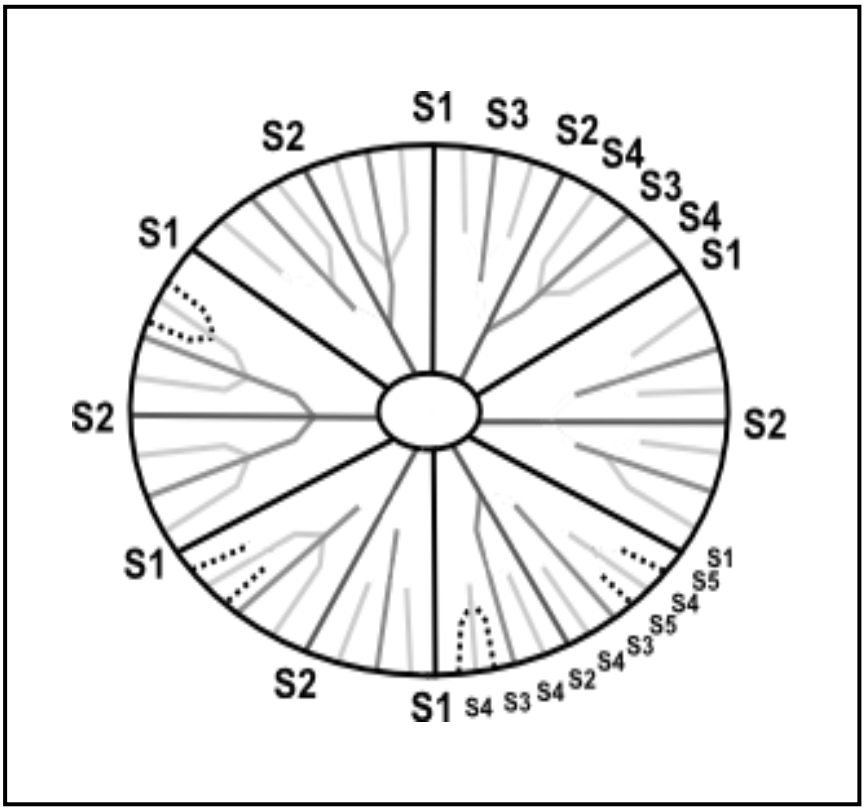


**Figure 3.1** Schematic diagram showing the basic septal plan found in *Siderastera siderea*. The septal cycles are labelled S1 to S5 in the order that they are produced (Diagram based on Figure 3 from Neves et al., 2010 and information in Veron, 2000a).

*Siderastrea siderea*

| Morphological character | Description |
|---|---|
| Colony shape | Juvenile colonies: encrusting |
| | Adult colonies: massive, typically rounded |
| Colony form | Cerioid |
| Corallite development | Pentagonal or hexagonal |
| Calice diameter | 3 – 5 mm |
| Calice relief | High |
| Corallite septal number | 44 - 50 |
| Septa | Thin and densely packed |
| | Typically 4 complete septal cycles |
| | Longer than in *S. radians* |
| | 6 – 8 septal teeth per mm |
| Continuity of septa | Discontinuous |
| Columella | Thin |
| Columella structure | Trabecular (papillose), deep fossa |
| Wall | Thin |
| Wall structure | Synapticulothecal |
| Synapticulae | 3 – 5 rings |
| Budding type | Extramural |

**Table 3.2** *Siderastrea siderea* key diagnostic characters (NMITA, 2011; Vaughan, 1919; Neves et al., 2010; Foster, 1980a, Beck and Budd, 2008; Budd and Guzmán, 1994).

### *3.2.1.2 Siderastrea radians* (Pallas, 1766)

A single dome-shaped encrusting colony of *Siderastrea radians* was collected live from shallow water reefs (>3 m depth) growing in Whalebone Bay, St George's Island on the north shore of Bermuda (32° 21.868' N, 64° 42.762' W). The sample (NHMUK AZ 4879) was collected in July 1976 by Jill Darrell (NHM).

*S. radians* typically form massive colonies up to 10 cm in diameter (Lirman et al., 2003) that may occur as mounds embedded within shallow reef communities or as free-living, mobile spheres (Duerden, 1904; Veron, 2000a). Typical growth rates for western Atlantic colonies range between 5 - 12 mm $yr^{-1}$ (Cortés and Risk, 1985). The species is common in marginal environments characterised by high sedimentation and suboptimal salinity (Lirman et al., 2003). The basic corallite plan for the species is shown in Figure 3.2. The morphological features of *S. radians* are listed in Table 3.3.

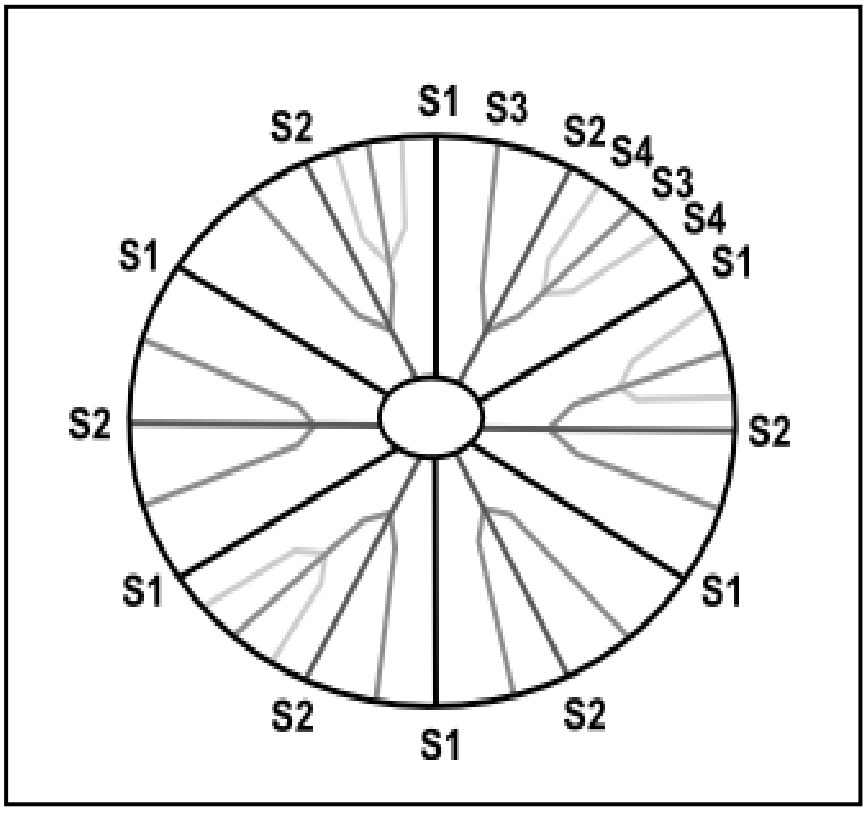


**Figure 3.2** Schematic diagram showing the basic septal pattern found in *Siderastera radians*. The septal cycles are labelled S1 to S4. Cycles 1 to 3 are complete but cycle 4 is incomplete (Diagram based on Figure 3 from Neves et al., 2010 and information in Veron, 2000a).*Siderastera radians.*

| Morphological character | Description |
|---|---|
| Colony shape | Massive dome-shaped or encrusting colonies |
| | Occasionally free-living, mobile spheres |
| Colony form | Cerioid |
| Corallite development | Sub-hexagonal and rather irregular |
| Calice diameter | 2.5 – 3.5 mm |
| Calice relief | Moderate |
| Corallite septal number | 30 - 40 |
| Septa | Irregularly spaced and variable thickness |
| | 3 complete septal cycles, 4$^{th}$ incomplete |
| | Shorter than in *S. siderea* |
| Continuity of septa | Continuous |
| Columella | Thick |
| Columella structure | Trabecular (solid), intermediate fossa depth |
| Wall | Thick |
| Wall structure | Synapticulothecal |
| Synapticulae | 2 – 3 rings |
| Budding type | Extramural |

**Table 3.3** *Siderastrea radians* key diagnostic characters
(NMITA, 2011; Vaughan, 1919; Neves et al., 2010; Foster, 1980a; Beck and Budd, 2008).

### 3.2.2 Miocene corals

Six fossil zooanthellate reef corals were collected from the Cantaure Formation, Paraguaná Peninsula, Estado Falcón, Venezuela (Chapter 2).

Three species of corals are represented in the early Miocene fossil assemblage investigated in this thesis: *Siderastrea conferta*, *Montastraea limbata*, and a *Porites sp*. The coral genera represented in the Cantaure assemblage examined here are typical of Early to Middle Miocene Caribbean carbonate build-ups characterised by small, species-poor patch reefs dominated by *Montastraea* and *Porites* (Budd, 2000; Budd et al., 1989; Budd et al., 1995; Vaughan, 1919).

| Coral | Specimen No | Year | Location (Venezuela) | Sample size (cm) |
|---|---|---|---|---|
| *S. conferta* | NHMUK AZ 4874 | 2009 | Cantaure Fm | 11.1 x 6.2 x 7.3 |
| *S. conferta* | NHMUK AZ 4875 | 2009 | Cantuare Fm | 5.9 x 2.8 x 9.5 |
| *M. limbata* | NHMUK AZ 4876 | 2009 | Cantaure Fm | 7.1 x 3.6 x 6.2 |
| *M. limbata* | NHMUK AZ 4877 | 2009 | Cantaure Fm | 11.3 x 5.3 x 6.7 |
| *M. limbata* | NHMUK AZ 4878 | 2009 | Cantaure Fm | 5.7 x 2.5 x 7.6 |
| *Porites sp* | NHMUK AZ 3140 | 2009 | Canature Fm | 11.8 x 6.6 x 6.4 |

**Table 3.4** Fossil coral specimens from the Canature Fm, Paraguaná Peninsula, Venezuela.

#### *3.2.2.1 Siderastrea conferta* (Duncan, 1863)

*Siderastrea conferta* forms massive rounded to sub-columnar (up to 34 cm tall and 31 cm thick) colonies that have been recorded from diverse Miocene reef deposits in Puerto Rico, Anguilla, Panama and Antigua (Vaughan, 1919; Budd et al., 1989; Johnson and Kirby, 2006; Duncan, 1863). The basic corallite plan for the species is shown in Figure 3.3 and the morphological features of *S. conferta* are listed in Table 3.4.

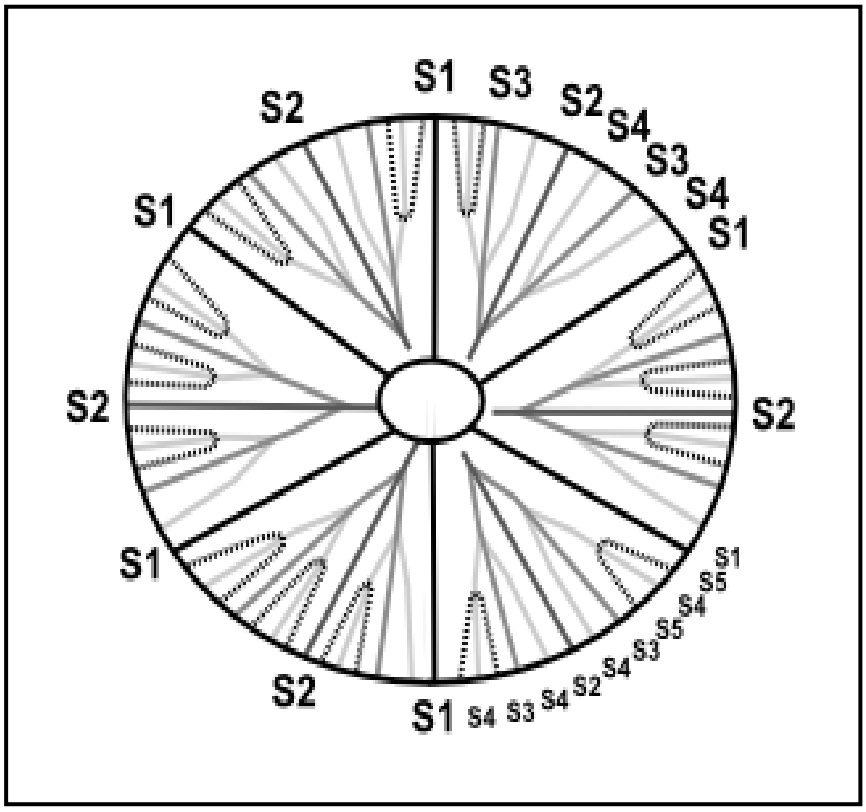


**Figure 3.3** Schematic diagram showing the basic septal pattern found in *Siderastera conferta*. The septal cycles are labelled S1 to S5. (Diagram based on information in Duncan (1863) and Vaughan, (1919).

*Siderastrea conferta*

| Morphological character | Description |
|---|---|
| Colony shape | Massive (rounded to columnar) |
| Colony form | Cerioid |
| Corallite development | Polygonal |
| Calice diameter | 6 - 8 mm |
| Calice relief | Low |
| Corallite septal number | >60 |
| Septa | Linear, gracile and crowded |
| | >4 septal cycles |
| Continuity of septa | Discontinuous |
| Columella | Thin and weakly developed |
| Columella structure | Trabecular (papillose) |
| Wall | Thin |
| Wall structure | Synapticulothecal |
| Synapticulae | >3 |
| Budding type | Extramural |

**Table 3.5** *Siderastrea conferta* key diagnostic characters (NMITA, 2011; Duncan, 1863; Vaughan, 1919; Foster, 1980a).

*S. conferta* was named *Isostraea conferta* by Duncan (1863) in his original taxonomic description. The species was subsequently recombined as *Siderastrea conferta* by Vaughan in 1919.

### *3.2.2.2 Montastraea limbata* (Duncan, 1863)

The genus *Montastraea* is a poorly-defined taxon that exhibits considerable morphological variation typically forming massive dome-shaped or flat colonies characterised by plocoid growth (cylindrical corallites possessing distinct walls and separated from one another by coenosteum) and extramural budding (Veron, 2000b). The corallites are monocentric (single polyps occupy individual corallites) and septothecal (the walls are formed by thickening of the septa) with well-developed, discontinuous costae. Corallite diameters range from 2 to 10 mm depending on the species and environmental conditions (NMITA, 2011; Veron, 2000b; Foster, 1980b).

Species within the genus are differentiated using diagnostic characters including corallite diameter, the number of septal cycles, relative septal length and width, costal architecture, relative costal length and width, and the structure of the columella (Veron, 2000b; Vaughan, 1919).

Ten extant species of *Montastraea* are recognised worldwide, four of which occur in the Caribbean: *M. annularis*, *M. faveolata, M, franksi, M. cavernosa,* (Veron, 2000b). Species of *Montastraea* have formed an important component of Caribbean reef communities for over 22 million years (Budd, 1991) and eleven fossil species, including three *M. limbata* morphotypes, have been documented from diverse Neogene reef deposits throughout the region (NMITA, 2011).

*Montastraea limbata* forms massive, rather irregular columns up to ~10 cm in height. The corallites are approximately circular in outline with diameters that range from 3 to 6 mm. Inter-corallite distances range from 4 to 6 mm. *M. limbata* has been recorded in Miocene deposits from Trinidad, Curaçao and the Dominican Republic (Duncan, 1863; NMITA,2011; Foster, 1983). The basic corallite plan for the species is shown in Figure 3.4 and the morphological features of *M. limbata* are listed in Table 3.5.

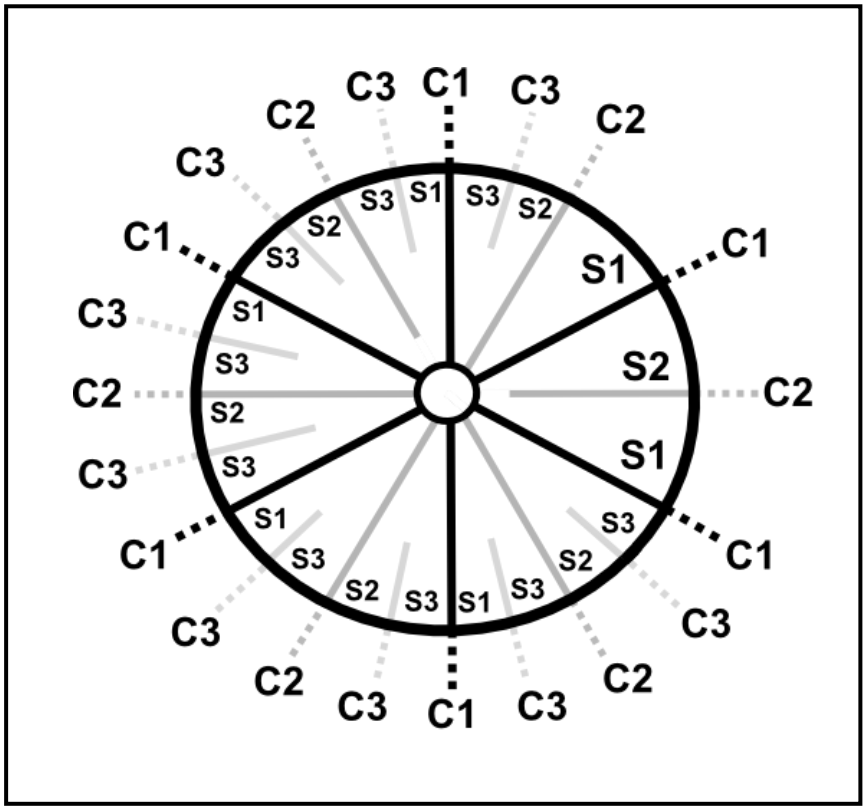


**Figure 3.4** Schematic diagram showing the basic septal pattern found in *M. limbata*. The septal cycles are labelled S1 to S3. C1, C2, and C3 refer to the costae that extend beyond the corallite wall (Diagram based on information in Vaughan, 1919 and Foster, 1983; Figure 1F).

*Montastraea limbata*

| Morphological character | Description |
|---|---|
| Colony shape | Massive (thin columns) |
| Colony form | Plocoid |
| Corallite development | Circular and unequal in size |
| Calice relief | Low |
| Calice diameter | 3.5 – 5.0 mm |
| Corallite spacing | 4 – 6 mm |
| | Corallites separated by coenosteum |
| Corallite septal number | ~24 |
| Costae | Usually alternately large and small |
| Septa | Secondary septa thinner than primary septa |
| | 3 septal cycles, occasionally incomplete 4th |
| Columella | Rudimentary |
| Columella structure | Trabecular and discontinuous |
| Wall structure | Septothecal |
| Budding type | Extramural |

**Table 3.6** *Montastraea limbata* key diagnostic characters
(Duncan, 1863; Vaughan, 1919; NMITA, 2011)

*Montastraea limbata* was named *Phyllocoenia limbata* by Duncan (1863) when the species was originally described. The coral was later recombined as *Orbicella limbata* by Vaughan (1919) and finally *Montastraea limbata* by Frost and Langenheim (1974).

#### *3.2.2.3 Porites* (Link, 1807)

The genus *Porites* represents one of the most successful, abundant and widespread reef-building corals for over 20 million years (Frost, 1977). Modern *Porites* are cosmopolitan throughout the tropics and occupy the largest range of any extant warm-water reef building coral (Veron, 2000b). Despite the importance of *Porites* in global coral reef ecosystems, species identification and taxonomy remain extremely problematic (Veron, 2000b; Forsman et al., 2009) due to the considerable morphological variation seen within individual colonies, within species and between species that reflect both underlying genetic differences and a phenotypically plastic response to a wide range of environmental factors (Forsman et al., 2009; Brakel, 1977).

Modern *Porites* may form platy (encrusting or laminar), branching or massive colonies. Massive forms are typically spherical or hemispherical when juvenile and dome-shaped when mature, producing large mounds over 5 m in diameter (Veron, 2000b). Colony growth may be plocoid, subcerioid or cerioid and budding is extramural. Corallites are generally small (<1.5 to 10 mm), irregular, perforated and highly variable in character depending on environmental conditions and underlying genetics (Forsman, 2003; NMITA, http://porites.geology.uiowa.edu/database/corals/systemat/porites.htm). Calices may be widely spaced with a well-developed wall reticulum (Type I *Porites*) or closely spaced with a poorly-developed wall reticulum (Type II *Porites*).

Fifty-two extant species of *Porites* are recognised worldwide, six of which occur in the Caribbean: *P. asteroides*, *P. colonensis*, *P. branneri*, *P. porites*, *P. furcata*, and *P. divaricata* (Veron, 2000b). Nine fossil species (*P. carrizensis*, *P. chipolanum*, *P. baracoaensis*, *P. convivatoris*, *P. anguillensis*, *P. trinities*, *P. macdonaldi*, *P. portoricensis*, and *P. waylandi*) have been documented from Neogene reef deposits across the Caribbean region (NMITA, 2011). The basic corallite plan for the genus is shown in Figure 3.5 and the key morphological features of *Porites* are listed in Table 3.6.

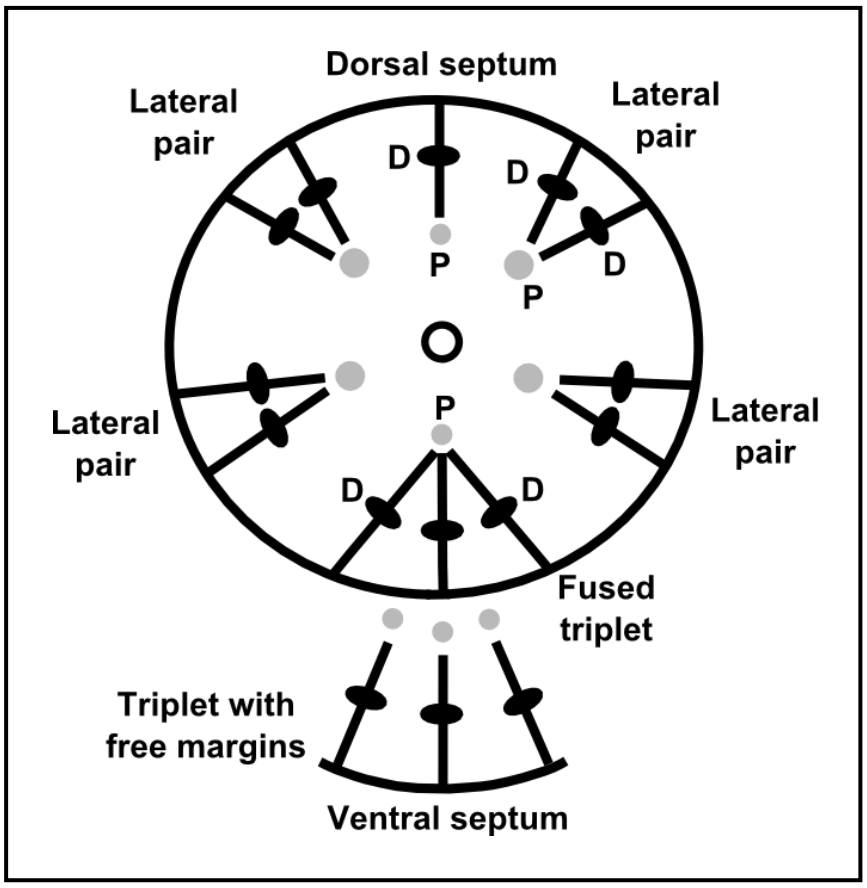


**Figure 3.5** Schematic diagram showing the basic septal pattern found in *Porites*. 'D' refers to the denticles (vertical pillars resembling pali that are arranged along the upper surface of the septa at fixed intervals). 'P' refers to the pali. (Diagram based on information in Veron, 2000b and Figure 1, pp279).

Fossil *Porites* sp

| Morphological character | Description |
|---|---|
| Colony shape | Encrusting, platy, branching or massive |
| Colony form | Plocoid |
| Corallite distribution | Even or uneven |
| Corallite septal number | Typically 12 but may have up to 20 septa |
| Calice relief | Low, intermediate or high |
| Calice diameter | <1.2 – 2.0 mm |
| Lobes | Paliform |
| Pali | 2 – 4 up to 6 - 8 |
| Palar ring | Wide, intermediate or narrow |
| Columella structure | Trabecular and discontinuous |
| Columella development | Strong (columella > pali) |
| | Intermediate (columella = pali) |
| | Weak (columella < pali) |
| Wall structure | Synapticulothecal |
| | Single (1 trabecula) |
| | Compound (2 or more trabeculae) |
| Budding type | Extramural |

**Table 3.7** *Porites* key diagnostic characters (NMITA, 2011).

Species within the genus *Porites* are differentiated using diagnostic characters such as corallite diameter and the distribution of corallites, relative length of the septa, the number and distribution of pali and denticles, and the structure of the columella, radii, synapticular rings and corallite walls (Veron, 2000b).

### 3.3 LABORATORY METHODS

Flow diagram showing the pathway used for the preparation and analysis of the corals

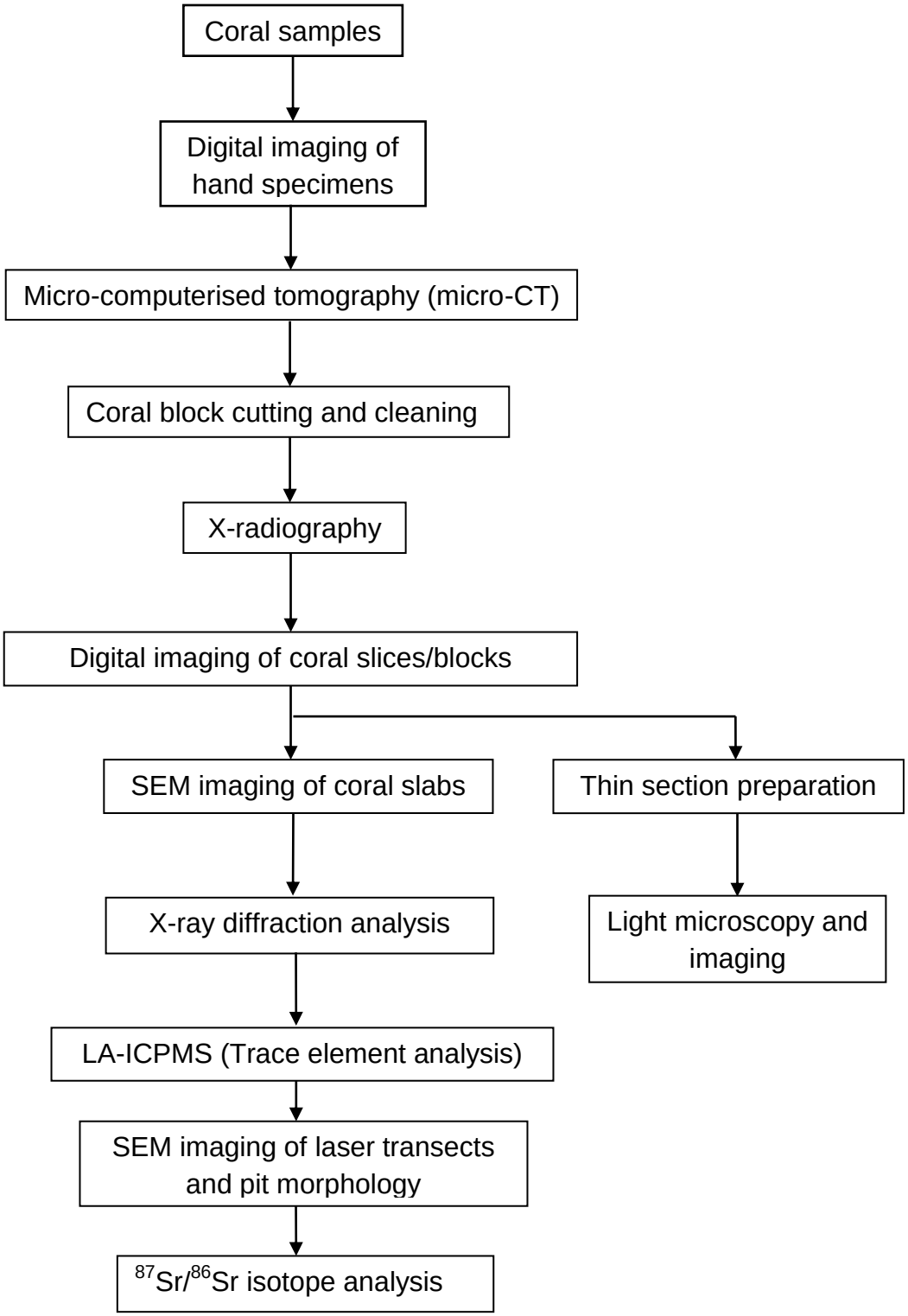

## 3.4 IMAGING AND X-RAY DIFFRACTION

### 3.4.1 Digital imaging

Digital photographic images were acquired for each of the coral heads before and after slicing in order to document the appearance of the corals in hand specimen.

#### *3.4.1.1 Preparation of coral heads for imaging*

The coral heads were washed under running tap water to remove adherent sediment and loose material and then rinsed three times in MilliQ water in order to flush out the tap water. The wet corals were air-dried in a clean-air hood following the final rinse prior to being stored in clean, labelled, self-sealing polythene bags.

#### *3.4.1.2 Digital photography*

Each coral was placed in turn on a clean contrasting surface with a scale-bar positioned adjacent to the specimen. Images were acquired using a Canon EOS 350D 8 megapixel camera fitted with a Canon 35 – 70 mm digital lens and built-in automatic flash unit (Canon Inc, Tokyo, Japan). Canon software was used to download the images from the camera onto a laptop computer. The digital photographic images presented in this thesis were edited using Adobe Photoshop Elements 7.0 software (Adobe Systems Inc, California, USA) and exported as Tiff (Tagged Image File Format) files. The Tiff file format offers the option of preserving the quality and resolution of the original images by allowing image data to be stored, edited and re-saved either without image compression or with image compression using lossless compression algorithms which is important for resolving skeletal architecture and features associated with diagenetic alteration.

### 3.4.2 Micro-computerised tomography (micro-CT)

Micro-CT imaging was undertaken to assess the distribution and extent of diagenetic alteration and macro-bioerosion and to determine the optimum plane for slicing the corals for geochemical analysis.

Over the last decade micro-CT has developed into an important tool for palaeontological research because it permits high-resolution, three-dimensional (3-D) imaging of external and internal features of samples enabling structural and taxonomic problems to be addressed without the destruction of the material being investigated (e.g. Roche et al, 2011; Roche et al., 2010). This is of particular relevance for fossil material and museum specimens. The disadvantages of the technique are the high cost and limited access (Schönburg and Shields, 2008) although these problems are likely to be reduced as more machines are commissioned.

#### *3.4.2.1 Preparation of coral samples for micro-CT*

The clean coral heads selected for examination (Table 3.7) were loaded separately into cardboard tubes and packed with plastic foam blocks to hold the specimens in place.

| SAMPLE | CORAL SPECIES | CT FILE NAME |
|---|---|---|
| NHMUK AZ 4879 (Bermuda) | *Siderastrea radians* | Sid radians D |
| NHMUK AZ 4878 (Venezuela) | *Montastraea limbata* | Mont 301.7 D |
| NHMUK AZ 4878 (Venezuela) | *Montastraea limbata* | Mont 301.7 E |
| NHMUK AZ 4878 (Venezuela) | *Montastraea limbata* | Mont 301.7 F |
| NHMUK AZ 3140 (Venezuela) | *Porites sp* | Por 3919 SP2 |

**Table 3.8** Coral samples selected for micro-CT scanning

Each coral was arranged so that the X-ray beam traversed the shortest distance through the sample. Corals with a rectangular cross-section were positioned with the long axis orientated in the vertical plane. Encrusting and dome-shaped corals (e.g. *Siderastrea radians*) were positioned edge-on (Figure 3.6).

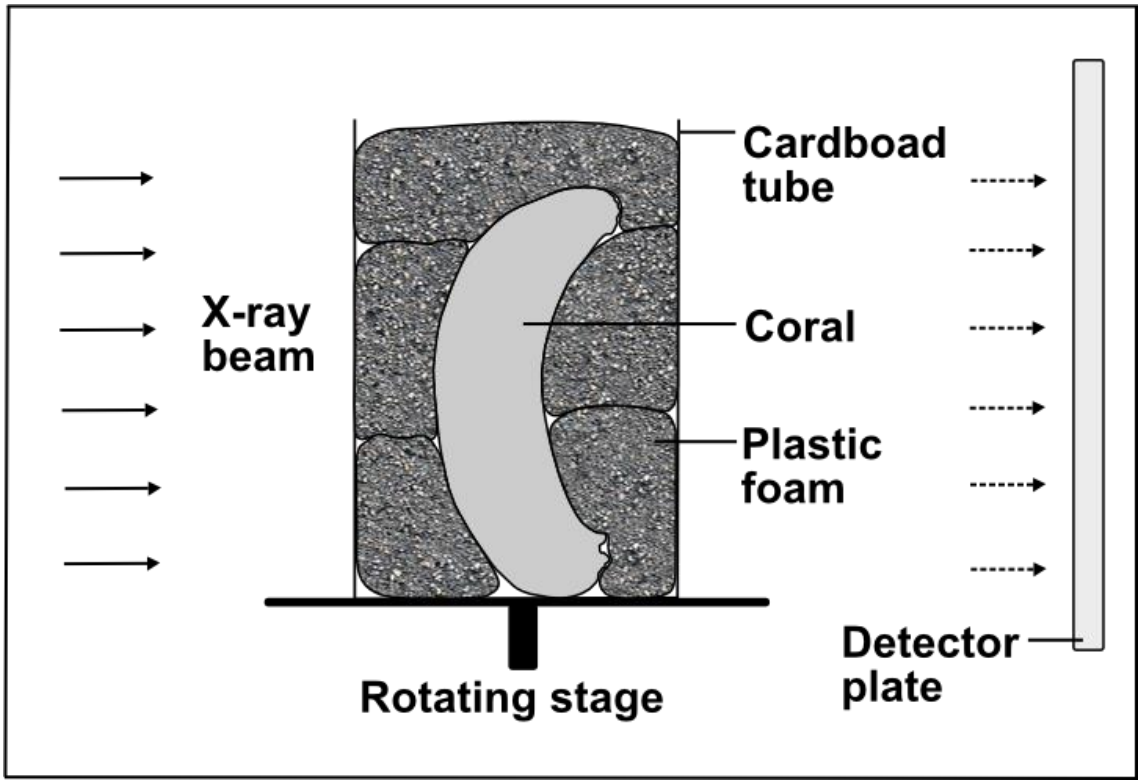


**Figure 3.6** Schematic cross-section through cardboard tube with dome-shaped, encrusting *Siderastrea radians* positioned edge-on for micro-CT scanning. Plastic foam blocks maintain the position of the coral and prevent movement during image acquisition.

### *3.4.2.2 Micro-CT imaging*

Tomographic data were acquired at the Natural History Museum EMMA Unit (London) on the Metris X-Tek HMX ST 225 cone-beam CT system (Nikon Metrology, Tring, UK) fitted with a four megapixel PerkinElmer XRD 1621 AN3 HS flat detector panel (PerkinElmer Inc, Massachusetts, USA). The cardboard specimen tubes were loaded in turn onto the rotating scan stage and a test image acquired to enable scan coverage, coral position and X-ray penetration to be assessed before full data acquisition. The corals were imaged using the following parameters:

Micro-CT imaging parameters:

| | |
|---|---|
| Target | Tungsten reflection |
| Focal spot size | 5 µm |
| Accelerating voltage | 225 kV |
| Current | 200 – 57 µA |
| Attenuator | 1.5 mm Cu (except for *S. conferta*) |
| Scan time | 780 – 1140 s |
| Rotation | $360^{o}$ |
| Projections | 3142 |
| Field of view | 250 mm diameter; 750 mm height |
| Scan resolution | $1/2000^{th}$ specimen height or diameter |

The cone beam micro-CT scanner produces 3-D representations of slices through the sample based on the differential absorption of the X-ray beam as it passes through material of different densities within the coral specimen (e.g. calcium carbonate skeletal elements and air-filled pore-spaces). A digital volume composed of three dimensional voxels (3-D pixels) is generated for each slice with each voxel assigned a grey-scale value based on the linear attenuation coefficient related to the density of the material being imaged (Roche et al., 2010).

3-D volumes were reconstructed from stacks comprising individual slices using CT PRO Version 2.0 (Nikon Metrology, Tring, UK) and visualised using VG Studio Max 2.0 (Volume Graphics, Heidelberg, Germany). A suitable plane parallel to growth was identified in each coral and landmarks mapped onto the surface of the CT volumes with the corresponding points marked on the coral specimens prior to sectioning. A laptop computer loaded with ImageJ (rsbweb.nih.gov/ij/), an open-source Java-based programme developed at the National Institutes of Health in the USA was used to visualise and analyse CT image stacks at RHUL.

### 3.4.3 Light microscopy

Observations on whole-coral blocks under the binocular microscope and on petrographic thin sections under plane-polarized light and cross-polarized light were made in order to evaluate skeletal aragonite preservation, identify diagenetic cements based on crystal morphology and assess dissolution, bioerosion and the distribution of diagenetic alteration.

#### *3.4.3.1 Thin section preparation*

Transverse and longitudinal thin sections of coral samples were produced in the rock preparation labs at RHUL by Neil Holloway. Small blocks of coral were set in epoxy resin and standard 0.03 mm thick, 60 x 20 mm petrographic thin sections produced by grinding and polishing with graded silicon carbide (400, 800 and 1200) on a wet glass lap.

#### *3.4.3.2 Light microscope imaging*

Coral thin sections were examined under the microscope in both plane and polarised light at magnifications ranging from 10x to 40x. Images illustrating skeletal preservation and evidence of diagenetic alteration were taken at RHUL on a Nikon SMZ1000 microscope fitted with a Nikon charge-coupled device (CCD) for digital image acquisition (Nikon Instruments Europe B.V., Amstelveen, The Netherlands).

### 3.4.4 Scanning electron microscopy (SEM)

Scanning electron microscopy was carried out in the EMMA Unit at the Natural History Museum (NHM) in London in order to visually assess coral preservation and record evidence of diagenetic alteration and bioerosion. Visual assessment of skeletal architecture and preservation is essential for interpreting variations in trace element geochemistry.

#### *3.4.4.1 Scanning electron microscope imaging*

Imaging was performed on a Leo 1455 VP variable pressure SEM (Carl Zeiss AG, Oberkochen, Germany) equipped with four-quadrant solid-state

backscattered electron (BSE), variable pressure secondary electron (SE), and energy dispersive X-ray (EDX) detectors (X-Max detector, Oxford Instruments, Oxford, U.K.) permitting non-destructive imaging and qualitative element (EDX) analysis to be undertaken on uncoated samples when operated under low vacuum pressures.

The SEM was operated at 20 kV under a vacuum pressure of 15 Pa at working distances of 13 - 18 mm depending on the size of the coral samples under investigation. Digital SEM images of structural and diagenetic features were acquired at magnifications up to 3000 x with QBS diodes 1 and 4 switched off to obtain optimum topographic and structural visualisation.

### 3.4.5 X-radiography

X-radiography is routinely used for visualising the density bands associated with skeletal growth in scleractinian corals. Measurement of the distance between growth band couplets permits annual growth rates to be calculated. Coral skeletal density may also be assessed from X-radiographs revealing the presence of diagenetic cement infill, dissolution or bioerosion.

#### *3.4.5.1 X-radiographic imaging*

X-ray radiographs of the corals were acquired in the Radiology Department at Papworth Hospital in Cambridge using a Philips Digital Diagnost X-ray system coupled to a flat detector plate with a resolution of 143 µm pixel size (Philips Healthcare [Europe], Best, The Netherlands).

The corals were placed directly onto the surface of the horizontally orientated detector plate. The X-ray tube was positioned vertically above the detector and the height adjusted to give a detector-focus distance of 100 cm. The X-ray beam was collimated and a single exposure made using factors of 40 kV and 8 mAs. The X-radiographs were exported as Dicom images and edited using ImageJ.

### 3.4.6 X-ray diffraction (XRD)

Quantitative estimates of aragonite and calcite modal concentrations were obtained by XRD to screen the corals for diagenetic alteration. XRD analysis is

a useful tool for screening for the presence of calcite (and other mineral contaminants). However XRD is not able to distinguish between primary skeletal aragonite and secondary aragonite cement and therefore other investigations (e.g. light and scanning electron microscopy) are needed to identify secondary aragonite.

#### *3.4.6.1 Sample preparation for XRD*

Five coral samples were selected for XRD analysis in order to screen for diagenetic alteration. The samples and the sampling sites are documented in Table 3.9. Coral material was removed from the surface of each coral sample block using a clean, angled dissection needle. Only a single surface was used for sampling in order to preserve an intact surface for LA-ICPMS analysis although multiple sampling sites on that surface were utilised where possible. Single samples were taken from the *M. limbata* specimens due to the difficulty of sampling the thick coral walls.

| Coral specimen | Sample | Description of sample site |
|---|---|---|
| *S. conferta* NHMUK AZ 4874 | Sample 1 | Clean area, top |
| | Sample 2 | Clean area, lower left |
| | Sample 3 | Clean area, right base |
| *S. conferta* NHMUK AZ 4875 | Sample 1 | Clean area, top |
| | Sample 2 | Clean area, middle |
| | Sample 3 | Clean area, lower left |
| *M. limbata* NHMUK AZ 4876 | Sample 1 | Clean area, middle right edge |
| *M. limbata* NHMUK AZ 4878 | Sample 1 | Clean wall area, left base |
| *Porites* sp NHMUK AZ 3140 | Sample 1 | Clean area, middle base |
| | Sample 2 | Clean area, middle top |

**Table 3.9** Coral samples and sampling sites selected for XRD analysis.

Powdered samples were produced by crushing ~10 mg of coral in a clean agate bowl for ~30 seconds. A couple of drops of de-ionised water were added to the powder and the mixture stirred to produce a smooth suspension that was spread in a film across the bottom half of a clean slide. The slides were then placed in a warm oven to dry off prior to analysis. The pestle and mortar were cleaned between each sample to prevent cross contamination.

#### *3.4.6.2 XRD analysis*

XRD analysis was carried out by Dave Alderton at Royal Holloway University of London. The samples were analysed on a Philips 3710 diffractometer (PANanalytical, Almelo, The Netherlands) using Cu *K*-α radiation over diffraction angles (2θ) of 20 – 37 in order to include the major peaks for aragonite, calcite and quartz. The peaks were interpreted by using a conversion chart of 2θ to angstrom units (D-spacing) for Cu *K-α* radiation and data cards published in the Mineral Powder Diffraction File Data book (Joint Committee on Powder Diffraction Standards, 1993).

A compilation of the data used to interpret the XRD graphs is shown in Appendix 2.

Limits of detection for calcite in aragonite were determined to be ~1- 2%. Modal concentrations were calculated using the peak area analysis equation of Milliman (1974).

## 3.5 GEOCHEMICAL ANALYSIS

### 3.5.1 Measurement of element/Ca ratios by laser ablation inductively-coupled plasma mass spectrometry (LA-ICPMS)

Over the last 15 years LA-ICPMS has become an important tool for palaeo-climate research because the technique permits rapid simultaneous high-spatial resolution analysis of suites of important proxy trace elements (Sinclair et al., 1998).

### *3.5.1.1 Sample preparation for LA-ICPMS*

Four fossil coral samples and one modern corals (Table 3.10) were selected for analysis.

| SAMPLE | CORALSPECIES | AGE |
|---|---|---|
| NHMUK AZ 4874 (Venezuela) | *Siderastrea conferta* | late Early Miocene |
| NHMUK AZ 4875 (Venezuela) | *Siderastrea conferta* | late Early Miocene |
| NHMUK AZ 4876 (Venezuela) | *Montastraea limbata* | late Early Miocene |
| NHMUK AZ 4878 (Venezuela) | *Montastraea limbata* | late Early Miocene |
| NHMUK AZ 4879 (Bermuda) | *Siderastrea radians* | modern |

**Table 3.10** Coral samples selected for element/Ca geochemical analysis

The corals were sliced parallel to the main growth axis following 3-D x-ray tomography with an irrigated diamond blade rock saw and cut into 5.0 cm x 2.0 cm x 0.5 cm blocks. The blocks were cleaned repeatedly in an ultrasonic bath for 15 minutes in Rectapur Acetone (BDH) followed by Methanol HPLC (Lab-Scan Analytical Sciences) and MilliQ water before being air-dried under a laminar flow hood and stored in clean, self-sealing polythene bags.

### *3.5.1.2 Laser ablation inductively coupled mass spectrometry*

Geochemical analysis was carried out at Royal Holloway University of London (RHUL) using a custom-built ArF excimer (193 nm) laser ablation system (prototype RESOlution M-50, Resonetics LLC, USA) coupled to a two-volume laser ablation cell (Laurin Technic, Australia) and an Agilent 7500ce quadrupole ICPMS. Horizontal profiling was chosen for the analysis of palaeo-environmental geochemical proxies because this method permits continuous time-resolved sampling of the corals along carefully chosen predetermined transects. Depth profiling was chosen for the analysis of diagenetic cements because it permits very high-resolution sampling of small discrete targeted regions of the coral and allows an assessment of cement thickness to be made

in conjunction with SEM. High-resolution depth and lateral profiling requires fast signal washout from the ablation chamber and signal smoothing prior to entry into the mass spectrometer. The laser system at RHUL meets these requirements with the small effective (1-2 $cm^3$) volume of the funnel-shaped ablation chamber within the Laurin cell providing fast signal washout (~3.5 s/two orders of magnitude with 'squid' fitted) and the addition of a signal smoothing manifold ('squid') upstream of the ICP-MS to smooth the signals and remove signal beating (spectral skew) produced by the interplay between ICPMS sample dwell time and slow (<5 Hz) laser repetition rates (Müller et al, 2009).

Coral samples and standards were mounted in sample holders and scanned on a flat-bed Epson scanner (Seiko Epson Corporation, Tokyo, Japan) at a resolution of 800 dpi prior to loading into the ablation cell. The scanned images are imported into the laser control system in order to facilitate co-ordination of the sample and the stage.

Horizontal profile transects were cleaned prior to data acquisition by ablating at a repetition rate of 60 Hz and a scan speed of 10 mm $min^{-1}$. Data were acquired by ablating along the cleaned horizontal transects in the direction of growth with a 300 µm x 50 µm rectangular slit and laser parameters of ~63 mJ and 10 Hz. The laser was operated with a 55% attenuator giving a fluence of ~ 3.5 $J/cm^2$ at the specimen surface. Background counts were collected over intervals of 45 seconds pre- and post-ablation and standards were analysed directly before and after data acquisition.

### 3.5.2 Laser ablation depth profile analysis

Five depth profile analyses were acquired for primary skeletal aragonite and diagenetically altered regions using a spot size of 57µm at a laser repetition rate of 5 Hz and an energy density (fluence) at the sample surface of ~2.5 $J/cm^2$.

Ablation takes place within the funnel-shaped upper chamber of the Laurin cell in an atmosphere of pure helium. The sample aerosol is transported to the ICPMS via a signal smoothing manifold ('squid') in helium to which a stream of argon carrier gas (flow rate, 6 ml/min) admixed with nitrogen is admitted. The addition of di-atomic nitrogen gas has been reported to enhance sensitivity (Durrant, 1994). Background counts were collected over intervals of 30

seconds prior to each spot analysis and averaged counts used to correct the measured sample and standard ion intensities. A suite of isotopes (m/z) were measured including $^{11}B$, $^{25}Mg$, $^{88}Sr$, $^{138}Ba$, and $^{238}U$. Calcium was measured for use as an internal standard in order to correct for variations in ablation yield. Limits of detection were determined by calculating the ablation yield equivalent to three times the standard deviation of the background counts. Data are expressed as molar ratios relative to calcium. Time-matched element concentrations were calculated for each profile by taking equivalent time-slice measurements of a NIST 612 multi-element glass standard using GeoReM NIST SRM 612 preferred values (Jochum et al., 2011). Averaged background counts collected over 30s intervals before and after each analysis were used to correct standard and sample ion intensities. A USGS MACS-3 pressed-powder carbonate standard was utilised to evaluate the accuracy of the data. Although reference values have yet to be formally published for the MACS-3 standard, preliminary values provided by Steve Wilson (pers comm.) have been taken as the baseline for comparing the measured concentrations presented in this study. The analyses of the MACS-3 standards and coral samples were conducted over four separate daily sessions and as a result show some day to day variability (Appendix 2). The variability for boron between analytical sessions has been adjusted to the mean value of 9.86 ± 1.33 ppm (1 SD) in the absence of reference values for boron. The variations seen in boron and magnesium reflect the compositional heterogeneity in the NIST 612 glass standards (e.g. for B >10% reported by Eggins and Shelley, 2002), subtle differences in daily tuning and the difficulty of accurately measuring light elements due to mass bias effects. For strontium, the variation reflects differences in detector response to high count rates.

### 3.5.3 Measurement of the depth of material removed per laser pulse

The depth of material removed per laser pulse was determined in order to facilitate interpretation of variation in element/Ca concentration with depth.

Pits of different depths were produced by pulsing the laser 50, 100, 200, 300 and 500 times onto the surface of a polished block of aragonite derived from the hinge of the giant clam *Tridacna*. The data were acquired with a spot size of 96

μm at a laser repetition rate of 10 Hz and a fluence of 2.2 J/cm$^2$ at the surface of the aragonite block. SEM imaging of the laser pits was performed on the LEO 1455 VP variable pressure microscope in the EMMA Unit at the NHM in London. The microscope was operated at 15 kV under a vacuum pressure of 15 Pa at a working distance of 18 mm with the detector set up to obtain maximum topographic information. Each laser pit was imaged twice at a magnification of 1500 x with the specimen tilt altered by 6$^o$ between the first and second images to enable production of stereoscopic pairs. Contrast and brightness were set at 20.9% and 36.5% respectively in order to ensure good visualisation of surface features for optimum image registration. The image data was processed in INCA (Oxford Instruments, UK) and PaintShop Pro (Corel Corporation, Canada) prior to 3-D pit reconstruction and depth analysis with MeX 4.2 software (Alicona, Austria). The resultant depth of material removed per laser pulse was found to be remarkably consistent for both shallow and deeper pits, ranging from 81 to 84 nm with an average of 83 ± 1 nm which has been used to create element ratio-depth plots.

### 3.5.4 $^{87}Sr/^{86}Sr$ isotope analysis

The stratigraphic age of four fossil coral samples representing two species (*S. conferta* and *M. limbata*) were estimated from the $^{87}Sr/^{86}Sr$ isotope ratios preserved in the primary aragonite. These data are used to additionally constrain the published age of the Cantaure Formation based on nannofossil and foraminiferal biostratigraphy (Rey, 1996; Diaz de Gamero, 1974). Sample/chemical preparation and isotope analysis were undertaken at RHUL in laboratories with class 100 000 or better filtered air.

$^{87}Sr/^{86}Sr$ isotope analysis and age estimation is applicable solely to marine minerals since the method is based on changes in the $^{87}Sr/^{86}Sr$ value of strontium dissolved in the world's oceans over time and the assumption that at any given point in time, the strontium isotope ratio of seawater is homogenous throughout the world's oceans due to the residence time of strontium in seawater (~$10^6$) far exceeding the mixing time (~$10^3$) of the oceans (McArthur et al, 2012). The $^{87}Sr/^{86}Sr$ in seawater varies through time due to the influence of a number of processes (McArthur et al, 2012). Changes in the rate of

continental weathering affect the flux of detrital terrigenous material with high strontium $^{87}Sr/^{86}Sr$ values into the oceans while variation in the rate of ocean crust formation and hydrothermal exchange at spreading centres affect the input of strontium with low $^{87}Sr/^{86}Sr$ values into the oceans. Dissolution of carbonates beneath the carbonate compensation depth on the sea floor releases strontium with $^{87}Sr/^{86}Sr$ values similar to that of the seawater (McArthur, 1994; Oslick et al, 1994)

#### *3.5.4.1 Sample preparation for $^{87}Sr/^{86}Sr$ isotope analysis*

Four fossil coral samples were chosen for analysis (Table 3.11). Well-preserved regions in each coral sample block were identified and screened using both light and scanning electron microscopy in order to exclude diagenetic cements and evidence of bioerosion/alteration. Powdered samples (Table 3.11) were obtained by hand-drilling the targeted regions using a Proxxon micro-drill (Proxxon GmbH, Niersbach, Germany) fitted with a fine-point diamond drill-bit (1 mm maximum diameter). Each sample was stored in clean, labelled Labco extainers prior to digestion and analysis.

All the equipment and chemicals used in the analyses were cleaned and prepared before use. Beakers and lids were cleaned in 16M $HNO_3$ heated to 80$^{o}$C for 48 hours and then stored in MilliQ $H_2O$. Prior to use the beakers and lids were removed from the MilliQ with tongs and submerged in fresh MilliQ heated to 100$^{o}$C on a hotplate for 60 minutes before air drying under a clean hood. Nitric acid was sub-boiled in a FEP still.

The powdered aragonite samples were placed in clean beakers and dissolved in 0.5 ml MilliQ to which a few drops of concentrated $HNO_3$ was added followed by evaporation overnight on a hotplate set at 100$^{o}$C. The residues were digested in 0.75 ml 4M $HNO_3$ heated to 100$^{o}$C for 1 hour on a hotplate. The sample liquid was cooled and then centrifuged for 6 minutes in order to remove any remaining detrital material.

| FOSSIL CORAL SAMPLES | WEIGHT (g) |
|---|---|
| NHMUK AZ 4874 (*Siderastrea conferta*) | 0.04633 |
| NHMUK AZ 4875 (*Siderastrea conferta*) | 0.02850 |
| NHMUK AZ 4876 (*Montastraea limbata*) | 0.01889 |
| NHMUK AZ 4878 (*Montastraea limbata*) | 0.00828 |

**Table 3.11** Fossil coral samples selected for $^{87}Sr/^{86}Sr$ isotope analysis

### *3.5.4.2 Strontium separation chromatography*

Pipette tips were prepared for chromatography by snipping the ends off and packing the base of the tips with frit. Frit is porous to fluids but not the Sr-spec resin. The frit-loaded pipette tips stored in 10% $HNO_3$ were cleaned by passing 4M $HNO_3$ followed by MilliQ through tips prior to loading with 0.3 g EiChrom® 50-100 µm Sr-spec resin, an Sr-selective extraction chromatographic resin (Horowitz et al, 1992). The spec-resin was cleaned and conditioned by passing 4M $HNO_3$, MilliQ, 4M $HNO_3$ and 3 x MilliQ through the tips. 0.5 ml of sample liquid was added to each column and washed with 1.5 ml 8M $HNO_3$ and the Sr eluted in MilliQ. The elutant was dried down on a hotplate at 100$^o$ C and then re-dissolved in 1 ml 8M $HNO_3$ before repeating the chromatography steps using 2.5 ml 8M $HNO_3$ and MilliQ water. The samples were finally re-dissolved in 2.5M HCL and loaded onto degassed rhenium filaments preconditioned with 1 µl 10% phosphoric acid ($H_3PO_4$) and 1 µl tantalum fluoride ($TaF_5$) emitter.

### *3.5.4.3 'Cathodeon' bead preparation*

'Cathodeon' beads were cleaned by grinding off the old filament material and residues using a hand-drill fitted with a burr before spot welding new rhenium filament strips between the bead posts. Rhenium was selected because the filaments are thicker and able to take higher currents for longer and are better suited for analyses of small samples with low Sr concentrations. The beads were placed in a clean Pyrex beaker and boiled in MilliQ on a hotplate for 45

minutes and then rinsed twice in clean MilliQ. After drying in an oven overnight, the beads were degassed in a vacuum better than <0.001 Pa under a current load of 5 A for 5 minutes. The current was stepped down to 3.5 A then 2 A for a further 5 minutes each. The beads were removed and stored in a bead-box for a minimum of 24 hours to allow the filaments to oxidise before sample loading.

#### *3.5.4.4 Preparation and cleaning of the sample-holder and turret assembly*

The sample holders were unscrewed from the turret assembly and placed on a clean tray. The exit slits were removed from the metal blocks and cleaned on both sides with a cotton bud moistened with 10% $HNO_3$. The exit slits and the metal blocks were then placed in a clean Pyrex beaker and covered with MilliQ and concentrated $HNO_3$ in volume ratios of 2:3 and 1:3 respectively and boiled at 100$^{o}$C on a hotplate in a fume cupboard for 20 minutes with a glass cover placed over the beaker. The acid fluid was poured away and the slits and blocks cooled before being rinsed three times in MilliQ. Fresh MilliQ was added to the beaker and the slits and blocks ultrasonicated for 10 minutes to remove any remaining adherent particulate material. The slits and blocks were then rinsed in MilliQ, drained and dried in an oven for ~ 20 minutes. The sample holders were then reassembled and screwed back onto the turret assembly.

#### *3.5.4.5 Isotopic analysis*

Loaded beads were placed in a 16-turret sample-holder and analysed on a VG354 multi-collector (five collectors) thermal ionization mass spectrometer at RHUL using the multidynamic procedure of Thirlwall (1991). Analayses were performed at an accelerating potential of 8 kV with source and flight tube vacuums better than 5 x $10^{-5}$ and 7 x $10^{-7}$ Pa respectively. All samples were analysed automatically using VG Fisons software modified by M.F. Thirlwall.

#### *3.5.4.6 Sr isotope data handling and correction*

The data were corrected for mass fractionation by normalization to an $^{86}Sr/^{88}Sr$ value of 0.1194 using a power law. $^{87}Rb$ was subtracted using the measured value of $^{85}Rb$ and an $^{85}Rb/^{87}Rb$ ratio of 2.59265 (Steiger and Jäger, 1977). $^{87}Sr/^{86}Sr$ analyses of the Sr carbonate standard NIST SRM 987 gave a

value of 0.710269 ± 0.000009 (2σ) while long-term (~24 months) analyses of the NIST SRM 987 standard yielded an average $^{87}Sr/^{86}Sr$ value of 0.710258 ± 0.000017(2σ). All data were corrected to NIST SRM 987 using the accepted value of 0.710248.

#### *3.5.4.7 Determination of fossil coral age using strontium isotope stratigraphy*

Fossil coral ages were determined by correlating the coral strontium isotope data with the values in the IS Look-Up table V4: 08/04 (McArthur and Howarth, 2004; McArthur et al., 2001).

# CHAPTER 4

IMAGING AND ASSESSMENT OF CORAL PRESERVATION

## 4.1 GENERAL INTRODUCTION

Chapter 4 presents visual evidence documenting skeletal preservation and diagenetic alteration in the modern and fossil coral specimens obtained by photographic imaging, light and electron microscopy and X-radiography. These data are compared with X-ray diffraction analyses in order to show the importance of microscopy in screening for the presence of secondary aragonite cement.

Detailed descriptions of the distribution and morphology of aragonite, calcite and brucite cements identified in the modern coral samples are presented and the importance of the role of endobiotic organisms in the erosion of skeletal material and the deposition of diagenetic cements is discussed.

The complex diagenetic history of the fossil corals is illustrated by the range of cements, their sequence of deposition and the presence of hydrocarbon charging. Observations on the distribution and morphology of aragonite, calcite, pyrite and dolomite cements and hydrocarbon deposits are presented and the importance of meteoric and vadose diagenetic environments on the deposition of calcite cements is discussed. Some of the observations presented in this chapter are included in Griffiths et al. (2013).

Primary coral aragonite is metastable and may be affected by a range of diagenetic processes such as dissolution, cementation, neomorphism, bioerosion, dolomitisation, and micritization (Tucker and Wright, 1990; Flügel, 2004). Dissolution refers to the chemical removal of skeletal material and metastable cements and occurs when fluids undersaturated in carbonate are present in pore spaces and voids. Diagenetic settings that favour dissolution include meteoric, deep burial and deep sea environments (Flügel, 2004). Cementation comprises a range complex chemical processes that lead to the nucleation and precipitation of crystals from fluids supersaturated with aragonite, calcite or other minerals (Tucker and Wright, 1990; Flügel, 2004). The precipitation of exotic cements such as brucite involves microenvironments within the coral in which the chemistry of the pore fluids is altered by the activity of endolithic organisms and the presence of organic biofilms (Nothdurft and Webb, 2009). Neomorphism refers to transformation processes that involve the dissolution and re-precipitation of minerals or their polymorphs in the presence

of water (Flügel, 2004). Bioerosion entails the removal of skeletal aragonite by grazing, etching or boring organisms (e.g. fish, urchins, acrothoracican barnacles, clionid sponges, marine molluscs, polychaetes, bivalves, algae, fungi and bacteria) and involves the complex interplay between chemical dissolution and mechanical abrasion (Hutchings, 1986). Dolomitisation involves the replacement of original calcium carbonate with magnesium carbonate due to the action of magnesium-rich pore fluids on the chemistry of the carbonates (Flügel, 2004). Biological micritization entails the formation of microcrystalline calcite crystals 1 – 4 µm in diameter due to the activities of microboring organisms such as algae, fungi or cyanobacteria (Scholle and Ulmer-Scholle, 2003).

The diagenesis of carbonates is principally controlled by crystal mineralogy and chemistry, pore-fluid chemistry and rate of flow, dissolution and precipitation rates, grain size (i.e. the surface area available for reactions) and interactions with organic substances and the activity of living organisms (Flügel, 2004; Walter and Morse, 1984; Nothdurft et al., 2005; Nothdurft et al., 2007; Nothdurft and Web, 2009).

Diagenetic alteration may commence very early on, sometimes within a few days of skeletal deposition (Nothdurft et al., 2007) and because significant temperature anomalies are recorded by geochemical proxies in the presence of cements and dissolution it is therefore essential to rigorously assess the preservation of coral specimens prior to geochemical analysis.

The aims of this chapter are to:

1. Document the visual appearance of the modern and Miocene coral specimens in hand specimen.

2. Assess diagenetic cemention and dissolution in Miocene corals using light microscopy.

3. Examine and document skeletal preservation in modern and Miocene corals in the scanning electron microscope.

4. Interpret the radiographic appearance of skeletal structures and diagenetic alteration in modern and Miocene coral samples.

5. Compare the results of XRD analysis with visual analysis under the light and electron microscopes to show the importance of microscopy for identifying secondary aragonite cements.

## 4.2 DESCRIPTION OF THE CORALS IN HAND SPECIMEN

### 4.2.1 Modern coral samples in hand specimen

Both the modern corals show evidence of bioerosion. The upper surface of *Siderastrea radians* (NHMUK AZ 4879) has been penetrated by macro-boring organisms creating pits ~6 mm in diameter in the corallum. Close inspection of the pits reveals some are lined by a sub-millimetre layer of material while others possess rims up to 2 mm across that surround the entrance to the boreholes (Figures 4.1a and b). Cross-sections through *S. radians* reveal orange, green/grey bands occupied by coloured algal endobionts. A prominent orange band is present just beneath the surface of the coral while more diffuse orange/red and green/grey bands lie in older, deeper regions of the corallum (Figure 4.1c). A tangential section through a macro-borehole with an internal diameter of 4 mm is seen at the base of the coral slice. The internal surface of the bore-hole has a 'chalky' appearance (Figure 4.1c) when examined under a stereo-microscope indicating dissolution and alteration of the original coral aragonite (James, 1974; Pingitore, 1976; McGregor and Gagan, 2003).

A cross-section through *S. siderea* (SID-D-1-l) is shown in Figure 4.1d. A very prominent bright pink/brown band is visible just below the surface of the coral. The pink/brown colouration is produced by the vital stain alizarin red S which has been administered to the live coral prior to harvesting in order to measure the growth of the coral *in situ.* Two sub-millimetre boreholes surrounded by altered white skeletal material are visible on the cut coral surface (black arrow).

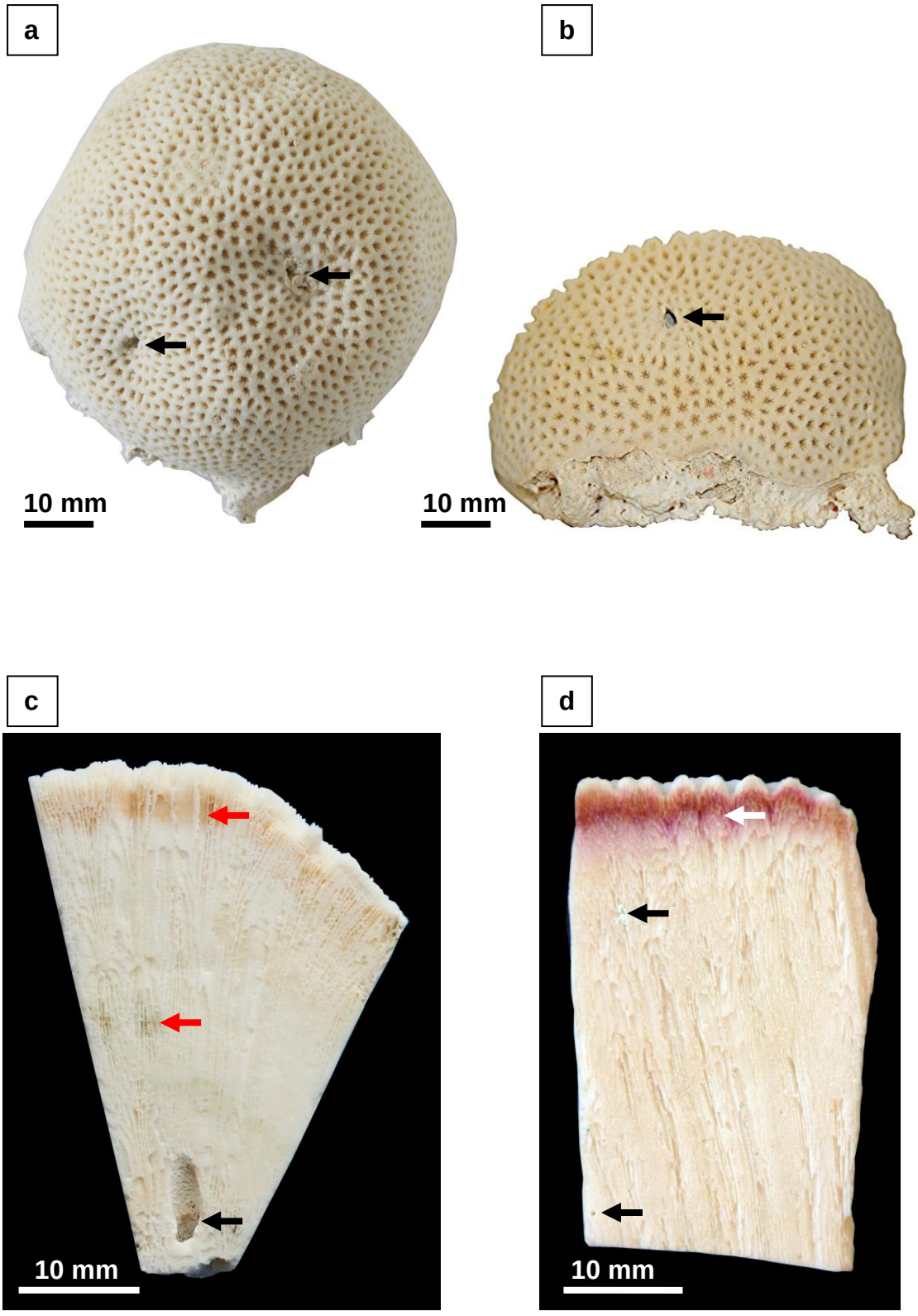
a
10 mm
b
10 mm
c
10 mm
d
10 mm

**Figure 4.1** (Previous page) photographs showing the appearance of the modern coral samples in hand specimen. **a – b** shows the dome-shaped encrusting morphology of *Siderastrea radians* (NHMUK AZ 4879). Macro-boreholes penetrate the surface of the corallum (black arrow). **c** Longitudinal section through *S. radians* showing endobiont-rich coloured bands (red arrow). A tangential section through a macro-borehole is visible at the base of the coral (black arrow) and is lined with 'chalky' altered aragonite. **d** A cross-section through *Siderastrea siderea* (SID-D-1-l). Pink/red alizarin red S stained band is present just beneath the tips of the coral skeleton. Micro-boreholes surrounded by 'chalky' altered skeletal material are visible on the cut coral surface (black arrow).

### 4.2.2 Miocene coral samples in hand specimen

All the fossil corals examined for this thesis show evidence of diagenetic alteration, bioerosion and hydrocarbon charging in hand specimen although the amount of alteration differs considerably between the coral samples (e.g. *Siderastrea conferta* NHMUK AZ 4875 and NHMUK AZ 4874).

#### *4.2.2.1 Surface weathering and staining*

The coralla are discoloured having been stained a pinkish-orange/brown colour by iron-rich minerals leached from the sediments in which the corals are buried. In addition, mid-grey surface discolouration caused by sub-aerial exposure and weathering is clearly visible in two coral specimens, (*Siderastrea conferta* NHMUK AZ 4874 and *Montastraea limbata* NHMUK AZ 4976). In *Siderastrea conferta* (NHMUK AZ 4874) the weathered zone forms a band parallel to the direction of growth indicating the coral was transported from life-position prior to burial (Figures 4.3a and 4.4a). However in the case of *Montastraea limbata* (NHMUK AZ 4976), the weathering has affected the uppermost surface of the coral suggesting preservation in life-position (Figure 4.6a). Excellent preservation of corallite skeletal architecture is seen on surfaces that have not been exposed to sub-aerial weathering (e.g. *Siderastrea conferta* NHMUK AZ 4874; Figures 4.4a and b).

#### *4.2.2.2 Hydrocarbon charging*

The external surfaces of the corals reveal little evidence of hydrocarbon charging apart from localised black, oily patches visible at the base of *Sideratrea conferta* (NHMUK AZ 4874) and *Montastraea limbata* (NHMUK AZ 4878) (Figures 4.3a and 4.5c). However the sliced specimens show the coral pore spaces contain a significant amount of oil.

#### *4.2.2.3 Endolithic macroboring*

Evidence of macro-boring by the endolithic organism *Lithophaga* is observed in both *Montastraea limbata* (NHMUK AZ 4877) and *Porites* (NHMUK AZ 3140). The boreholes range in size from 3 mm to 12 mm and in some pits the sub-millimetre calcite lining (white arrow) produced by the bivalve are preserved *in situ* (Figure 4.7a) along with the bivalve itself (Figures 4.6b and 4.7b). Many of the boreholes are partially or totally in-filled by fine-grained sediments that have fallen into the pits (Figures 4.7a and 4.7b). Cross-cutting relationships are also visible on the surface of *Porites* (NHMUK AZ 3140) indicating multiple generations of infestation and boring activity (Figure 4.7a). The extensive distribution of boreholes over the surface of the *Porites* coral head suggests infestation and boring probably occurred after the death of the coral.

#### *4.2.2.4 Distribution of diagenetic alteration and hydrocarbon charging*

Longitudinal sections through the coral specimens reveal a patchy distribution of alteration and hydrocarbon ingress. However skeletal architecture and the connectedness or isolation of pore spaces and voids appears to exert some influence on the distribution of the cements and oil. For example abrupt changes between hydrocarbon and cement filled zones and ‘unaltered’ coral skeleton often coincide with the position of growth bands, thecal walls and dissepiments (Figures 4.2b; 4.3b and 4.6b)

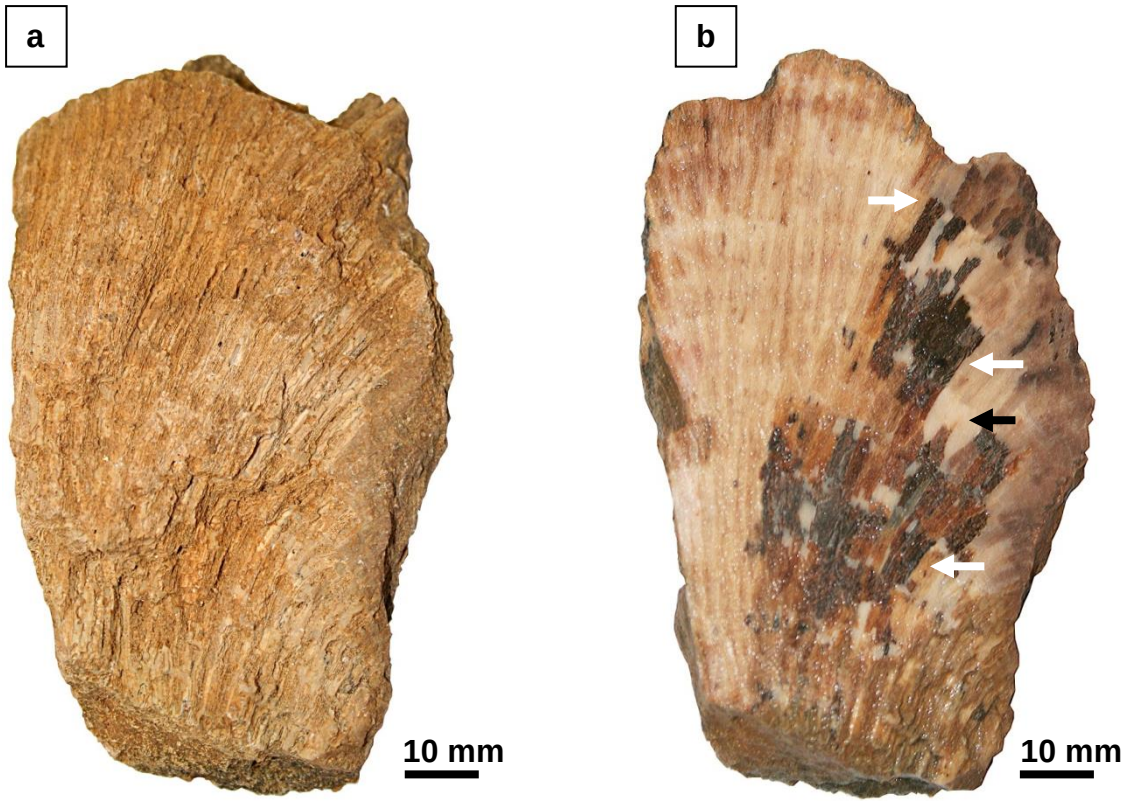


**Figure 4.2** Photographs showing the appearance of *Siderastrea conferta* (NHMUK AZ 4875). **a** Iron-stained corallum showing little external evidence of diagenetic alteration. **b** Extensive diagenetic alteration covering ~60% of the cut surface of the coral. Pale areas are filled with diagenetic cements (black arrow) and dark areas are charged with hydrocarbon. Growth bands and thecal walls are picked out by abrupt termination or change in diagenetic alteration (white arrow).

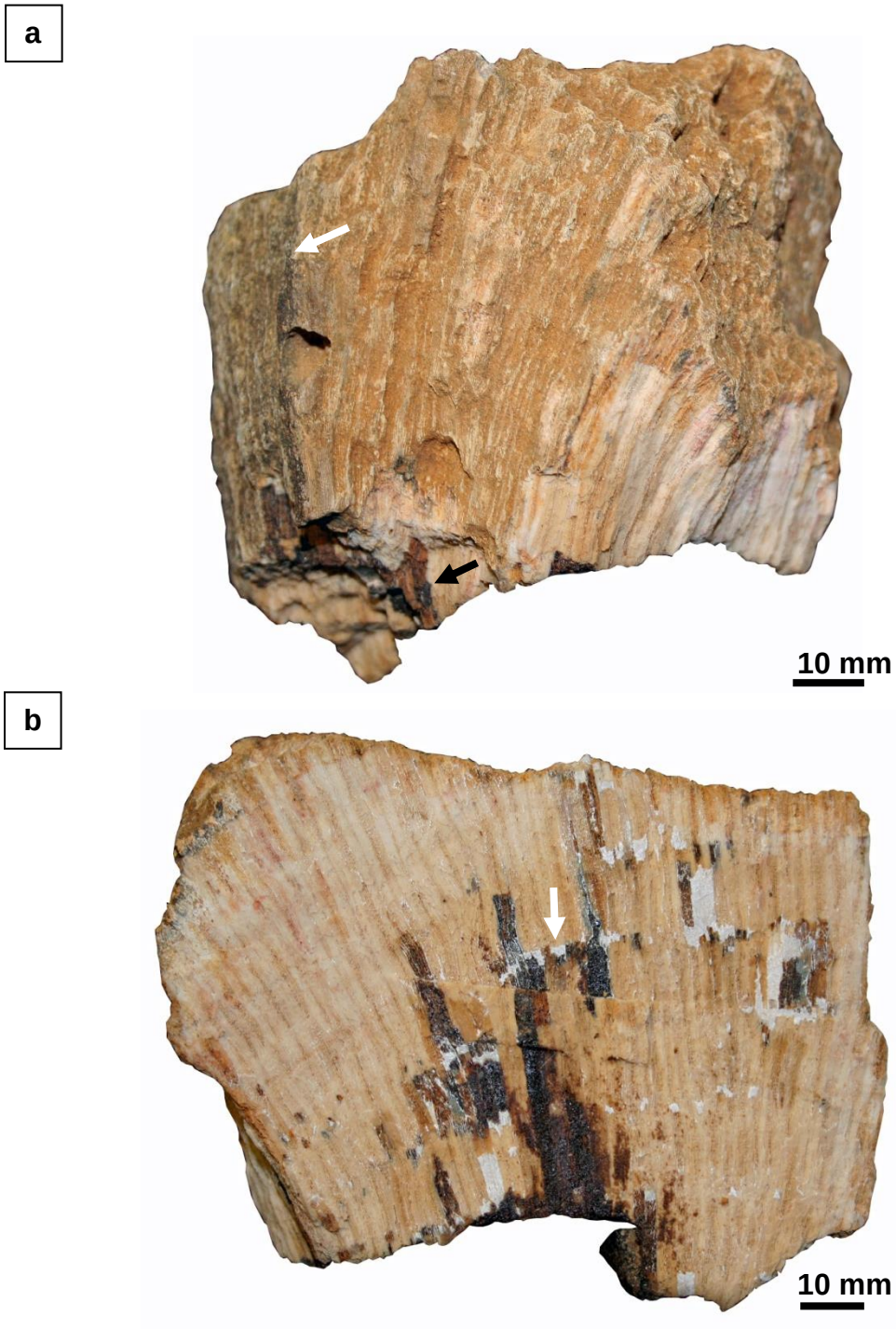


**Figure 4.3** Photographs illustrating the appearance of *Siderastrea conferta* (NHMUK AZ 4874). **a** Sub-aerial weathering has discoloured the left side indicating the coral was not buried in life position (white arrow). Black hydrocarbon staining is present at the base of the coral (black arrow). **b** Cement and hydrocarbon occupy ~15% of the cut coral surface. Growth bands are picked out by abrupt termination of zones of alteration (white arrow).

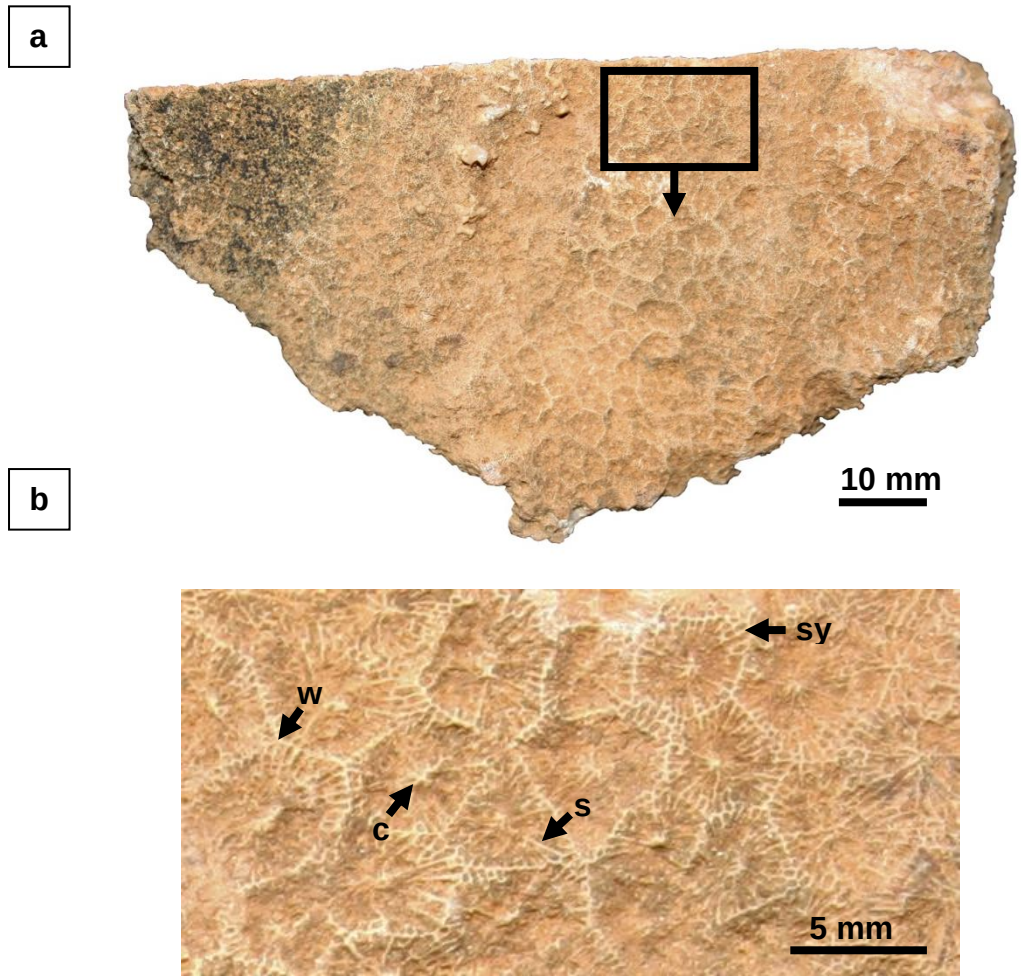


**Figure 4.4** Photographs showing corallite preservation in *Siderastrea conferta* (NHMUK AZ 4874). **a** Dark patch of surface weathering is visible on the left side of the coral. Irregular polygonal corallites are visible on the unweathered surface. **b** Magnified image showing the corallite walls (w), synapticulae (sy), septa (s) and columella (c) preserved on the surface of the coral.

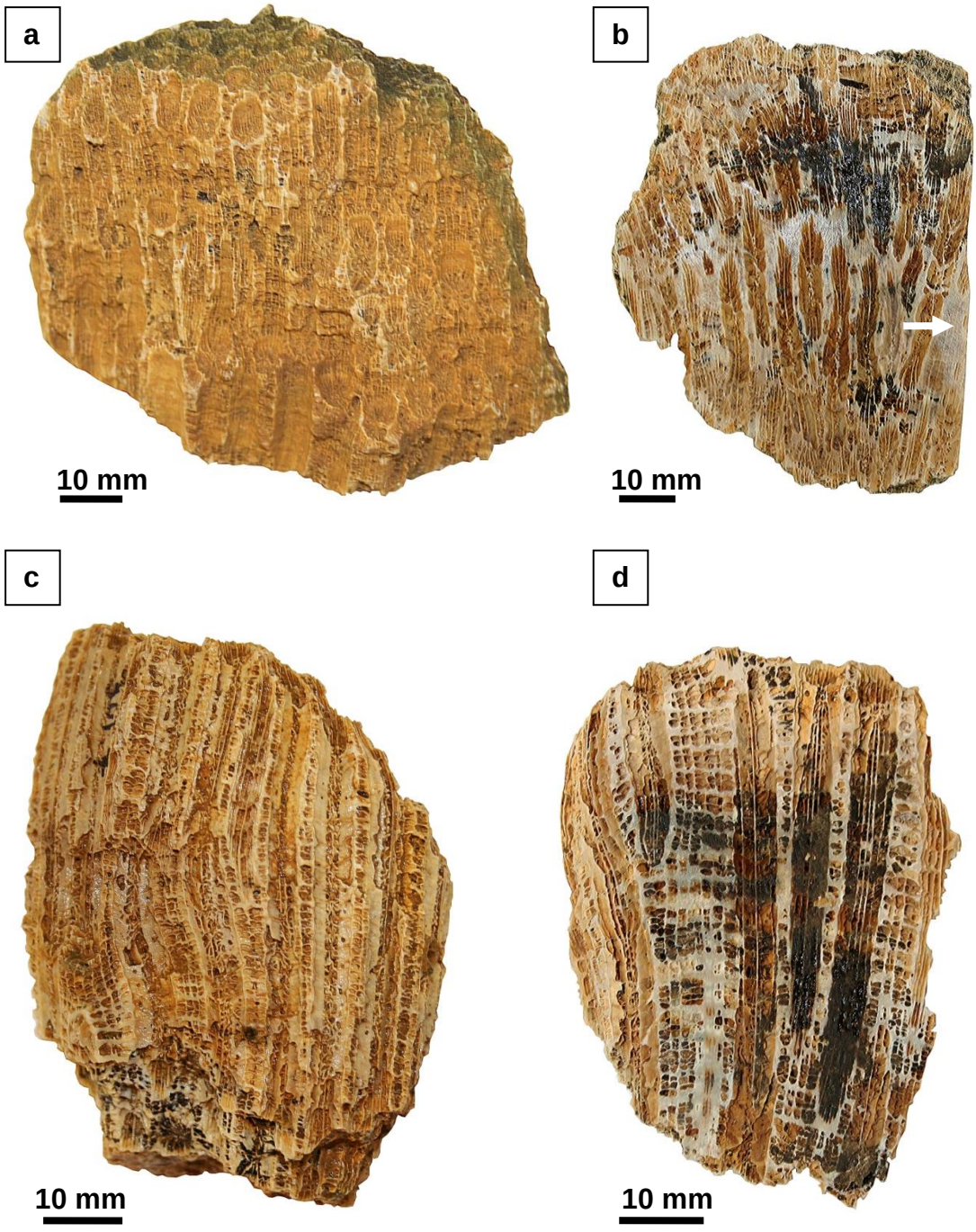


**Figure 4.5** Photographs illustrating coral preservation in *Montastraea limbata* (NHMUK AZ 4876) and (NHMUK AZ 4878). a NHMUK AZ 4976. Sub-aerial weathering on the upper surface of the coral suggests preservation in life position. b Tangential section showing black zones of hydrocarbon infill and pale areas of cementation (white arrow). c NHMUK AZ 4878. Oil and iron staining are visible on the coral surface while the cut surface reveals extensive oil infill and cementation occupying ~70% of the cut surface (d).

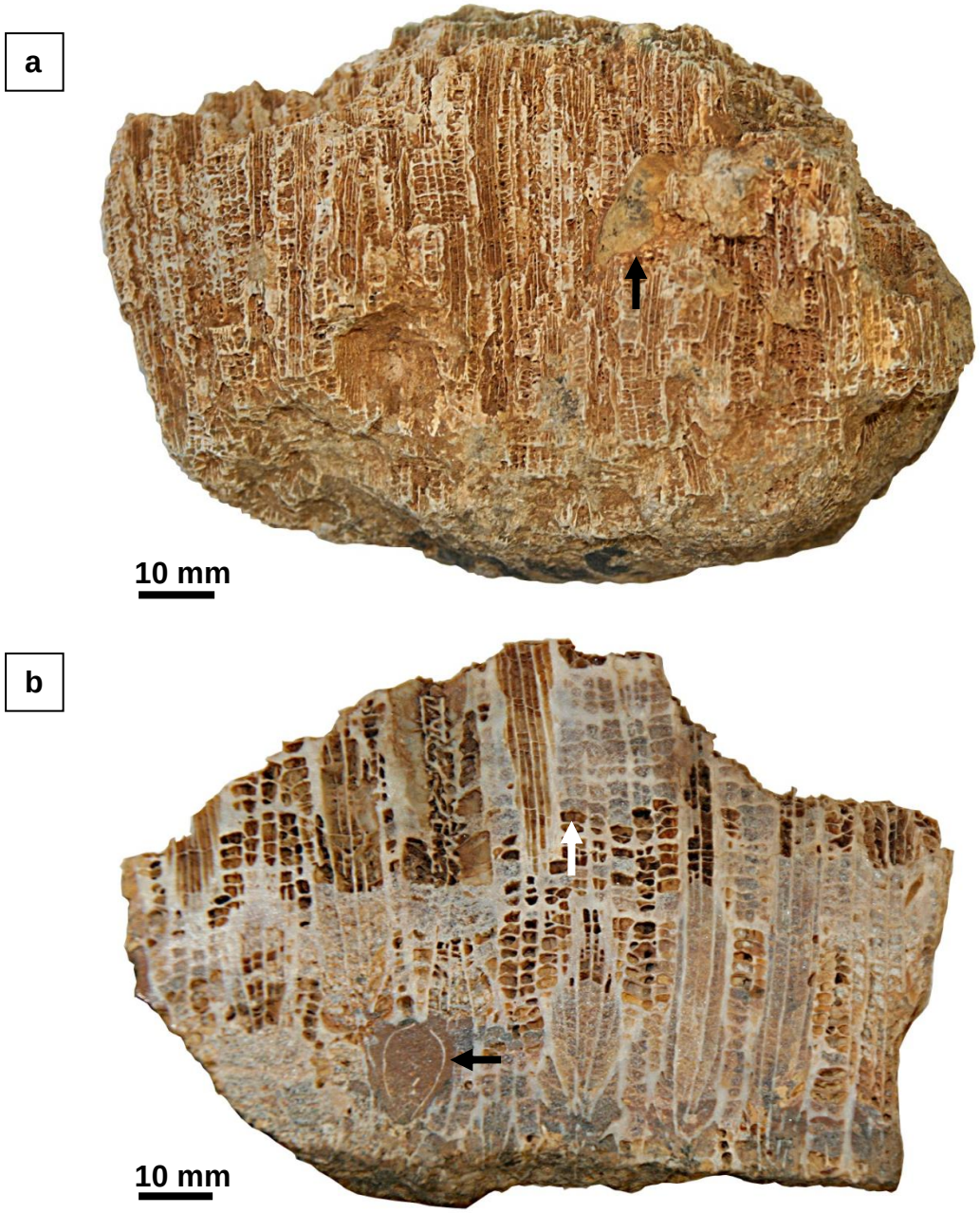


**Figure 4.6** Photographs illustrating coral preservation in *Montastraea limbata* (NHMUK AZ 4877). **a** Iron and oil stained coral with an unidentified macro-boring organism or shell fragment partially embedded in the coral skeleton (white arrow). **b** Cements and hydrocarbon fill ~85% of the sliced coral surface. Cement distribution is clearly influenced by skeletal structures such as dissepiments (white arrow). The endolithic macro-boring bivalve (*Lithophaga*) is visible in cross-section at the base of the coral (black arrow). Sediment and cement fill the valves and the borehole.

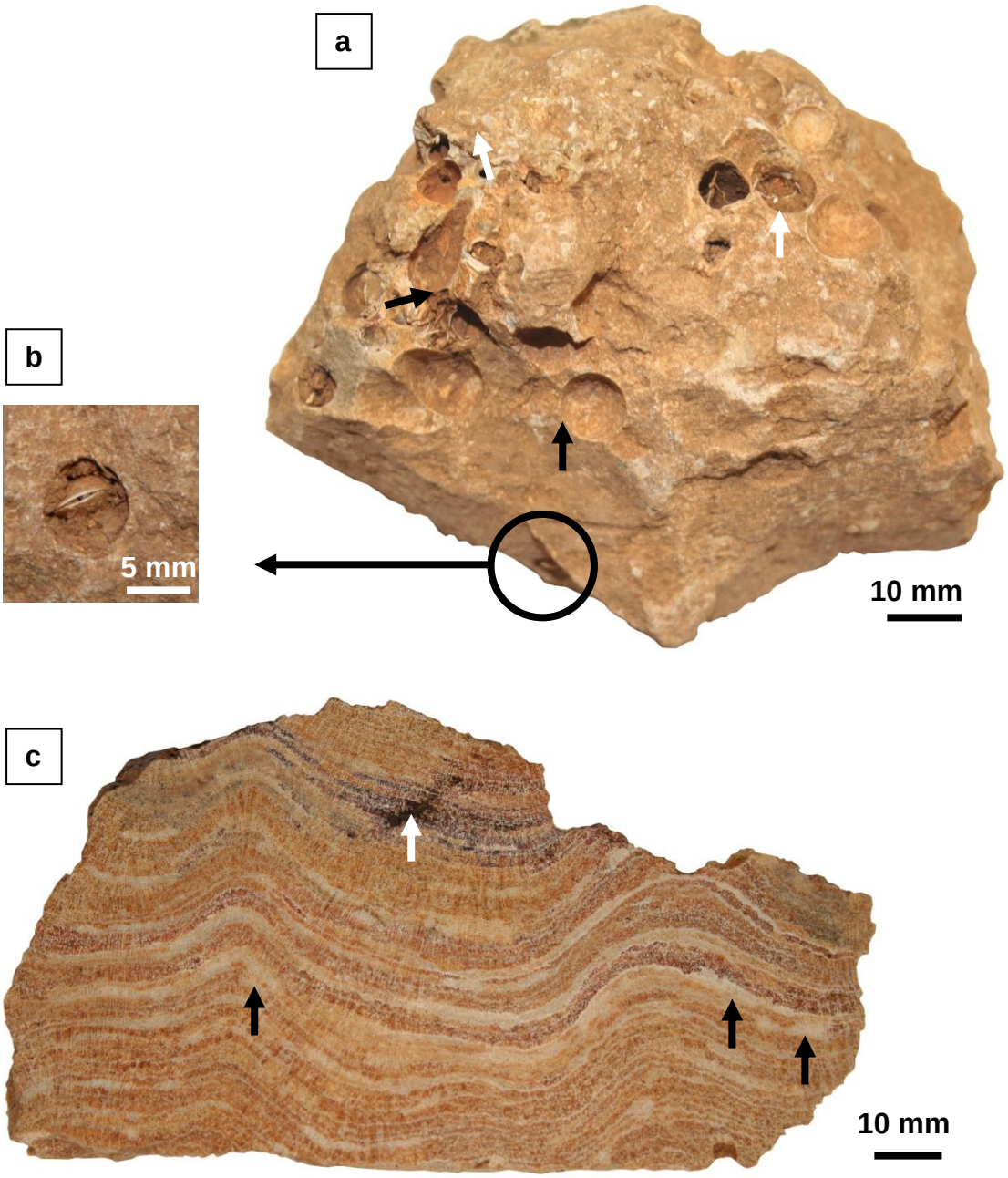


**Figure 4.7** Photographs illustrating coral preservation in *Porites* (NHMUK AZ 3140). **a** *Lithophaga* macro-boreholes pock the surface of the coral. Some boreholes are partially in-filled with sediment (white arrow) while others reveal cross-cutting relationships (black arrows) indicating multiple generations of infestation. **B** Image showing *Lithophaga* in life-position with the paired valves protruding from the borehole. **c** Longitudinal section through the coral showing pale bands of cementation (black arrows) and a dark region of skeletal dissolution and alteration (white arrow).

## 4.3 LIGHT MICROSCOPY

In this section observations made on blocks of fossil coral under reflected light and on petrographic thin sections under plane-polarised light and cross-polarised light are presented. Crystal morphology and texture were used to identify the mineralogy since aragonite and calcite have very similar optical properties when viewed in thin section under plane-polarised and cross-polarised light. Calcite and aragonite both appear as clear, colourless minerals with high relief under plane-polarised light and both possess high birefringence (0.172 and 0.156 respectively) under cross-polarised light (Kerr, 1977). Coral aragonite is distinguished by the fabric and appearance of the crystals and the presence of characteristic growth textures developed during skeletogenesis.

### 4.3.1 Observations on petrographic thin sections

Examination of the coral specimens at low magnifications reveals the geometry and gross structure of the corallites and permits an initial assessment of preservation to be made.

Figure 4.8a shows the gross morphology of the corallites and excellent preservation in a sample of *Siderastrea conferta* (NHMUK AZ 4875). The corallites form irregular polygons bounded by thin thecal walls with numerous linear septa. The septa are gracile and discontinuous and the columella is only weakly developed. Slender filamentous dissepiments are preserved and there is no evidence of gross cementation within this region of the coral. However, at higher magnification even well-preserved regions are shown to be affected by some diagenetic alteration. For example Figure 4.8b reveals the presence of localised deposits of calcite cement on skeletal surfaces in an otherwise well-preserved region of the coral.

Figure 4.11a illustrates heterogeneous diagenetic alteration and the gross morphology of the corallites in *Montastraea limbata* (NHMUK AZ 4876). The corallites are roughly circular and unequal in size ranging from 3.5 – 5.0 mm in diameter bounded by a thickened thecal wall. The costae extend out from the exterior of the thecal wall while the septa extend in towards the centre of the corallite. Both the septa and the costae alternate in size. The primary costae and septa are typically thicker than the secondaries. There is a rudimentary

columella. Gross diagenetic alteration has affected one corallite in this field of view. Calcite spar, micrite, sediment and hydrocarbons have been deposited within the pore spaces partially filling some and totally occluding others. At higher magnification, details of the skeletal structure and the presence of isolated patches of calcite cement become apparent (Figure 4.11b). The skeletal features include the dark linear mid-line grooves punctuated by shallow pits that represent the centres of calcification and the bundles of aragonite fibres (fasciculi) that from the arched scelerodermites visible along the margins of the septa. There are localised deposits of calcite consisting of scalenohedral crystals.

#### *4.3.1.1 Secondary aragonite cements*

Secondary aragonite cements are present in all the fossil coral specimens examined. The aragonite cements show a range of morphologies that include syntaxial isopachous fringes of acicular crystals, long blades and large blocky forms.

The acicular aragonite consists of long slender needles that typically form isopachous crusts of syntaxial crystals (Figures 4.9b; 4.12a). The crystals usually measure 10 µm but may attain lengths of ~ 60 µm (Figure 4.12a) and terminate in needle-like points. Acicular aragonite crystals may be distinguished from high-magnesium calcite forms by their morphology since aragonite crystals tend to be longer and thinner than those composed of high-Mg calcite (Scholle and Ulmer-Scholle, 2003).

Bladed aragonite cements consist of long (≤ 100 µm) crystals that typically terminate in flattened planar surfaces (Figures 4.10a; 4.13b). Aggregations of blades may form meshes of cement separated by voids that fill entire pore spaces (Figure 4.10a) or simply project into the pore space (Figure 4.13b).

Large blocky crystals of aragonite measuring up to 120 µm in length are present filling entire pore spaces (Figure 4.9a). The blocky crystals tend to be rather square or rectangular in outline.

#### *4.3.1.2 Calcite cements*

Calcite cements are present in all the fossil specimens examined. The cements occur in a range of forms that include microcrystalline deposits (micrite), equant to bladed crusts and pavements of anhedral spar.

Micrite typically forms dark envelopes around grains and skeletal elements (Figures 4.12d; 4.14a) although it may also be present as pore-filling cement (Figures 4.9c; 4.13a; 4.13e). Micrite is composed of high magnesium calcite with crystals less than 4 µm in diameter. Calcite also occurs as blocky and bladed crystals deposited on skeletal or cement substrates. The cement may be present as isolated patches (Figures 4.8b; 4.11b; 4.14b) or cover entire pore spaces (Figures 4.11a; 4.12b). The blocky crystals range in size up to ~ 50 µm and they may be equant (Figure 4.12b) or bladed (Figure 4. 14b). Calcite spar fills the pore spaces in the most poorly preserved regions of the corals. Drusy mosaics of anhedral calcite spar are well visualised in *Siderastrea conferta* (Figure 4.10b). The crystals form interlocking pavements with the largest crystals tending to occupy the centre of the pore spaces and the smaller crystals lining the perimeter. In *Montastraea limbata*, millimetre-sized single crystals of calcite spar fill entire pore spaces bounded by dissepiments and septa (Figure 4.12c) while adjacent pore spaces are occluded by large interlocking pavements of spar (Figures 4.12c; 4.12d; 4.13c). The large calcite crystals do not extend beyond the skeletal boundaries and form cross-cutting relationships. The lack of cross-cutting relationships is an important observation because it suggests that the calcite crystals may have been deposited in a meteoric vadose rather than a freshwater phreatic environment (Pingitore, 1976).

Meteoric vadose alteration results from chemical interactions between air and water present in skeletal pore spaces and soils surrounding the fossil corals (McGregor and Gagan, 2003). Vadose alteration is characterised by dissolution, precipitation of calcite cements, fabric selective replacement of skeletal aragonite and neomorphism (James, 1974; Longman, 1980; McGregor and Gagan, 2003). The morphology of the calcite crystals and heterogeneous cementation reflects the patchy distribution of water within the pore spaces, pore space connectivity and the length of time water was present within the

voids (James, 1974: Longman, 1980; McGregor and Gagan, 2003). Vadose calcite cement morphologies range from pendant and meniscal crusts consisting of fine equant crystals (Longman, 1980) to mosaics of irregular interlocking crystals (Pingitore, 1976) and large single crystals (McGregor and Gagan, 2003) that fill entire pore spaces. Fabric selective replacement in vadose environments is characterised by calcite deposition within skeletal boundaries (Pingitore, 1976; McGregor and Gagan, 2003).

Longman (1980) noted that diagenesis in the active freshwater phreatic zone may involve leaching, neomorphism and the deposition of pavements of interlocking equant calcite crystals that enlarge towards the centre of the pore spaces. In addition, Pingitore (1976) described distinctive cross-cutting relationships in which large calcite crystals had overgrown skeletal boundaries in Pleistocene corals from Barbados that had undergone freshwater phreatic diagenesis. Although dissolution, neomorphism and deposition of calcite cements were observed in the Miocene fossil corals, no cross-cutting relationships were identified.

#### *4.3.1.3 Calcite neomorphism*

Calcite has replaced aragonite cements in the poorly preserved regions of the corals (Figures 4.13c; 4.13d). For example Figure 4.13c shows a pore space lined with long acicular crystals and filled with calcite spar. The acicular crystals would probably have originally been composed of aragonite however this been replaced by calcite leaving a palimpsest of the first generation of cement. Further analyses such as trace element geochemistry or examination of mineral inclusions are necessary to confirm the identity of the original cement since the products of the aragonite to calcite transformation can have high Sr contents and preserve relict aragonite inclusions (Scholle and Ulmer-Scholle, 2003).

Neomorphism has also affected skeletal aragonite in the worst preserved regions of the coral specimens (Figures 4.10b; 4.13d). For example, Figure 4.10b shows clear blocky crystals of calcite spar ranged along the internal margins of the septal walls replacing the original aragonite fibre bundles of the sclerodermites.

#### *4.3.1.4 Hydrocarbons*

The corals have been charged with hydrocarbon during a period of burial and these appear as brown staining within the pore spaces or coating skeletal surfaces or cement crystals (Figures 4.9a; 4.9b). Hydrocarbon charging clearly postdates earlier episodes of marine diagenesis since many of the pore spaces that are filled with oil also preserve aragonite and calcite cements deposited on the skeletal surfaces (Figures 4.12b; 4.13b; b.13d; 4.14c).

#### *4.3.1.5 Cement and hydrocarbon distribution*

The cements and hydrocarbons are heterogeneously distributed throughout the corals and it is clear that skeletal architecture plays an important role permitting oil or supersaturated pore fluids to circulate through interconnected pore spaces and voids while preventing its ingress into others due to the presence of skeletal elements such as dissepiments (Figures 4.9a; 4.13a). Cement distribution may also have been influenced by the presence of hydrocarbons in the pore spaces blocking the flow of aqueous fluids including those responsible for diagenetic alteration (Scholle and Ulmer-Scholle, 2003).

#### *4.3.1.6 Detrital grains*

Detrital quartz grains are present in some pore spaces (Figures 4.11a; 4.13e). The subangular to subrounded grains are very bright under plane-polarised light and exhibit undulose extinction when rotated under crossed-nicols.

### 4.3.2 Binocular microscopy

Images of whole coral samples acquired under the binocular microscope are shown in Figures 4.15a – 4.15f. Examination of the fossil corals under the binocular microscope provides a good overview of skeletal preservation. Areas of diagenetic alteration may be quite extensive in poorly preserved regions of the corals (Figure 4.15d) but in other regions cementation may be much more localised (Figure 4.15c) or absent (Figure 4.15a). Acicular and blocky cements are clearly identifiable lining pore-spaces and forming sparkling crusts on skeletal surfaces (Figures 4.15c; 4.15d). Rhombic crystals are also visible on

some surfaces and these may represent dolomites (Figure 4.15e). Meshes of large blocky crystals (Figure 5.15f), pavements of interlocking calcite spar (Figure 4.15b) or cemented detrital grains (Figure 4.15e) may totally occlude pore spaces reducing the porosity of the corals. Hydrocarbon charging and iron oxides leached from the surrounding surface sediments have stained many of the coral surfaces and cements brown/red-brown (Figure 4.15).

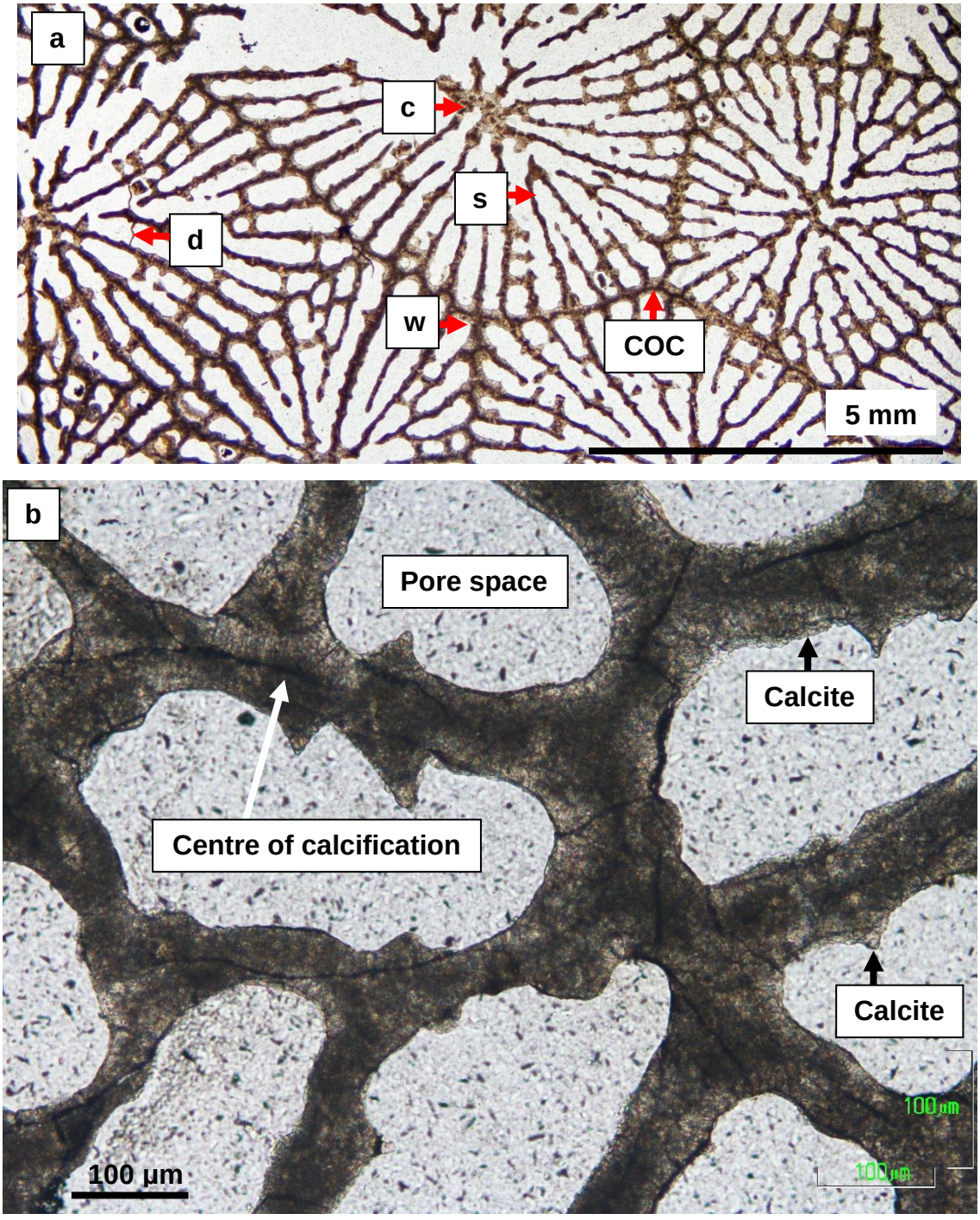


**Figure 4.8** Transmitted light images of thin sections showing skeletal structure in *Siderastrea conferta.* **a** Irregular polygonal corallites (NHMUK AZ 4875). Corallite wall (w), septa (s), columella (c), centres of calcification (COC), and slender dissepiment (d) **b** Skeletal structures and diagenetic cement (calcite) seen at higher magnification (NHMUK AZ 4874).

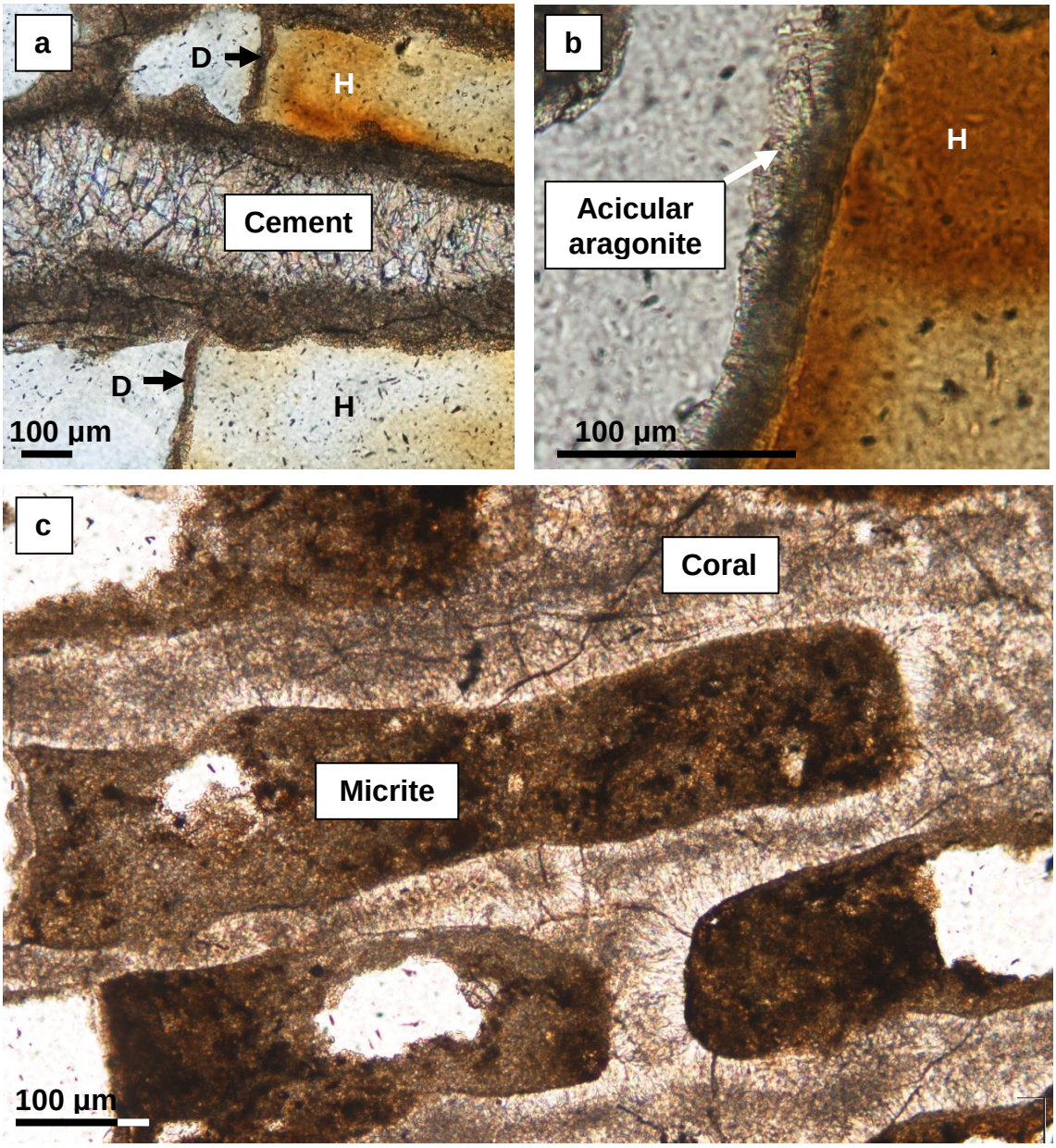


**Figure 4.9** Transmitted light images showing the heterogeneous localised distribution of cement, hydrocarbon and micrite in *Siderastrea conferta* (NHMUK AZ 4874). **a** Blocky cement and hydrocarbons (H) fill adjacent pore spaces. Thin coral dissepiments (D) have prevented the migration of the hydrocarbon into neighbouring pore spaces. **b** A higher magnification image showing a slender dissepiment separating a pore space cemented with acicular aragonite from an adjacent hydrocarbon-filled pore. **c** Dark micritic material partially occluding several adjacent pore spaces.

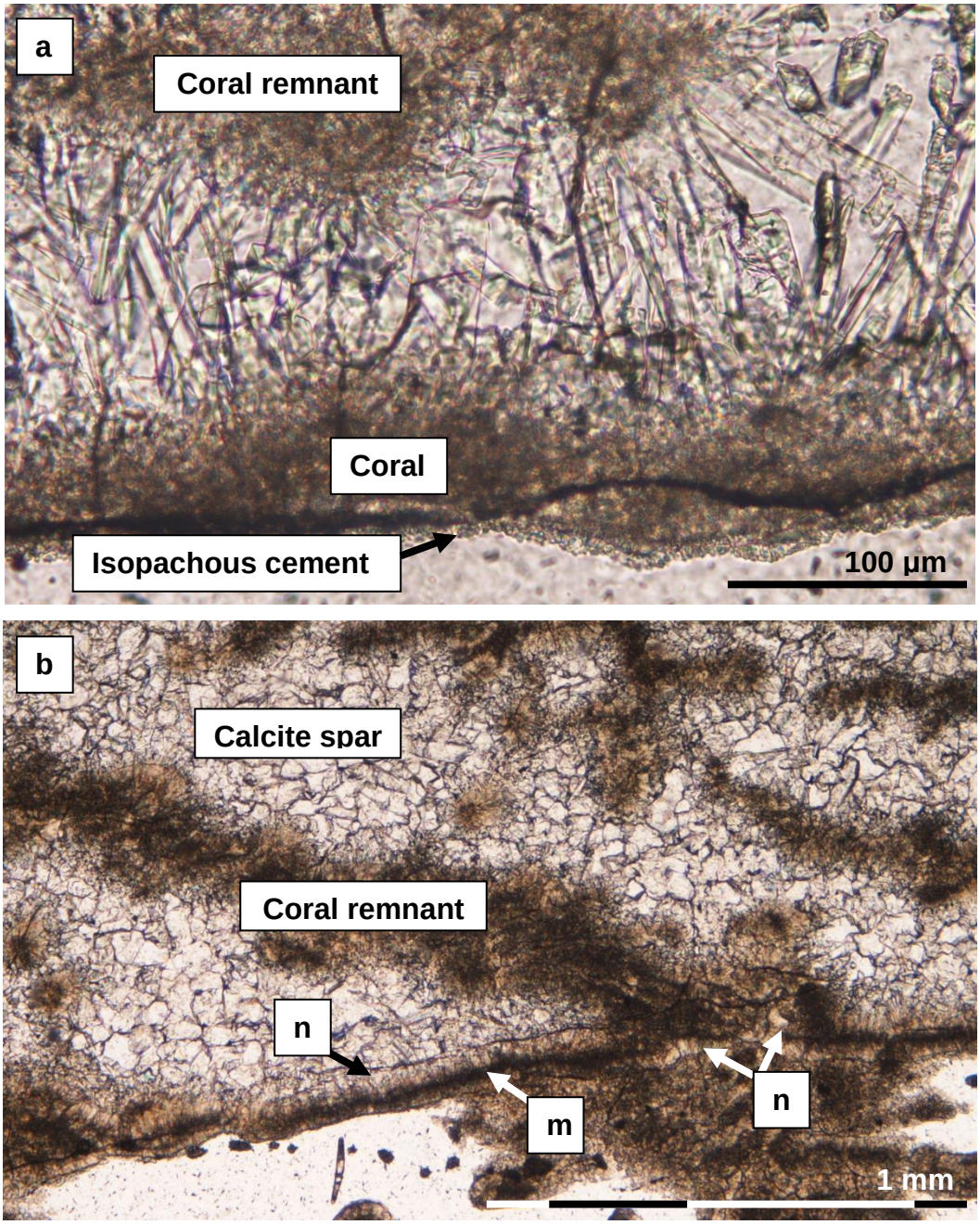


**Figure 4.10** Images showing aragonite and calcite cements in *Siderastrea conferta* (NHMUK AZ 4874). **a** Long (~70 µm) syntaxial aragonite crystals fill a void between skeletal remnants. A fringe of isopachous cement is seen at the bottom of the image. **b** Drusy calcite spar fills the voids between remnants of the coral skeleton disrupted dissolution. At the base of the image, original coral skeletal aragonite has been replaced by neomorphic calcite (n). Dark micrite (m) has filled the dissolution-widened centres of calcification.

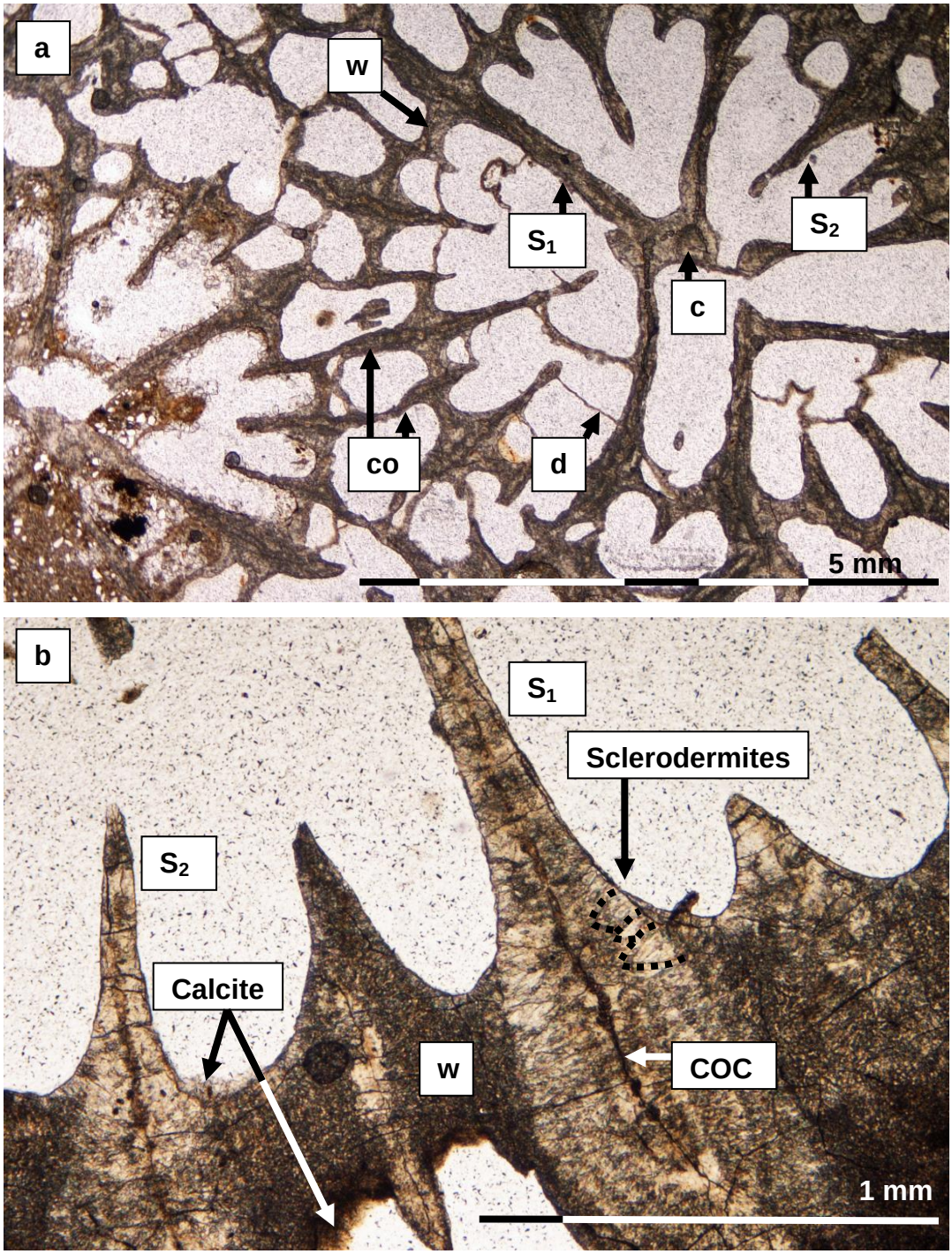


**Figure 4.11** Transmitted light images of thin sections showing the skeletal morphology of *Montastraea limbata.* **a** NHMUK AZ 4876 corallite wall (w), primary septa ($s_1$), secondary septa ($s_2$), columella (c), costae (co), and slender dissepiment (d). **b** NHMUK AZ 4877 higher magnification image showing dark centre of calcification (COC). Dashed lines delineate the arched sclerodermites comprised of bundles of aragonite fibres (fasciculi). Calcite cement is present.

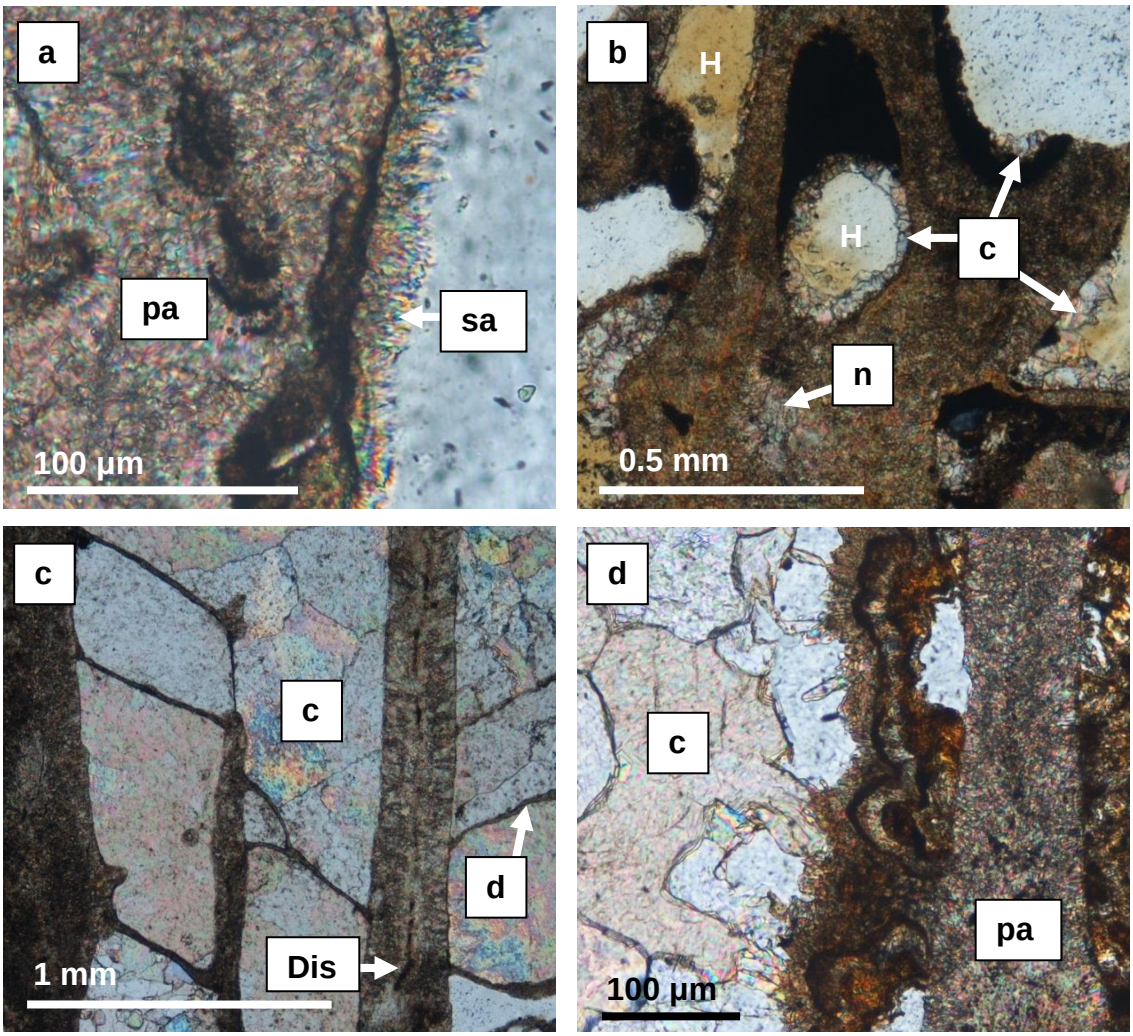


**Figure 4.12** Images showing diagenetic cements in *Montastraea limbata* (NHMUK AZ 4877) in thin section under transmitted/polarised light. **a** Primary (pa) and secondary aragonite (sa). The secondary aragonite consists of acicular crystals up to 30 µm in length. **b** Scalenohedral and blocky equant calcite crystals line voids that have subsequently been filled with hydrocarbon (H). Calcite is also present in a neomorphosed region of the coral skeleton (n). **c** Voids filled with calcite spar (c). Single large calcite spar crystals occupy the spaces delineated between the septa and dissepiments on the left side of the image. Note that the large calcite crystals do not cross-cut the skeletal elements. Selective dissolution (Dis) has widened the centres of calcification (dark line). **d** Arched layers of cement intercalated with dark micrites and hydrocarbons. Mosaics of calcite crystals (c) have subsequently filled the remaining pore space.

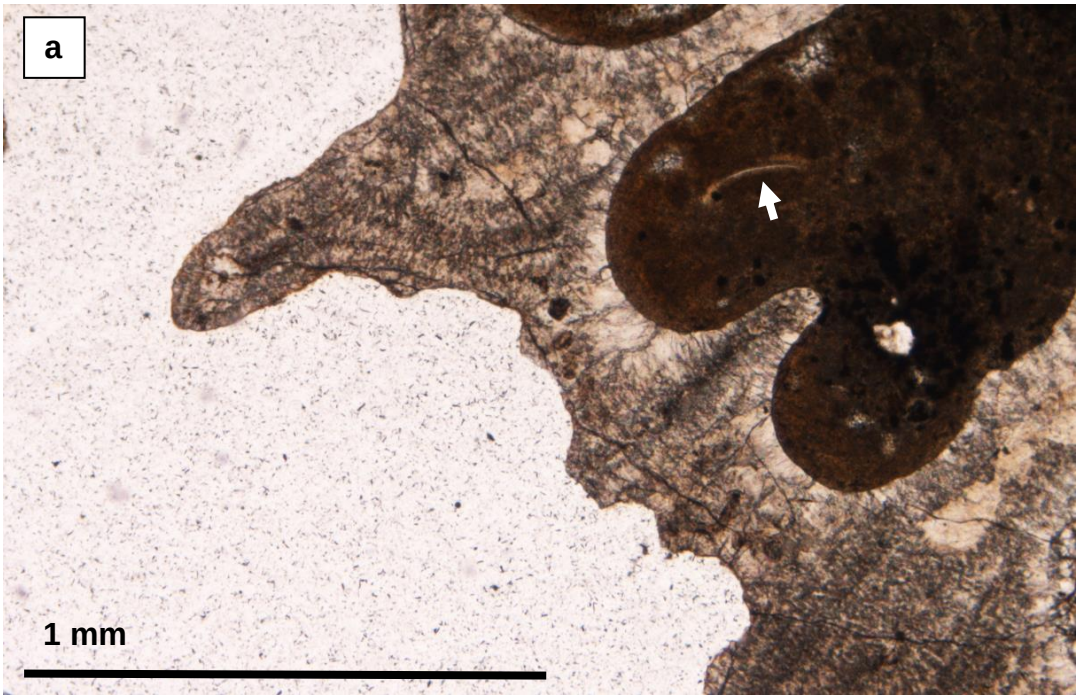
a
1 mm

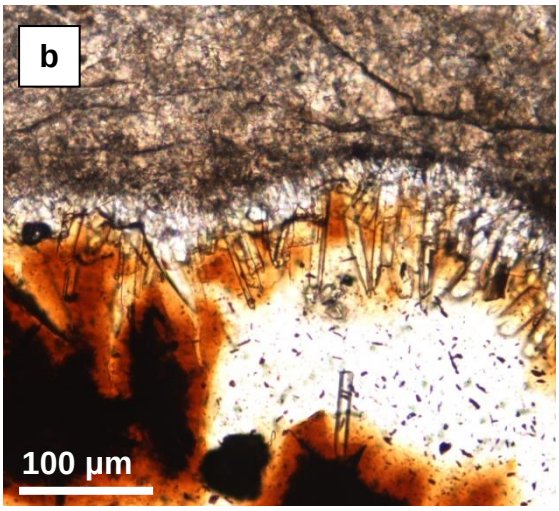
b
100 µm

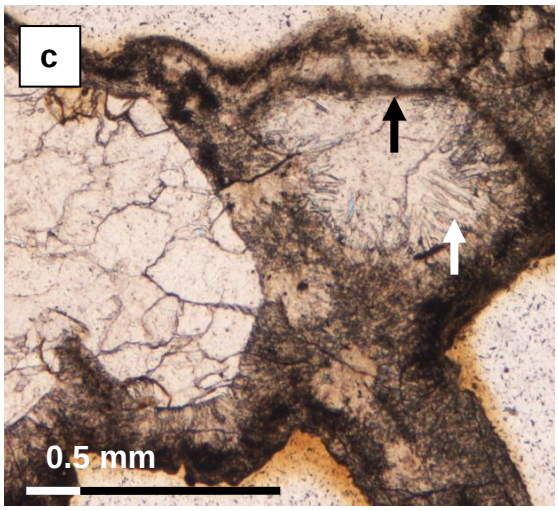
c
0.5 mm

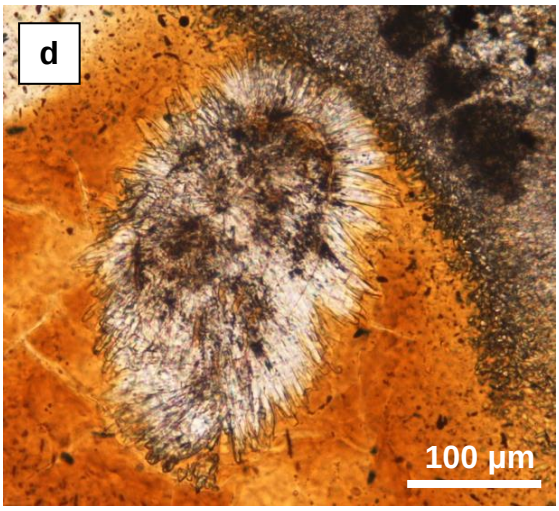
d
100 µm

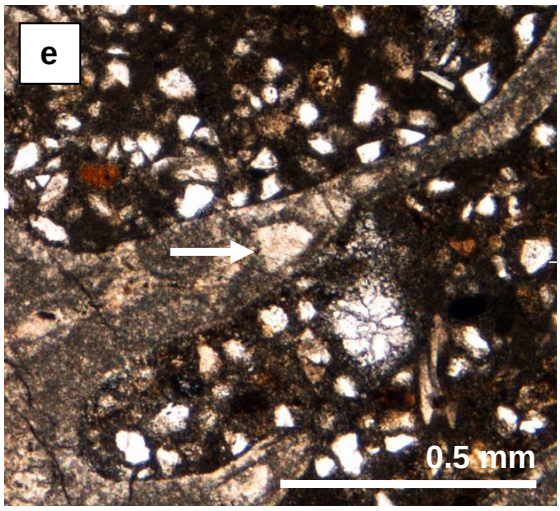
e
0.5 mm

**Figure 4.13** (Previous page) plane polarised light images showing the micrites and diagenetic cements in *Montastraea limbata* (NHMUK AZ 4876). **a** A thecal wall bounds the interior of a corallite filled with dark sediment and micrite. An isolated shell fragment is suspended in the dark material (arrow). The void outside the corallite wall remains free of cements and sediment. **b** Long (≥ 100 µm) acicular needles of aragonite extend beyond an irregular fringe of shorter crystals that have been deposited in a pore space which has subsequently been charged with hydrocarbons. **c** A drusy mosaic of calcite spar fills two pore spaces in this image. Traces of long acicular aragonite needles that have been altered to calcite can be seen in the smaller of the voids (white arrow). A dark rather diffuse layer of micrite has been deposited on some of the coral surfaces (black arrow) while pale zones of alteration are seen within some skeletal elements. **d** A coat of long acicular needles covers a skeletal remnant that has undergone dissolution and neophorphism. The acicular crystals are thickened and have been transformed to calcite and hydrocarbons have subsequently filled the remaining pore space. **e** Diagenetically altered septa (arrow) enclose pore spaces filled with clear subangular to subrounded detrital grains suspended in a matrix of dark micrite. Voids within the matrix have been filled with a mosaic of calcite spar.

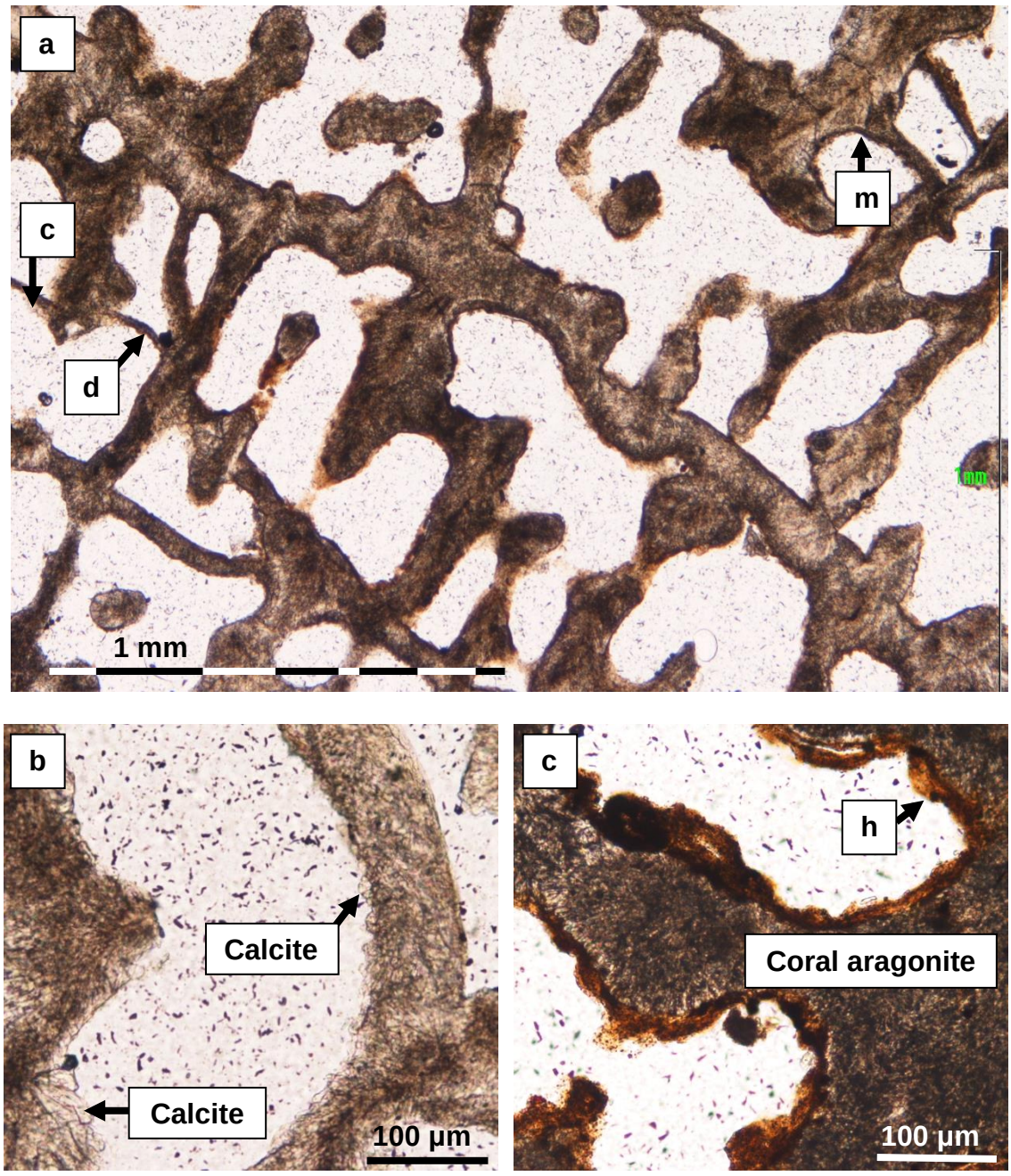


**Figure 4.14** Plane polarised light images showing oil and cements in *Porites* (NHMUK AZ 3140). **a** Calcite (c) and dark micrite (m) cements cover skeletal surfaces. Slender dissepiments (d) are preserved. **b** Blocky calcite crystals deposited on skeletal surfaces. **c** Hydrocarbon deposits (h) coat the coral skeleton.

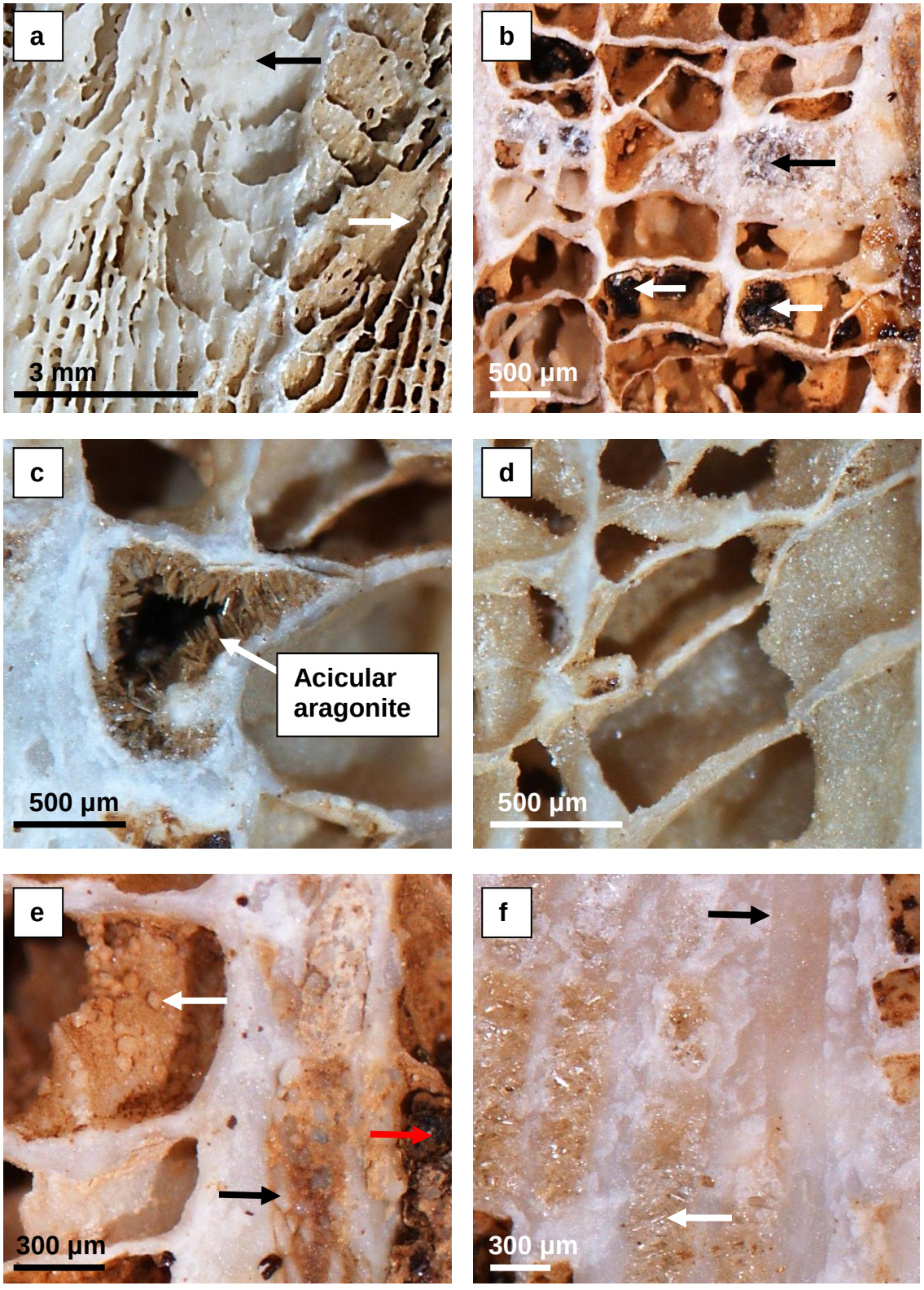
a
3 mm
b
500 µm
c
Acicular aragonite
500 µm
d
500 µm
e
300 µm
f
300 µm

**Figure 4.15** (Previous page) binocular microscope images illustrating diagenetic alteration and cementation. **a** A well-preserved corallite (black arrow) is separated from an adjacent hydrocarbon-stained corallite (white arrow) by a slender thecal wall (*Siderastrea* NHMUK AZ 4875). **b** Bituminous hydrocarbon deposits (white arrow) and diagenetic cements (black arrow) occlude pore spaces and voids (*Montastraea* NHMUK AZ 4876). **c** Acicular aragonite cement coated in a film of oil line a pore space (*Montastraea* NHMUK AZ 4876). **d** Glistening diagenetic cements cover skeletal surfaces in *Montastraea* (NHMUK AZ 4876). **e** Pore spaces filled with skeletal fragments, sediments and cement (black arrow), bitumen (red arrow) and rhombic crystals (white arrow) that may represent dolomite (NHMUK AZ 4876). **f** Large diagenetic cement crystals (white arrow) fill pore spaces adjacent to a laser track (black arrow) (NHMUK AZ 4876).

## 4.4 SCANNING ELECTRON MICROSCOPY

### 4.4.1 Modern corals

Examination of the modern coral specimens *Siderastrea radians* (NHMUK AZ 4879) and *Siderastrea siderea* (SID-D-1-l) in the SEM revealed the presence of early marine diagenetic cements and evidence for bio-erosion by both macro- and micro-boring organisms. The cements are composed of aragonite, high-magnesium calcite and brucite and exhibit a range of morphologies. The distribution of the cements and bio-erosion within each of the corals is very heterogeneous with regions of excellent preservation (Figures 4.16a, 4.19a) juxtaposed with regions that are less well-preserved (Figure 4.16d). A detailed discussion of early marine diagenesis in *Siderastrea radians* is given in Griffiths et al. (2013), Appendix 4.

#### *4.4.1.1 Secondary aragonite cements*

Secondary aragonite is the most common and widely distributed cement in the modern coral samples examined in this thesis. The aragonite cements exhibit a range of different morphologies including needles, clumps, and rods.

Acicular (needle) aragonite is the most common morphology encountered and typically consists of elongate, slender crystals up to 30 µm in length and 1 µm in diameter (Figure 4.16b). Acicular aragonite crystals terminate in sharp, needle-like points although larger crystals often terminate in rather more blunt apices. Needle aragonite typically forms syntaxial isopachous fringes covering the surface of the coral skeleton (Figure 4.16c). Syntaxial overgrowths develop in the same crystallographic orientation and in optical continuity with the underlying primary skeletal aragonite fibre bundles. Aggregations of needles are also observed forming clumps 5 – 10 µm in diameter with an overall syntaxial fabric. A rather more unusual clumped morphology is observed in *Siderastrea siderea* (SID-D-1-l). Here the aragonite needles are fused across a narrow base (<10 µm) and then fan outwards to form a spray 40 µm in length (Figure 4.19e).

Rods of aragonite cement are less common than acicular aragonite but where they are present they are usually found in association with needle aragonite and regions of bio-erosion. The rods, measuring 5 - 10 µm in diameter, are composed of small aggregations of fused angular or irregular polygonal crystals that terminate in smooth planar surfaces (Figure 4.19b). Clusters of long slender aragonite rods up to 40 µm in length are also observed forming dense meshes with voids between the crystals. The long rods also terminate in smooth flat surfaces except where fracturing has produced stepped morphologies (Figure 4.18d).

The distribution of secondary aragonite is patchy although in some cavities it may cover relatively large areas of the skeletal surface. The zones of cementation may be well demarcated and terminate abruptly or they may appear to gradually merge into regions of normal skeletal aragonite as the size of the cement crystals decreases towards the periphery of the altered areas (Figure 4.20). Skeletal architecture also plays an important role in the distribution of aragonite cements. Needle aragonite is commonly observed covering surfaces close to dissepiments particularly in the region where the dissepiments join the septal walls (Figure 4.16d). Needle aragonite cements also occur in association with brucite cements and immediately adjacent to regions affected by bio-erosion such as sponge galleries and micro-borings

(described below) where the activities of biological agents and organic films mediate and facilitate the deposition of the cements.

Aragonite cements are a common product of early marine diagenesis in phreatic and vadose marine environments (Tucker and Wright, 1990; Scholle and Ulmer-Scholle, 2003; Nothdurft and Webb, 2009).

#### *4.4.1.2 High-magnesium calcite cements (HMC)*

High-magnesium calcite cements are present in both modern coral samples but are rather less common than secondary aragonite. HMC cements are heterogeneously distributed and are often present in regions heavily infested with endolithic micro-boring organisms. HMC typically occurs as splays of elongate flattened crystals that flare and then taper to triangular points (Figures 4.16e, 4.17a, 4.17b, 4.19d). The splays may attain lengths of up to 50 µm and widths of 10 – 15 µm and typically occur in small clusters although pairs and single splays are also represented. 'Butterfly' structures composed of pairs of horizontally opposed splays were also observed in both the modern specimens. Unlike the 'butterfly' structures described by Nothdurft and Webb (2009), no evidence of a central nucleation point was observed in the specimens examined here (Figure 4.17b). The apparent lack of a central nucleation point may be due to overprinting or the size of nucleation points are too small to be discerned.

A single boulder-like mass of HMC composed of an aggregation of closely-packed flared and tapered HMC crystals was observed in *Siderastrea radians* (NHMUK AZ 4879). The mass measures ~60 µm x 30 µm x 40 µm and is found in a region heavily etched and pitted by micro-boring endobionts. The presence of a borehole in the cement mass itself suggests that boring activity continued after the deposition of the cement (Figure 4.17c).

#### *4.4.1.3 Brucite cement*

Brucite [$Mg(OH)_2$] cements display a range of different morphologies occurring as rosettes, plates and splays. They are closely associated with micro-boring and fine acicular aragonite cements although they are less common than secondary aragonite. The rosettes form dome-shaped mounds up to 40 µm in diameter. In cross-section the mounds are seen to consist of

concentric layers, 1 - 2 µm thick, composed of palisades of slender crystals. Close examination of individual palisade crystals reveals subtle density banding that probably reflect cycles of crystal growth. The concentric layers forming the rosettes are separated by sub-micron scale voids that may represent organic biofilms that have since disappeared (Figure 4.18a). Plates comprise single brucite crystals <1 µm thick and 5 – 10 µm in diameter with curved perimeters. Plates may occur singly or several may fuse and form woven waffle-like aggregations (Figure 4.18b). Distinctive flat, X-shaped encrusting splays up to ~30 µm in length are also present although they represent the least common morphology (Figure 4.18c).

Brucite is not normally precipitated because it is under-saturated in seawater. However brucite cements have been described in live-collected corals from the Great Barrier Reef and the Florida Keys where they appear to be associated with organic biofilms and endolithic micro-organisms such as filamentous green algae, cyanobacteria and fungi (Nothdurft et al., 2005; Nothdurft and Webb, 2009; Buster and Holmes, 2006). Nothdurft et al. (2005) have proposed a sequence of bio-facilitated chemical reactions whereby microenvironments with radically altered pore water chemistry may be generated in spaces incorporating organic material/biofilms and mediated by endolithic microbial activity, resulting in the precipitation of brucite in loci where $Mg^{2+}$ activity and pH levels are high and $\rho CO_2$ levels are low.

#### *4.4.1.4 Bioerosion*

Both modern corals reveal evidence of extensive bioerosion by micro-boring organisms (Figure 4.18d). The activities of endolithic algae, cyanobacteria and fungi have pitted and etched wandering tracks on the skeletal surfaces of the corals. The micro-boreholes typically measure less than 10 µm in diameter and in some cases micro-boring activity clearly postdates the deposition of secondary acicular and rod aragonite because the cements are pitted with micro-boreholes (Figures 4.17c, 4.18d).

Distinctive sponge borings termed ‘galleries’ are also observed in both the modern corals. The galleries consist of concave scalloped depressions up to 35 µm across etched into the surface of the coral skeleton. Aggregations of

javelin-like sponge spicules and clumps of organic material are preserved in one of the galleries indicating the presence of living sponges within the coral when the specimen was collected. Syntaxial acicular aragonite cements are commonly associated with the sponge galleries and there is evidence of extensive micro-boring activity with boreholes pitting and cutting across the scalloped depressions of the sponge galleries (Figure 4.18f). Older sponge galleries are covered with syntaxial aragonite overgrowths (Figure 4.19c).

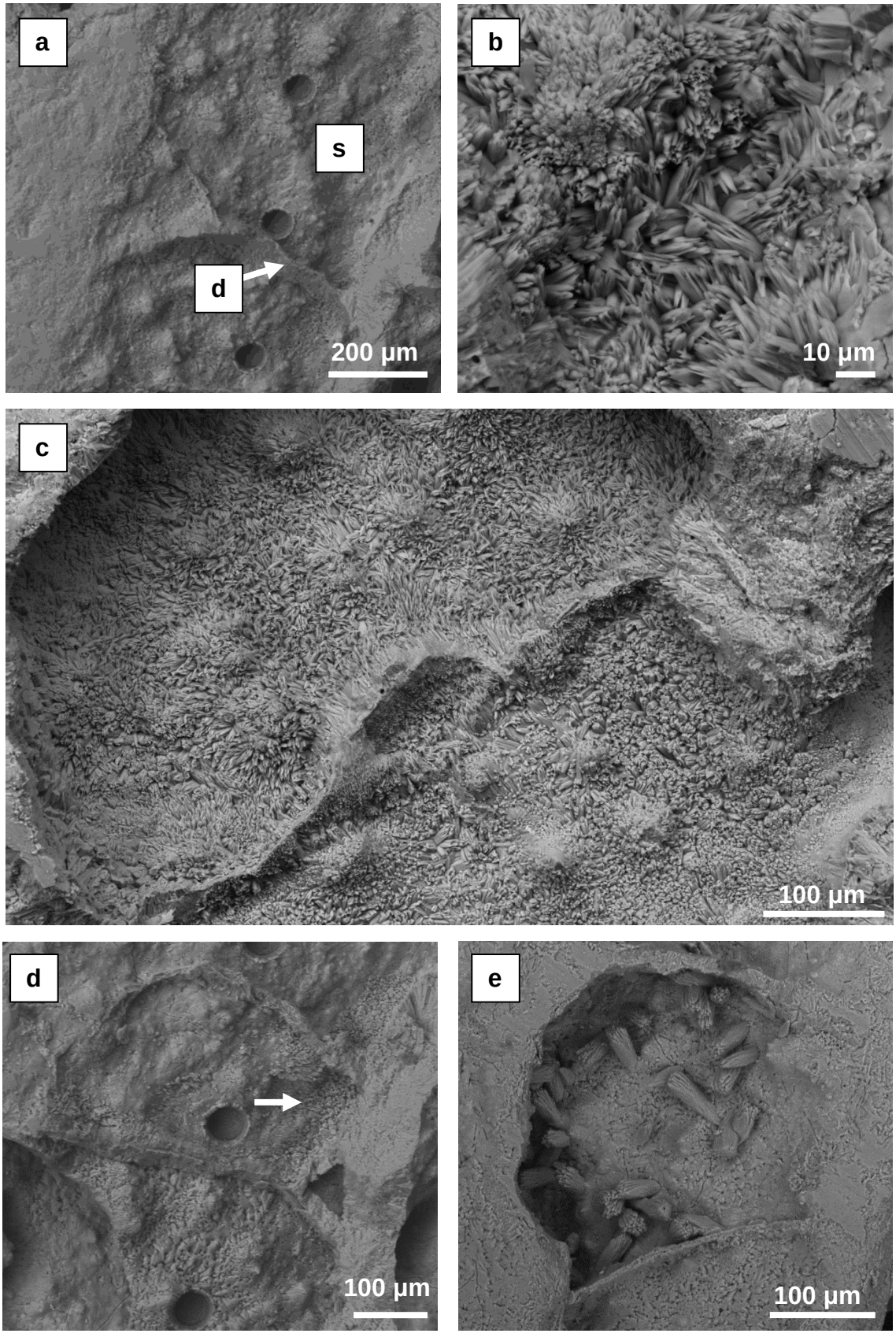
a
s
d
200 µm
b
10 µm
c
100 µm
d
100 µm
e
100 µm

**Figure 4.16** (Previous page) images showing preservation in modern *Siderastrea radians* (NHMUK AZ 4879). **a** Well-preserved coral skeleton showing an ornamented septal wall (s) divided by a thin horizontal dissepiment (d). Three circular laser ablation pits (57 µm diameter) that form part of a depth-profile trace element sample track are visible in this view. **b** Tufts of syntaxial acicular aragonite cement covers the surface of the coral skeleton. The crystals range in length from 10 – 20 µm**).** **c** Image showing part of an extensive zone of syntaxial acicular aragonite cement deposited on a septal surface. **d** Aragonite cement deposited in the angles formed between the dissepiments and the thecal wall (arrow). **e** High magnesium calcite splays deposited in a void bounded above and below by thin dissepiments.

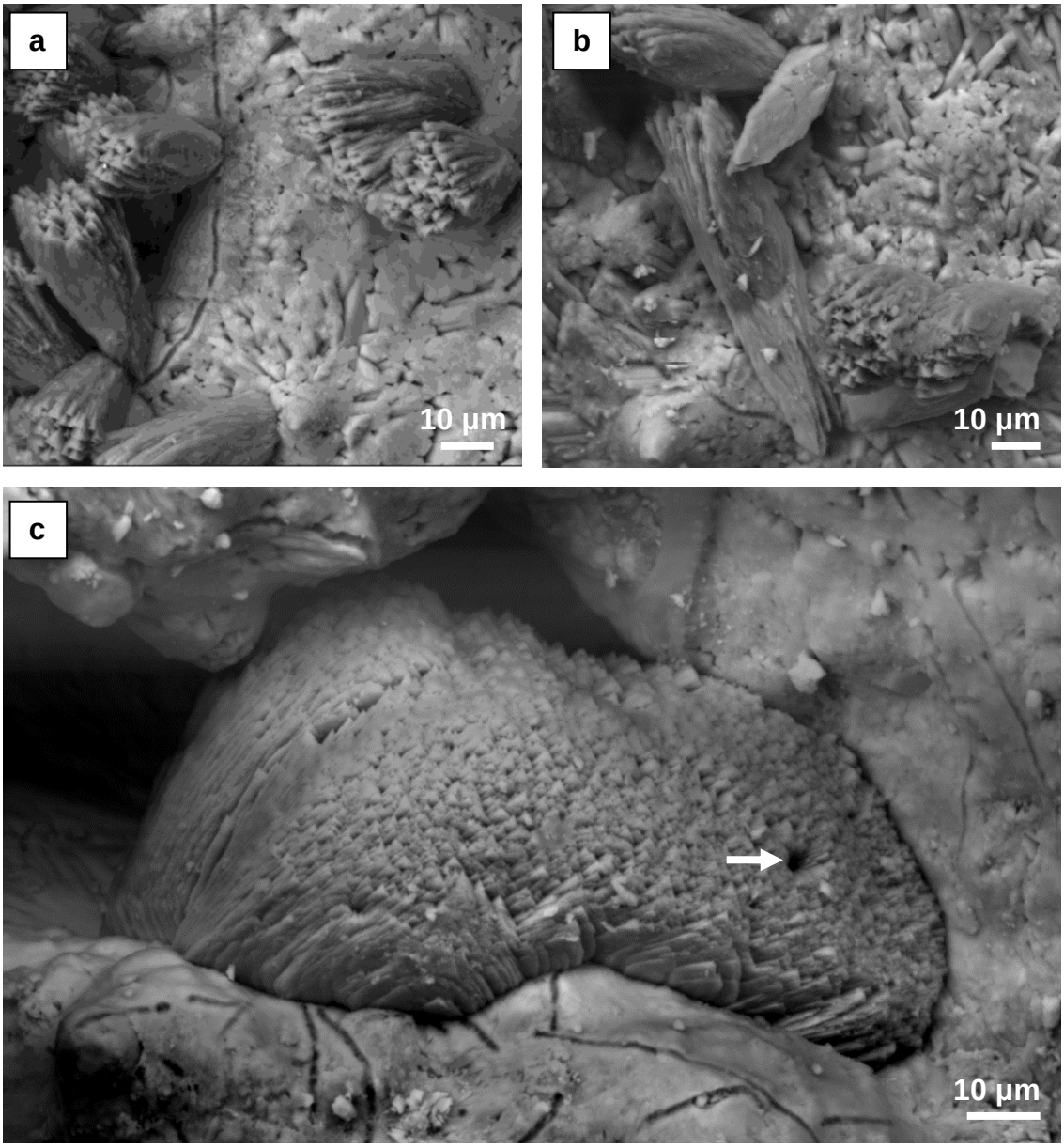


**Figure 4.17** High magnesium calcite (HMC) cements in modern *Siderastrea radians* (NHMUK AZ 4879). **a** Clusters of HMC splays associated with micro-boring activity. The splays consist of aggregations of elongate flared crystals that terminate in distinctive triangular points. **b** Horizontally opposed HMC splay ('butterfly structure') lacking an obvious central nucleation point. **c** Large boulder-shaped HMC splay associated with extensive bioerosion. The HMC is pitted by a borehole (arrow) indicating that micro-boring activity persisted after the deposition of the cement.

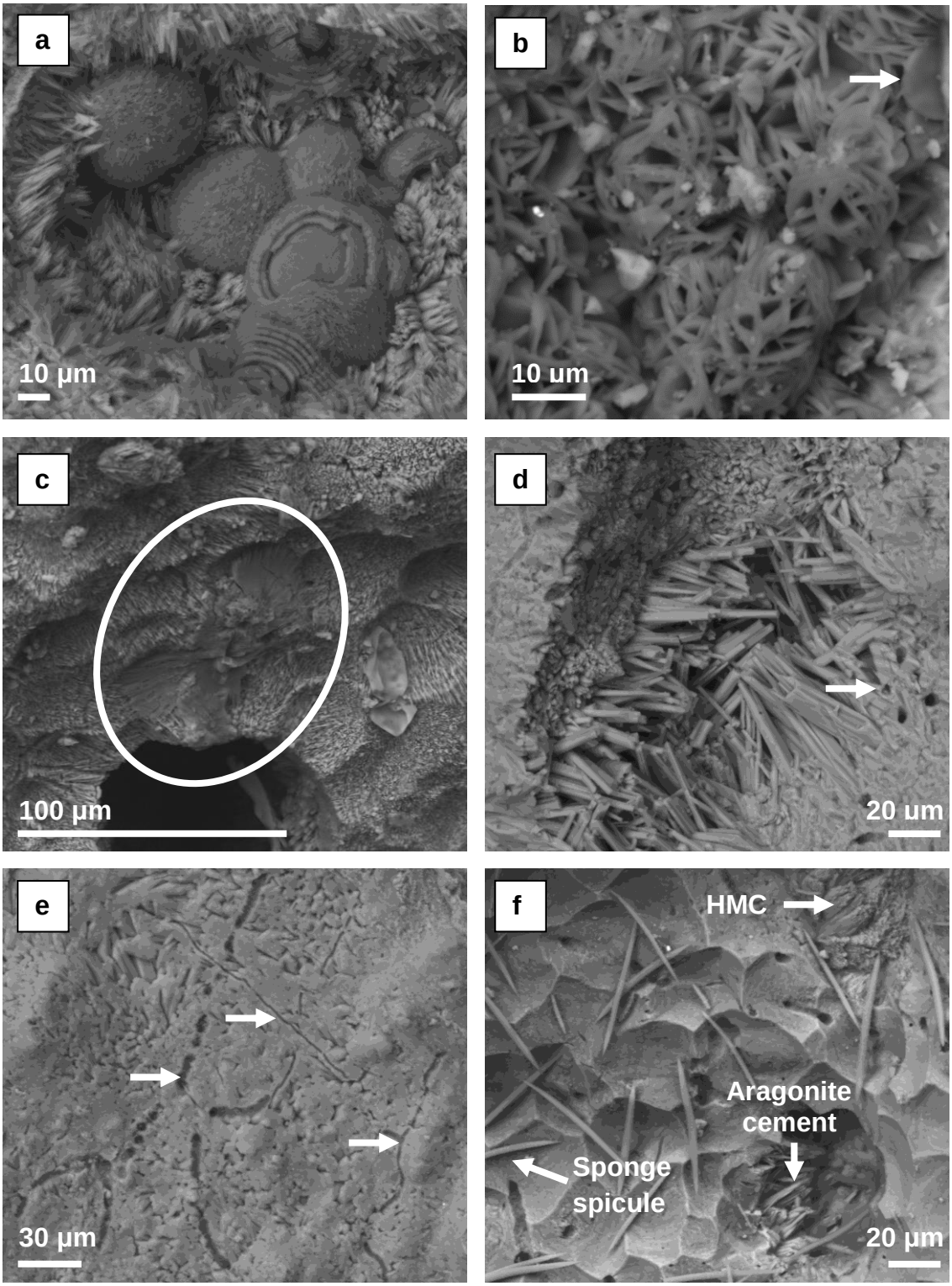
a
10 µm
b
10 µm
c
100 µm
d
20 µm
e
30 µm
f
HMC
Aragonite cement
Sponge spicule
20 µm

**Fig 4.18** (Previous page) brucite and bioerosion in modern siderastreid corals. **a** Brucite rosettes cushioned amongst delicate aragonite needles. The rosettes consist of palisades of slender crystals that form concentric layers separated by <1µm voids (NHMUK AZ 4879). **b** Aggregations of brucite plates consisting of single (arrow) or fused discs up to 10 µm in diameter (NHMUK AZ 4879). **c** The close association between bioerosion and cement deposition is clearly illustrated by the presence of an isopachous layer of acicular aragonite covering the scalloped depressions of an abandoned sponge gallery. Flat X-shaped splays of brucite have subsequently been deposited over the aragonite forming a crust (SID-D-1-l). **d** A void lined with an isopachous layer of aragonite cement and filled with a mesh of long (~60 µm) syntaxial rods and needles of aragonite. In addition, micro-boring activity has affected both the coral skeleton (black arrow) and the cements (white arrow) (NHMUK AZ 4879). **e** Trace evidence of the activities of micro-boring endolithic organisms such as fungi, green algae and cyanobacteria. The micro-borers typically form pits or tracks <10 µm in diameter (NHMUK AZ 4879). **f** Scalloped sponge gallery littered with sponge spicules. Tufts of acicular aragonite fill a pair of enlarged cavities within the gallery. The aragonite cement in the lowermost cavity is draped with a thin organic film. The scalloped depressions of the sponge gallery have been cut across by numerous micro-boreholes ~10 µm in diameter (NHMUK AZ 4879).

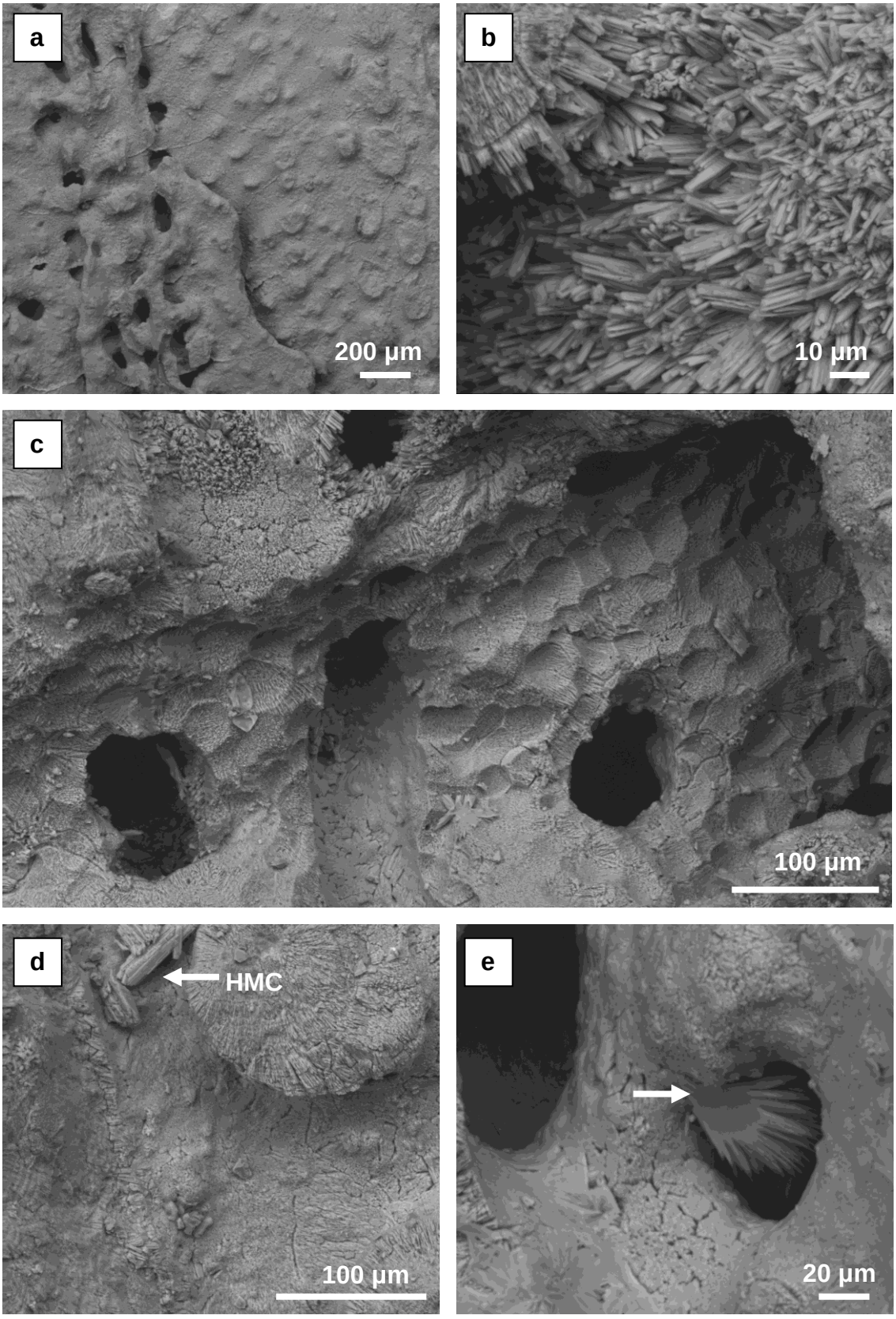
a
200 µm
b
10 µm
c
100 µm
d
HMC
100 µm
e
20 µm

**Fig 4.19** (Previous page) scanning electron micrographs illustrating the preservation of the modern coral sample *Siderastrea siderea* (SID-D-1-l). **a** Well-preserved region coral skeleton displaying unaltered slender dissepiments (d) and skeletal ornamentation (o). **b** Clumps of syntaxial aragonite cement cover a skeletal surface. The cement consists of clumps of angular aragonite rods up to 20 µm length terminating in broad planar surfaces. **c** Abandoned sponge gallery covered by a thin layer of syntaxial aragonite cement. Clumps of aragonite rods blanket the skeletal surface above the gallery. **d** High-magnesium calcite splays. **e** Spray consisting of a cluster of acicular needles fused at the base and splayed at the top. The individual crystals terminate in delicate points.

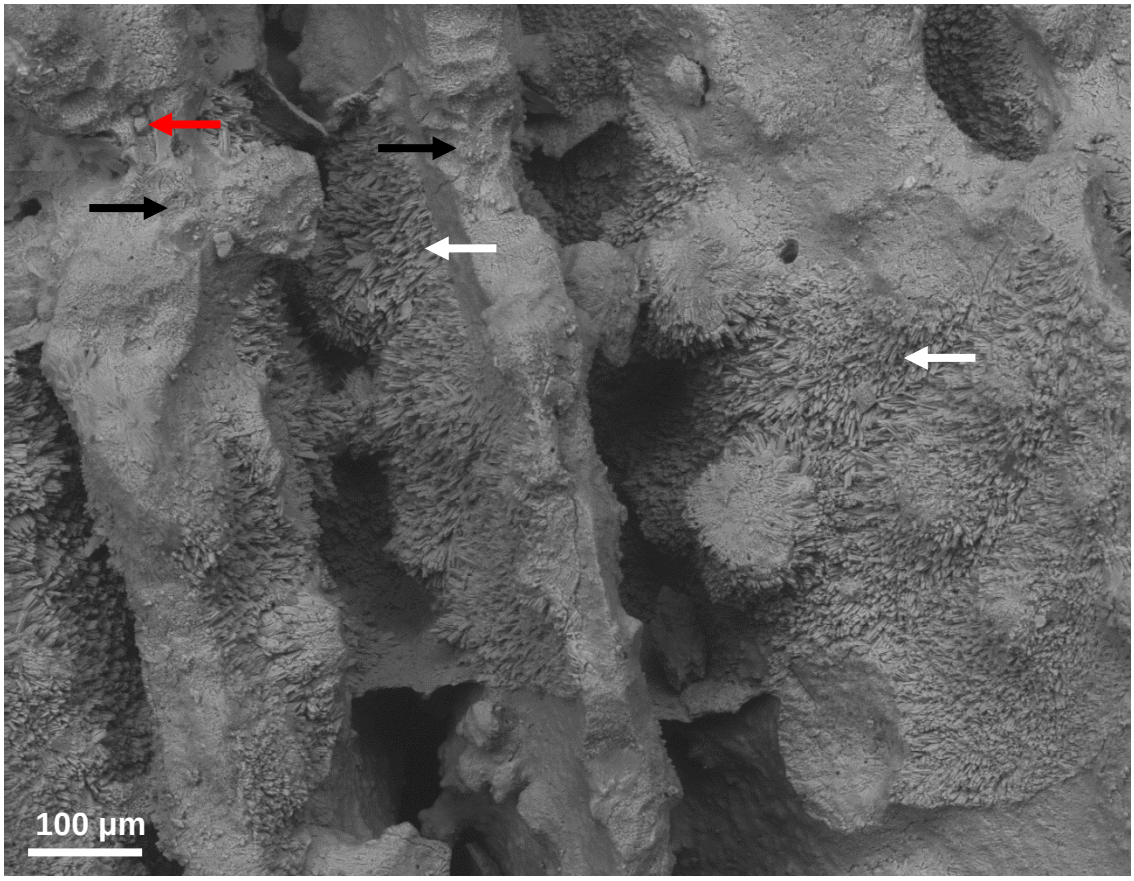


**Fig 4.20** Scanning electron micrograph illustrating the close relationship between sponge galleries (black arrow) and acicular aragonite cements (white arrow). Note the presence of sponge chips lodged in a depression (red arrow). Syntaxial aragonite cements have started to over-grow the sponge galleries in this field of view indicating that they are old and have been abandoned (*Siderastrea* siderea; SID-D-1-l).

### 4.4.2 Fossil corals

Scanning electron microscope observation reveals evidence for diagenetic alteration and bioerosion in all of the fossil samples examined. Cements and hydrocarbons (oil and bituminous residues) are present in many of the pore spaces while micro-boring and dissolution have etched many of the skeletal surfaces. However, the distribution of diagenetic alteration is heterogeneous and varies considerably within the corals resulting in zones of excellent preservation (Figures 4.21a; 4.21b; 4.22a; 4.25a) juxtaposed with less well-preserved areas (Figure 4.22f). In some regions, remarkable preservation has conserved features such as the growth increments on the inferior surfaces of the dissepiments (Figure 4.21b).

#### *4.4.2.1 Secondary aragonite cements*

The cements found in the fossil corals are predominantly composed of secondary aragonite precipitated directly onto the primary aragonite of the coral skeleton from supersaturated pore-waters. Cement crystal growth is typically syntaxial (Figure 4.21c white arrow) although some aragonite cements appear to have been deposited on organic films that have since disappeared leaving a sub-micron gap between the primary and secondary aragonites (Figure 4.22d). The aragonite cements exhibit a range of diagenetic textures that include slender acicular needles that terminate in sharp points (Figures 4.21c and 4.24a), small bladed forms (Figure 4.21c black arrow), long (≤ 100 μm), lath-like crystals that terminate in either chamfered (Figure 4.22c) or planar surfaces (Figure 4.22d). Secondary aragonite may also form huge blocky crystals that almost completely fill the pore spaces in which they have grown (Figures 4.21f; 4.21b). Crystal size varies from 10 μm for small bladed forms up to 120 μm for large blocky crystals. Acicular needles typically reach lengths of 20 μm. Cements consisting of acicular needles and small blades typically form closely-spaced isopachous fringes and crusts mirroring the dense packing of the underlying primary aragonite crystals (Figures 4.21c; 4.21e; 4.23c; 4.23e). Spaces and voids open up between the cement crystals as they grow away from the primary aragonite (Figure 4.21c) producing meshes when the crystals become very large (Figures 4.21f; 4.22b; 4.22d). Large blocky-aragonite

cements are found exclusively in the fossil corals. They occasionally occur in pore spaces lined with acicular aragonite needles (Figure 4.22b). This arrangement suggests either contemporaneous selective overgrowth of crystals in favourable orientations during the precipitation of the acicular aragonite needles or a later diagenetic phase in which the large blocky crystals have grown through an earlier generation of aragonite cement. Aragonite cements are a common product of early marine diagenesis in phreatic and vadose marine environments (Tucker and Wright, 1990; Scholle and Ulmer-Scholle, 2003; Nothdurft and Webb, 2009), although they may also be precipitated in meteoric environments permeated by saline ground water in arid climates (Scholle and Ulmer-Scholle, 2003).

#### *4.4.2.2 Calcite cements*

Calcite cements exhibiting a range of morphologies are seen under the SEM in all the fossil corals examined. The cements typically consist of irregular blocky masses and interlocking rhombs measuring 50 µm in diameter (Figure 4.23c). The cements may be deposited directly onto skeletal aragonite or overlie a previous generation of cement. For example, in *Montastraea* (NHMUK AZ 4877) the calcite cement overlies an isopachous layer of acicular aragonite that is clearly visible in the interstices between the masses of calcite crystals. In addition, large crystals of calcite (≥100 µm) are also present in *Montastraea*. These crystals form interlocking masses that completely occlude the pore spaces that they occupy (Figure 4.23b).

Calcite may be precipitated in meteoric and burial diagenetic environments producing cements with a range of diagenetic textures and chemical compositions (James, 1974; McGregor and Gagan, 2003; Scholle and Ulmer-Scholle, 2003). The activities of boring endobionts (e.g. *Lithophaga*) may also result in the precipitation of calcite cements (Jones and Pemberton, 1988).

#### *4.4.2.3 Iron sulphides*

Pyrite (FeS) deposits are found in all the fossil corals examined where they appear as bright amalgamations of crystals in back scattered electron SEM images. The pyrite deposits exhibit a range of crystal morphologies that include

octohedra, pyritohedra and amorphous anhedral masses (Figures 4.21d; 4.26a; 4.26b). The crystals range in size from ~30 µm for octahedral forms down to ~10 µm for pyritohedral forms.

#### *4.4.2.4 Dolomite*

Dolomite [$CaMg(CO_3)_2$] deposits are present in two specimens of *Montastraea limbata* (NHMUK AZ 4877 and 4878). The crystals are rhombic in shape and measure up to 60 µm in length. The rhombs may occur singly (Figure 4.23d) or in interlocking masses comprised of a number of crystals (Figure 4.23e). Close examination of the crystal faces reveals they have curved surfaces characteristic of non-planar dolomite (Figure 4.23e).

#### *4.4.2.5 Brucite*

Brucite cements have not been positively identified in any of the fossil coral samples examined under the SEM. However this may be due to overprinting by later cement deposits, dissolution or the absence of suitable pore fluid chemistry and nucleating conditions. For example, Figure 4.23 shows a cross-section through laminated mounds of cement separated by voids overlain by cements and hydrocarbon deposits. The mounds are composed of layers of cement less than 10 µm thick separated by voids of less than 5 µm. The cement is composed of palisades of crystals aligned orthogonal to the direction of the layering. The laminated mounds are overlain by a thick (>120 µm) layer of bladed aragonite cements and hydrocarbon deposits that clearly post-date the deposition of the laminated mounds.

#### *4.4.2.6 Hydrocarbons*

Hydrocarbons (bituminous residues) are present in all the fossil corals investigated. Under the SEM the bitumen appears as dark amorphous masses that fill entire pore spaces (Figure 4.21e; Figure 4.23a) or form thick crusts that cover the underlying skeletal surfaces or cements (Figure 4. 23e; Figure 4.24). Many of the bituminous deposits possess cracked surfaces and have shrunk away from the pore space walls or underlying cements due to desiccation and contraction (Figure 4.23a; Figure 4.24a).

#### *4.4.2.7 Bioerosion and micro-boring*

Evidence of extensive bioerosion and micro-boring activity is seen in all the specimens based on SEM observation of random sections of each sample. The micro-boreholes occur in all parts of the coral skeleton and typically measure <10 µm in diameter (Figure 4.26b). Sinuous branching tracks etched onto smooth skeletal aragonite are also observed in a single sample of *Montastraea limbata* (NHMUK AZ 4878). The tracks range in diameter from 3 – 5 µm and have a banded appearance due to the presence of strands of remnant skeletal material left behind as the organism has repeatedly stopped and then advanced (Figure 4.22e). Boring activity is not confined to skeletal aragonite as some of the cements also bear pits and etched tracks (Figure 4.21d; The identity of the micro-boring organisms is unknown but they are most likely to be representatives of the green algae, fungi and cyanobacteria based on the evidence from modern corals.

Sponge galleries were not observed in any regions of the coral specimens surveyed under the SEM.

#### *4.4.2.8 Dissolution*

Dissolution processes have affected all the fossil corals with evidence of widened centres of calcification and the presence of pitted and eroded skeletal aragonite fibres and cements. The centres of calcification are composed of miniscule (<1 µm) randomly orientated granules (Cohen et al., 2001; Cuif and Dauphin, 2005) that form distinct mid-line structures with axes aligned parallel to the direction of growth within the thecal and septal walls (Perrin, 2003). The sub-micron sized grains of the centres of calcification are particularly vulnerable to dissolution because they possess large surface area to volume ratios (Walter and Morse, 1984). In Figure 4.21d, the mid-line groove has been widened and material removed by dissolution producing two enlarged pits down the centre of the septal wall. In addition, a number of the radiating bundles of aragonite fibres and the pyrite crystals deposited on the surface of the skeletal aragonite appear pitted and etched. Some pitting may be due to bioerosion although the etched surfaces appear to have been created by dissolution processes because they involve larger areas of the crystal surfaces and do not form sinuous tracks.

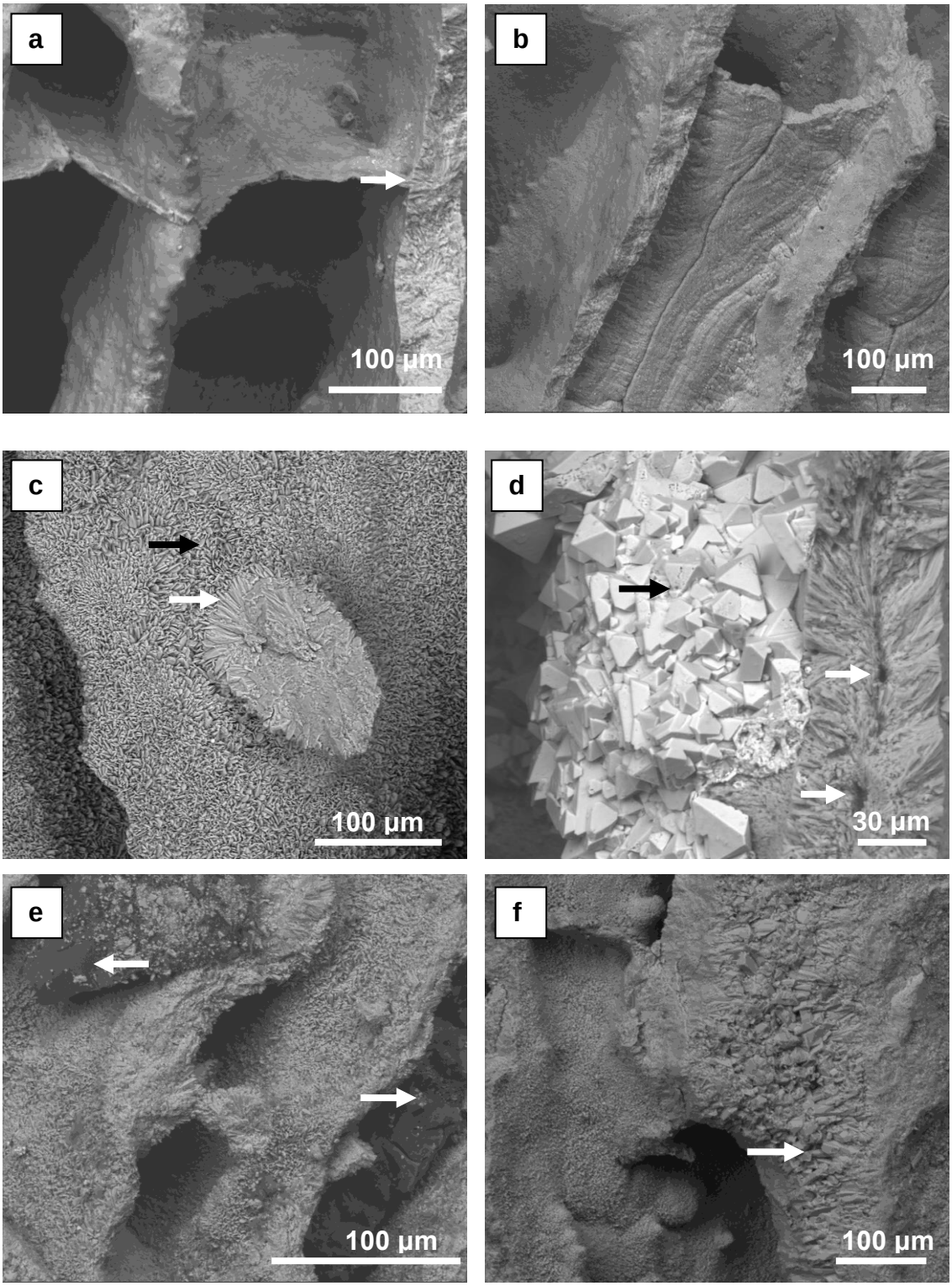
a
100 µm
b
100 µm
c
100 µm
d
30 µm
e
100 µm
f
100 µm

**Figure 4.21** (Previous page) scanning electron micrographs illustrating skeletal preservation and cementation in the fossil coral *Siderastrea conferta.* **a** Well-preserved skeletal architecture and aragonite. Radiating bundles of aragonite crystals (arrow) are clearly visible in the fractured surface of the septal wall (NHMUK AZ 4874). **b** Growth bands are visible on the inferior surface of a dissepiment attesting to exceptional preservation in this region of the coral (NHMUK AZ 4875). **c** Isopachous layer of bladed aragonite cement (black arrow) covers the skeletal surfaces. Syntaxial acicular aragonite crystals (white arrow) extend from the surface of a skeletal element (NHMUK AZ 4874). **d** Octohedral pyrite crystals up to 30 µm in length deposited within a pore space. Some of the crystals possess pitted and etched surfaces possibly due to micro-boring (black arrow) and dissolution. Selective dissolution has removed some of the micro-granules that comprise the centres of calcification leaving voids (arrow) along the midline of the fractured wall visible on the right of the image (NHMUK AZ 4875). **e** Amorphous deposits of bituminous hydrocarbon (arrows) fill pore spaces lined with an earlier generation of acicular aragonite cement (NHMUK AZ 4875). **f** Blocky aragonite crystals up to ~40 µm in length fill a pore space (arrow) adjacent to skeletal surfaces cemented with acicular aragonite (NHMUK AZ 4874).

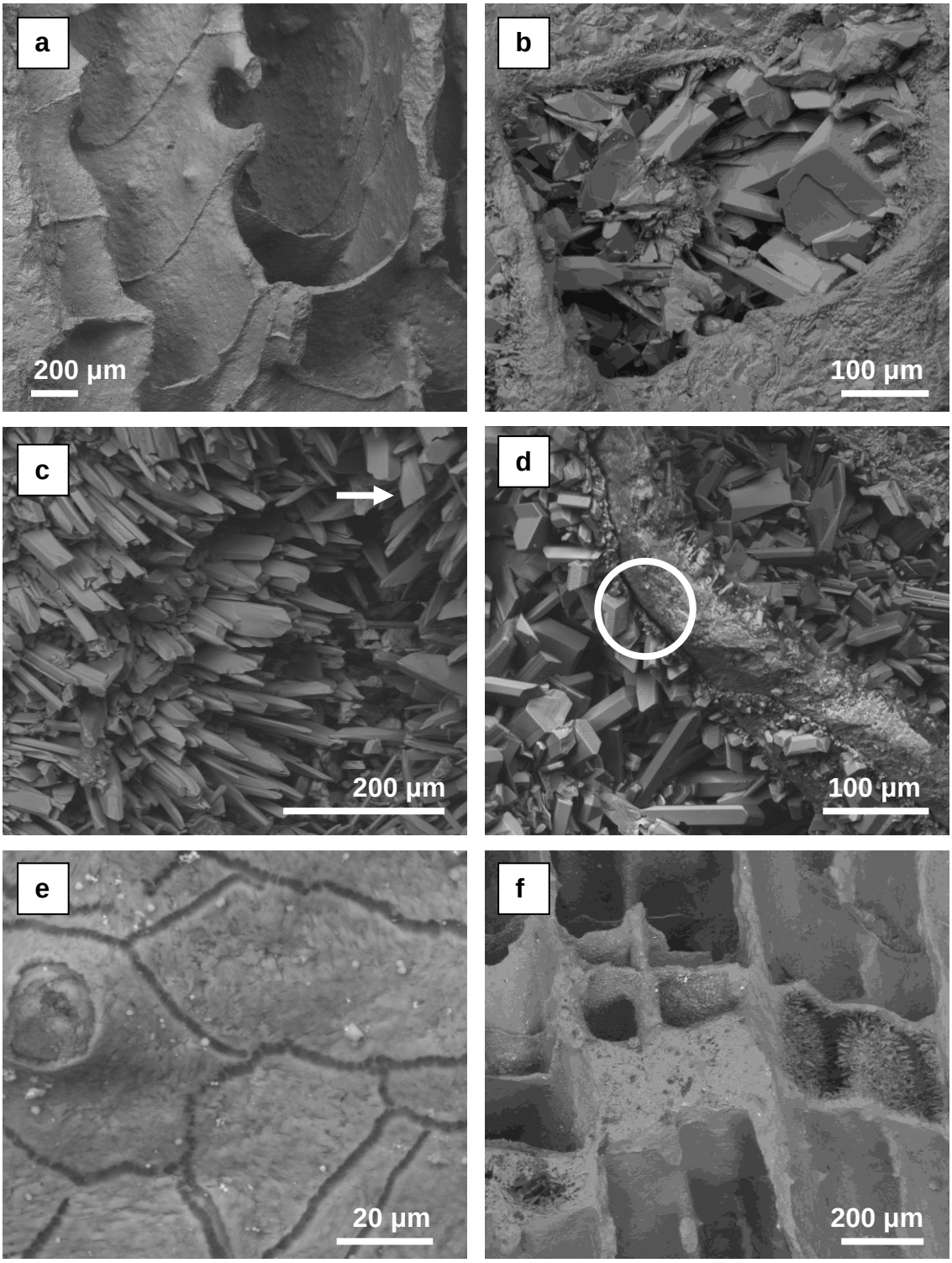
a
200 µm
b
100 µm
c
200 µm
d
100 µm
e
20 µm
f
200 µm

**Figure 4.22** (Previous page) scanning electron micrographs illustrating skeletal preservation and cementation in the fossil coral *Montastraea limbata.* **a** Unaltered smooth ornamented skeletal surfaces and intact slender dissepiments (NHMUK AZ 4878). **b** Huge blocky aragonite crystals up to ~120 µm in length fill a pore space that is lined by an isopachous layer comprising aciclular aragonite crystals up to 10 µm in length (NHMUK AZ 4878). **c** Aggregations of long (~80 µm) bladed and fused acicular aragonite crystals (NHMUK AZ 4876). The bladed crystals typically terminate in broad chisel-like chamfered surfaces (arrow) (NHMUK AZ 4878). **d** Large angular crystals and a thin layer of cement separated from the skeletal surface by a narrow void (open circle) suggesting that cement deposition occurred on a surface that has not been preserved such as an organic biofilm (NHMUK AZ 4876). **e** Sinuous tracks less than 10 µm in diameter etched by micro-boring organisms on smooth skeletal surfaces (NHMUK AZ 4878). **f** Low magnification view showing heterogeneously distributed cements juxtaposed with regions of excellent preservation. The cements comprise long acicular and massive blocky pore occluding crystals (NHMUK AZ 4878).

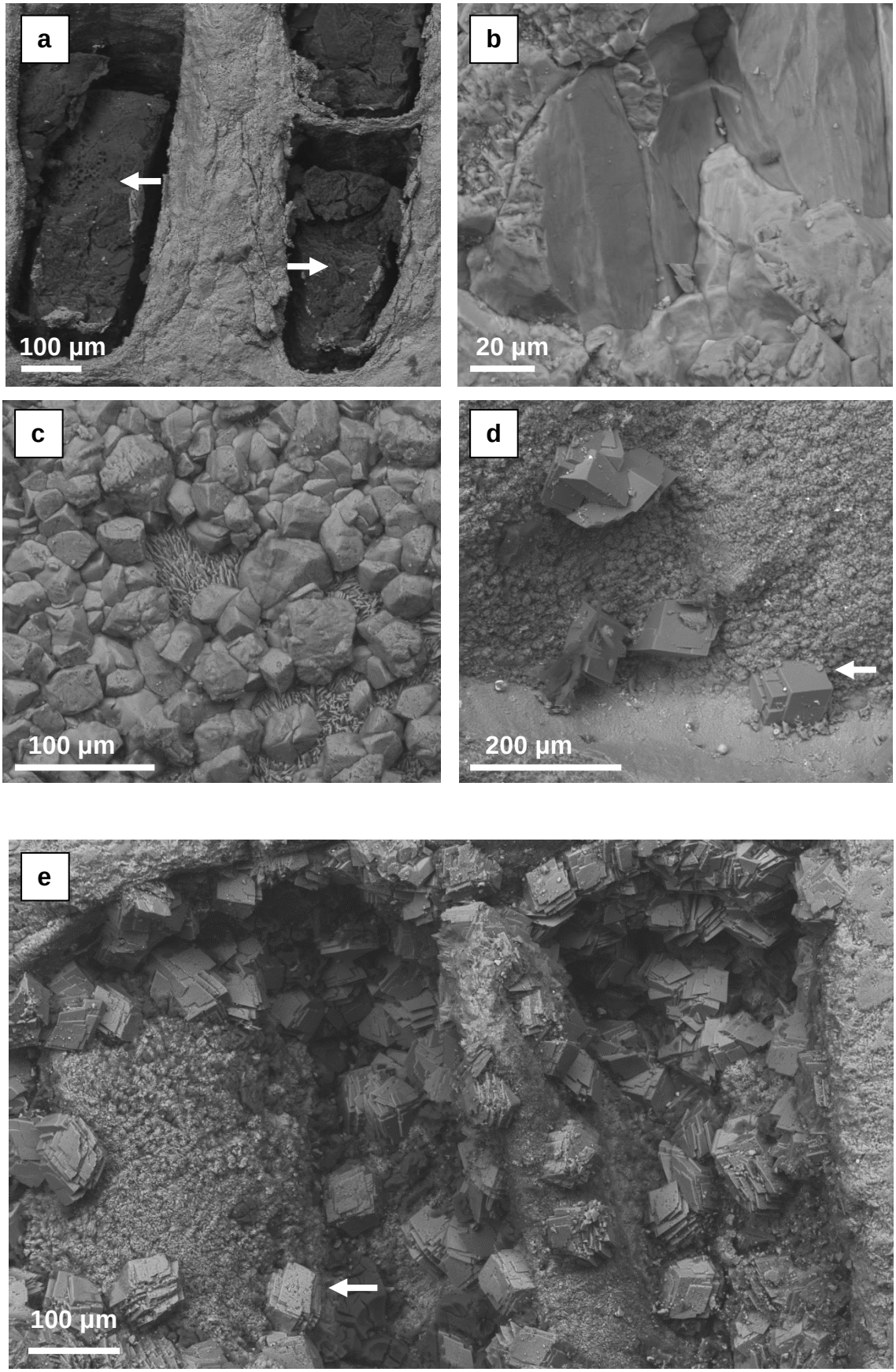
a
100 µm
b
20 µm
c
100 µm
d
200 µm
e
100 µm

**Figure 4.23** (Previous page) scanning electron micrographs illustrating skeletal preservation and cementation in the fossil coral *Montastraea limbata.* **a** Amorphous masses of bitumen deposited within pore spaces. The dark lumps of bitumen appear cracked and desiccated and shrinkage has opened voids between the hydrocarbon and the pore space walls (NHMUK AZ 4876). **b** Calcite spar completely occludes a pore space (NHMUK AZ 4877). **c** Irregular calcite masses and interlocking rhombs deposited over a previous generation of acicular aragonite cement visible in the interstitial spaces between the calcite cements. Many of the calcite crystals bear etched and pitted surfaces and possess a rather irregular outline (NHMUK AZ 4877) due to micro-boring and dissolution. **d** Large rhombohedral dolomite crystals deposited on a cemented and etched coral skeletal surface (NHMUK AZ 4878). **e** Clusters of non-planar dolomite crystals deposited on a cemented and etched coral surface. The non-planar dolomite consists of platy rhombohedra with distinctive curved crystal faces (arrow). Dark amorphous masses of desiccated hydrocarbon are also present overlying the rough cemented skeletal surface and the dolomite (NHMUK AZ 4877).

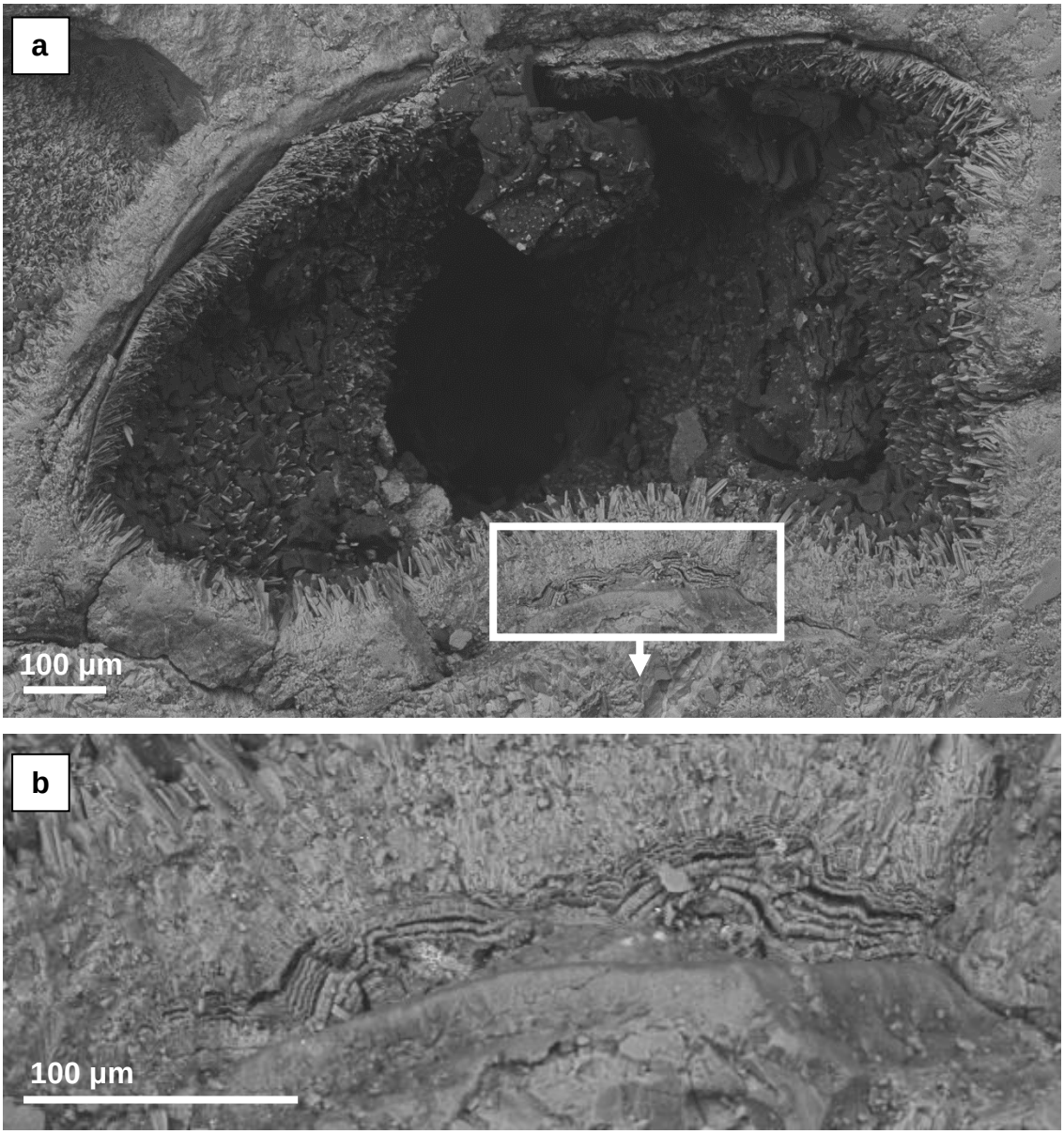


**Figure 4.24** Scanning electron micrographs illustrating skeletal preservation and cementation in the fossil coral *Montastraea limbata.* **a** Pore space lined with acicular aragonite cement coated with bituminous hydrocarbons. Beneath the layer of acicular aragonite there are thin layers of cement forming rippling rounded mounds (box). **b** Magnified image showing the arrangement and construction of the cement layers. The layers are less than 10 µm thick and are separated from one another by voids less than 5 µm in width. The cements appear to be composed of palisades of crystals aligned orthogonal to the direction of the layering (NHMUK AZ 4877).

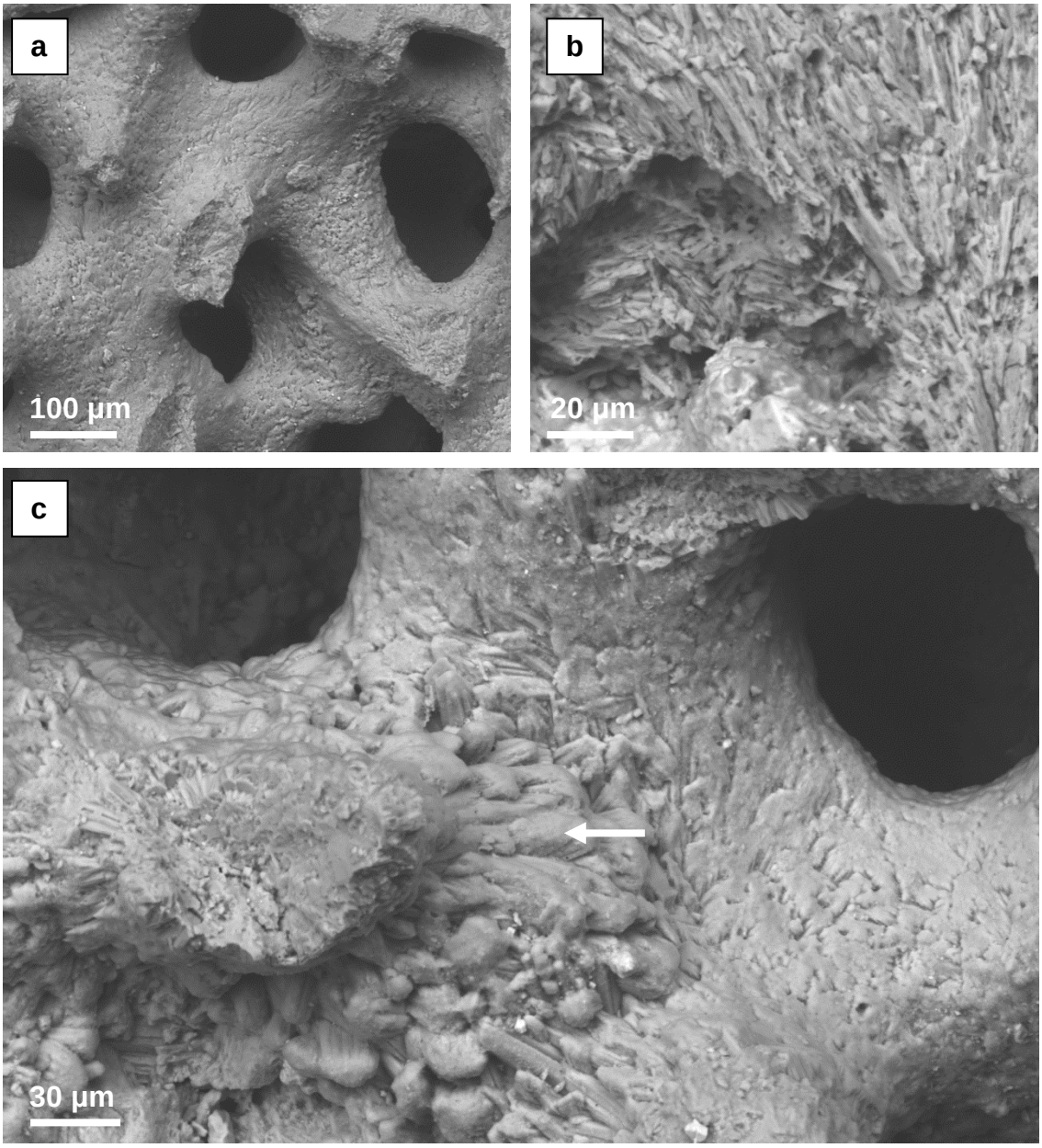


**Figure 4.25** Scanning electron micrographs illustrating skeletal preservation and cementation in the fossil coral *Porites* sp (NHMUK AZ 3140). **a** Smooth well-preserved skeletal architecture and aragonite. **b** Severely eroded aragonite crystals pitted and etched by dissolution processes. **c** Aberrant skeletal aragonite (arrow) produced by dissolution and selective syntaxial overgrowth of aragonite fibre bundles (fasciculi).

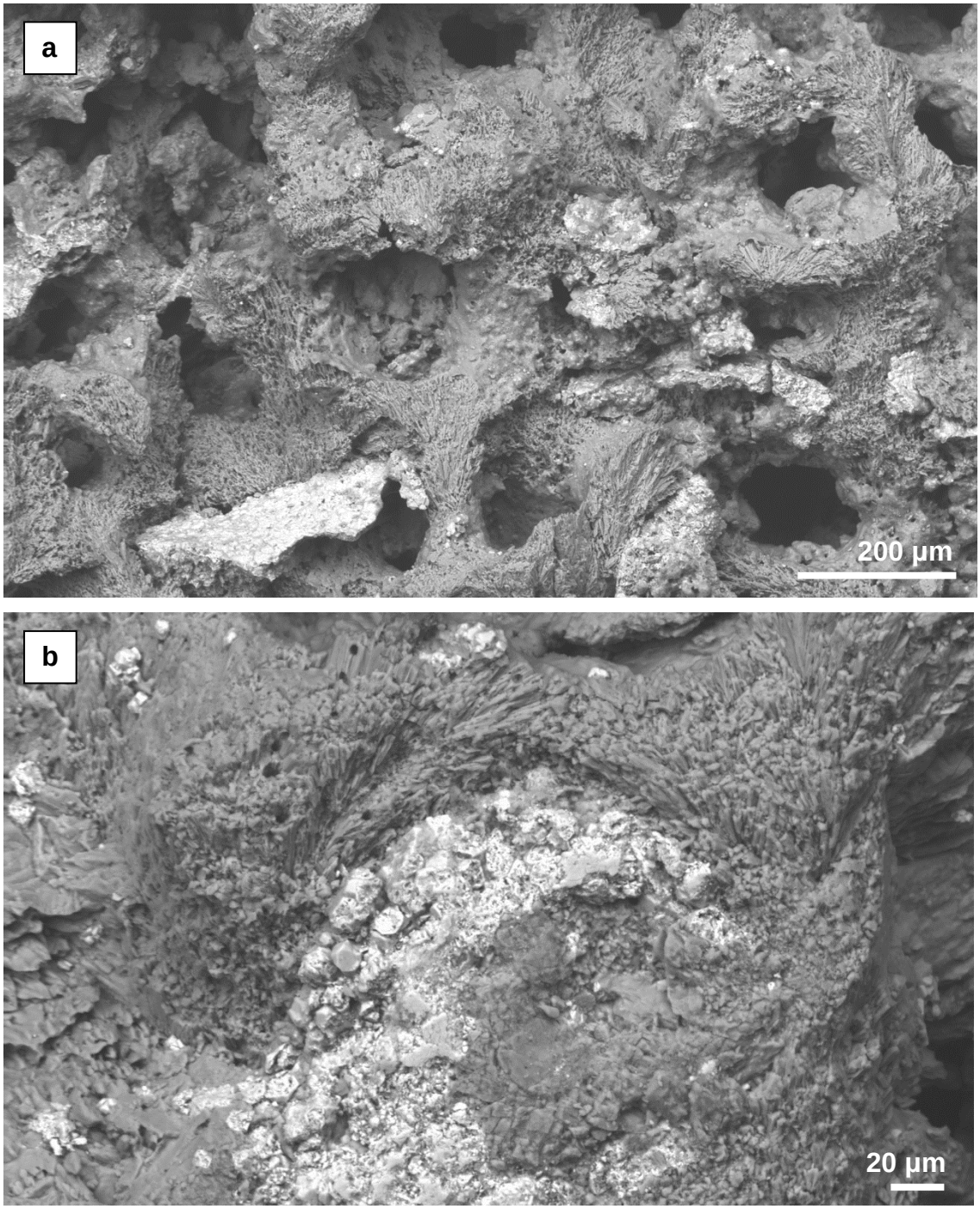


**Figure 4.26** Scanning electron micrographs illustrating skeletal preservation and cementation in the fossil coral *Porites* sp (NHMUK AZ 3140). **a** Aberrant skeletal architecture produced by cementation, dissolution and bio-erosion. **b** Pitted and etched pyrite masses fill a pore space in a heavily altered region of the coral skeleton. Micro-boreholes less than 10 µm in diameter pit the surface of the etched and eroded skeletal aragonite.

## 4.5 X-RADIOGRAPHY

The X-radiographs of the modern siderastreid corals reveal subtle changes in density aligned in the direction of growth and the absence of distinct annual growth couplets orthogonal to the growth direction. The sub-vertical banding is caused by the superposition of skeletal structures of different densities. The compact thecal walls form the pale radio-opaque bands whereas the more porous septal regions form the dark, more radio-lucent zones. The lack of clear annual density banding prevents the estimation of annual growth rates from the X-radiographs and other techniques have to be employed such as computerised tomography or tuning geochemical trace element cyclicity with records of annual temperature variation.

Dark radiolucent areas at the base of both modern specimens represent regions where skeletal material has been removed by endolithic boring organisms (white arrow). The line of low density oval pits (black arrow) visible in *Siderastrea radians* (NHMUK AZ 4879) represent sites where coral material has been sampled for stable isotope analysis.

The fossil siderastreid corals show similar radiographic appearances to those of modern *S. siderea* with subtle density banding aligned in the direction of coral growth and an absence of clear annual growth couplets. However faint density changes aligned orthogonal to the direction of growth at sub-annual distances are present and these may indicate either changes in growth rate or the amount of skeletal mineralisation. In addition there are patchy regions of increased density (black arrow) and porosity (white arrow) present in the coral samples. The sclerotic regions represent zones in which diagenetic alteration has thickened the skeletal architecture and reduced porosity. The porous regions are the result of dissolution, bioerosion or the removal of coral material for geochemical sampling.

X-radiographs of *Porites* are rather featureless because the superimposition of the various skeletal elements produces an image with fairly uniform density. However there are regions of reduced density (arrows) where dissolution has increased the porosity of the coral.

The skeletal architecture of *Montastraea limbata* is clearly seen on X-radiographs because the thick thecal walls and relatively large pore spaces

result in large density differences. Cemented regions of the coral produce irregular patches of increased radio-density while parts of the coral skeleton affected by dissolution or removal of material for sampling are more radiolucent.

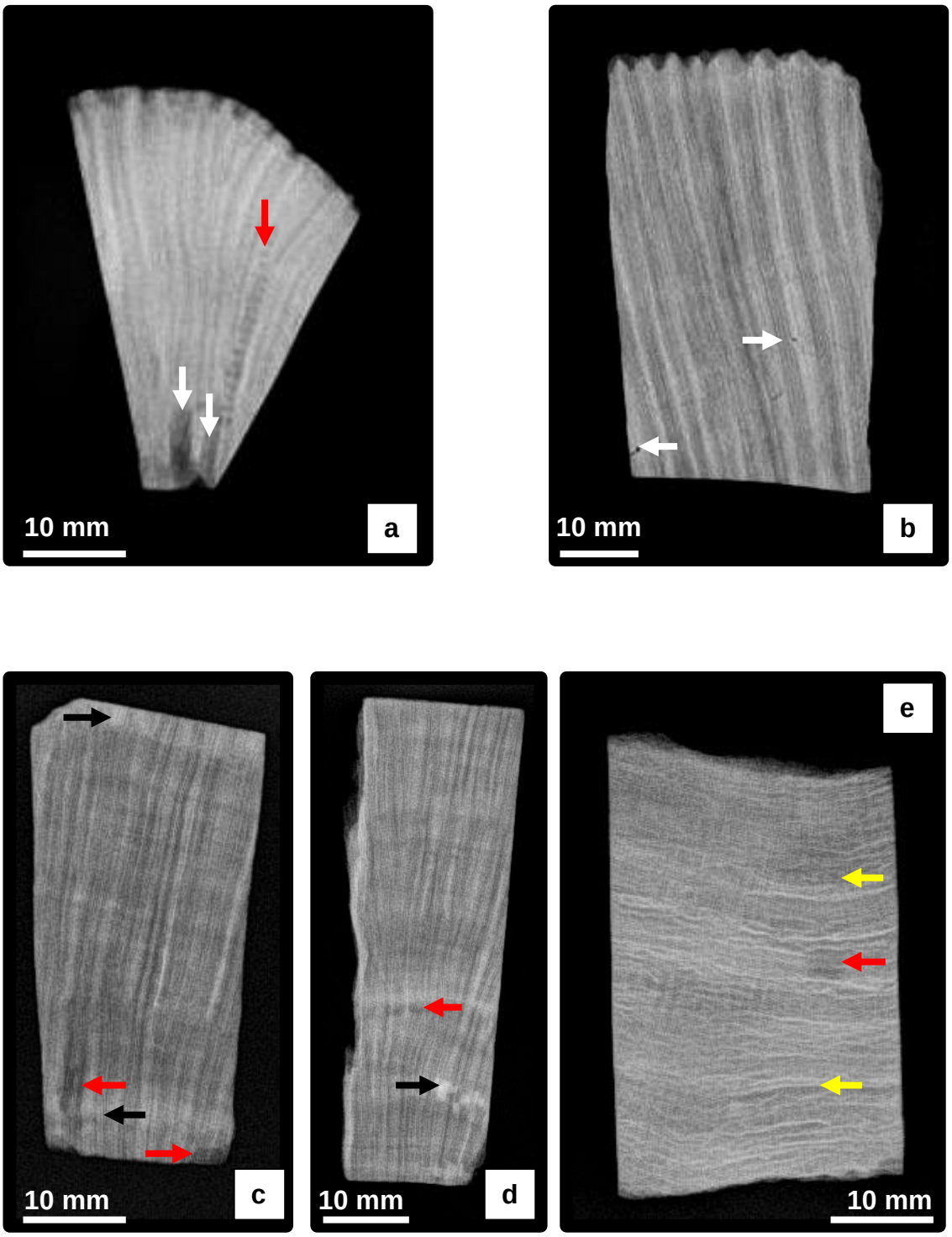

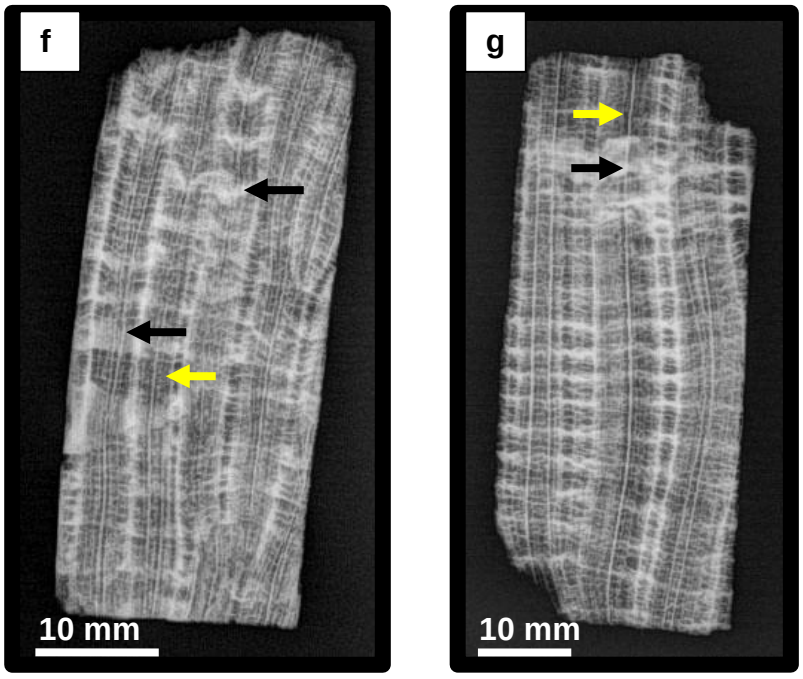


**Figure 4.27** (previous page and this page) X-radiographs of modern and fossil coral specimens. White arrows indicate regions of the coral affected by bioerosion producing distinctive radiolucent zones where coral material has been removed. Yellow arrows indicate radiolucent zones produced by dissolution processes. The red arrows indicate regions where coral material has been removed for sampling purposes. Black arrows indicate zones of increased skeletal density caused by cementation and sediment ingress. **a** *Siderastrea radians* NHMUK AZ 4879. **b** *Siderastrea siderea* SID-D-1-I. **c** *Siderastrea conferta* NHMUK AZ 4874. **d** *Siderea conferta* NHMUK AZ 4875. **e** *Porites* NHMUK AZ 3140. **f** *Montastraea limbata* NHMUK AZ 4876. **g** *Montastraea limbata* NHNUK AZ 4878.

### 4.6. X-RAY DIFFRACTION ANALYSIS

The results of the X-ray diffraction analyses are presented here. The samples, sampling sites and methodology are documented in Chapter 3 (Section 3.4.6).

Peaks for aragonite, calcite, quartz were identified from the 2-theta diffraction angle. The identity of the peak at 2-theta 30.2 is not known for certain but it may represent gypsum and this would be consistent with the presence of gypsum in some of the surface sediments (e.g. Locality 2).

Aragonite peaks in the XRD data may represent pristine skeletal aragonite or a combination of primary and secondary aragonite since they both produce the same X-ray diffraction pattern and therefore it is not possible to distinguish one from the other (McGregor and Abram, 2008). Rigorous screening of coral samples under the light microscope is therefore necessary in order to identify the presence of aragonite cements prior to any geochemical analysis.

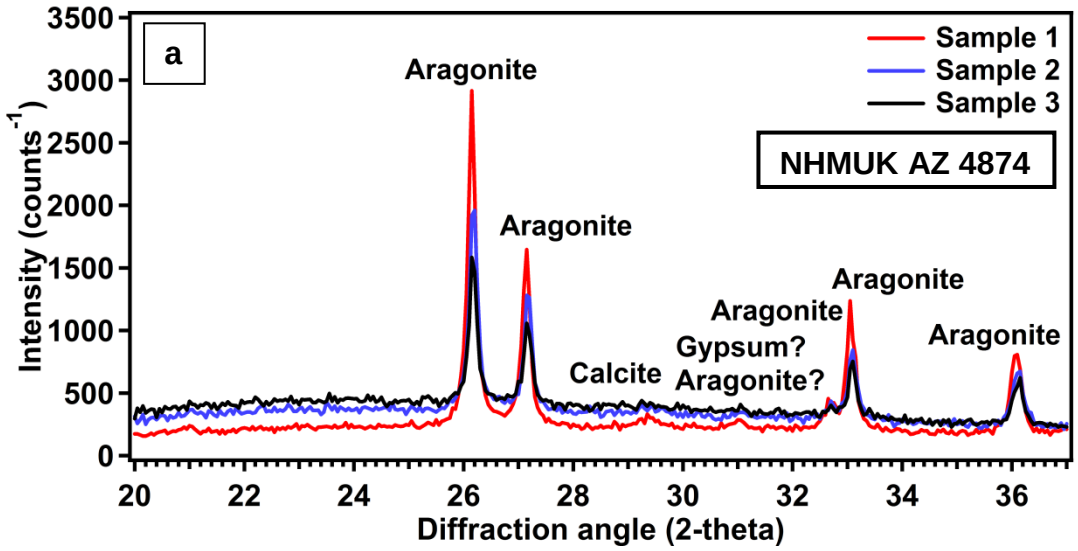

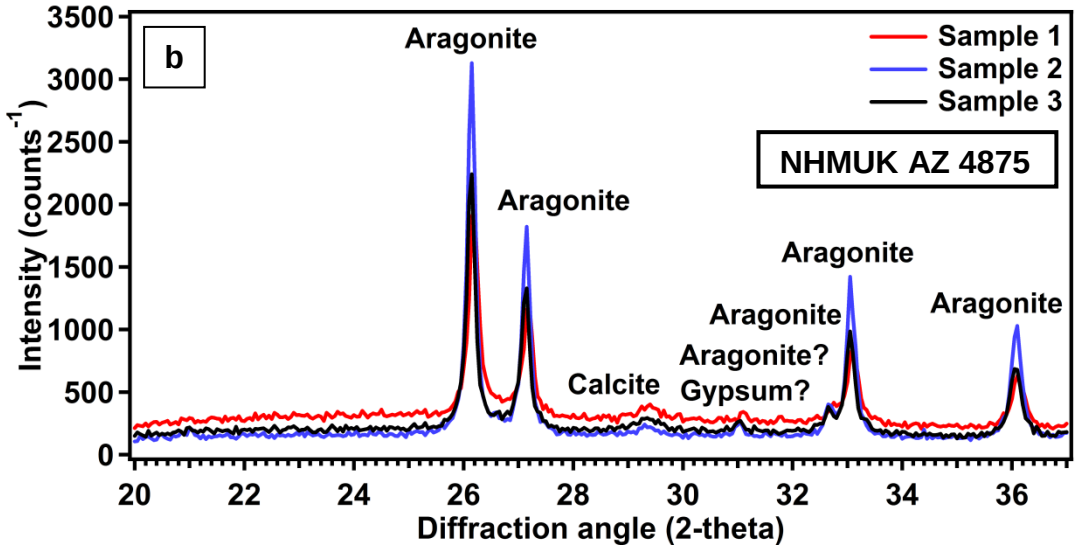
b
Aragonite
Aragonite
Aragonite
Aragonite
Aragonite
Aragonite?
Gypsum?
Calcite
Sample 1
Sample 2
Sample 3
NHMUK AZ 4875
Intensity (counts-1)
Diffraction angle (2-theta)

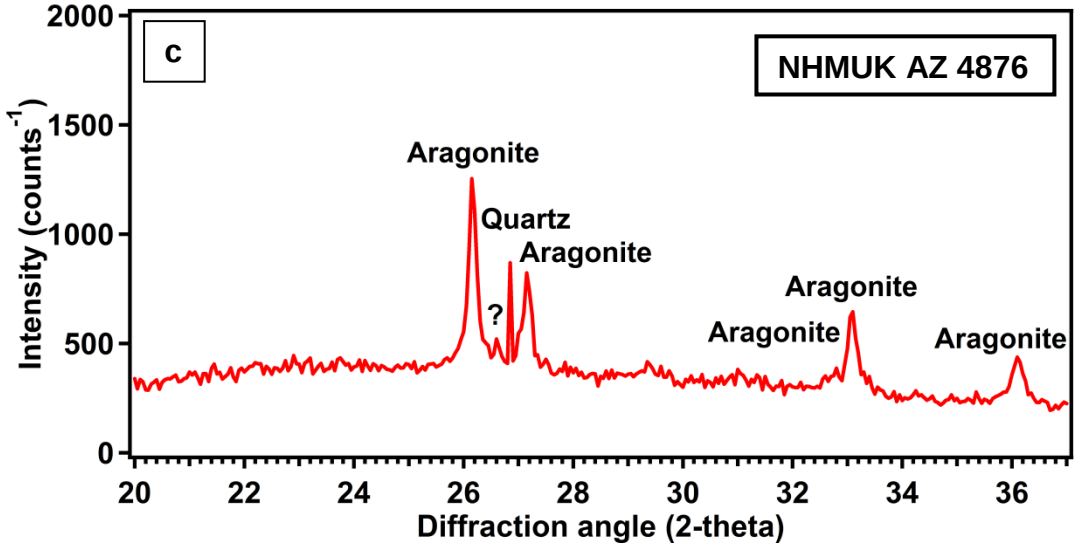
c
NHMUK AZ 4876
Aragonite
Quartz
Aragonite
?
Aragonite
Aragonite
Aragonite
Intensity (counts-1)
Diffraction angle (2-theta)

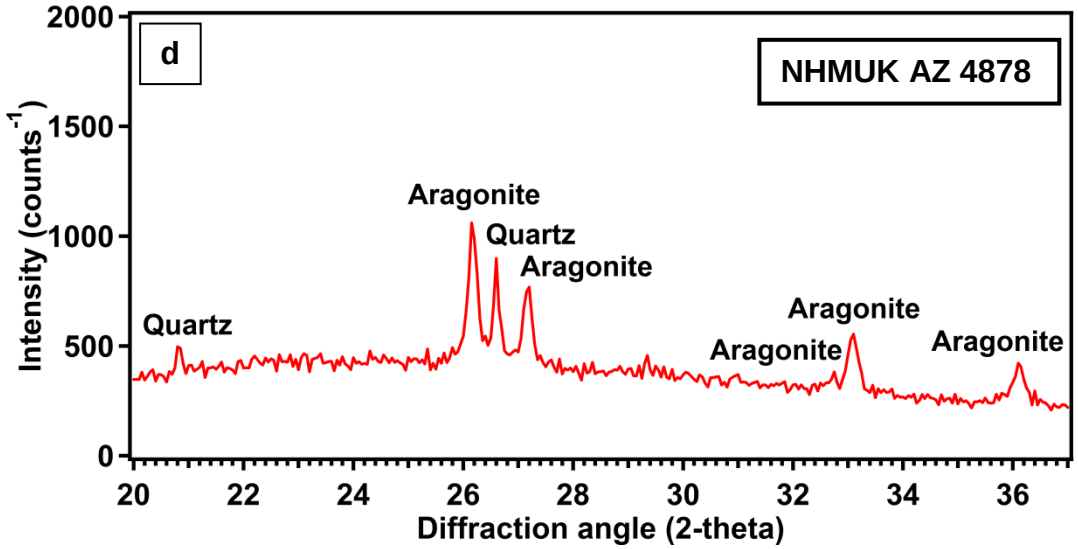
d
NHMUK AZ 4878
Aragonite
Quartz
Aragonite
Quartz
Aragonite
Aragonite
Aragonite
Intensity (counts-1)
Diffraction angle (2-theta)

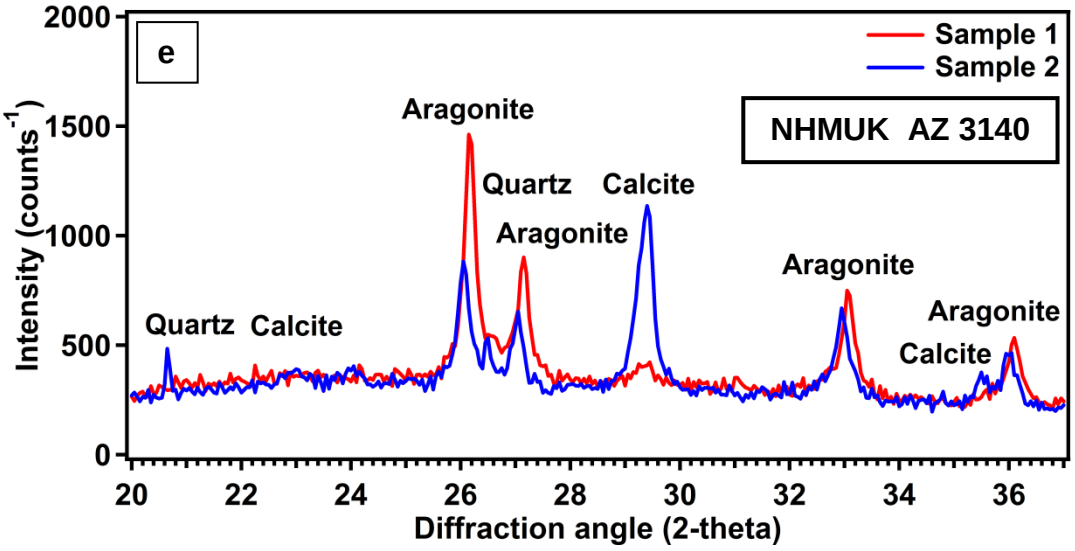


**Figure 4.28** XRD data plots for the fossil coral samples. Aragonite, calcite, quartz and gypsum peaks are shown.

## 4.7 ASSESSMENT OF PRESERVATION OF PRIMARY ARAGONITE IN MODERN AND FOSSIL CORAL SPECIMENS

Light microscope and scanning electron microscope images illustrating well preserved primary skeletal aragonite are shown in Figure 4.29. The pore spaces and micro-anatomy of the coral skeleton are clearly seen in petrographic thin section (Figures 4.29a – 4.29f). The dark/opaque regions lying in the mid-line of the coral septae represent the COCs. The COCs are composed of clusters of randomly orientated sub-micron sized grains of aragonite often surrounded by a zone of 1 μm-sized aragonite grains and slender laths that appear brown in plain polarized light (Wainwright, 1963). Radiating outwards from the COCs are groups of slender aragonite crystals that form the fasciculi. Bundles of fasciculi form the distinctive 'U'-shaped sclerodermites that comprise the main structural building blocks of the coral skeleton (James, 1974; Cohen and McConnaughey, 2003). The surface of the coral skeleton is covered by a smooth layer of micro-crystalline aragonite

(Constantz, 1986) that may appear brown when viewed in plain polarized light (Figures 4.29c- 4.29f).

Under the scanning electron microscope, the skeletal surfaces appear smooth and devoid of diagenetic cements although evidence of endolithic micro-boring activity is present in some cement-free regions of the modern coral (Figure 4.29h). Skeletal ornamentation in the form of small papillae are visible on some of the coral surfaces (e.g. Figures 4.29g and 4.29k). The slender horizontal/oblique dissepiments that once separated the living polyps from the older parts of the skeleton during coral growth are preserved (e.g. Figure 4.29i and 4.29k) and radiating bundles of aragonite fibres are clearly seen in the surfaces of fractured skeletal walls ( Figure 4.29j).

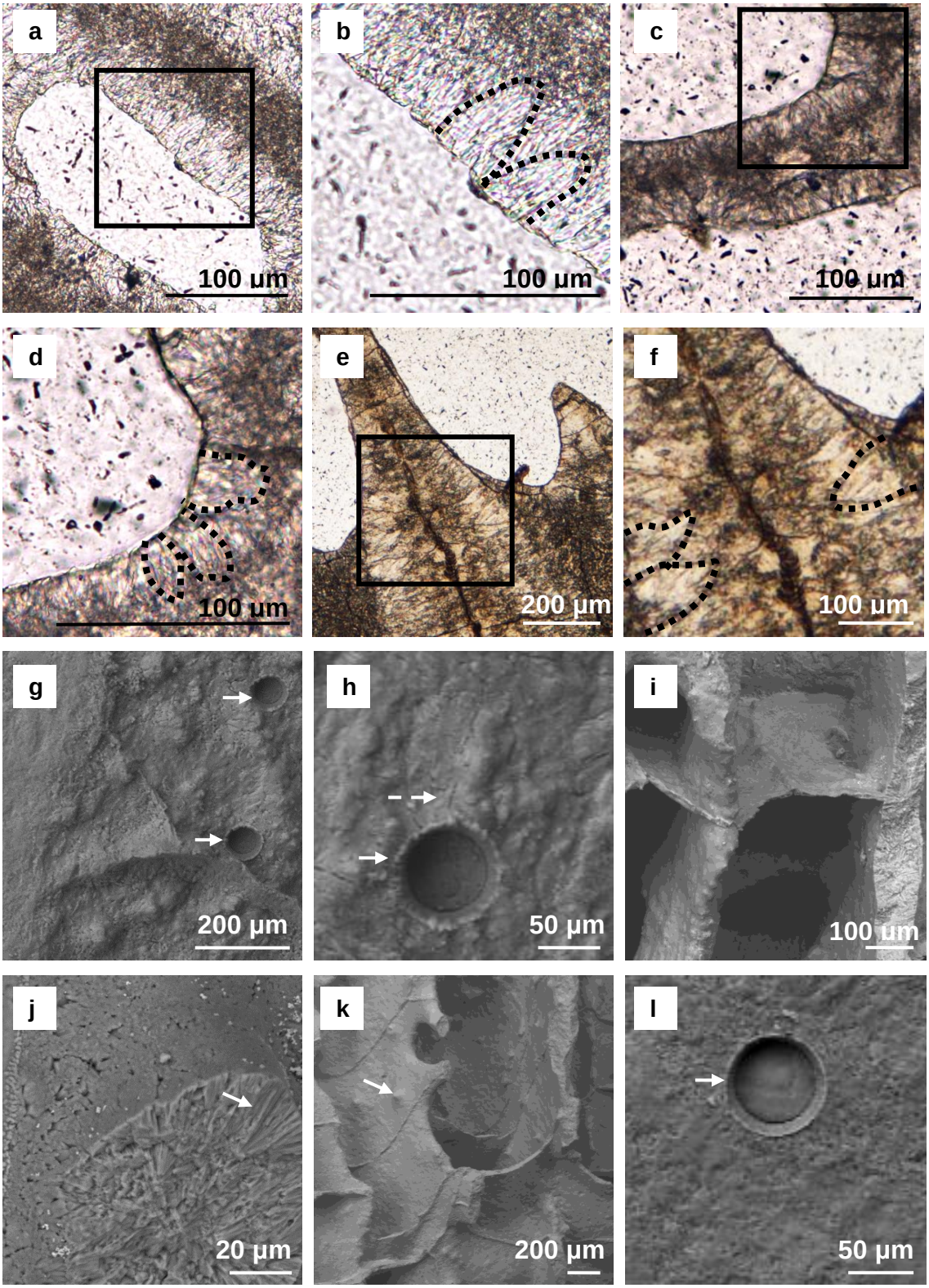


**Figure 4.29** Transmitted light microscope images and scanning electron micrographs illustrating well-preserved primary skeletal aragonite in modern *S. radians* and fossil *S. conferta* and *M. limbata.* The boxes indicate areas imaged

at higher magnification for each specimen. The dashed lines outline the 'U'-shaped sclerodermites comprised of bundles of aragonite fibres. The dark lines present in the midline of the skeletal elements represent the COCs composed of randomly orientated sub-micron sized aragonite granules. The surfaces of the skeletal elements are covered by a thin layer of microcrystalline aragonite (Constantz, 1986) and these smooth surfaces are well seen in the SEM images. (a) Low magnification image showing a clean pore space and the appearance of the COCs and sclerodermites in thin section (NHMUK AZ 4879). (b) Higher magnification image showing the 'U'-shaped sclerodermites (NHMUK AZ 4879). (c) Low magnification image showing well-preserved primary aragonite. The dark line visible on the surface of the coral aragonite represents the opaque micro-crystalline aragonite deposited over the surface of the planed-off aragonite fibre bundles of the sclerodermites (NHMUK AZ 4874). (d) Higher magnification image showing well-preserved aragonite fibre bundles (NHMUK AZ 4874). (e) Low magnification image showing a portion of a corallite wall and the radiating septae. The dark midline COCs are well visualised as are the radiating bundles of aragonite fibres forming the sclerodermites (NHMUK AZ 4876). (f) Higher magnification image showing the dark midline COCs and radiating bundles of aragonite fibres (NHMUK AZ 4876). (g) SEM image showing the skeletal surface of a specimen of the modern coral *S. radians.* A slender dissepiment runs diagonally down to the lower right and two laser pits (arrow) are visible. Rounded mounds on the coral surfaces (NHMUK AZ 4879). (h) Higher magnification SEM image showing a laser pit penetrating the smooth skeletal surface. Micro-boring organisms have etched fine grooves (dashed arrow) onto the coral surface (NHMUK AZ 4879). (i) Low magnification image showing slender dissepiments and smooth skeletal surfaces in a fossil *S. conferta* specimen (NHMUK AZ 4874). (j) Higher magnification image showing the radiating bundles of aragonite fibres in a fractured coral wall (NHMUK AZ 4874). (k) Low magnification image showing the smooth skeletal surfaces and slender dissepiments in a specimen of fossil *M. limbata.* Skeletal ornaments (arrow) form rounded papillae (NHMUK AZ 4878). (l) Laser pit (arrow) penetrates the smooth skeletal surface in a well preserved region of *M. limbata* (NHMUK 4876).

## 4.8 CONCLUSIONS

- The modern live-collected coral samples are affected by macro-boring and endolithic micro-boring organisms. Distinctive scalloped galleries produced by clionid sponges are common. Some galleries contain aggregations of javelin-shaped sponge spicules indicating live sponges were present when the specimen was harvested

- Early marine aragonite, high-magnesium calcite and brucite cements are present in the modern coral specimens

- Acicular and blocky aragonite, calcite, pyrite, dolomite and hydrocarbon residues are present in the fossil coral samples. The often complex diagenetic textures record a history of early marine diagenesis followed by burial and hydrocarbon charging before uplift into the present day vadose meteoric environment

- Light and scanning electron microscopy are essential for distinguishing aragonite cements that cannot be detected by XRD analysis

- Cement distribution is heterogeneous. Zones of excellent preservation are observed juxtaposed against altered regions

# CHAPTER 5

## THE EFFECT OF CEMENTS ON ELEMENT/Ca RATIOS IN FOSSIL CORALS: IMPLICATIONS FOR PALAEO-SST RECONSTRUCTIONS

## 5.1 GENERAL INTRODUCTION

Chapter 5 presents the results of high-spatial resolution depth-profile LA-ICPMS analyses of Sr/Ca, Mg/Ca, Ba/Ca, B/Ca and U/Ca in pristine skeletal aragonite, aragonite and calcite cements and hydrocarbon crusts in fossil *S. conferta* (NHMUK AZ 4874, 4875) and *M. limbata* (NHMUK AZ 4876, 4877, and 4878) and compares the results with those for pristine skeletal aragonite in a sample of the modern coral *S. radians* (NHMUK AZ 4879). The behaviour and chemistry of the proxy elements are discussed and estimates of the effect of 1% cement contamination on palaeo- sea-surface temperature reconstructions based on Sr/Ca, Mg/Ca, Ba/Ca, B/Ca and U/Ca proxies are presented and compared with the published literature. The sampling sites for each of the coral specimens are shown in Appendix 3 and the laser ablation depth profile methodology is described in Chapter 3 (Sections 3.5.1–3.5.3). Information in this chapter is based on Griffiths et al. (2013).

The aragonite skeletons of scleractinian corals are important geochemical archives for the reconstruction of palaeo-climates and environments. Sr/Ca, Mg/Ca, B/Ca and U/Ca ratios have been utilised as proxies for sea surface temperature (SST) (e.g. Corrège, 2006; Swart et al., 2002; Sinclair et al., 1998; Mitsuguchi et al., 1996; Min et al., 1995; Smith et al., 2006). Ba/Ca ratios have been used to examine soil erosion, flood events and upwelling (Fleitmann et al., 2007; McCulloch et al., 2003; Sinclair and McCulloch, 2004; Tudhope et al., 1996; Ourbak et al., 2006; Montaggioni et al., 2006).

However, the aragonite in coral skeletons is metastable and susceptible to diagenetic alteration. Although skeletal diagenesis and alteration fabrics have been studied for over thirty years ( e.g. James, 1974 ; Hubbard and Swart, 1982; Bar-Matthews et al., 1993; McGregor and Gagan, 2003; McGregor and Abram, 2008; Nothdurft et al., 2007; Nothdurft and Webb, 2009), it is only over the last decade that researchers have turned their attention to examining the effects of diagenesis on geochemical proxies used for palaeoclimate reconstructions (e.g. Enmar et al., 2000; Müller et al., 2001; McGregor and Gagan., 2003, Lazar et al., 2004; Quinn and Taylor, 2006;

Allison et al., 2007; Hendy et al., 2007; Nothdurft et al., 2009, Hathorne et al., 2011). It is clear from these studies that diagenetic alteration can be the source of significant error in palaeo-SST reconstructions. For example, Hendy et al. (2007) reported cool temperature anomalies in modern *Porites* affected by skeletal dissolution and secondary aragonite cementation. Calcite cements have even more dramatic effects on palaeo-SST reconstructions producing significant warm temperature anomalies (Allison et al., 2007).

The aims of this chapter are to:

1. Compare elemental ratios in primary skeletal aragonite with those in aragonite and calcite cements using high-spatial resolution depth-profile LA-ICPMS analyses

2. Quantify the effect of 1% contamination with diagenetic cements on element/Ca proxies used for palaeoenvironmental reconstructions.

## 5.2 GEOCHEMICAL COMPOSITION OF PRIMARY CORAL ARAGONITE AND CEMENTS

The trace element/Ca ratios for primary skeletal aragonite, cements and hydrocarbon-crusted surfaces are presented in Table 5.1. Estimates of the temperature anomalies produced by inclusion of 1% secondary aragonite or calcite cements in geochemical analyses of primary skeletal aragonite are shown in Table 5.2 and Figure 5.1.

### 5.3 Sr/Ca

Primary skeletal aragonite shows comparatively little variation in Sr/Ca in both modern and fossil corals with values ranging from 8.5 – 8.7 mmol $mol^{-1}$ (Table 5.1 and Figure 5.2). However the Sr/Ca ratios recorded for cemented regions differ significantly from those of the primary aragonite. Aragonite cements are characterised by high Sr/Ca ratios (10.8 – 13.5 mmol $mol^{-1}$) compared to primary skeletal aragonite whereas calcite cements are

significantly depleted in Sr/Ca (0.4 mmol $mol^{-1}$). The presence of hydrocarbon crusts produces a small increase Sr/Ca values (9.0 – 9.7 mmol mol-1) compared with primary aragonite although these values may also include a contribution from cryptic aragonite cement underlying the hydrocarbon crusts.

**Table 5.1** Composition of skeletal aragonite and diagenetic cements in modern and Miocene corals determined by LA-ICPMS

| Coral samples | Sr/Ca (mmol/mol) | Mg/Ca (mmol/mol) | Ba/Ca (µmol/mol) | B/Ca (µmol/mol) | U/Ca (µmol/mol) |
|---|---|---|---|---|---|
| Primary aragonite (Errors are reported as 1 SD) | | | | | |
| NHMUK AZ 4879 | 8.72 ± 0.26 | 2.10 ± 0.36 | 4.87 ± 0.39 | 284.65 ± 4.26 | 1.81 ± 0.27 |
| NHMUK AZ 4874 | 8.59 ± 0.22 | 3.05 ± 0.33 | 14.99 ± 3.68 | 476.69 ± 15.06 | 0.36 ± 0.08 |
| NHMUK AZ 4875 | 8.62 ± 0.14 | 2.82 ± 0.24 | 11.37 ± 3.52 | 327.01 ± 9.20 | 0.40 ± 0.04 |
| NHMUK AZ 4876 | 8.49 ± 0.11 | 3.36 ± 0.17 | 7.63 ± 0.45 | 643.71 ± 3.80 | 0.35 ± 0.08 |
| NHMUK AZ 4878 | 8.68 ± 0.28 | 3.17 ± 0.52 | 9.25 ± 2.05 | 587.10 ± 38.94 | 0.54 ± 0.20 |
| Bladed aragonite cement | | | | | |
| NHMUK AZ 4874 | 13.53 ± 0.94 | 0.98 ± 0.35 | 83.62 ± 4.25 | 116.49 ± 15.91 | 1.08 ± 0.11 |
| NHMUK AZ 4876 | 10.75 ± 0.46 | 0.37 ± 0.07 | 13.00 ± 2.44 | 119.80 ± 32.61 | 0.81 ± 0.19 |
| Hydrocarbon coated aragonite | | | | | |
| NHMUK AZ 4875 | 9.07 ± 0.30 | 2.28 ± 0.29 | 21.39 ± 3.37 | 322.42 ± 09.05 | 0.56 ± 0.08 |
| NHMUK AZ 4876 | 9.72 ± 0.24 | 1.73 ± 0.23 | 17.50 ± 3.07 | 477.84 ± 17.60 | 1.24 ± 0.14 |
| Calcite cement | | | | | |
| NHMUK AZ 4877 | 0.41 ± 0.03 | 47.65 ± 2.46 | 1.55 ± 0.23 | 51.56 ± 2.28 | 1.02 ± 0.31 |

**Table 5.1** Composition of skeletal aragonite and diagenetic cements in modern and Miocene corals determined by LA-ICPMS

| Coral samples | Sr/Ca (mmol/mol) | Mg/Ca (mmol/mol) | Ba/Ca (µmol/mol) | B/Ca (µmol/mol) | U/Ca (µmol/mol) |
|---|---|---|---|---|---|
| Blocky aragonite cement | | | | | |
| NHMUK AZ 4874 | 13.26 ± 0.96 | 0.12 ± 0.05 | 27.97 ± 6.64 | 35.82 ± 10.51 | 0.11 ± 0.03 |
| NHMUK AZ 4875 | 12.65 ± 0.56 | 0.10 ± 0.04 | 21.13 ± 3.21 | 54.09 ± 2.34 | 0.03 ± 0.01 |
| NHMUK AZ 4876 | 13.16 ± 0.98 | 0.11 ± 0.07 | 10.06 ± 1.75 | 31.15 ± 2.83 | 0.89 ± 0.27 |
| NHMUK AZ 4878 | 12.73 ± 2.53 | 0.12 ± 0.04 | 8.98 ± 4.21 | 21.72 ± 4.75 | 0.07 ± 0.07 |

| Coral samples | Sr/Ca (mmol/mol) | Mg/Ca (mmol/mol) | Ba/Ca (µmol/mol) | B/Ca (µmol/mol) | U/Ca (µmol/mol) |
|---|---|---|---|---|---|
| Primary aragonite mean values used for temperature anomaly calculations | | | | | |
| NHMUK AZ 4874 | 8.59 | 3.05 | ------ | 476.69 | 0.36 |
| NHMUK AZ 4875 | 8.62 | 2.82 | ------ | 327.01 | 0.40 |
| NHMUK AZ 4876 | 8.49 | 3.36 | ------ | 643.71 | 0.35 |
| NHMUK AZ 4877 | 8.59 | 3.27 | ------ | 615.41 | 0.45 |
| NHMUK AZ 4878 | 8.68 | 3.17 | ------ | 587.10 | 0.54 |

**Table 5.2** Estimates of proxy temperature anomalies with the inclusion of 1% aragonite or calcite cement contamination

| Coral samples | Sr/Ca ($^{o}$C) | Mg/Ca ($^{o}$C) | Ba/Ca ($^{o}$C) | B/Ca ($^{o}$C) | U/Ca ($^{o}$C) |
|---|---|---|---|---|---|
| Bladed aragonite cement | | | | | |
| NHMUK AZ 4874 | -1.26 | -0.13 | ------ | 0.17 | -0.15 |
| NHMUK AZ 4876 | -0.48 | -0.18 | ------ | 0.25 | -0.10 |
| Hydrocarbon coated aragonite | | | | | |
| NHMUK AZ 4875 | -0.11 | -0.00 | ------ | 0.00 | 0.00 |
| NHMUK AZ 4876 | -0.26 | -0.10 | ------ | 0.00 | -0.20 |
| Calcite cement | | | | | |
| NHMUK AZ 4877 | 1.73 | 2.97 | ------ | 0.27 | -0.12 |
| Blocky aragonite cement | | | | | |
| NHMUK AZ 4874 | -1.20 | -0.18 | ------ | 0.21 | 0.00 |
| NHMUK AZ 4875 | -1.03 | -0.17 | ------ | 0.13 | 0.00 |
| NHMUK AZ 4876 | -0.99 | -0.20 | ------ | 0.20 | -0.12 |
| NHMUK AZ 4878 | -0.86 | -0.19 | ------ | 0.27 | -0.10 |

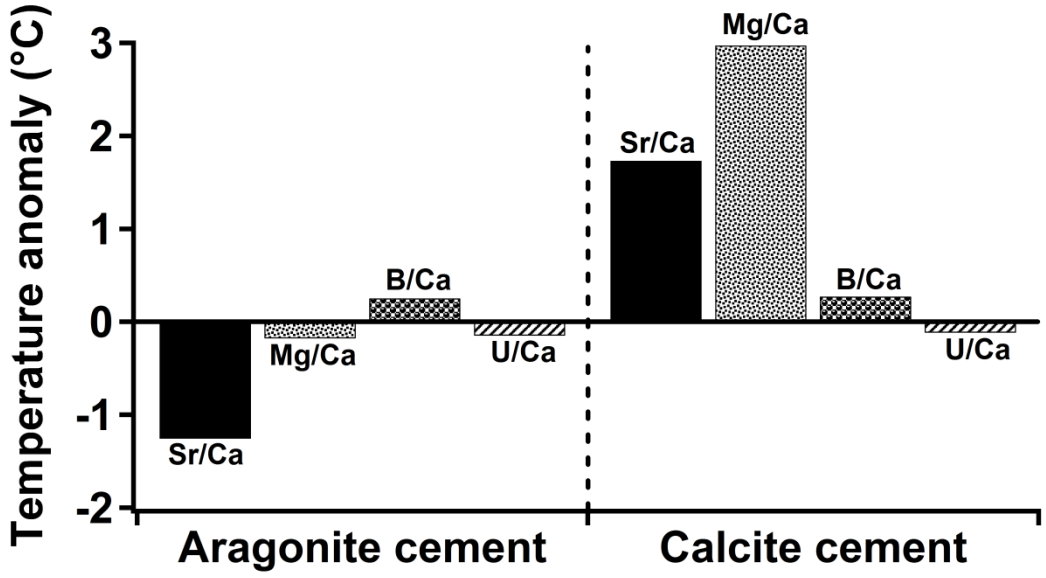


**Figure 5.1** Estimated proxy temperature anomalies resulting from the inclusion of 1% aragonite or calcite cement in geochemical analyses.

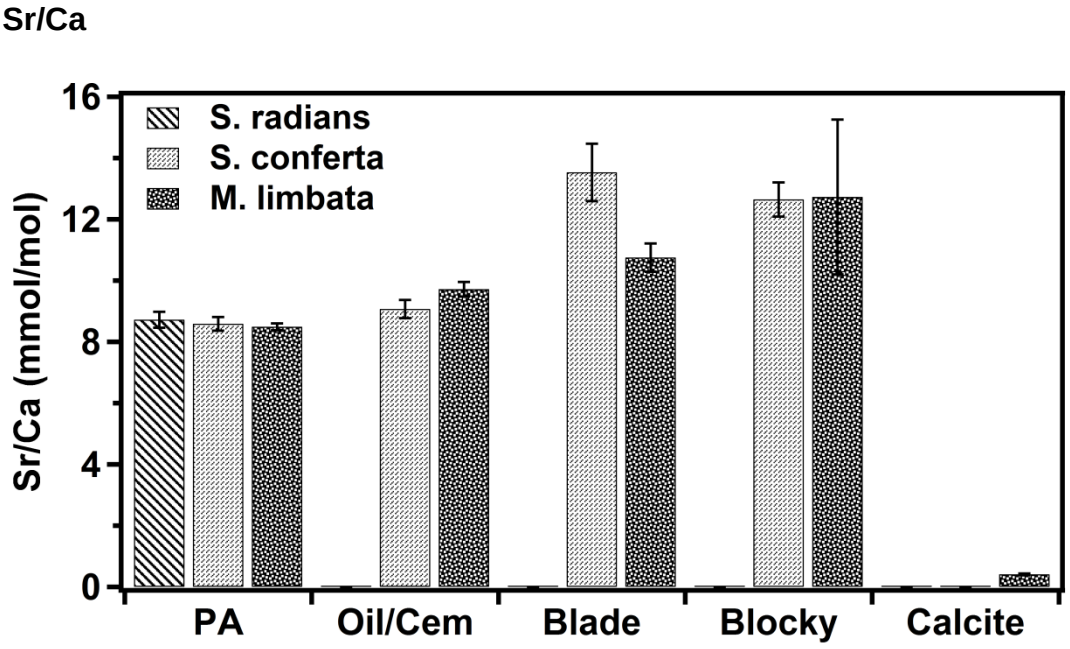


**Figure 5.2** Graph showing Sr/Ca ratios for primary aragonite, hydrocarbon crusts and diagenetic cements.

### 5.3.1 Sr/Ca ratios in skeletal aragonite and diagenetic cements

The Sr/Ca ratios recorded for primary skeletal aragonite in this study are higher than those reported by Sinclair et al. (1998) for modern *Porites mayeri* (7.90 – 8.41 mmol $mol^{-1}$) from the Great Barrier Reef (GBR) but lower than those reported by Hendy et al. (2007) for modern GBR *Porites* (8.9 – 9.05 mmol $mol^{-1}$) and Allison et al. (2007) for Pleistocene fossil *Porites* from the Hawaiian Islands (8.95 – 9.47 mmol $mol^{-1}$). However, considering both the different species and geological times represented in conjunction with the SST-dependence of Sr/Ca in coral aragonite, the data for Sr/Ca in primary skeletal aragonite overall compare well with the literature.

The Sr/Ca ratios reported here for bladed aragonite cement are in good agreement with those reported by Allison et al. (2007) however those for blocky aragonite cements are ~10% higher. The results for Sr/Ca in calcite cements (0.41mmol/$mol^{-1}$) are also significantly lower than those reported by Allison et al. (2007). These differences are attributed to a combination of secular changes in Sr/Ca in seawater since the Miocene (Lear et al., 2003), variations in local seawater chemistry (e.g. de Deckker, 2004), pore-water chemistry, temporal environmental changes (e.g. de Villiers et al., 1994) and differences between bulk analytical techniques such as TIMS and high-resolution LA-ICPMS and SIMS analyses.

The Sr/Ca signatures of aragonite and calcite cements are controlled by differences in crystal lattice organisation and the partition coefficients of Sr. Aragonite has an orthorhombic crystal habit with large lattice spaces that favour the inclusion of elements with ionic radii greater than Ca (0.99 Å) such as Sr, Ba and U (Veizer, 1983; Swart, 2009). Carbonate Sr/Ca ratios depend principally on the partition coefficient for Sr ($K_{Sr}$) and the Sr/Ca and pH of the pore fluid from which the cements precipitated (Veizer, 1983; Allison et al., 2007). $K_{Sr/Ca}$ values for inorganic aragonite range from 1.24 at 15$^{o}$C - 1.089 at 35$^{o}$C (Gaetani and Cohen, 2006) favouring the incorporation of $Sr^{2+}$ either by direct substitution for $Ca^{2+}$, insertion into interstitial spaces between lattice planes or loci created by lattice defects (Veizer, 1983). Calcite possesses a hexagonal scalenohedral crystal habit with a crystal lattice that favours the inclusion of

trace elements with ionic radii smaller than that of Ca such as Mg, Mn and Cd (Swart, 2009). Calcite cements therefore discriminate against trace elements with ionic radii greater than $Ca^{2+}$ (Swart, 2009) resulting in lower Sr/Ca ratios. Inorganic calcite $K_{Sr}$ values reported in the literature range from 0.021 - 0.13 (Tesoriero and Pankow, 1996; Veizer, 1983).

### 5.3.2 Diagenetic cements and estimated Sr/Ca temperature anomalies

Using the equations of Maupin et al. (2008) for *Siderastrea* (Sr/Ca [mmol $mol^{-1}$] = 10.008 - 0.039 * [SST]$^{o}$C) and Swart et al. (2002) for *Montastraea* (Sr/Ca [mmol $mol^{-1}$] = 10.165 - 0.0471 * [SST]$^{o}$C) estimates for 1% bladed or blocky aragonite cement contamination produce cool temperature anomalies ranging from 1.0 to 1.2$^{o}$C in fossil *Siderastrea*. Incorporation of similar percentages of bladed aragonite cement in *Montastraea* lowers SSTs by 0.5$^{o}$C while contamination with blocky aragonite lowers SSTs by 1.2$^{o}$C. Contamination of skeletal aragonite with 1% calcite increases SSTs by 1.7$^{o}$C in *Montastraea* (Table 5.2 and Figure 5.1). Incorporation of secondary aragonite in analyses of skeletal aragonite produces cool SST anomalies ranging from 0.2$^{o}$C for 1% contamination up to 10$^{o}$C for severely altered corals (Allison et al., 2007; Quinn and Taylor, 2006). The results reported here for diagenetic cements found in Miocene corals show good agreement with those reported by Hendy et al., (2007) and Allison et al., (2007).

Hydrocarbon crusts do not appear to affect temperature reconstructions unless they form a veneer over fringes of cement (e.g. NHMUK AZ 4876). The inclusion of calcite cements in geochemical analyses produce significant warm SST anomalies (McGregor and Gagan, 2002; Allison et al., 2007). The estimated warm temperature anomaly reported here is higher than the 1.0 – 1.5$^{o}$C warm temperature anomalies reported in the literature (Allison et al., 2007; McGregor and Gagan, 2002) due to the very low Sr/Ca ratio found in the calcite cement infilling the Miocene *Montastraea.*

### 5.4 Mg/Ca

Mg/Ca ratios in primary aragonite range from 2.1 - 3.4 mmol $mol^{-1}$ (Table 5.1 and Figure 5.3) whereas in the aragonite cements Mg/Ca ratios are depleted (0.1 - 0.9 mmol $mol^{-1}$) compared to primary skeletal aragonite. Amongst the different aragonite cements, blocky aragonite cements show greater Mg/Ca depletion than other aragonite cement morphologies. The calcite cements in fossil *Montastraea* are characterised by greatly elevated Mg/Ca ratios (47.6 mmol $mol^{-1}$) consistent with the presence of high magnesium calcite (Swart, 2009).

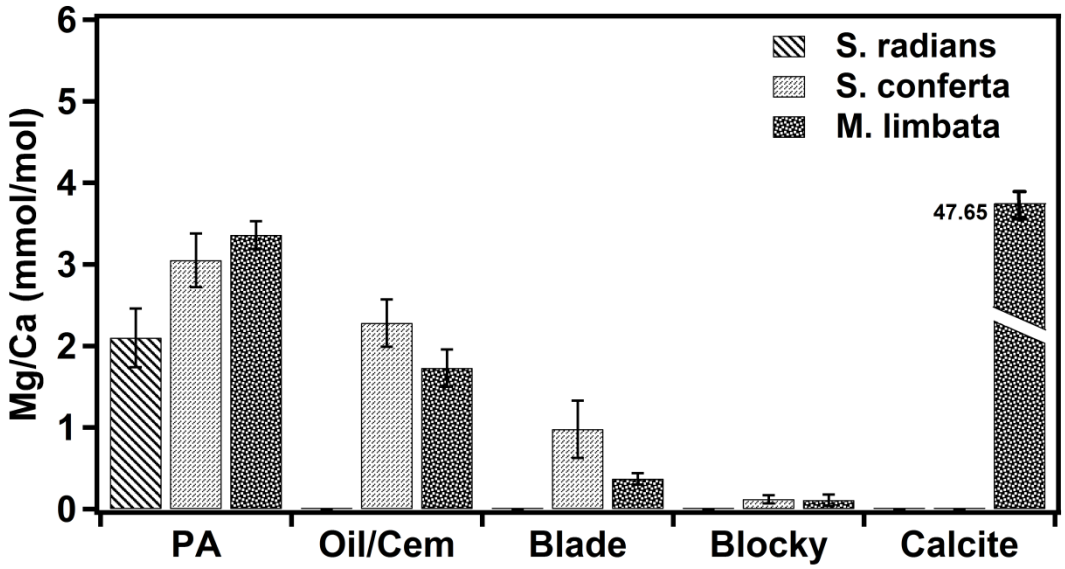


**Figure 5.3** Graph showing Mg/Ca ratios for primary aragonite, hydrocarbon crusts and diagenetic cements.

#### 5.4.1 Mg/Ca ratios in skeletal aragonite and diagenetic cements

The Mg/Ca values recorded in this study for modern and Miocene primary coral aragonite show good agreement with the values reported by Allison et al. (2007) but are lower than those documented by Hendy et al., (2007) and Sinclair et al., (1998) (3.8 - 4.8 mmol $mol^{-1}$ and 3.0 - 4.5 mmol $mol^{-1}$ respectively). These differences reflect a combination of temporal changes in $Mg/Ca_{seawater}$ over the last 25 million years (Dickson, 2002; Lowenstein et al. 2001; Stanley and Hardie, 1998), variations in environmental conditions and

poorly constrained Mg values in the NIST612 glass standard that introduce a bias of ~20% in Mg/Ca. However, the data for Mg/Ca ratios in aragonite and high magnesium calcite cements show reasonable agreement with those reported by Allison et al. (2007).

### 5.4.2 Diagenetic cements and estimated Mg/Ca temperature anomalies

Using the calibration Mg/Ca calibration equation of Sinclair et al., (1998) for *Porites* (Mg/Ca [mmol $mol^{-1}$] = 0.0 + 0.16 * [SST]$^{o}$C) in the absence of a genus specific equation, it is estimated that the incorporation of 1% aragonite cement would produce cool temperature anomalies of 0.2$^{o}$C. Contamination of primary skeletal aragonite with a similar percentage of calcite increased SST estimates by 2.7$^{o}$ C (Figure 5.1). Hydrocarbon crusts do not have a noticeable effect on Mg palaeo-temperature reconstructions. Hendy et al. (2007) reported a ~2$^{o}$C decrease in SST in Mg/Ca-based SST reconstructions while Allison et al. (2007) reported a ~0.2$^{o}$C decrease in palaeo-temperature with the inclusion of 1% aragonite cement.

Although Mg has been used for palaeo-SST reconstruction (Mitsuguchi et al., 1996; Sinclair et al., 1998) more recent work on the stability of Mg in coral aragonite suggests Mg/Ca may not be very reliable due to the complexity of Mg chemistry in carbonates (Finch and Allison, 2007).

Mg concentrations show considerable variation in biogenic carbonates such as the aragonite skeletons of corals (Meibom et al., 2008; Allison and Finch, 2007). The incorporation of Mg into aragonite and calcite involves complex structural changes in the crystal lattice and the presence of nano-domains of differing chemical composition. X-ray absorption fine structure (XAFS), extended X-ray absorption fine structure (EXAFS) and K-edge X-ray absorption near-edge structure (XANES) data show Mg substitution into aragonite is accomplished by 9-fold coordination and short bond lengths implying either significant distortion of the crystal lattice or the accommodation of Mg in nano-domains of an unknown phase (Finch and Allison, 2007). EXAFS data show that simple substitution of Mg into calcite is possible when accompanied by a high degree of structural relaxation. However variable XANES suggests Mg

exists in different competing coordination states and is present in Mg-rich nano-domains of dolomite or hunterite within the calcite (Finch and Allison, 2007). Partition coefficient data also attest to the difficulty of accommodating Mg in the lattices of aragonite and calcite with values quoted in the literature ranging from 0.005 - 0.0006 and 0.06 - 0.013 respectively (Veizer, 1983). Cohen and Gaetani (2010) report a partition coefficient of ~0.001 for Mg/Ca in coral aragonite although this decreases to ~0.0004 at slower crystal growth rates.

### 5.5 Ba/Ca

Ba/Ca ratios show considerable variation in both the primary skeletal aragonite of modern and fossil corals and in the cements (Table 5.1 and Figure 5.4). Ba/Ca values are considerably higher in the skeletal aragonite of fossil *Siderastrea* (11.3 - 14.9 μmol $mol^{-1}$) compared to those observed in modern *Siderastrea* and fossil *Montastraea* (4.8 – 9.3 μmol $mol^{-1}$). The differences observed in the skeletal coral aragonite Ba/Ca ratios may represent sampling bias introduced by the selection of restricted areas of the coral for analysis. Secondary aragonite cements are characterised by significantly higher Ba/Ca ratios than those encountered in the primary aragonite of the same coral samples with the exception of the blocky aragonite cement in *Montastraea* (NHMUK AZ 4878). Exceptionally high Ba/Ca values (~6 times primary aragonite) are encountered in the bladed aragonite cements encrusting fossil *Siderastrea* (NHMUK AZ 4874). The opposite trend is shown by calcite cements which are characterised by low (~1.5 μmol $mol^{-1}$) Ba/Ca ratios.

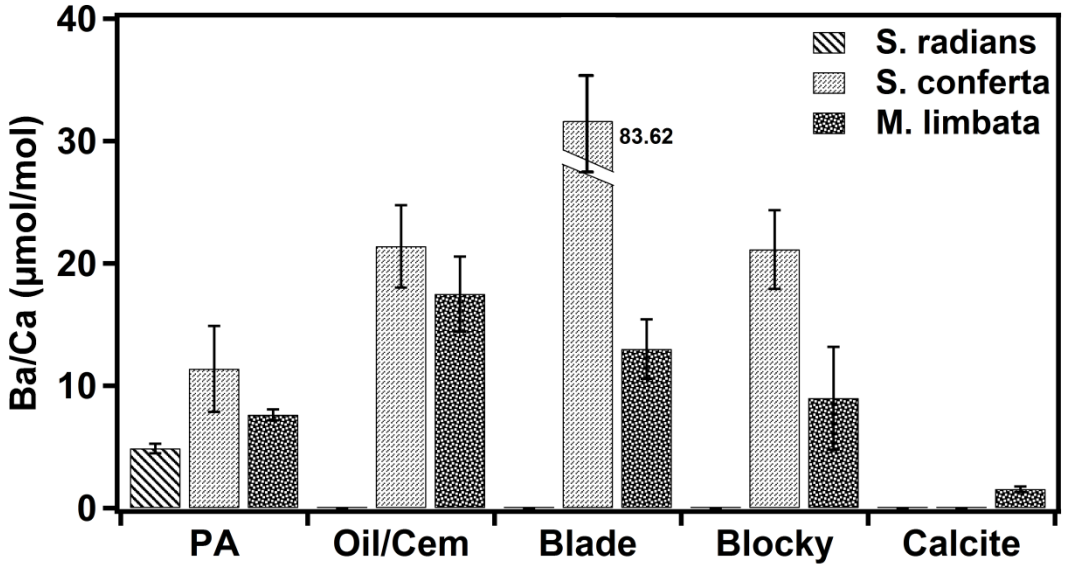


**Figure 5.4** Graph showing Ba/Ca ratios for primary aragonite, hydrocarbon crusts and diagenetic cements.

### 5.5.1 Ba/Ca ratios in skeletal aragonite and diagenetic cements

The Ba/Ca results for Miocene coral skeletal aragonite are higher than those reported by Allison et al. (2007) and Montaggioni et al. (2006) but show better agreement with the range of Ba/Ca ratios documented by Sinclair (2005). This is to be expected based on the oceanic location of the Hawaiian Islands (Allison et al., 2005) and New Caledonia (Montaggioni et al., 2006) versus the river plume-influenced inner coastal GBR (Sinclair et al., 2005) and the Miocene Paraguaná sampling site (Diaz de Gamero, 1996). Barium concentrations in coral aragonite are influenced by fluvial run-off and seasonal up-welling of cool, nutrient-rich water (exogenous abiotic factors), the growth and decay of phytoplankton blooms (exogenous biotic factors), and physiological processes within the corals themselves (endogenous biotic factors) (Sinclair, 2005). It is likely that all of these processes may have contributed to the high Ba/Ca values recorded in the Miocene corals as well as temporal changes, variation in local seawater chemistry and evidence for high terrigenous input in the shallow marine environment in which the Miocene corals grew.

Ba/Ca ratios are 2 – 20 times higher in the aragonite cements investigated in this study than those reported by Allison et al. (2007) although there is good agreement for calcite cements. Higher Ba/Ca ratios in aragonite cements are expected because the partition coefficients favour the inclusion of Ba in secondary aragonite but exclude Ba from calcite cement. The partition coefficient ($K_{Ba/Ca}$) for barium in inorganic aragonite varies from 2.99 - 1.64 depending on the temperature (15$^{o}$ C – 35$^{o}$ C) and the rate of crystal growth (Cohen and Gaetani, 2010) whereas in calcite the $K_{Ba}$ lies within the range 0.1 - 0.4 (Veizer, 1983) and is even lower (0.06 at 25$^{o}$ C) in corals that have undergone aragonite to calcite transformation (Pingitore and Eastman, 1985).

The data reported here suggest the inclusion of cements in coral analyses may significantly affect Ba/Ca ratios and overprint important palaeo-environmental signals.

**5.6 B/Ca**

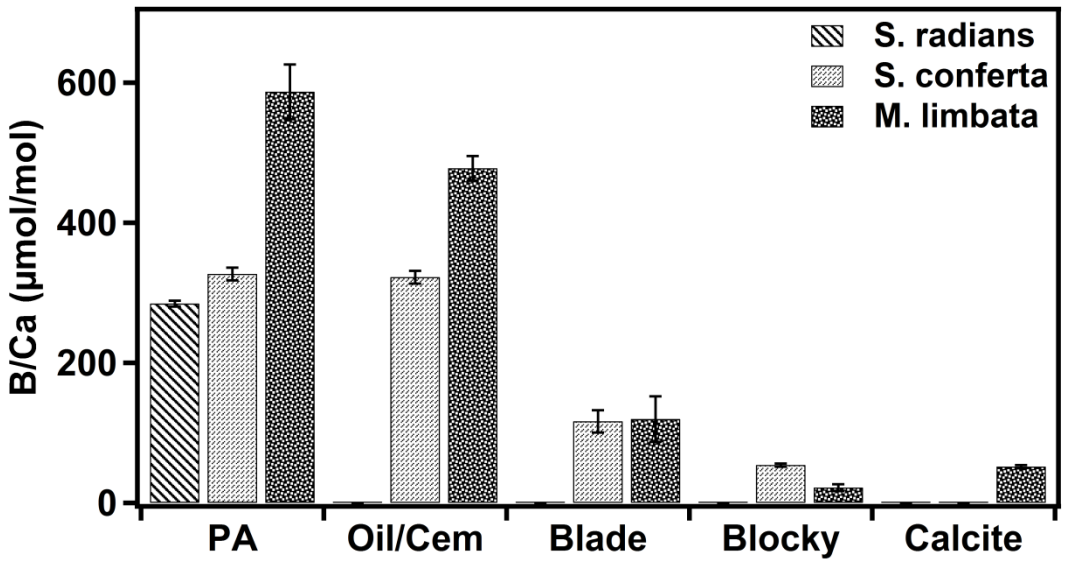


**Figure 5.5** Graph showing B/Ca ratios for primary aragonite, hydrocarbon crusts and diagenetic cements.

Primary skeletal aragonite B/Ca ratios vary considerably ranging from 284 – 643 μmol $mol^{-1}$ with the lowest values encountered in the modern *Siderastrea* and the highest in the Miocene *Montastraea* (Table 5.1 and Figure 5.5). Intermediate values (327 – 476 μmol $mol^{-1}$) are recorded in the Miocene *Siderastrea.* These differences may reflect the combined effects of intra- and inter- specific variation. B/Ca ratios are much lower in both aragonite and calcite cements, ranging from 116 – 119 μmol $mol^{-1}$ in bladed aragonite cements while those for blocky aragonite and calcite cements range between 21 – 54 μmol $mol^{-1}$. Hydrocarbon crusts record similar to the B/Ca values to those of primary skeletal aragonite.

### 5.6.1 B/Ca ratios in skeletal aragonite and diagenetic cements

The B/Ca ratios reported here for both the primary skeletal aragonite and the diagenetic cements are lower and show much greater variation than those reported by Allison et al. (2007) with the exception of skeletal aragonite in *Montastraea*.

Boron is a difficult element to measure accurately due to a lack of data for matrix-matched standards. In addition, the chemistry of boron in seawater and calcifying fluids is complex and largely controlled by the *p*H of the system. Aqueous boron exists primarily as two species; trigonally co-ordinated boric acid ($B[OH]_3$) and tetrahedrally co-ordinated borate ($B[OH]_4^-$) related by the following equilibrium equation that illustrates the importance of *p*H and speciation $B(OH)_3 + H_2O = H^+ + B(OH)_4^-$ (Pagani et al., 2005a).

Experiments investigating the behaviour and partitioning of boron in synthetic carbonates show boron uptake in aragonite>HMC>calcite when grown under identical conditions and that as boron concentration in the precipitating fluids increases, the amount of boron in the aragonite and calcite increases but the partition coefficient decreases (Hemming et al., 1995). In addition the concentration of B in inorganic calcite falls with decreasing *p*H (Sanyal et al., 2000) possibly as a result of a change in the relative proportions of boric acid and borate (Hobbs and Reardon, 1999; Hemming and Hanson, 1992). Allison

et al. (2007) attributed the decrease in B/Ca in diagenetic cements to a reduction in the *p*H of the precipitating pore fluids compared to that of seawater.

### 5.6.2 Diagenetic cements and estimated B/Ca temperature anomalies

Using the calibration equation of Sinclair et al., (1998) derived for *Porites* (B/Ca [µmol mol-1] = 1000 - 20.6 * [SST] $^{o}$C) in the absence of a species-specific equation, positive temperature anomalies of 0.1 to 0.3$^{o}$ C are estimated with the inclusion of 1% aragonite cement. Similar percentage contamination by calcite cement produces a positive temperature anomaly of 0.3 $^{o}$C (Fig. 12). The estimates recorded here show good agreement with those of Allison et al., (2007).

Boron is a potentially very useful because it has been suggested that it may vary not only with temperature but also with salinity and alkalinity because it is incorporated into aragonite as a complex anion (Gaillardet and Allègre, 1995) although Sinclair et al. (1998) were unable to confirm variations in boron with changes recorded in seawater salinity due to high seasonal rainfall patterns.

### 5.7. U/Ca

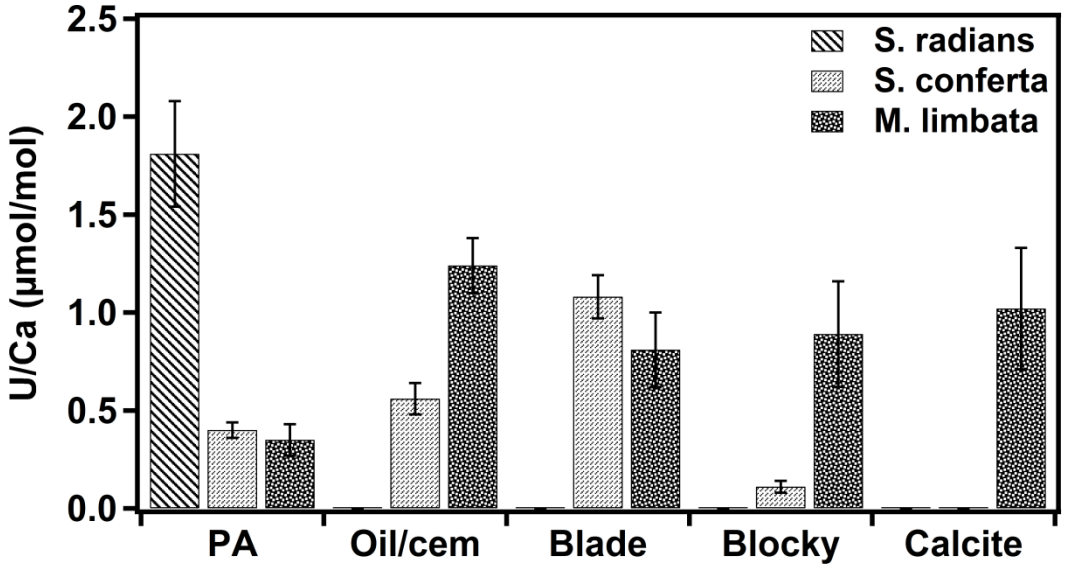


**Figure 5.6** Graph showing U/Ca ratios for primary aragonite, hydrocarbon crusts and diagenetic cements.

Skeletal aragonite U/Ca ratios are considerably higher in the modern *Siderastrea* than in the Miocene specimens (0.35 - 0.54 μmol $mol^{-1}$). However U/Ca ratios vary considerably in the diagenetic cements ranging from 0.03 – 1.24 μmol $mol^{-1}$ with no clear pattern of change evident in the concentration of uranium in either aragonite or calcite (Table 5.1 and Figure 5.6).

### 5.7.1 U/Ca ratios in skeletal aragonite and diagenetic cements

The U/Ca values recorded in this study for primary skeletal aragonite are 3 to 4 times lower than those reported by Allison et al. (2007). However U/Ca in the primary aragonite of the modern *Siderastrea* shows better agreement with their published data. Our data for aragonite cements show no obvious trend in variation although reports in the literature document enrichment of U/Ca in aragonite cements compared to primary skeletal aragonite (Lazar et al., 2004; Allison et al., 2007). Partition coefficients published by Lazar et al. (2004) show U/Ca is preferentially incorporated in aragonite cements compared to primary skeletal aragonite ($K_{U/Ca}$ = 2.4 and ~1 respectively) therefore the very low U/Ca ratios observed in the blocky aragonite cements in some of the Miocene coral samples are somewhat anomalous although changes in *p*H and/or crystal growth rates may have played a role as both these factors affect the partitioning of U in aragonite (Meece and Benninger, 1993).

Experimental results show low (<0.2) partition coefficients for U in calcite (Meece and Benninger, 1993) therefore low U/Ca ratios are to be expected. However our data show ~2x higher U/Ca ratio in calcite than in primary aragonite. Allison et al. (2007) hypothesized that precipitation under reducing conditions in the coral pore-space may explain the apparent enrichment of U in calcite cements.

### 5.7.2 Diagenetic cements and estimated U/Ca temperature anomalies

Lazar et al. (2004) estimated that a 5% decrease in skeletal porosity due to the precipitation of secondary aragonite would decrease the calculated palaeo-temperature by ~1$^{o}$ C. Negative temperature anomalies of 0.1 to 0.3$^{o}$ C are estimated in this study with the inclusion of 1% aragonite or calcite cements

(Fig. 12) using the calibration equation of Sinclair et al., (1998) derived for *Porites* (U/Ca [µmol mol-1] = 2.24 – 0.046 * [SST]$^{o}$ C). These estimated temperature anomalies show good agreement with those of Allison et al. (2007) for aragonite cements.

Uranium is believed to be incorporated into aragonite as a complex anion like boron and may vary not only with temperature but also salinity (Shen and Dunbar, 1995) although Sinclair et al. (1998) were unable to confirm the relationship with salinity. Corrège (2006) reported a 5-fold increase in sensitivity to SST for U/Ca compared to Sr/Ca although it is acknowledged that other factors such as the complex chemistry of U in seawater and the mechanism of its incorporation into coral aragonite may also influence U/Ca values (Min et al., 1995; Shen and Dunbar, 1995).

## 5.8 CONCLUSIONS

- Primary skeletal aragonite with unaltered geochemical signatures is preserved in the modern and fossil coral samples

- Diagenetic cements are present in the live-collected modern corals and the fossil coral samples examined in this thesis

- Aragonite, calcite and brucite cements are present in the modern coral samples. Aragonite (two different crystal morphologies), calcite, pyrite, dolomite and hydrocarbon residues are present in the fossil coral samples

- Aragonite cements are enriched in Sr/Ca and depleted in Mg/Ca decreasing reconstructed palaeo- sea-surface temperatures. The inclusion of 1% aragonite cement would significantly affect Sr/Ca sea-surface temperature estimates, producing cool temperature anomalies of up to -1.2$^{o}$C

- Calcite cements are highly enriched in Mg/Ca and depleted in Sr/Ca increasing reconstructed palaeo- sea-surface temperatures. The inclusion of 1% calcite cement would produce warm temperature anomalies of +1.7$^{o}$C

- Aragonite and calcite cements record significantly lower B/Ca values compared to primary aragonite. This result is important because boron shows greater sensitivity to SST than other more commonly utilised proxies such as Sr/Ca

- Aragonite cements are highly enriched in Ba/Ca which has major implications for reconstructing fluvial run-off and upwelling events

- Valid palaeo-environmental reconstructions may be possible by targeting regions of pristine skeletal preservation using LA-ICPMS or SIMS

# CHAPTER 6

## THE AGE OF THE CANTAURE FORMATION

## 6.1 GENERAL INTRODUCTION

During the late 1960's, the age of the Cantaure Formation was poorly constrained due to confusion among malacologists regarding the exact location and stratigraphy of the type section. However by the mid-1970's, this problem was being addressed. In 1974, Hunter and Bartok published a complete re-description of Cantaure Formation type section and an age of latest Early Miocene (Burdigalian/Langhian) was produced by Díaz de Gamero (1974) based on microfossil biostratigraphy. In this work, Díaz de Gamero (1974) placed the Cantaure Formation within the *Globigerinatella insueta* and *Praeorbulina glomerosa* (N7-N8) planktonic foraminiferal biozones of Blow (1969). This age was later confirmed by Rey (1996) based on calcareous nannofossil biostratigraphy placing the Cantaure Formation in the *Sphenolithus herteromorphus* and *Helicosphaera ampliaperta* (NN4-NN5) biozones of Martini (1971). The biostratigraphy is shown in Figure 6.1.

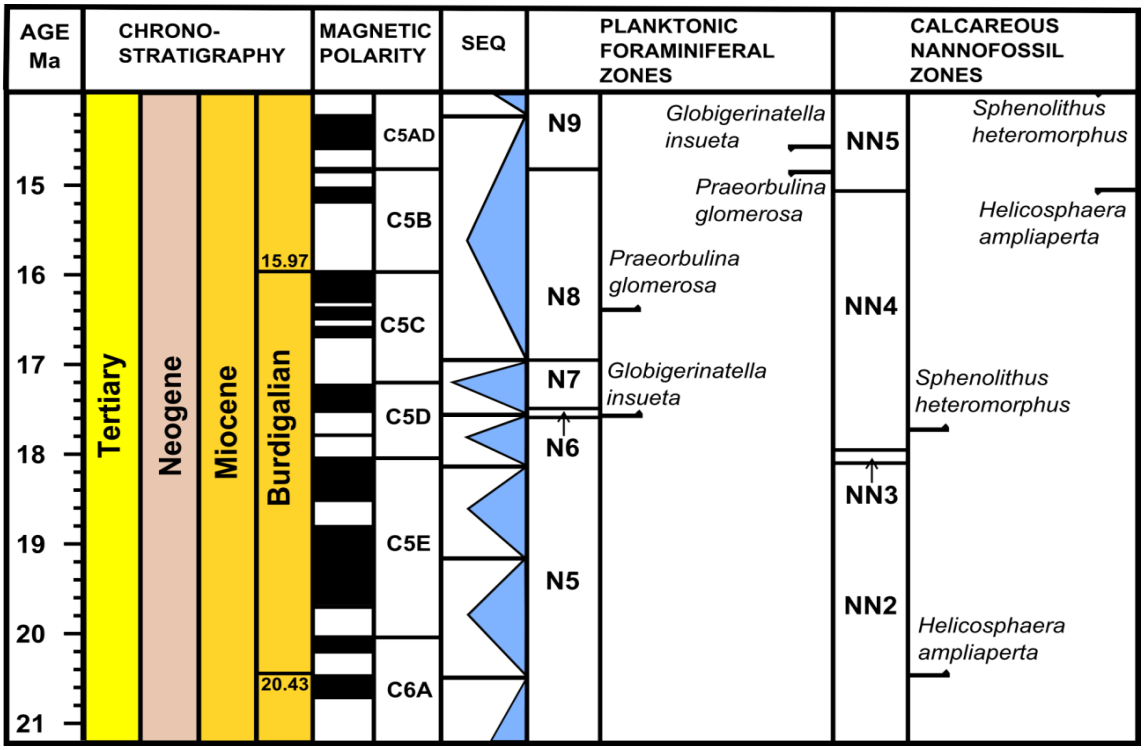

**Figure 6.1** Chronostratigraphy and biostratigraphic zonal marker species for planktonic foraminera and calcareous nannofossils. (Figure 6.1 is based on stratigraphic information presented in Gradstein et al., 2004).

### 6.2 CORAL AGE ESTIMATION

Presented here for the first time are age estimations for the Cantaure Formation based on $^{87}Sr/^{86}Sr$ isotope stratigraphy. All previous age estimations have been based solely on micropalaeontological studies (e.g. Díaz de Gamero, 1974; Rey, 1996). A full description of sample preparation and the methods used for $^{87}Sr/^{86}Sr$ isotope analysis are given in Chapter 3 (Section 3.5.4). The $^{87}Sr/^{86}Sr$ isotope data and estimated ages for the fossil corals are shown in Table 6.1. The mean age of the fossil corals lie between 16.34 and 16.60 Ma (Table 6.1 and Figure 6.2) placing them in the Burdigalian stage (20.43 – 15.97 Ma) of the Miocene epoch.

| Coral sample | $^{87}Sr/^{86}Sr$ (± 2 SD) | Estimated age (Ma) | | |
|---|---|---|---|---|
| | | > limit | Mean | < limit |
| NHMUK AZ 4874 | 0.708693 ± 10 | 16.05 | 16.44 | 16.86 |
| NHMUK AZ 4875 | 0.708699 ± 11 | 15.96 | 16.34 | 16.75 |
| NHMUK AZ 4876 | 0.708684 ± 12 | 16.20 | 16.60 | 17.02 |
| NHMUK AZ 4878 | 0.708687 ± 12 | 16.15 | 16.55 | 16.97 |

Long-term (~24 month) analyses of the NIST SRM 987 standard at RHUL gave an average $^{87}Sr/^{86}Sr$ value of 0.710258 ± 0.000017.

**Table 6.1** $^{87}Sr/^{86}Sr$ isotope data and coral age estimation

Age estimations are based on data in SIS Look-Up Table Version 4: 08/04 (McArthur, J.M. and Howarth, R.J. 2004; McArthur J.M. and Howarth, R.J., 2001). The upper and lower age limits have been calculated using the

uncertainty in the long-term external reproducibility (± 0.000017) combined with the uncertainty (95% confidence limits) computed for the mean age in Look-Up Table Version 4: 08/04.

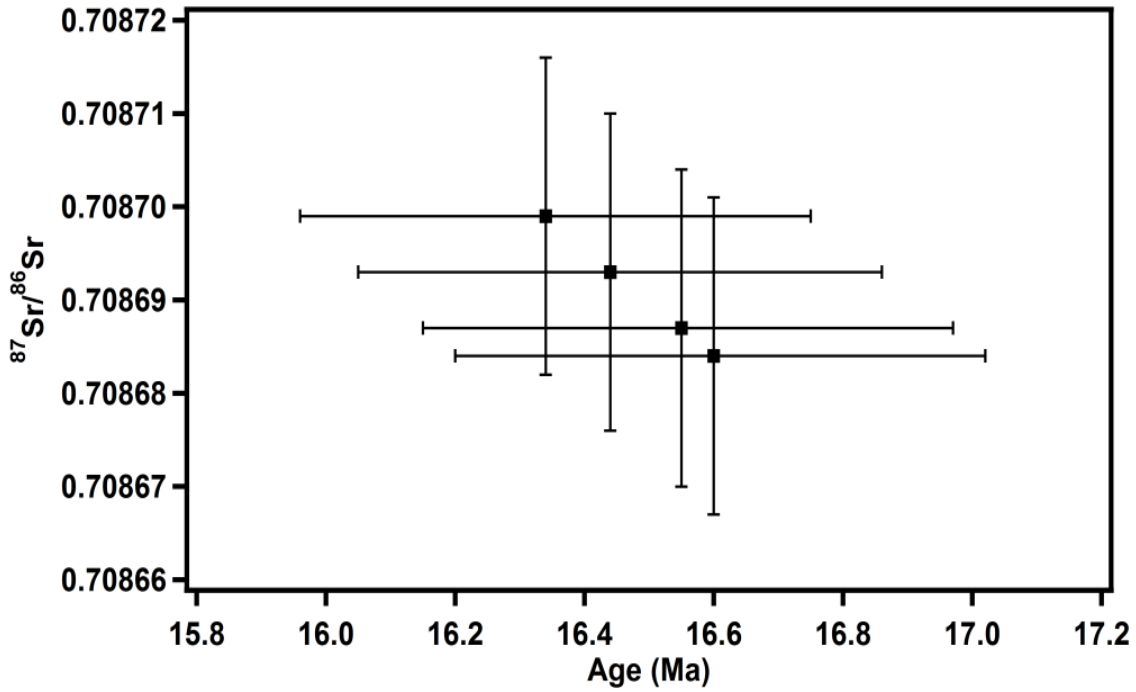


**Figure 6.2** Plot showing $^{87}Sr/^{86}Sr$ age correlations for the fossil coral samples based on information in Table 6.1. Age estimates are derived from the SIS Look-Up table V4: 08/04 (McArthur et al., 2001; McArthur and Howarth, 2004).

Strontium isotope stratigraphy is well-suited to dating corals thought to be Early Miocene in age because marine $^{87}Sr/^{86}Sr$ rapidly changes during this time period. The steep gradient of the $^{87}Sr/^{86}Sr$ isotope curve during the Early Miocene facilitates age estimation because it reduces the impact of small errors introduced by the unavoidable inclusion of skeletal impurities and during sample preparation and the mass spectrometry analysis process (McArthur et al, 2012).

The coral strontium isotope age estimations presented here provide additional confirmation of the published Burdigalian biostratigraphic age estimates for the Cantaure Formation based on the identification of the N7-N8 (*Globigerinatella insueta* and *Praeorbulina glomerosa*) planktonic foraminiferal

zones by Díaz de Gamero (1974) and the nannofossil biozones NN4-NN5 (*Helicosphaera ampliaperta* and *Sphenolithus heteromorphus*) by Rey (1996).

The strontium isotope coral age estimates presented here for the Cantaure samples are unique. This is the first time that corals of this age have been dated using $^{87}Sr/^{86}Sr$ isotope stratigraphy. Denniston et al. (2008) used uranium-lead ($^{238}U/^{206}Pb$–$^{207}Pb/^{206}Pb$) inverse linear concordia methods and $^{87}Sr/^{86}Sr$ isotope stratigraphy to date well-preserved 5.5 Ma corals from the Dominican Republic while Mertz-Kraus et al. (2009) reported strontium isotope ages of 10-9 Ma for well-preserved corals from Crete that have been extensively studied (e.g. Brachert et al., 2006; Mertz-Kraus et al., 2008). The paucity of published data on the geochemistry and isotope dating of 'deep-time' scleractinian corals reflects the difficulty of finding specimens that preserve unaltered geochemical signatures (Brachert et al., 2006).

# CHAPTER 7

SUMMARY AND CONCLUSIONS

## 7.1 SUMMARY

A suite of fossil corals comprising three species (*Siderastrea conferta, Montastraea limbata* and *Porites* sp) collected from the Early Miocene Cantaure Formation on the Paraguaná Peninsula, Falcón State, Venezuela were investigated and compared with two modern siderastreid specimens from Bermuda (*S.radians*) and Florida (*S.siderea*).

The overall aims of the study were to:-

1. Document and compare skeletal preservation and diagenetic alteration using imaging, XRD analysis and X-ray radiography.

2. Evaluate and compare element/Ca ratios in primary skeletal aragonite with those in different cements using LA-ICPMS depth profile analysis in modern and fossil corals.

3. Quantify the effect of diagenetic cements on element/Ca proxies used for palaeo-temperature and palaeo-environmental reconstructions and compare them with those reported in the literature for much younger corals.

4. Estimate the age of the fossil corals using $^{87}Sr/^{86}Sr$ isotope stratigraphy to confirm the published Early Miocene (Burdigalian) bio-stratigraphic age assigned to the Cantaure Formation.

### 7.1.1 Assessment of skeletal preservation and diagenetic alteration

Light and electron microscopy was used to make observations on modern and fossil coral in order to evaluate primary skeletal aragonite preservation, identify diagenetic cements based on crystal morphology and assess dissolution, bioerosion and the distribution of diagenetic alteration. X-ray radiography was carried out in order to visualise annual banding and to assess the gross distribution of cementation and dissolution. Quantitative estimates of aragonite and calcite modal concentrations were obtained by XRD to screen the

corals for diagenetic alteration but were shown to be inadequate because the technique is not able to distinguish secondary aragonite cement.

#### *7.1.1.1 Observations on preservation and diagenesis*

All the corals examined in this study record a history of the diagenetic environments through which they have passed. Both the modern specimens exhibit evidence of early marine diagenesis in keeping with the shallow marine environments from which they were live-collected. However the fossil corals preserve a much more complex diagenetic history that reflects the shallow marine, burial and sub-aerial terrestrial environments that they have been exposed to. The most remarkable feature of the fossil specimens is the excellent preservation of regions of unaltered primary skeletal aragonite that have retained their original geochemical signatures.

#### *7.1.1.2 Modern coral diagenesis*

Examination of the modern corals in the SEM revealed the presence of early marine diagenetic cements and evidence for bioerosion by both macro- and micro-boring organisms. The cements are composed of aragonite, high-magnesium calcite and brucite and exhibit a range of morphologies. Cement distribution is very heterogeneous with a number of factors such as skeletal architecture, skeletal porosity and the presence of endolithic organisms and organic biofilms influencing the precipitation of cements (Nothdurft and Webb, 2009; Hendy et al., 2007).

Secondary aragonite cements are the most common and consist primarily of slender acicular crystals that terminate in a sharp point. Aragonite rod cements are also observed in the modern corals. Rod cements are composed of slender, fused clusters of aragonite crystals arranged in dense crystal meshes. The rods terminate in smooth flat planar surfaces that occasionally exhibit a stepped morphology due to fracturing. Aragonite cements may be deposited as a result of biological activity by endolithic organisms resident within coralla (Nothdurft and Webb, 2009) or by other diagenetic processes such as chemical dissolution and re-precipitation of aragonite within coral colonies living in shallow marine environments such as the Great Barrier Reef (Hendy et al., 2007).

High-magnesium calcite cements (HMC) occur as splays of elongate flattened crystals that taper to triangular points. The splays usually form small clusters although pairs and single splays are also represented. HMC cements typically occur in zones affected by micro-boring and bioerosion. Nothdurft and Webb (2009) described similar HMC splay morphologies associated with microboring and bioerosion in modern Great Barrier Reef corals and there is experimental evidence suggesting organic biofilms may play a role in the precipitation of HMC splay cements (Meldrum and Hyde, 2001).

Brucite [$Mg(OH)_2$] cements occur as pillows and tufts closely associated with micro-boring and fine acicular aragonite cements although they are less common than secondary aragonite and like the other cements show a patchy distribution. The pillows form dome-shaped mounds up to 40 μm in diameter and in cross-section the mounds are seen to consist of concentric layers composed of palisades of slender crystals. The concentric layers are separated by sub-micron scale voids that may represent organic biofilms that have since disappeared. Tufts are scattered among acicular aragonite needle cements and consist of small aggregations of crystal plates. The plates have curved perimeters giving the tufts an arcuate outline. The importance of biological agents and organic biofilms in facilitating the concentration and deposition of exotic cements within the pore spaces of living corals is well-illustrated by the precipitation of brucite which is undersaturated in seawater (Nothdurft et al., 2005).

Bioerosion involving both macro- and micro-boring organisms has affected the corals. Macro-boring activity is concentrated in the older parts of the colonies with limited penetration of the younger skeletal zones. Cross-sections through some of the boreholes reveal chalky, altered skeletal fabrics produced by bioerosion and dissolution while others contain desiccated ribbons of organic material that once may have lined the borings. Extensive micro-boring activity by endolithic algae and fungi have also pitted and etched the skeletal surfaces. In some instances, micro-boring activity clearly postdates the deposition of secondary acicular and rod aragonite because the cements are pitted with micro-boreholes.

Distinctive sponge galleries are also observed in the modern corals. The galleries consist of concave scalloped depressions up to 35 μm across etched

into the skeletal surface. Acicular aragonite cements are commonly associated with the galleries and there is evidence of extensive micro-boring activity with boreholes pitting and cross-cutting the scalloped depressions. Aggregations of sponge spicules and clumps of organic material are preserved indicating the presence of living sponges within the colony when the specimens was collected.

#### *7.1.1.3 Fossil coral diagenesis*

Light and scanning electron microscope observation revealed evidence for diagenetic alteration and bioerosion in all of the fossil samples examined. Cements and hydrocarbons (oil and bituminous residues) are present in many of the pore spaces, while dissolution, macro- and micro-boring have played an important role in the diagenesis of the fossil corals. As in the modern corals, the distribution of diagenetic alteration is heterogeneous and varies considerably within the specimens resulting in zones of excellent skeletal preservation juxtaposed with less well-preserved areas.

The diagenetic cements are predominantly composed of secondary aragonite precipitated directly onto the primary aragonite of the coral skeleton although some cements appear to have been deposited on organic films that have since disappeared leaving a break between the primary and secondary aragonites. The aragonite cements exhibit a range of diagenetic textures that include slender acicular needles, small bladed forms, long, lath-like crystals that terminate in chisel-like chamfered surfaces and very large blocky crystals. Crystal size varies from 10 μm for small bladed forms up to 120 μm for large blocky crystals. The large blocky crystals typically occur in pore spaces lined with acicular aragonite needles suggesting either selective overgrowth of the original acicular cements or that they were deposited in a later diagenetic event.

Aragonite cements are a common product of early marine diagenesis in vadose and phreatic marine environments (Nothdurft and Webb, 2009; Hendy et al., 2007; Tucker and Wright, 1990; Longman, 1980) although they may also be precipitated in meteoric environments permeated by saline ground water in arid climates (Scholle and Ulmer-Scholle, 2003). Dissolution of primary skeletal material and reprecipitation as secondary aragaonite are likely to have occurred in the early diagenetic history of the fossil corals and biological agents such as

sponges, fungi and microbial endobionts are also expected to have played an important role in the deposition of early marine aragonite cements in the Miocene corals just as they do in modern coral environments. Indeed, evidence of enhanced boring activity by sponges, bivalves and sipunculid worms were found in Miocene Caribbean corals that had survived the regional Oligocene-Miocene transition compared to Oligocene examples attesting to an active endobiotic assemblage (Edinger and Risk, 1994).

Calcite cements were also observed in all the fossil corals examined. Under the light microscope, microcrystalline deposits (micrite), equant to bladed crusts lining skeletal voids and pavements of anhedral spar and single crystals filling entire pore-spaces were identified. Calcite replacement of skeletal aragonite was also documented and in some very poorly preserved regions of the fossil corals there has been almost complete destruction of skeletal features (e.g. Figure 4.10b). SEM imaging revealed regions in which voids were either partially or completely filled by irregular blocky masses of calcite or occasionally completely occluded by large interlocking crystals.

The most important diagenetic environments affecting the preservation of the fossil corals and the deposition of calcite cements are the meteoric vadose and phreatic zones (Longman, 1980; James, 1974; Pingitore, 1976; McGregor and Gagan, 2003).

Meteoric vadose alteration results from chemical interactions between air and water present in skeletal pore spaces and soils surrounding the fossil corals (McGregor and Gagan, 2003). Vadose alteration is characterised by dissolution, precipitation of calcite cements, fabric selective replacement of skeletal aragonite and neomorphism (James, 1974; Longman, 1980; McGregor and Gagan, 2003). The morphology of the calcite crystals and heterogeneous cementation reflects the patchy distribution of water within the pore spaces, pore space connectivity and the length of time water was present within the voids (James, 1974: Longman, 1980; McGregor and Gagan, 2003). Vadose calcite cement morphologies range from pendant and meniscal crusts consisting of fine equant crystals (Longman, 1980) to mosaics of irregular interlocking crystals (Pingitore, 1976) and large single crystals (McGregor and Gagan, 2003) that fill entire pore spaces. Fabric selective replacement in

vadose environments is characterised by calcite deposition within skeletal boundaries (Pingitore, 1976; McGregor and Gagan, 2003).

Longman (1980) noted that diagenesis in the active freshwater phreatic zone may involve leaching, neomorphism and the deposition of pavements of interlocking equant calcite crystals that enlarge towards the centre of the pore spaces. In addition, Pingitore (1976) described distinctive cross-cutting relationships in which large calcite crystals had overgrown skeletal boundaries in Pleistocene corals from Barbados that had undergone freshwater phreatic diagenesis. Although dissolution, neomorphism and deposition of calcite cements were observed in the Miocene fossil corals, no cross-cutting relationships were identified.

Minor calcite deposits within the fossil corals are associated with endolithic organisms such as *Lithophaga* which produce thin calcite linings for their boreholes. The presence of *Lithophaga* boreholes not only alters the structural integrity of the coral heads but may also influence the local distribution of diagenetic cements in pore-spaces adjacent to the borings (Jones and Pemberton, 1988).

Hydrocarbon charging has occurred during burial and therefore oil and bituminous residues are also found in the fossil specimens. In thin section, oil-filled pore spaces and voids appear brown and discoloured. In the SEM, the bituminous deposits appear as dark amorphous lumps of material that either occlude the pore spaces or form thick layers that cover the cements and underlying skeletal material. The presence of cements lining pore spaces filled with oil and bitumen suggest hydrocarbon charging postdates secondary aragonite deposition. Hydrocarbon charging may also facilitate the preservation of unstable carbonate phases such as aragonite by blocking the ingress of aqueous diagenetic fluids (Scholle and Ulmer-Scholle, 2003).

Pyrite (FeS) deposits are found in all the fossil corals examined where they appear as bright amalgamations of crystals in back scattered SEM images. Crystal morphologies include octohedra, pyritohedra and amorphous anhedral masses. Crystal sizes range from ~30 µm for octahedral forms down to ~10 µm for pyritohedral forms.

Non-planar dolomite [$CaMg(CO_3)_2$] deposits are present in two specimens of *Montastraea limbata* (NHMUK AZ 4877 and 4878). The crystals are rhombic in shape, possess curved crystal faces and measure up to 60 µm in length.

Evidence of dissolution was observed in the corals with widening of the centres of calcification (COC) exposed in fractured skeletal walls. COCs are especially vulnerable to dissolution because they are comprised of miniscule (<1 µm) randomly orientated granules (Cohen et al., 2001; Cuif and Dauphin, 2005) with high surface area to volume ratios (Walter and Morse, 1984). Dissolution textures are well visualised under the SEM and typified by pitted and etched aragonite fibres (e.g. Figure 4.25b) and widened COCs (e.g. Figure 4.21d).

The activities of micro-boring organisms are seen in all the coral specimens under the SEM. Micro-boreholes penetrate the coral skeleton and are often observed associated with diagenetic cements. In addition some skeletal surfaces have been etched with meandering, branching and anastomosing grooves measuring 3-7 µm in diameter. These grooves are of similar diameter to the micro-bored pits. A wide range of endolithic boring organisms have been recorded in live corals collected from a range of environments on the Great Barrier Reef. Microboreholes with diameters less than 10 µm were attributed to the activities of green algae, cyanobacteria and fungi (Nothdurft and Webb, 2009).

### 7.1.2 Geochemical composition of primary coral aragonite and secondary cements

The data show significant compositional differences between the element/Ca ratios of primary skeletal aragonite compared to diagenetic cements composed of aragonite and calcite. Based on the observed cement compositions, the resulting temperature anomalies produced by inclusion of 1% secondary aragonite or calcite cements in analyses of primary skeletal aragonite have been estimated.

#### *7.1.2.1 Sr/Ca*

Primary skeletal aragonite shows comparatively little variation in Sr/Ca in both modern and fossil specimens with values ranging from 8.49-8.72 mmol

$mol^{-1}$. The data for Sr/Ca in primary skeletal aragonite overall compare well with literature data such as those for the modern Great Barrier Reef (GBR) (*Porites*: 8.9-9.0 mmol $mol^{-1}$; Hendy at al. (2007)), Pleistocene fossil *Porites* from the Hawaiian Islands (8.9-9.5 mmol $mol^{-1}$; Allison et al. (2007)) or modern GBR *Porites mayeri* (7.90-8.41 mmol $mol^{-1}$; Sinclair et al. (1998)) taking into account both the different species and the geological times represented in conjunction with the SST-dependence of Sr/Ca in coral aragonite .

In contrast, the Sr/Ca ratios in aragonite cements are significantly higher than primary coral aragonite with average values for cements ranging from 10.8-13.5 mmol $mol^{-1}$, whereas calcite cements are significantly depleted in Sr relative to primary aragonite (Sr/Ca=0.41 mmol $mol^{-1}$). The observed Sr/Ca ratios for bladed aragonite cement are in good agreement with those reported by Allison et al. (2007), with those for blocky aragonite cements some 10% higher, whereas those for calcite cements are significantly lower (60%) than published by Allison et al. (2007); such differences likely reflect variations in pore-water chemistry during diagenesis. Using the equations of Maupin et al. (2008) for *Siderastrea* (Sr/Ca [mmol $mol^{-1}$] = 10.008 - 0.039 * [SST]$^{o}$ C) and Swart et al. (2002) for *Montastraea* (Sr/Ca [mmol $mol^{-1}$] = 10.165 - 0.0471 * [SST]$^{o}$ C) estimates for the inclusion of 1% aragonite cement would produce cool temperature anomalies of 1.0-1.2$^{o}$ C in fossil *Siderastrea*. Incorporation of similar percentages of bladed aragonite cement would lower SSTs by 0.4$^{o}$ C in *Montastraea,* while contamination with blocky aragonite would lower SSTs by 1.2$^{o}$ C. Contamination of skeletal aragonite with 1% calcite increases SST estimates by 1.7$^{o}$ C in *Montastraea* (Fig. 8). These results show good agreement with those reported by McGregor and Gagan (2003), Quinn and Taylor (2006), Hendy et al. (2007) and Allison et al. (2007). Hydrocarbon crusts do not appear to affect temperature reconstructions unless they form a veneer over fringes of cement (e.g. NHMUK AZ 4876).

#### *7.1.2.2 Mg/Ca*

Mg/Ca ratios in primary coral aragonite cluster around 3 mmol $mol^{-1}$ (range 2.1-3.4), whereas Mg/Ca ratios in aragonite cements are significantly lower (0.1-1.0 mmol $mol^{-1}$). Amongst the different cement types, blocky aragonite cements show greater Mg/Ca depletion than other aragonite cement

morphologies. On the other hand, calcite cements in fossil *Montastraea* are characterised by greatly elevated Mg/Ca ratios (44.0-50.5 mmol $mol^{-1}$) consistent with the presence of high magnesium calcite (Swart, 2009). The Mg/Ca values measured in primary Miocene and modern coral aragonite show good agreement with the values reported by Allison et al. (2007) but are lower than those documented by Hendy et al. (2007) and Sinclair et al. (1998) (3.8-4.8 mmol $mol^{-1}$ and 3.0-4.5 mmol $mol^{-1}$ respectively). The data reported in this thesis for Mg/Ca ratios in aragonite and high magnesium calcite cements show reasonable agreement with those reported by Allison et al. (2007). Differences are attributed to a combination of secular changes in $Mg/Ca_{seawater}$ since the Miocene (Stanley and Hardie, 1998), overall variation in environmental conditions (e.g. SST) but also a ~20-25% bias in Mg/Ca when standardizing with NIST612 because of its low and imprecise Mg value.

Although Mg has been used for palaeo-SST reconstruction (Mitsuguchi et al., 1996; Sinclair et al., 1998) more recent work on the stability of Mg in coral aragonite suggests Mg/Ca may not be very reliable due to the complexity of Mg chemistry in aragonitic carbonates (Watanabe et al., 2001; Finch and Allison, 2007). An estimate - using the calibration Mg/Ca calibration equation of Sinclair et al. (1998) for *Porites* (Mg/Ca [mmol $mol^{-1}$] = 0.0 + 0.16 * [SST]$^{o}$ C) in the absence of a genus specific equation – suggests that the incorporation of 1% aragonite cement would produce cool temperature anomalies of 0.2$^{o}$ C. Contamination of primary skeletal aragonite with a similar percentage of calcite increases SST estimates by 2.7$^{o}$ C; these are all in good agreement with those reported by Hendy et al. (2007) or Allison et al. (2007).

#### *7.1.2.3 B/Ca*

Primary skeletal aragonite B/Ca ratios vary considerably and range between 285-644 µmol $mol^{-1}$. The lowest values are recorded for modern *Siderastrea* (285 µmol $mol^{-1}$), intermediate values (327-477 µmol $mol^{-1}$) occur in Miocene *Siderastrea* and the highest (587-644) are recorded in Miocene *Montastraea.* The difference in B/Ca ratios between modern and Miocene corals reflects different environmental conditions (Bermuda vs. southern Caribbean) and possible secular changes in B/Ca seawater chemistry (Simon et al., 2006), whereas inter- and intra-specific variation is suggested for the two Miocene

genera *Siderastrea* and *Montastraea*. Crucially, B/Ca ratios in both aragonite and calcite cements are much lower and range between 22-120 μmol $mol^{-1}$. Calcite and large blocky aragonite cements show uniformly low values, whereas bladed aragonite shows systematically increasing B/Ca values with depth that approach those for primary coral aragonite. The B/Ca ratios reported here for both primary skeletal aragonite and diagenetic cements are lower and show greater variation than those reported by Allison et al. (2007) with the exception of skeletal aragonite in *Montastraea.*

Using the calibration equation of Sinclair et al. (1998) derived for *Porites* (B/Ca [μmol $mol^{-1}$] = 1000 - 20.6 * [SST]$^{o}$ C) in absence of a species-specific equation, produce positive temperature anomalies of 0.1 to 0.3$^{o}$ C with the inclusion of 1% aragonite cement. Similar percentage contamination by calcite cement results in a positive temperature anomaly of 0.3$^{o}$ C; these estimates are in good agreement with Allison et al. (2007).

#### *7.1.2.4 Ba/Ca*

Ba/Ca ratios show considerable variation in both the primary skeletal aragonite of modern and fossil corals and in the cements. Ba/Ca values are considerably higher in the skeletal aragonite of fossil *Siderastrea* (11.4-15.0 μmol $mol^{-1}$) compared to those observed in modern *Siderastrea* and fossil *Montastraea* (4.9-9.3 μmol $mol^{-1}$). While some of the differences observed likely represent sampling bias introduced by the selection of restricted areas of the different (Miocene) corals, the different oceanographic settings for the modern and fossil corals strongly influences this too. The Ba/Ca results for Miocene coral skeletal aragonite reported in this thesis are higher than those published by Allison et al. (2007) and Montaggioni et al. (2006), but show better agreement with the range of Ba/Ca ratios documented by Sinclair (2005). This is to be expected based on the oceanic location of the Hawaiian Islands (Allison et al., 2007) and New Caledonia (Montaggioni et al., 2006) versus the river plume-influenced inner coastal GBR (Sinclair et al., 2005) and the Miocene Paraguaná sampling site (Diaz de Gamero, 1996). Barium concentrations in coral aragonite are influenced by fluvial run-off and seasonal up-welling of cool, nutrient-rich water (exogenous abiotic factors), the growth and decay of phytoplankton blooms (exogenous biotic factors), and physiological processes within the

corals themselves (endogenous biotic factors; Sinclair, 2005). Most importantly, secondary aragonite cements are characterised by significantly higher Ba/Ca ratios than those encountered in the skeletal aragonite of the same coral samples with the exception of the blocky aragonite cement in *Montastraea* (NHMUK AZ 4878). Exceptionally high Ba/Ca values (>6x primary aragonite) are encountered in the bladed aragonite cements encrusting fossil *Siderastrea* (NHMUK AZ 4874. Calcite cements show the opposite trend as they are characterised by low Ba/Ca ratios (~1.6 μmol $mol^{-1}$).

Ba/Ca ratios are 2 - 20x higher in the aragonite cements investigated in this study than those reported by Allison et al. (2007), although there is good agreement for calcite cements. Higher Ba/Ca ratios in aragonite cements are expected because the partition coefficients favour the inclusion of barium in secondary aragonite but exclude Ba from calcite. Taken together, these data suggest that the inclusion of cements in coral analyses can significantly affect Ba/Ca ratios and overprint important palaeo-environmental signatures such as soil erosion, flood events and upwelling (Fleitmann et al., 2007; McCulloch et al., 2003; Montaggioni et al., 2006).

#### *7.1.2.5 U/Ca*

Skeletal aragonite U/Ca ratios are higher (~4x) in the modern *Siderastrea* than in the Miocene specimens (0.35-0.54 μmol $mol^{-1}$). U/Ca ratios vary considerably in the diagenetic cements ranging from 0.1-1.2 μmol $mol^{-1}$ with no clear pattern of change evident in the concentration of uranium in either aragonite or calcite. The U/Ca values reported here for fossil coral primary skeletal aragonite are 3 to 4x lower than those reported by Allison et al. (2007), but the values for modern *Siderastrea* show good agreement with their data.

Bladed aragonite cements record elevated U/Ca ratios relative to primary skeletal aragonite and also show indications of depth-related decrease towards values of coral aragonite. Both the low U/Ca ratios observed in blocky aragonite cements and the elevated U/Ca ratio in calcite cements in some of the Miocene coral samples are somewhat anomalous, although changes in *p*H and/or crystal growth rates may have played a role as both these factors affect the partitioning of U in aragonite (Meece and Benninger, 1993). Experimental results show low (<0.2) partition coefficients for U in calcite (Meece and

Benninger, 1993), therefore low U/Ca ratios are to be expected. Limited negative temperature anomalies of 0.1 to 0.3$^{o}$ C are recorded in this study with the inclusion of 1% aragonite or calcite cements using the calibration equation of Sinclair et al., (1998) derived for *Porites* (U/Ca [µmol mol-1] = 2.24 – 0.046 * [SST]$^{o}$ C), although this depends on which aragonite cement predominates. These temperature anomalies show good agreement with those of Allison et al. (2007) for aragonite cements.

## 7.2 CONCLUSIONS

- This thesis documents primary skeletal aragonite preservation with intact geochemical signatures in Early Miocene corals (confirmed via Sr isotope stratigraphy). This is the first time that corals of this age have been analysed and shown to preserve unaltered geochemical signatures.

- Diagenetic cements are present in live-collected modern and fossil corals. Aragonite, high-Mg calcite and brucite cements are found in the modern corals. Aragonite, calcite, pyrite and dolomite cements are present in the fossil corals. Blocky and bladed aragonite cements types are the most common phases. All the cements show very heterogeneous and patchy distributions influenced by factors such as skeletal architecture, pore connectedness, endobiont activity and the presence of organic biofilms. The prevalence of aragonite cements renders XRD screening insufficient for diagenetic assessment.

- Aragonite cements are enriched in Sr/Ca and depleted in Mg/Ca, decreasing reconstructed palaeo-SST. The inclusion of 1% aragonite would significantly affect Sr/Ca SST estimates, producing cool temperature anomalies of up to -1.2$^{o}$C. Calcite cements are depleted in Sr/Ca and enriched in Mg/Ca increasing the reconstructed palaeo-SST. The inclusion of 1% calcite cement would produce warm temperature anomalies of +1.7$^{o}$ C. B/Ca ratios are significantly lower in both aragonite and calcite cements compared to primary aragonite, which is highly relevant given the greater SST sensitivity of B/Ca relative to other

relevant element/Ca ratios such as Sr/Ca in corals. No uniform 'cement signature' was found for U/Ca.

- Secondary aragonite cements are very strongly enriched (~6-10-fold) in Ba/Ca relative to primary coral aragonite, which is significant for the reconstruction of palaeo- runoff or upwelling events using corals.
- Although diagenetic processes have affected the fossil corals, it is still possible to recover useful proxy data by carefully targeting zones of excellent preservation using LA-ICPMS or SIMS.

- Coral age estimations of ~16 Ma years based on strontium isotope stratigraphy are unique and confirm the published Burdigalian age of the Cantaure Formation based on biostratigraphy.

- LA-ICPMS allows fast and accurate analysis at the high resolution needed for palaeo-environmental reconstructions with little sample preparation.

# References

Acevedo, R., Morelock, J., Olivieri, R.A. 1989. Modification of coral reef zonation by terrigenous sediment stress. Palaios, 4, 92-100.

Aguilera, O., Rodrigues de Aguilera, D. 2003. Two new otolith-based sciaenid species of the genus *Plagioscion* from South American Neogene marine sediments. Journal of Paleontology, 77, 1133-1138.

Aguilera, O., Rodrigues de Aguilera, D. 2004. New Miocene otolith-based sciaenid species (Pisces, Perciformes) from Venezuela. Paleontology Special Paper, 71, 49-59.

Aguilera, O. A., Moraes-Santos, H., Costa, S., Ohe, F., Jaramillo, C., Nogueira, A. 2013. Ariid sea catfishes from the coeval Pirabas (Northeastern Brazil), Cantaure, Castillo (Northwestern Venezuela), and Castilletes (North Colombia) formations (early Miocene), with description of three new species. Swiss Journal of Palaeontology, doi: 10.1007/s13358-013-0052-4.

Alarcón, C. 2001. Paraguaná xeric scrub (NT1313), http://www.worldwildlife.org/wildworld/profiles/terrestrial/nt/nt1313_full.html Accessed 20/07/2009.

Allison, N., Finch, A.A. 2007. High temporal resolution Mg/Ca and Ba/Ca records in modern Porites lobata corals. Geochemistry, Geophysics, Geosystems, 8, Q05001.

Allison, N., Finch, A.A., Webster, J.M., Clague, D.A. 2007. Palaeoenvironmental records from fossil corals: The effects of submarine diagenesis on temperature and climate estimates. Geochimica et Cosmochimica Acta, 71, 4693-4703.

AquaMODIS Sea-surface temperature. http://oceancolor.gsfc.nasa.gov/cgi/13 Accessed 17/10/2010.

Bar-Matthews, M., Wasserburg, G.J., Chen, J.H. 1993. Diagenesis of fossil coral skeletons: Correlation between trace elements, textures and 234U/238U. Geochimica et Cosmochimica Acta, 57, 257-276.

Beck, B.R., Budd, A.F. 2008. Evolutionary patterns within the reef coral *Siderastrea* in the Mio-Pliocene of the Dominican Republic. Evolutionary stasis and change in the Dominican Republic Neogene, Topics in Geobiology, 30, 125-145.

Beers, J. R., Herman, S. S. 1969. The ecology of inshore plankton populations in Bermuda. Part 1. Seasonal variation in the hydrography and nutrient chemistry. Bulletin of Marine Science, 19, 253-278.

Blow, W. H. 1969. Late Middle Eocene to Recent planktonic foraminiferal biostratigraphy. Proceedings of the 1st International Conference on Planktonic Microfossils, Geneva, 1967, 199-422.

Brachert, T.C., Reuter, M., Felis, T., Kroeger, K.F., Lohmann, G., Micheels, A., Fassoulas, C. 2006. Porites corals from Crete (Greece) open a window into Late Miocene (10 Ma) seasonal and interannual climate variability. Earth and Planetary Science Letters, 245, 81-94.

Brakel, W.H. 1977. Corallite variation in *Porites* and the species problem in corals. Proceedings 3rd International Coral Reef Symposium, Miami, 2, 457-462.

Budd, A.F. 1991. Neogene paleontology in the Northern Dominican Republic. 11. The Family Faviidae (Anthozoa: Scleractinia), Part 1, Bulletin of American Paleontology, 101, 5-83.

Budd, A.F. 2000. Diversity and extinction in the Cenozoic history of Caribbean reefs. Coral Reefs, 19, 25-35.

Budd, A.F., Guzmán, H.M. 1994. *Siderastrea glynni*, a new species of scleractinian coral (Cnidaria, Anthozoa) from the Eastern Pacific. Proceedings of the Biological Society of Washington, 107, 591-599.

Budd, A.F., Johnson, K.G., Edwards, J.C. 1989. Miocene coral assemblages in Anguilla, BWI, and their implications for the interpretation of vertical succession on fossil reefs. Palaios, 4, 264-275.

Budd, A.F., Johnson, K.G., Edwards, J.C. 1995. Caribbean reef coral diversity during the Early to Middle Miocene: an example from the Anguilla Formation. Coral Reefs, 14, 109-117.

Buster, N.A., Holmes, C.W. 2006. Magnesium content within the skeletal architecture of the coral *Montastraea faveolata*: locations of brucite precipitation and implications for fine-scale data interpretation. Coral Reefs, 25, 243-253.

Coates, A.G., Aubry, M-P., Berggren, W.A., Collins, L.S., Kunk, M. 2003. Early Neogene history of the Central American arc from Bocas del Toro, western Panama. Geological Society of America Bulletin, 115, 271-287.

Cohen, A.L., Gaetani, G.A. 2010. Ion partitioning and the geochemistry of coral skeletons: solving the mystery of the vital effect. EMU Notes in Mineralogy, 11, 377-397.

Cohen, A.L., Layne, G.D., Hart, S.R., Lobel, P.S. 2001. Kinetic control of skeletal Sr/Ca in a symbiotic coral: implications for the palaeotemperature proxy. Paleoceanography, 16, 20-26.

Cohen, A.L., McConnaughey, T.A. 2003. Geochemical perspectives on coral mineralization. Reviews in mineralogy and geochemistry, 54, 151-187.

Constantz, B.R. 1986. Coral skeleton construction: A physiochemically dominated process. Palaios, 1, 152-157.

Corrège, T. 2006. Sea surface temperature and salinity reconstruction from coral geochemical tracers. Palaeogeography, Palaeoclimatology, Palaeoecology, 232, 408-428.

Cortés, J.N., Risk, M.J. 1985. A reef under siltation stress, Cahuita, Costa Rica. Bulletin of Marine Science, 36, 339-356.

Cuif, J.P. 1975. Caractères morphologiques, microstructuraux et systématiques des Pachythecalidae, nouvelle famille de Madréporaires triasiques. Geobios, 8, 157-180.

Cuif, J-P., Dauphin, Y. 2005. The two-step mode of growth in the scleractinian coral skeletons from the micrometer to the overall scale. Journal of Structural Biology, 150, 319-331.

De Deckker, P. 2004. On the celestite-secreting Acantharia and their effect on seawater strontium to calcium ratios. Hydrobiologica, 517, 1-77.

Denniston, R.F., Asmeron, Y., Polyak, V.Y., McNeill, D.F., Klaus, J.S., Cole, P., Budd, A.F. 2008. Caribbean chronostratigraphy refined with U-Pb dating of a Miocene coral. Geology, 36, 151-154.

De Villiers, S., Shen, G.T., Nelson, B.K. 1994. The Sr/Ca–temperature relationship in coralline aragonite: Influence of variation in (Sr/Ca)seawater and skeletal growth parameters. Geochimica et Cosmochimica Acta, 58, 197-208.

Díaz de Gamero, M.L. 1974. Microfauna y edad de la Formacion Cantaure, Peninsula de Paraguana, Venezuela. Boletin Informativo Asociacion Venezolana de Geologia, Mineria y Petroleo, 17, 41-47.

Díaz de Gamero. M.L. 1996. The changing course of the Orinoco River during the Neogene: a review. Palaeogeography, Palaeoclimatology, Palaeoecology, 123, 385-402.

Dickson, J. 2002. Fossil echinoderms as monitor of the Mg/Ca ratio of Phanerozoic oceans. Science, 298, 1222-1224.

Duerden, J.E. 1904. The coral *Siderastrea radians* and its postlarval development. Carnegie Institution of Washington Publication No 20, 129; Plate 10. http://www.archive.org/details/coralsiderastrea00duer.

Dullo, W-C. 1984. Progressive diagenetic sequence of aragonite structures: Pleistocene coral reefs and their modern counterparts on the eastern Red Sea coast, Saudi Arabia. Palaeontographica Americana, 54, 254-260.

Duncan, P.M. 1863. On the fossil corals of the West Indian Islands. Quarterly Journal of the Geological Society of London, 19, 406-458.

Durrant, S.F. 1994. Feasibility of improvement in analytical performance in laser ablation inductively coupled plasma-mass spectrometry (LA-ICP-MS) by addition of nitrogen to the argon plasma. Fresenius' Journal of Analytical Chemistry, 349, 768-771.

Eggins, S.M., Shelley, J.M.G. 2002. Compositional heterogeneity in NIST SRM 610-617 glasses. Geostandards Newsletter, 26, 269-286.

Edinger, E.N., Risk, M.J. 1994. Oligocene-Miocene extinction and geographic restriction of Caribbean corals: Roles of turbidity, temperature and nutrients. Palaios, 9, 576-598.

Edinger, E.N., Risk, M.J. 1995. Preferential survivorship of brooding corals in a regional extinction. Paleobiology, 21, 200-219.

Edwards, E. J., Diaz, M. 2006. Ecological physiology of *Pereskia guamacho*, a cactus with leaves. Plant, Cell and Environment, 29, 247-256.

Ellis, J., & Solander, D. C. 1786. The Natural History of Many Curious and Uncommon Zoophytes, Collected from Various Parts of the Globe by the Late John Ellis. Systematically Arranged and Described by the Late Daniel Solander. Benjamin White and Son, London.

Enmar, R., Stein, M., Bar-Matthews, M., Sass, E., Katz, A., Lazar, B. 2000. Diagenesis in live corals from the Gulf of Aqaba. I. The effect on paleo-oceanography tracers. Geochimica et Cosmochimica Acta, 64, 3123-3132.

Esteves, J. A., Padron, V. 1996. Nuevas especies de gasteropodos de la Formacion Cantaure, Peninsula de Paraguaná. Acta Cientifica Venezolana, 47, 301.

Finch, A.A., Allison, N. 2007. Coordination of Sr and Mg in calcite and aragonite. Mineralogical Magazine, 71, 539-552.

Fleitmann, D., Dunbar, R., McCulloch, M., Mudelsee, M., Vuille, M., McClanahan, T., Cole, J., Eggins, S. 2007. East African soil erosion recorded in a 300 year old coral colony from Kenya. Geophysical Research Letters, 34, L04401. doi: 10.1029/2006GL028525.

Flügel, E. 2004. Diagenesis, porosity, and dolomitisation. Chapter 7. Microfacies of carbonate rocks. Analysis, interpretation and application. Springer-Verlag, Berlin, pp267-338.

Forsman, Z. H. 2003. Phylogeny and phylogeography of *Porites* and *Siderastrea* (Scleractinia: Cnidaria) species in the Caribbean and Eastern Pacific; based on the nuclear ribosomal ITS region. PhD thesis, University of Houston, Texas, USA, 3-5.

Forsman, Z.H., Barshis, D.J., Hunter, C.L., Toonen, R.J. 2009. Shape-shifting corals: Molecular markers show morphology is evolutionarily plastic in *Porites.* BMC Evolutionary Biology, 9:45, doi 10.1186/1471-2148-9-45.

Foster, A.B. 1980a. Ecology and morphology of the Caribbean Mio-Pliocene reef-coral *Siderastrea.* Acta Palaeontologica Polonica, 25, 439-452.

Foster, A.B. 1980b. Environmental variation in skeletal morphology within the Caribbean reef corals *Montastraea annularis* and *Siderastrea sidera.* Bulletin of Marine Science, 30, 678-709.

Foster, A.B. 1983. The relationship between corallite morphology and colony shape in some massive reef-corals. Coral Reefs, 2, 19-25.

Frech, F. 1890. Die Korallenfauna de Trias. Die Korallen der juvavischen Triasprovinz. Palaeontographica, 37, 1-116.

Frost, S.H. 1977. Miocene to Holocene evolution of Caribbean province reef-building corals. Proceedings of the 3rd International Coral Reef Symposium, Miami, 2, 353-359.

Frost, S.H., Harbour, J.L., Beach, D.K., Realini, M.J., Harris, P.M. 1983. Oligocene reef tract development, southwestern Puerto Rico. Sedimenta, 9, 1-144.

Frost, S.H., Langenheim, R.L. 1974. Cenozoic reef facies. Northern Illinois University Press, Chicago, pp1-388.

Gaetani, G.A., Cohen, A.L. 2006. Element partitioning during precipitation of aragonite from seawater: A framework for understanding paleoproxies. Geochimica et Cosmochimica Acta, 70, 4617-4634.

Gaillardet, J., Allègre, C.J. 1995. Boron isotopic composition of corals: Seawater or diagenesis record. Earth and Planetary Science Letters, 136, 3-4, 665-676.

Gardner, T.A., Cote, I.M., Gill., J.Z., Grant, A., Watkinson, A.R. 2003. Long-term region-wide declines in Caribbean corals. Science, 301, 958-960.

Garrett, P., Smith, D.L., Wilson, A.O., Patriquin, D. 1971. Physiography, ecology and sediments of two Bermuda patch reefs. Journal of Geology, 79, 647-668.

GeoReM database, http://georem.mpch-mainz.gwdg.de. Accessed 23/03/2009.

Gradstein, F.M., Ogg, J.G., Smith, A.G. (Eds). 2004. The Geologic Time Scale 2004. Cambrige University Press, Cambridge, UK. 384-430.

Griffiths, N., Mueller, W., Johnson, K.G., Aguilera, O.A. 2013. Evaluation of the effect of diagenetic cements on element/Ca ratios in aragonitic Early Miocene (~16 Ma) Caribbean corals: Implications for 'deep-time' palaeo-environmental reconstructions. Palaeogeography, Palaeoclimatology, Palaeoecology, 369, 185-200. (http:/dx.doi.org/10.1016/j.palaeo.2012.10.018).

Guzmán, H.M., Burns, K., Jackson, J.B.C. 1994. Injury, regeneration and growth of Caribbean corals after a major oil spill in Panama. Marine Ecology Progress Series, 105, 231-241.

Guzmán, H.M., Tudhope, A.W. 1998. Seasonal variation in skeletal extension rate and stable isotopic ($^{13}C/^{12}C$ and $^{18}O/^{16}O$) composition in response to several environmental variables in the Caribbean reef coral *Siderastera siderea.* Marine Ecology Progress Series, 166, 109-118.

Gyory J., Mariano, A.J., Ryan, E.H. The Loop Current. http://oceancurrents.rsmas.miami.edu/atlantic/loop-current.html Acccessed 20/06/2011

Gyory, J., Rowe, E., Mariano, A.J., Ryan, E.H. The Florida Current. http://oceancurrents.rsmas.miami.edu/atlantic/florida.html Accessed 20/06/2011

Halley, R.B., Vacher, H.L., Shinn, E.A. 2004. Geology and hydrogeology of the Florida Keys. Developments in Sedimentology, 54, 217-248.

Hallock, P., Schlager, W. 1986. Nutrient excess and the demise of coral reefs and carbonate platforms. Palaios, 1, 389-398.

Hathorne, E.C., Felis, T., James, R.H., Thomas, A. 2011. Laser ablation ICP-MS screening of corals for diagenetically affected areas applied to Tahiti corals from the last glaciation. Geochimica et Cosmochimica Acta, 75, 1490-1506.

Hemming, N.G., Hanson, G.N. 1992. Boron isotopic composition and concentration in modern marine carbonates. Geochimica et Cosmochimica Acta, 56, 537-543.

Hemming, N.G., Reeder, R.J., Hanson, G.N. 1995. Mineral-fluid partitioning and isotopic fractionation of boron in synthetic calcium carbonate. Geochimica et Cosmochimica Acta, 59, 371-379.

Hendy, E.J., Gagan, M.K., Lough, J.M., McCulloch, M., deMenocal, P.B. 2007. Impact of skeletal dissolution and secondary aragonite on trace element and isotopic climate proxies in *Porites* corals. Paleoceanography, 22, PA4101. doi:10.1029/2007PA001462.

Hobbs, M.Y., Reardon, E.J. 1999. Effect of pH on boron coprecipitation by calcite: Further evidence for nonequilibrium partitioning of trace elements. Geochimica et Cosmochimica Acta, 63, 1013-1021.

Hoorn, C. 1993. Marine incursions and the influence of Andean tectonics on the Miocene depositional history of northwestern Amazonia: Results of a palynostratigraphic study. Palaeogeography, Palaeoclimatoogy, Palaeoecology, 105, 267-309.

Hoorn, C. 1994. Fluvial palaeoenvironments in the intracratonic Amazonas Basin (Early Miocene - early Middle Miocene, Colombia). Palaeogeography, Palaeoclimatology, Palaeoecology, 109, 1-54.

Hoorn, C., Wesselingh, F.P., Hovikoski, J., Guerrero, J. 2010. The development of the Amazonian meg-wetland (Miocene; Brazil, Colombia, Peru, Bolivia). In: Hoorn, C., Wesselingh, F.P. (Eds). Amazonia, landscape and species evolution: A look into the past. Blackwell Publishing, 123-142.

Horowitz, E.P., Chiarizia, R., Dietz, M.L. 1992. A novel strontium-selective extraction chromatographic resin. Sovlent Extration and Ion Exchange,10, 313-336.

Hovikoski, J., Wesselingh, F.P., Räsänen, M., Gingras, M., Vonhof, H.B. 2010. Marine influence in Amazonia: Evidence from the geological record. ). In: Hoorn, C., Wesselingh, F.P. (Eds). Amazonia, landscape and species evolution: A look into the past. Blackwell Publishing,143-161.

Hubbard, J.A.E.B., Swart, P.K. 1982. Sequence and style in scleractinian coral preservation in reefs and associated facies. Palaeogeography, Palaeoclimatology, Palaeoecology, 37, 165-219.

Hughes, T.P., Baird, A.H., Bellwood, D.R., Card, M., Connolly, S.R., Folke, C., Grossberg, R., Hoegh-Guldberg, O., Jackson, J.B.C., Kleypas, J., Lough, J.M., Marshall, P., Nyström, M., Palumbi, S.R., Pandolfi, J.M., Rosen, B., Roughgarden, J. 2003. Climate change, human impacts and the resilience of coral reefs. Science, 301, 929-933.

Hunter, V. F., Bartok, P. 1974. The age and correlation of the tertiary sediments of the Paraguaná Peninsula, Venezuela. Boletin Informativo Asociation Venezolana de Geologia, Mineria y Petroleo, 17, 143-154.

Hutchings, P.A. 1986. Biological destruction of coral reefs. Coral Reefs, 4, 239-252.

Ivany, L.C., Peters, S.C., Wilkinson, B.H., Lohmann, K.C., Reimer, B.A. 2004. Composition of the early Oligocene ocean from coral stable isotope and elemental chemistry. Geobiology, 2, 97-106.

James, N.P. 1974. Diagenesis of scleractinian corals in the subaerial vadose environment. Journal of Paleontology, 48, 785-799.

Jochum, K.P., Weis, U., Stoll, B., Kuzmin, D., Yang, Q., Raczek, I., Jacob, D.E., Stracke, A., Birbaum, K., Frick, D.A., Günther, D., Enzweiler, J. 2011. Determination of reference values for NIST SRM 610-617 glasses following ISO Guidelines. Geostandards and Geoanalytical Research, 35, 397-429.

Johnson, K.G. 2001. Middle Miocene recovery of Caribbean reef corals; new data from the Tamana Formation, Trinidad. Journal of Paleontology, 75, 513-526.

Johnson, K.G., Jackson, J.B.C., Budd, A.F. 2008. Caribbean reef development was independent of coral diversity over 28 million years. Science, 819, 1521-1523.

Johnson, K. G., Kirby, M. X. 2006. The Emperador Limestone rediscovered: Early Miocene corals from the Culebra Formation. Panama Journal of Paleontology, 80, 283-293.

Joint Committee on Powder Diffraction Standards. 1993. Mineral Powder Diffraction File Databook. Sets 1-42. International Centre for Diffraction Data, Pennsylvania, USA.

Jones, B., Pemberton, S.G. 1988. Lithophaga borings and their influence on the diagenesis of corals in the Pleistocene Ironshore Formation of Grand Cayman Island, British West Indies. Palaios, 3, 3-21.

Jung, P. 1965. Miocene mollusca from the Paraguaná Peninsula, Venezuela. Bulletins of American Paleontology, 4, 389-652.

Kerr, P.F. 1977. Optical Mineralogy, 4th edition. McGraw-Hill, New York. pp 429.

Kleypas, J., Buddemeir, R.W., Archer, D., Gattuso, J.P., Langdon., C., Opdyke, B.N. 1999. Geochemical consequences of increased atmospheric carbon dioxide on coral reefs. Science, 284, 118-120.

Lazar, B., Enmar, R., Schossberger, M., Bar-Matthews, M., Halicz, L., Stein, M. 2004. Diagenetic effects on the distribution of uranium in live and Holocene corals from the Gulf of Aqaba. Geochimica et Cosmochimica Acta, 68, 4583-4593.

Lear, C.H., Elderfiled, H., Wilson, P.A. 2003. A Cenozoic seawater Sr/Ca record from benthic foraminiferal calcite and its application in dertermining global weathering fluxes. Earth and Planetary Science Letters, 208, 69-84.

Link, A.F. 1807. Beschreibung der Naturalien-Sammlungen der Universität Rostok,3, 161-165

Lirman, D., Orlando, B., Maciá, S., Manzello, D., Kaufman, L., Biber, P., Jones, T. 2003. Coral communities of Biscayne Bay, Florida and adjacent offshore areas: diversity, abundance, distribution, and environmental correlates. Aquatic Conservation: Marine and Freshwater Ecosystems, 13, 121-135.

Longman, M.W. 1980. Carbonate diagenetic textures from nearsurface diagenetic environments. AAPG Bulletin, 64, 461-487.

Lorente, M. A. 1997. Cantaure Formation, Stratigraphic Lexion of Venezuela. http://www.pdvsa.com/lexico/c19w.htm
Accessed 05/03/2009.

Lowenstein, T., Timofeeff, M., Brennan, S., Hardie, L., Demicco, R. 2001. Oscillations in Phanerozoic seawater chemistry: Evidence from fluid inclusions. Science, 294, 1068-1088.

Martini, E. 1971. Standard Tertiary and Quaternary calcareous nannoplankton zonation, in Proceedings of the Second Planktonic Conference Roma 1970. A. Farinacci (Ed) , Edizioni Tecnoscienza, Rome, 2, 739-785.

Maupin, C.R., Quinn, T.M., Halley, R.B. 2008. Extracting a climate signal from the skeletal geochemistry of the Caribbean coral *Siderastrea siderea*. Geochemistry, Geophysics, Geosystems, 9, Q12012.

McArthur, J.M. 1994. Recent trends in strontium isotope stratigraphy. Terra Nova, 6, 331-358.

McArthur, J.M., Howarth, R.J. 2004. Strontium isotope stratigraphy. In: F.M. Gradstein, J.G. Ogg and A.G. Smith (Eds), A Geological Timescale 2004, Cambridge University Press, 589pp.

McArthur, J.M., Howarth, R.J., Sheilds, G.A. 2012. Strontium isotope stratigraphy. In: F.M. Gradstein, J.G. Ogg and A.G. Smith (Eds), A Geological Timescale 2012, Cambridge University Press, doi: 10.1016/B978-0-444-59425-9.00007-X

McArthur, J.M., Howarth, R.J., Bailey, T. R. 2001. Strontium isotope stratigraphy: LOWESS Version 3. Best-fit line to the marine Sr-isotope curve for 0 to 509 Ma and accompanying look-up table for deriving numerical age. Journal of Geology, 109, 155-169.

McCulloch, M., Fallon, S., Wyndham, T., Hendy, E., Lough, J., Barnes, D. 2003. Coral record of increased sediment flux to the inner Great Barrier Reef since European settlement. Nature, 421, 727-730.

McGregor, H.V., Abram, N.J. 2008. Images of diagenetic textures in *Porites* corals from Papua New Guinea and Indonesia. Geochemistry, Geophysics, Geosystems, 9, Q10013. doi:10.1029/2008GC002093.

McGregor, H.V., Gagan, M.K. 2003. Diagenesis and geochemistry of *Porites* corals from Papua New Guinea: Implications for paleoclimate reconstruction. Geochimica et Cosmochimica Acta, 67, 2147-2156.

Meece, D.E., Benninger, L.K. 1993. The coprecipitation of Pu and other radionuclides with $CaCO_3$. Geochimica et Cosmochimica Acta, 57, 1447-1458.

Meibom, A., Cuif, J-P., Houlbreque, F., Mostefaoui, S., Dauphin, Y., Meibom, K.L., Dunbar, R. 2008. Compositional variations at ultra-structure length scales in coral skeleton. Geochimica et Cosmochimica Acta, 72, 1555-1569.

Meldrum, F.C., Hyde, S.T. 2001. Morphological influence of magnesium and organic additives on the precipitation of calcite. Journal of Crystal Growth, 231, 544-558.

Mertz-Kraus, R., Brachert, T.C., Jochum, K.P., Reuter, M., Stoll, B. 2009. LA-ICP-MS analysis on coral growth increments reveal heavy winter rain in the Eastern Mediterranean at 9 Ma. Palaeogeography, Palaeoclimatology, Palaeoecology, 273, 25-40.

Mertz-Kraus, R., Brachert, T.C., Reuter, M. 2008. *Tarbellastraea* (Scleractinia): A new stable isotope archive for Late Miocene paleoenvironments in the Mediterranean. Palaeogeography, Palaeoclimatology, Palaeoecology, 257, 294-307.

Mertz-Kraus, R., Brachert, T.C., Reuter, M., Galer, S.J.G., Fassoulas, C., Iliopoulos, G. 2009. Late Miocene sea surface salininy variability and paleoclimate conditions in the Eastern Mediterranean inferred from coral aragonite $\delta^{18}O$. Chemical Geology, 262, 202-216.

Milliman, J.D. 1974. Marine Carbonates, Springer-Verlag, Berlin, pp23.

Miloslavich, P., Klein, E., Yerena, E., Martin, A. 2003. Marine biodiversity in Venezuela: status and perspectives. Gayana, 67, 275-301.

Min, G. R., Edwards, R.L., Taylor, F.W., Recy, J., Gallup, C.D., Beck, J.W. 1995. Annual cycles of U/Ca in coral skeletons and U/Ca thermometry. Geochimica et Cosmochimica Acta, 59, 2025-2042.

Mitsuguchi, T., Matsumoto, E., Abe, O., Uchida, T., Isdale, P. 1996. Mg/Ca thermometry in coral skeletons. Science, 274, 961-963.

Montaggioni, L.F., Le Cornec, F., Corrège, T., Cabioch, G. 2006. Coral barium/calcium record of mid-Holocene upwelling activity in New Caledonia, south-west Pacific. Palaeogeography, Palaeoclimatology, Palaeoecology, 237, 436-455.

Müller, A., Gagan, M.K., McCulloch, M.T. 2001. Early marine diagenesis in corals and geochemical consequences for paleoceanographic reconstructions. Geophysical Research Letters, 28, 4471-4474.

Müller, W., Shelley, M., Miller, P., Broude, S. 2009. Initial performance metrics of a new custom-designed ArF excimer LA-ICPMS system coupled to a two-volume laser ablation cell. Journal of Analytical Atomic Spectrometry, 24, 209-214.

Muthiga, A.N., Szmant, A.M. 1987. The effects of salinity stress on the rates of aerobic respiration and photosynthesis in the hermatypic coral *Siderastrea siderea*. Biological Bulletin, 173, 539-551.

National Institutes of Health (USA).
rsbweb.nih.gov/ij/
Accessed 12/01/2010

Neves, E.G., da Silveira, F.L., Pichon, M., Johnsson, R. 2010. Cnidaria, Scleractinia, Siderastreidae, *Siderastrea sidereal* (Ellis and Solander, 1786): Hartt Expedition and the first record of a Caribbean siderastreid in tropical Southwestern Atlantic. Check List, Journal of Species Lists and Distribution, 6, 505-510.

Neogene Marine Biota of Tropical America (NMITA),
http://eusmilia.geology.uiowa.edu/database/corals/systemat/ssidera.htm
http://eusmilia.geology.uiowa.edu/database/corals/systemat/sradia.htm
http://eusmilia.geology.uiowa.edu/database/corals/systemat/sidatrea.htm
http://eusmilia.geology.uiowa.edu/database/corals/systemat/montrae1.htm
http://porites.geology.uiowa.edu/database/corals/systemat/porites1.htm
http://porites.geology.uiowa.edu/database/corals/systemat/porites2.htm
(Accessed 20/01/2011)

NOAA Marine Sanctuaries
http://floridakeys.noaa.gov/fknms_map/sanctuaryzoneboundaries.pdf
(Accessed 19/05/2010)

Nolf, D., Aguilera, O. 1998. Fish otoliths from the Cantaure Formation (Early Miocene of Venezuela). Bulletin de l'Institut Royal des Sciences Naturelles de Belgique, 68, 237-262.

Nothdurft, L.D., Webb, G.E. 2009. Earliest diagenesis in scleractinian coral skeletons: Implications for palaeoclimate-sensitive geochemical archives. Facies, 55, 161-201.

Nothdurft, L.D., Webb, G.E., Bostrom, T., Rintoul, L. 2007. Calcite-filled borings in the most recently deposited skeleton in live-collected *Porites* (Scleractinia): Implications for trace element archives. Geochimica et Cosmochimica Acta, 71, 5423-5438.

Nothdurft, L.D., Webb, G.E., Buster, N.A., Holmes, C.W., Sorauf, J.E. 2005. Brucite microbialites in living coral skeletons: Indicators of extreme microenvironments in shallow marine settings. Geology, 33, 169-172.

Oslick, J.S., Miller, K.G., Feigenson, M.D., Wright, J.D. 1994. Oligocene - Miocene stontium isotopes: stratigraphic revisions and correlations to an inferred glacioeustatic record. Palaeoceanography, 9, 427-443.

Ourbak,T., Corrège, T., Malaizé, B., Le Cornec, F., Charlier, K., Peyrouquet, J.P. 2006. A high-resolution investigation of temperature, salinity, and upwelling activity proxies in corals. Geochemistry, Geophysics, Geosystems, 7, Q03013.

Pagani, M., Lemarchand, D., Spivack, A., Gaillardet, J. 2005a. A critical evaluation of the boron isotope-pH proxy: The accuracy of ancient ocean pH estimates. Geochimica et Cosmochimica Acta, 69, 953-961.

Pagani, M., Zachos, J.C., Freeman, K.H., Tipple, B., Bohaty, S. 2005b. Marked decline in atmospheric carbon dioxide concentration during the Paleogene. Science, 309, 600-6003.

Pallas, P.S. 1766. Elenchus Zoophytorum. Hagæ-Comitum: Franciscum Varrentrapp. pp322.

Parra, M., Mora., A., Jaramillo, C., Veloza, G., Strecker, R. 2005. New stratigraphic data on the initiation of mountain building at the Eastern Front of the Columbian Eastern Cordillera. In: International Symposium on Andean Geodynamics, Barcelona.

Perrin, C. 2003. Compositional heterogeneity and microstructural diversity of coral skeletons: implications for taxonomy and control of early diagenesis. Coral Reefs, 22, 109-120.

Pindell, J.L., Higgs, R., Dewey, J.F. 1998. Cenozoic palinspastic reconstruction, paleogeographic evolution, and hydrocarbon setting of the northern margin of South America. In: Pindell, J.L., Drake, C.L. (Eds) Paleogeographic evolution and non-glacial eustasy, Northern South America. Tulsa, Society for Sedimentary Geology, 45-86.

Pingitore Jr, N. E. 1976. Vadose and phreatic diagenesis: Processes, products and their recognition in corals. Journal of Sedimentary Petrology, 46, 985-1006.

Pingitore Jr, N.E., Eastman, M.P. 1985. Barium partitioning during the transformation of corals from aragonite to calcite. Chemical Geology, 48, 183-187.

Pitts, P.A., Smith, N.P. Tracking Florida Bay water across Hawk Channel using salinity as a natural tracer. http://www.aoml.noaa.gov/flbay/pitts.html Accessed 07/07/2011.

Quinn, T.M., Taylor, F.W. 2006. SST artifacts in coral proxy records produced by early marine diagenesis in a modern coral from Rabaoul, Papua New Guinea. Geophysical Research Letters, 33, L04601. doi:10.1029/2005GL024972.

Rey, O. 1996. Estratigraphia de la Peninsula de Paraguana, Venezuela. Revista de la Facultad de Ingenieria, 11, 35-45.

Roche, R.C., Abel, R.L., Johnson, K.G., Perry, C.T. 2010. Quantification of porosity in *Acropora pulchra* (Brook 1891) using X-ray micro-computed tomography techniques. Journal of Experimental Marine Biology and Ecology, 396, 1-9.

Roche, R.C., Abel, R.L., Johnson, K.G., Perry, C.T. 2011. Spatial variation in porosity and skeletal element characteristics in apical tips of the branching coral *Acropora pulchra* (Brook, 1891). Coral Reefs, 30, 195-201

Roulier, L.M., Quinn, T.M. 1995. Seasonal- to decadal-scale climatic variability in southwest Florida during the middle Pliocene: Inferences from a coralline stable isotope record. Paleoceanography, 10, 429-443.

Sanyal, A., Nugent, M., Reeder, R.J., Bijma, J. 2000. Seawater pH control on the boron isotopic composition of calcite: Evidence from inorganic calcite precipitation experiments. Geochimica et Cosmochimica Acta, 64, 1551-1555.

Scholle, P.A., Ulmer-Scholle, D.S. 2003. A colour guide to the petrography of carbonate rocks. AAPG Memoir 77, U.S.A.

Schönburg, C.H., Shields, G. 2008. Micro-computed tomography for studies of *Entobia*: transparent substrate versus modern technology. Current Developments in Bioerosion, Earlangen Earth Conference Series, doi: 10.1007/978-3.540-77598-0_8.

Schroeder, E., Stommel, H. 1969. How representative is the series of *Panulirus* stations of monthly mean conditions off Bermuda? Progress in Oceanography, 5, 31-40.

Shen G.T., Dunbar, R.B. 1995. Environmental controls on uranium in reef corals. Geochimica et Cosmochimica Acta, 59, 2009-2024.

Simon L., Lecuyer C., Marechal C. and Coltice N. 2006. Modelling the geochemical cycle of boron: Implications for the long-term d11B evolution of seawater and oceanic crust. Chemical Geology, 225, 61–76.

Sinclair, D.J. 2005. Non-river flood barium signals in skeletons of corals from coastal Queensland, Australia. Earth and Planetary Science Letters, 237, 354-369.

Sinclair, D.J., Kinsley, L.P., McCulloch, M.T. 1998. High resolution analysis of trace elements in corals by laser ablation ICP-MS. Geochimica et Cosmochimica Acta, 62, 1889-1901.

Sinclair, D.J. and McCulloch, M. T. 2004. Corals record low mobile barium concentrations in the Burdekin river during the 1974 flood: Evidence for limited Ba supply to rivers? Palaeogeography, Palaeoclimatology, Palaeoecology, 214, 155-174.

Smith, J.F., Quinn, T.M., Helmle, K.P., Halley, R.B. 2006. Reproducibility of geochemical signals in the Atlantic coral *Montastraea faveolata*. Paleoceanography, 21, PA1010.

Spalding, M.D., Ravilious, C., Green, E.P. 2001. Chapter 1. The world of coral reefs. World Atlas of Coral Reefs. 1st edition. Berkley, USA: UNEP World Conservation Monitoring Centre, University of California Press, 14-45.

Stanley, S., Hardie, L. 1998. Secular oscillations in the carbonate mineralogy of reef-building and sediment-producing organisms driven by tectonically forced shifts in seawater chemistry. Palaeogeography, Palaeoclimatology, Palaeoecology, 144, 3-19.

Steiger, R.H., Jäger, E. 1977. Subcommission on geochronology: Convention on the use of decay constants in geo- and cosmochronology. Earth and Planetary Science Letters, 36, 359-362.

Stolarski, J. 2003. Three-dimensional micro- and nanno structural characteristics of the scleractinian coral skeleton: A biocalcification proxy. Acta Palaeontologica Polonica, 48, 497-530.

Swart, P.K., Elderfield, H., Greaves, M.J. 2002. A high-resolution calibration of Sr/Ca thermometry using the Caribbean coral *Montastraea annularis*. Geochemistry, Geophysics, Geosystems, 3, 8402. doi:10.1029/2002GC000306.

Swart, P.K. 2009. Trace elements in carbonates. http://mgg.rsmas.miami.edu/groups/sil/TraceElements.pdf. Accessed 11/01/2011.

Tambutté, S., Holcomb, M., Ferrier-Pagès, C., Reynaud, S., Tambutté, E., Zoccola, D., Allemand, D. 2011. Coral biomineralization: From the gene to the environment. Journal of Experimental Marine Biology and Ecology, 408, 58-78.

Tesoriero, A.J., Pankow, J.F. 1996. The solid solution partitioning of $Sr^{2+}$, $Ba^{2+}$ and $Cd^{2+}$ to calcite. Geochimica et Cosmochimica Acta, 60, 1053-1063.

Thirlwall, M.F. 1991. Long-term reproducibility of multicollector Sr and Nd isotope ratio analysis. Chemical Geology (Isotope Geochemistry Section) 94, 85-104.

Thomas, D. J., MacDonald, W. D. 1970. The Cantaure Formation of the Paraguaná Peninsula. Boletin Informativo Asociacion Venezolana de Geologia, Mineria y Petroleo, 13, 177-179.

Tucker, M.E., Wright, V.P. 1990. Diagenetic processes, products and environments. Chapter 7, Carbonate Sedimentology, Blackwell Science, Oxford, 314-364.

Tudhope, A.W., Chilcott, C.P., McCulloch, M.T., Cook, E.R., Chappell, J., Ellam, R.M., Lea, D.W., Lough, J.M., Shimmield, G.B. 2001. Variability in the El Niño – Southern oscillation through a glacial-interglacial cycle. Science, 291, 1511-1517.

Tudhope, A.W., Lea, D.W., Shimmield, G.B., Chilcott, C.P., Head, S. 1996. Monsoon climate and Arabian Sea coastal upwelling recorded in massive corals from southern Oman. Palaios, 11, 347-361.
U.S. National Climatic Data Centre. http://www.ncdc.noaa.gov/oa/ncdc.html Accessed 01/06/2010.

Vacher H.L., Rowe, M.P. 2004. Geology and hydrogeology of Bermuda. Developments in Sedimentology, 54, 35-90.

Vaughan, T.W. 1919. Fossil corals from Central America, Cuba, and Porto Rico, with an account of the American Tertiary, Pleistocene, and recent coral reefs. Smithsonian Institution, United States National Museum Bulletin, 103, 189-524.

Veizer, J. 1983. Chemical diagensis of carbonates: theory and application of trace element technique. In: M.A. Arthur., T.F. Anderson., I.R. Kaplan., J. Veizer., L.S. Land (Eds). Stable Isotopes in sedimentary geology, SEPM Short Course No 10, 3-1 to 3-100. SEPM, Dallas, U.S.A.

Von der Heydt, A., Dijkstra, H.A. 2005. Flow reorganizations in the Panama Seaway. A caure for the demise of Miocene corals? Geophysical Research Letters, 32, L02609.

Veron, J.E.N. 2000a. Corals of the World. Volume 2. Australian Institute of Marine Science, Townsville, Australia. pp. 138-143.

Veron, J.E.N. 2000b. Corals of the World. Volume 3. Australian Institute of Marine Science, Townsville, Australia, 212-225; 276-345.

Wainwright, S.A. 1963. Skeletal organization in the coral, *Pocillopora damicornis.* Quarterly Journal of Microscopical Sciences, 104, 169-183.

Walter, L.M., Morse, J.W. 1984. Reactive surface area of skeletal carbonates during dissolution: effect of grain size. Journal of Sedimentary Petrology, 54, 1081-1090.

Watanabe, T., Minagawa, M., Oba, T., Winter, A. 2001. Pretreatment of coral aragonite for Mg and Sr analysis: Implications for coral thermometers. Geochemical Journal, 35, 265-269.

Weiss, M.P. 1994. Oligocene limestones of Antigua, West Indies: Neptune succeeds Vulcan. Caribbean Journal of Science, 30, 1-29.

Welsh, B.L., Bessette, D., Herring, J.P., Read, L.M. 1979. Mechanisms for detrital cycling in nearshore waters at Bermuda. Bulletin of Marine Science, 29, 125-139.

Wyndham, T., McCulloch, M., Fallon, S., Alibert, C. 2004. High-resolution coral records of rare earth elements in coastal seawater: biogeochemical cycling and a new environmental proxy. Geochimica et Cosmochimica Acta, 68, 2067-2080.

Zachos, J.C., Shackleton, N.J., Revenaugh, J.S., Pälike, H., Flower, B.P. 2001. Climate response to orbital forcing across the Oligocene-Miocene boundary. Science, 292, 274-278.

# Appendix 1

Fossil fish otoliths are very abundant in the Cantaure Formation and have been extensively researched in order to document species diversity and reconstruct palaeo-environmental conditions during the Early Miocene in north-western Venezuela (Nolf and Aguilera, 1998; Aguilera and Rodrigues de Aguilera, 2003; Aguilera and Rodrigues de Aguilera 2004; Aguilera et al, 2013).

The fossil fish otoliths documented here were collected during a field trip to Venezuela undertaken in 2009. The otoliths were identified to species level where possible using published taxonomic descriptions and images (Nolf and Aguilera, 1998; Aguilera and Rodrigues de Aguilera, 2003; Aguilera and Rodrigues de Aguilera 2004).

Thin sections were prepared from several of the otoliths in order to investigate their state of preservation and suitability for geochemical analysis but were found to be heavily contaminated by hydrocarbon ingress. No further work was carried out on the otolith material. The fossil otoliths and prepared thin sections are currently stored in the Earth Science Department, Royal Holloway University of London.

A list of the species identified from the Canature Formation during the field excursion undertaken for this research are listed on the following page along with the fossil coral species collected on the same field trip.

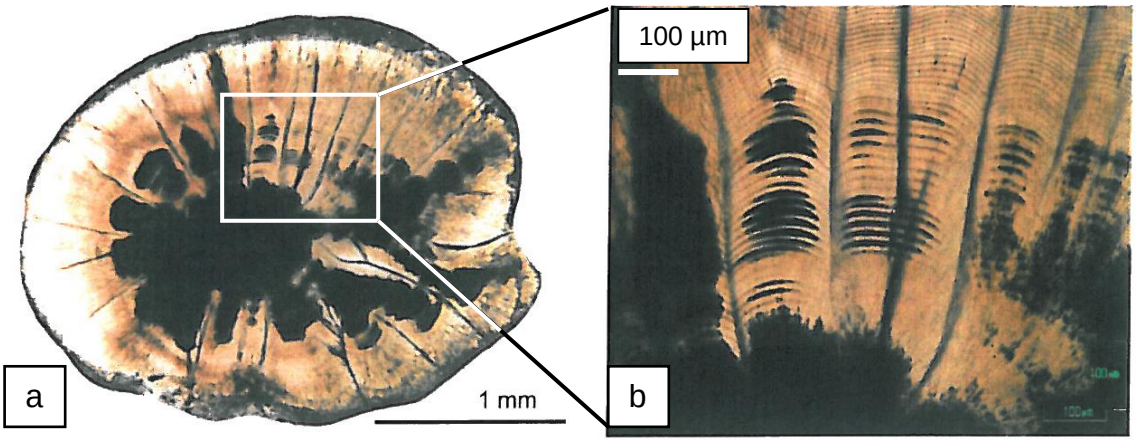


Light micrograph showing oil contamination within fossil *Diaphus* sp otolith (a). Daily growth band couplets consisting of dark (organic) and light (aragonite) layers. Note oil-contaminated organic layers (b).

# Appendix 1

Otolith-based fish species from the Cantaure Formation, Falcón State, Venezuela.

| FAMILY | SPECIES |
|---|---|
| CONGRIDAE | *Arisoma balearicus* (DeLaroche, 1980) |
| | *Conger* sp |
| | *Hildebrandia flavus* (Goode & Bean, 1896) |
| HETERENCHELYDIAE | *Pythonichthys* sp |
| ARIIDAE | *Bagre marinus* (Mitchill, 1815) |
| | *Genidens genidens* (Valenciennes, 1840) |
| MYCTOPHIDAE | *Diaphus* sp |
| CENTROPOMIDAE | *Centropomus* sp |
| APOGONIDAE | *Apogon* sp |
| LACTARIIDAE | *Lactarius aff atlanticus* (Steubaut & Jonet, 1982) |
| LUTJANIDAE | *Pristipomoides* sp |
| HAEMULIDAE | *Haemulon* sp |
| | *Orthopristis* sp |
| SCIAENIDAE | *Aplodinotus* sp |
| | *Aplodinotus longecaudatus* (Nolf & Aguilera, 1998) |
| | *Aplodinotus hoffmani* (Nolf & Aguilera, 1998) |
| | *Cynoscion* sp |
| | *Equetus* sp |
| | *Equetus davidandrewi* (Nolf & Aguilera, 1998) |
| | *Equetus aff punctatus* (Bloch & Schneider, 1801) |
| | *Larimus aff breviceps* (Cuvier, 1830) |
| | *Larimus henrii* (Nolf & Aguilera, 1998) |
| | *Larimus steurbauti* (Nolf & Aguilera, 1998) |
| | *Pachyurus jungi* (Aguilera & Aguilera, 2004) |
| | *Paralonchurus schwarzhansi* (Aguilera & Aguilera, 2004) |
| | *Plagioscion* sp |
| | *Plagioscion marinus* (Aguilera & Aguilera, 2004) |
| | *Protosciaena neritica* (Aguilera & Aguilera, 2004) |
| | *Sciaenops* sp |
| | *Sciaenops reyesi* (Aguilera & Aguilera, 2004) |
| GOBIIDAE | Gobiidae |
| BOTHIDAE | Bothidae |
| | *Citharichthys* sp |
| ACROPOMATIDAE | *Parascombrops aff argyreus* (Alcock, 1969) |

# Appendix 1

Coral species from the Cantaure Formation, Falcón State, Venezuela. (Identifications provided by K.G. Johnson, NHM, London).

Zooanthellate corals

| FAMILY | SPECIES |
|---|---|
| PORITIDAE | *Porites* sp |
| SIDERASTREIDAE | *Siderastrea conferta* (Duncan, 1863) |
| FAVIIDAE | *Montastraea limbata* (Duncan, 1863) |
| FAVIIDAE | *Solenastrea* sp |

Azooanthellate corals

| FAMILY | SPECIES |
|---|---|
| DENDROPHYLLIIDAE | *Dendrophyllia* sp |

# Appendix 2

Mineral Powder Diffraction File Databook. Sets 1-42. 1993. International Centre for Diffraction Data, Pennsylvania, USA. (King et al. 1993)
Conversion chart of 2θ to angstroms (D-spacing) for Cu *K-α* radiation compiled by M.J. Smith, University of Durham, UK.

Aragonite (Card N$^{o}$ 41-1475)

| dÅ | % most abundant peak | 2(θ) Cu *K-α* |
|---|---|---|
| 4.212 | 3 | 21.1 |
| 3.984 | 1 | 22.3 |
| 3.397 | 100 | 26.2 |
| 3.274 | 50 | 27.2 |
| 2.872 | 6 | 31.1 |
| 2.733 | 9 | 32.8 |
| 2.702 | 60 | 33.1 |
| 2.481 | 40 | 36.2 |

Calcite (synthetic) (Card N$^{o}$ 5-586)

| dÅ | % most abundant peak | 2(θ) Cu *K-α* |
|---|---|---|
| 3.86 | 12 | 23.05 |
| 3.035 | 100 | 29.4 |
| 2.845 | 3 | 31.45 |
| 2.495 | 14 | 36.0 |

Quartz (synthetic) (Card N$^{o}$ 33-1161)

| dÅ | % most abundant peak | 2(θ) Cu *K-α* |
|---|---|---|
| 4.257 | 22 | 20.85 |
| 3.342 | 100 | 26.7 |
| 2.457 | 8 | 36.55 |

**Laser ablation depth profile analyses**
**MACS-3 data obtained for separate analytical sessions**

| | B | Mg | Sr | Ba | U |
|---|---|---|---|---|---|
| Preliminary reference values USGS (ppm) | n.a. | 1756 | 6700 | 58.7 | 1.52 |
| ± | n.a. | 136 | 350 | 2 | 0.04 |
| rel ± [%] | n.a. | 7.74 | 5.18 | 3.41 | 2.63 |
| Mean overall (ppm) | 9.86 | 2169.19 | 6263.66 | 58.04 | 1.37 |
| 1 SD | 1.33 | 94.60 | 334.71 | 1.71 | 0.23 |
| 1 RSD (%) | 13.45 | 4.36 | 5.34 | 2.95 | 16.87 |
| # analyses | 30 | 30 | 30 | 30 | 30 |
| Mean (ppm) 23/04/2010 | 8.45 | 2242.15 | 6569.63 | 58.43 | 1.34 |
| 1 SD | 0.63 | 36.86 | 187.76 | 2.46 | 0.31 |
| 1 RSD (%) | 7.42 | 1.64 | 2.86 | 4.20 | 23.01 |
| # analyses | 6 | 6 | 6 | 6 | 6 |
| Mean (ppm) 19/05/2010 | 9.45 | 2225.29 | 5911.22 | 58.55 | 1.38 |
| 1 SD | 0.48 | 60.28 | 125.95 | 0.93 | 0.22 |
| 1 RSD (%) | 5.07 | 2.71 | 2.13 | 1.59 | 15.77 |
| # analyses | 12 | 12 | 12 | 12 | 12 |
| Mean (ppm) 06/07/2010 | 11.65 | 2091.04 | 6538.80 | 57.72 | 1.41 |
| 1 SD | 0.92 | 63.67 | 160.90 | 1.94 | 0.23 |
| 1 RSD (%) | 7.93 | 3.04 | 2.46 | 3.36 | 16.43 |
| # analyses | 8 | 8 | 8 | 8 | 8 |
| Mean (ppm) 26/01/2011 | 9.64 | 2047.72 | 6311.74 | 56.60 | 1.31 |
| 1 SD | 0.54 | 47.51 | 128.85 | 1.41 | 0.22 |
| 1 RSD (%) | 5.57 | 2.32 | 2.04 | 2.49 | 16.93 |
| # analyses | 4 | 4 | 4 | 4 | 4 |
| **Correction factors applied** | | | | | |
| Session 23/04/2010 | 1.168 | 0.967 | 0.953 | ------ | ------ |
| Session 19/05/2010 | 1.043 | 0.975 | 1.060 | ------ | ------ |
| Session 06/07/2010 | 0.847 | 1.037 | 0.958 | ------ | ------ |
| Session 26/01/2011 | 1.023 | 1.059 | ------ | ------ | ------ |

# Appendix 3

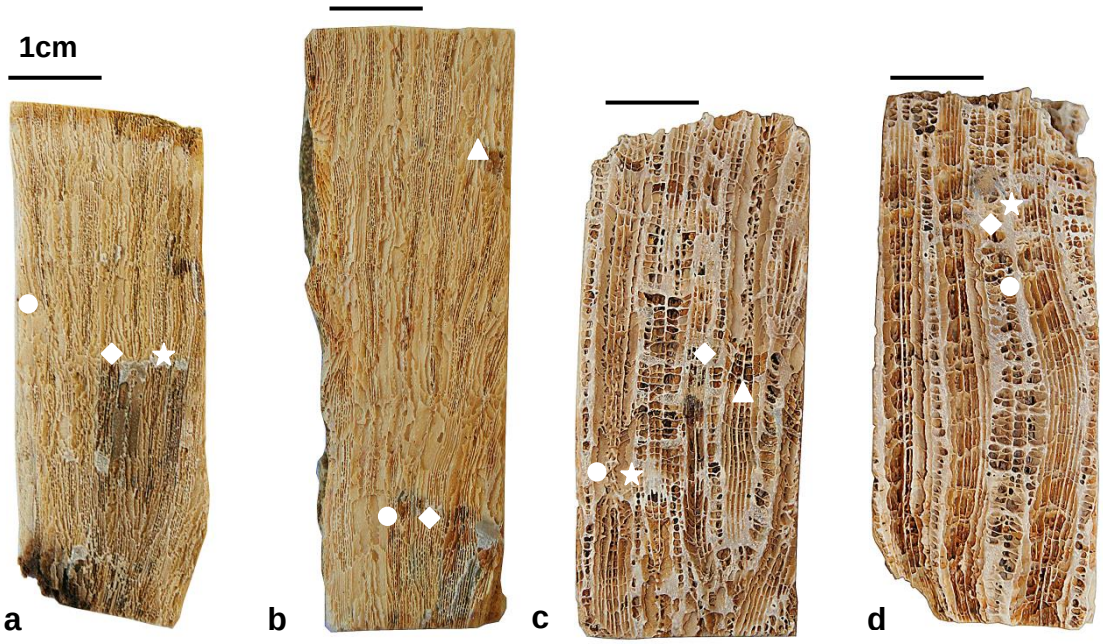


NHMUK AZ 4874
*S. conferta*

NHMUK AZ 4875
*S. conferta*

NHMUK AZ 4876
*M. limbata*

NHMUK AZ 4878
*M. limbata*

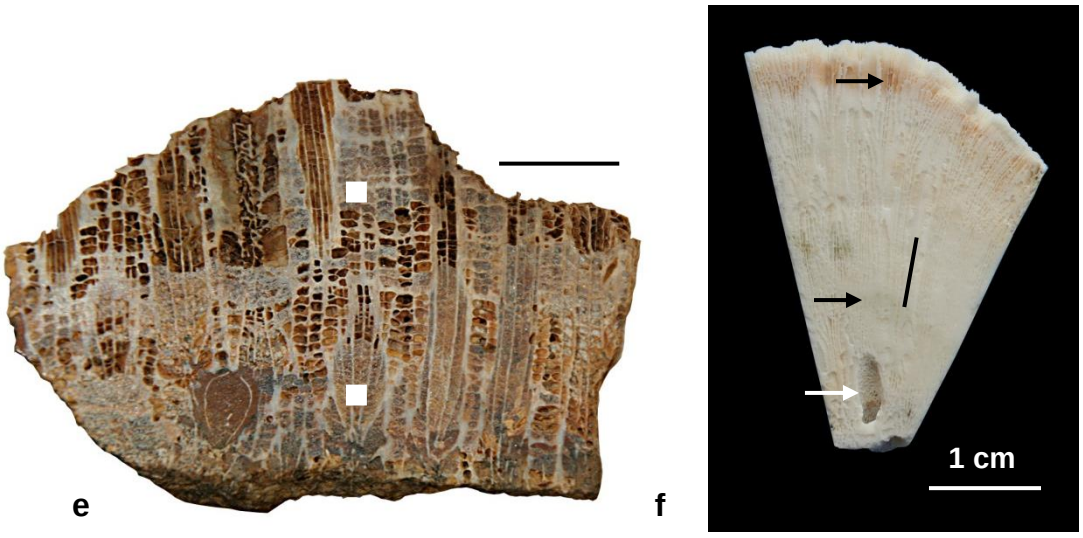


NHMUK AZ 4877
*M. limbata*

NHMUK AZ 4879
*S. radians* (modern)

a – e. Digital images showing the slabs of Miocene coral samples investigated and the regions targeted for laser ablation. Circles = primary aragonite sample sites, diamonds = blocky aragonite, stars = bladed aragonite, and triangles = hydrocarbon coated aragonite/cement. Squares indicate calcite cement sample sites. (f). Sliced block of modern *Siderastrea radians* showing the position of the sampling track (black line). Algal bands (black arrows) and macroboring (white arrow) are visible in the cut slab.

| Primary aragonite | B/Ca | Mg/Ca | Sr/Ca | Ba/Ca | U/Ca |
|---|---|---|---|---|---|
| **NHMUK AZ 4879** | 283.75 | 1.77 | 8.97 | 4.74 | 2.09 |
| | 281.89 | 1.84 | 8.97 | 4.63 | 2.04 |
| | 289.43 | 2.19 | 8.51 | 5.50 | 1.63 |
| | 288.58 | 2.04 | 8.76 | 4.51 | 1.81 |
| | 279.58 | 2.67 | 8.40 | 4.99 | 1.45 |
| Average | 284.65 | 2.10 | 8.72 | 4.87 | 1.81 |
| Standard deviation | 4.26 | 0.36 | 0.26 | 0.39 | 0.27 |
| Standard error | 1.90 | 0.16 | 0.12 | 0.18 | 0.12 |
| | | | | | |
| **NHMUK AZ 4874** | 492.54 | 2.77 | 8.76 | 15.53 | 0.41 |
| | 481.68 | 2.96 | 8.72 | 16.65 | 0.37 |
| | 487.41 | 3.62 | 8.34 | 10.61 | 0.26 |
| | 457.90 | 2.93 | 8.37 | 12.26 | 0.33 |
| | 463.92 | 2.95 | 8.79 | 19.92 | 0.45 |
| Average | 476.69 | 3.05 | 8.59 | 14.99 | 0.36 |
| Standard deviation | 15.06 | 0.33 | 0.22 | 3.68 | 0.08 |
| Standard error | 6.74 | 0.15 | 0.10 | 1.64 | 0.03 |
| | | | | | |
| **NHMUK AZ 4875** | 324.36 | 2.96 | 8.68 | 13.89 | 0.40 |
| | 312.67 | 3.13 | 8.79 | 10.95 | 0.39 |
| | 328.72 | 2.82 | 8.69 | 15.65 | 0.44 |
| | 336.44 | 2.54 | 8.51 | 6.71 | 0.35 |
| | 332.87 | 2.63 | 8.45 | 9.65 | 0.43 |
| Average | 327.01 | 2.82 | 8.62 | 11.37 | 0.40 |
| Standard deviation | 9.20 | 0.24 | 0.14 | 3.52 | 0.04 |
| Standard error | 4.12 | 0.11 | 0.06 | 1.57 | 0.02 |
| | | | | | |
| **NHMUK AZ 4876** | 640.12 | 3.42 | 8.56 | 7.77 | 0.31 |
| | 640.21 | 3.18 | 8.58 | 7.82 | 0.35 |
| | 642.84 | 3.45 | 8.57 | 8.15 | 0.35 |
| | 648.01 | 3.55 | 8.35 | 6.96 | 0.27 |
| | 647.38 | 3.19 | 8.40 | 7.46 | 0.47 |
| Average | 643.71 | 3.36 | 8.49 | 7.63 | 0.35 |
| Standard deviation | 3.80 | 0.17 | 0.11 | 0.45 | 0.08 |
| Standard error | 1.70 | 0.07 | 0.05 | 0.20 | 0.03 |

| Primary aragonite | B/Ca | Mg/Ca | Sr/Ca | Ba/Ca | U/Ca |
|---|---|---|---|---|---|
| **NHMUK AZ 4878** | 604.17 | 2.75 | 8.77 | 9.88 | 0.68 |
| | 633.35 | 4.01 | 8.87 | 10.28 | 0.65 |
| | 535.26 | 2.80 | 8.94 | 11.77 | 0.71 |
| | 602.36 | 2.97 | 8.56 | 6.83 | 0.37 |
| | 560.36 | 3.31 | 8.26 | 7.48 | 0.28 |
| Average | 587.10 | 3.17 | 8.68 | 9.25 | 0.54 |
| Standard deviation | 38.94 | 0.52 | 0.28 | 2.05 | 0.20 |
| Standard error | 17.41 | 0.23 | 0.12 | 0.92 | 0.09 |

| Bladed aragonite | B/Ca | Mg/Ca | Sr/Ca | Ba/Ca | U/Ca |
|---|---|---|---|---|---|
| **NHMUK AZ 4874** | 121.14 | 0.84 | 14.49 | 82.22 | 1.07 |
| | 127.97 | 0.85 | 12.08 | 77.22 | 1.13 |
| | 122.92 | 1.59 | 13.29 | 86.30 | 1.03 |
| | 88.43 | 0.83 | 13.63 | 88.30 | 0.93 |
| | 121.99 | 0.77 | 14.18 | 84.05 | 1.23 |
| Average | 116.49 | 0.98 | 13.53 | 83.62 | 1.08 |
| Standard deviation | 15.91 | 0.35 | 0.94 | 4.25 | 0.11 |
| Standard error | 7.12 | 0.15 | 0.42 | 1.90 | 0.05 |
| **NHMUK AZ 4876** | 165.01 | 0.46 | 10.78 | 14.35 | 1.02 |
| | 142.20 | 0.39 | 11.14 | 14.48 | 0.85 |
| | 89.79 | 0.33 | 11.25 | 12.60 | 0.73 |
| | 108.14 | 0.38 | 10.18 | 14.68 | 0.91 |
| | 93.87 | 0.28 | 10.41 | 8.89 | 0.52 |
| Average | 119.80 | 0.37 | 10.75 | 13.00 | 0.81 |
| Standard deviation | 32.61 | 0.07 | 0.46 | 2.44 | 0.19 |
| Standard error | 14.59 | 0.03 | 0.21 | 1.09 | 0.09 |

**Calculation of ∆ temp**

Sr/Ca (Siderastrea) = Maupin et al., (2008)
Sr/Ca (Montastraea) = Swart et al., (2002)
All other temperature calibrations = Sinclair et al., (1998)

| Bladed aragonite | B/Ca | Mg/Ca | Sr/Ca | Ba/Ca | U/Ca |
|---|---|---|---|---|---|
| NHMUK AZ 4874 | 0.17 | -0.13 | -1.26 | 0 | -0.15 |
| NHMUK AZ 4876 | 0.25 | -0.18 | -0.48 | 0 | -0.1 |

| Blocky aragonite | B/Ca | Mg/Ca | Sr/Ca | Ba/Ca | U/Ca |
|---|---|---|---|---|---|
| **NHMUK AZ 4874** | 32.03 | 0.10 | 11.94 | 20.86 | 0.09 |
| | 54.45 | 0.21 | 14.48 | 38.50 | 0.17 |
| | 31.16 | 0.10 | 12.77 | 24.57 | 0.10 |
| | 32.61 | 0.09 | 13.64 | 26.26 | 0.10 |
| | 28.85 | 0.09 | 13.50 | 28.75 | 0.10 |
| Average | 35.82 | 0.12 | 13.26 | 27.79 | 0.11 |
| Standard deviation | 10.51 | 0.05 | 0.96 | 6.64 | 0.03 |
| Standard error | 4.70 | 0.02 | 0.43 | 2.97 | 0.01 |
| **NHMUK AZ 4875** | 56.45 | 0.08 | 12.28 | 19.87 | 0.02 |
| | 55.01 | 0.09 | 13.07 | 21.37 | 0.02 |
| | 55.51 | 0.15 | 12.10 | 19.53 | 0.05 |
| | 52.79 | 0.13 | 13.41 | 26.54 | 0.04 |
| | 50.66 | 0.04 | 12.41 | 18.35 | 0.02 |
| Average | 54.09 | 0.10 | 12.65 | 21.13 | 0.03 |
| Standard deviation | 2.34 | 0.04 | 0.56 | 3.21 | 0.01 |
| Standard error | 1.05 | 0.02 | 0.25 | 1.44 | 0.01 |
| **NHMUK AZ 4876** | 29.71 | 0.05 | 14.49 | 11.26 | 1.29 |
| | 35.97 | 0.23 | 12.11 | 9.32 | 0.97 |
| | 31.38 | 0.10 | 13.41 | 12.32 | 0.57 |
| | 29.65 | 0.11 | 13.52 | 9.53 | 0.83 |
| | 29.05 | 0.04 | 12.29 | 7.86 | 0.80 |
| Average | 31.15 | 0.11 | 13.16 | 10.06 | 0.89 |
| Standard deviation | 2.83 | 0.07 | 0.98 | 1.75 | 0.27 |
| Standard error | 1.27 | 0.03 | 0.44 | 0.78 | 0.12 |
| **NHMUK AZ 4878** | 29.86 | 0.15 | 17.08 | 8.83 | 0.17 |
| | 19.69 | 0.15 | 10.49 | 5.40 | 0.02 |
| | 19.07 | 0.10 | 12.38 | 11.17 | 0.03 |
| | 18.13 | 0.05 | 11.93 | 4.67 | 0.01 |
| | 21.86 | 0.14 | 11.77 | 14.86 | 0.09 |
| Average | 21.72 | 0.12 | 12.73 | 8.98 | 0.07 |
| Standard deviation | 4.75 | 0.04 | 2.53 | 4.21 | 0.07 |
| Standard error | 2.13 | 0.02 | 1.13 | 1.88 | 0.03 |

**Calculation of Δ temp**

Sr/Ca (Siderastrea) = Maupin et al., (2008)
Sr/Ca (Montastraea) = Swart et al., (2002)
All other temperature calibrations = Sinclair et al., (1998)

| **Blocky aragonite** | **B/Ca** | **Mg/Ca** | **Sr/Ca** | **Ba/Ca** | **U/Ca** |
|---|---|---|---|---|---|
| NHMUK AZ 4874 | 0.21 | -0.18 | -1.2 | 0 | 0.05 |
| NHMUK AZ 4875 | 0.13 | -0.17 | -1.03 | 0 | 0.08 |
| NHMUK AZ 4876 | 0.2 | -0.2 | -0.99 | 0 | -0.12 |
| NHMUK AZ 4878 | 0.27 | -0.19 | -0.86 | 0 | -0.1 |

| **Hydrocarbon** | **B/Ca** | **Mg/Ca** | **Sr/Ca** | **Ba/Ca** | **U/Ca** |
|---|---|---|---|---|---|
| **NHMUK AZ 4875** | 321.66 | 2.15 | 9.01 | 22.84 | 0.63 |
| | 323.93 | 2.04 | 9.57 | 24.25 | 0.65 |
| | 307.48 | 2.24 | 8.76 | 17.22 | 0.51 |
| | 328.82 | 2.78 | 8.96 | 18.34 | 0.45 |
| | 330.18 | 2.20 | 9.05 | 24.29 | 0.56 |
| Average | 322.42 | 2.28 | 9.07 | 21.39 | 0.56 |
| Standard deviation | 9.05 | 0.29 | 0.30 | 3.37 | 0.08 |
| Standard error | 4.05 | 0.13 | 0.14 | 1.51 | 0.04 |
| **NHMUK AZ 4876** | 460.31 | 1.46 | 9.80 | 14.68 | 1.08 |
| | 467.01 | 1.59 | 9.83 | 15.49 | 1.20 |
| | 481.70 | 1.89 | 9.86 | 22.53 | 1.28 |
| | 505.90 | 1.70 | 9.84 | 16.98 | 1.18 |
| | 474.30 | 2.03 | 9.29 | 17.80 | 1.45 |
| Average | 477.84 | 1.73 | 9.72 | 17.50 | 1.24 |
| Standard deviation | 17.60 | 0.23 | 0.24 | 3.07 | 0.14 |
| Standard error | 7.87 | 0.10 | 0.11 | 1.37 | 0.06 |

**Calculation of Δ temp**

Sr/Ca (Siderastrea) = Maupin et al., (2008)
Sr/Ca (Montastraea) = Swart et al., (2002)
All other temperature calibrations = Sinclair et al., (1998)

| **Hydrocarbon** | **B/Ca** | **Mg/Ca** | **Sr/Ca** | **Ba/Ca** | **U/Ca** |
|---|---|---|---|---|---|
| NHMUK AZ 4875 | 0 | -0.03 | -0.11 | 0 | -0.03 |
| NHMUK AZ 4876 | 0.08 | -0.1 | -0.26 | 0 | -0.2 |

| Calcite | B/Ca | Mg/Ca | Sr/Ca | Ba/Ca | U/Ca |
|---|---|---|---|---|---|
| **NHMUK AZ 4877** | 53.48 | 44.93 | 0.39 | 1.60 | 0.93 |
| | 52.12 | 48.00 | 0.44 | 1.51 | 0.82 |
| | 53.81 | 50.40 | 0.40 | 1.47 | 0.99 |
| | 49.79 | 45.32 | 0.44 | 1.89 | 0.78 |
| | 48.62 | 49.57 | 0.39 | 1.26 | 1.56 |
| Average | 51.56 | 47.65 | 0.41 | 1.55 | 1.02 |
| Standard deviation | 2.28 | 2.46 | 0.03 | 0.23 | 0.31 |
| Standard error | 1.02 | 1.10 | 0.01 | 0.10 | 0.14 |

**Calculation of $\Delta$ temp**

Sr/Ca (Siderastrea) = Maupin et al., (2008)
Sr/Ca (Montastraea) = Swart et al., (2002)
All other temperature calibrations = Sinclair et al., (1998)

| Calcite | B/Ca | Mg/Ca | Sr/Ca | Ba/Ca | U/Ca |
|---|---|---|---|---|---|
| NHMUK AZ 4877 | 0.27 | 2.97 | 1.73 | 0 | -0.12 |

# Appendix 4

Publications:

Griffiths, N., Müller, W., Johnson, K.G., Aguilera, O.A. 2013. *Evaluation of the effect of diagenetic cements on element/Ca ratios in aragonitic Early Miocene (~16 Ma) Caribbean corals: Implications for 'deep-time' palaeo-environmental reconstructions.* Palaeogeography, Palaeoclimatology, Palaeoecology, 369, 185-200. (http:/dx.doi.org/10.1016/j.palaeo.2012.10.018).